ISSN 1983-4195

50 YEARS IBRACON

# IBRACON Structures and Materials Journal

Revista IBRACON de Estruturas e Materiais

**Volume 15, Number 3**
June 2022

ISSN 1983-4195
Volume 15, Number 3

IBRACON

# Editorial

I am very honored to have been invited by our *Editor-in-Chief*, Prof. Guilherme Parsekian, to write this issue's editorial. IBRACON (Brazilian Concrete Institute), as you probably know, is celebrating its Jubilee this year of 2022. Fifty years of challenges and realizations dedicated to promoting the concrete industry in our country. This is a tremendous achievement and we all should be immensely proud of what have been done with sacrifice and dedication by members, board, staff, and all participants of our activities.

The *IBRACON Structures and Materials Journal (ISMJ)* is one of the most important realizations of our institute during these 50 years. In 2007, along with my colleagues, I participated in the creation of the *Structural Journal* and the *Materials Journal*. Later these two periodicals have been merged into the current format of the *IBRACON Structures and Materials Journal (ISMJ)*. Many difficulties and challenges had to be dealt with over this period, but we have succeeded to consolidate our publication, while improving its editorial quality. Since then, the IBRACON Journal has built a positive reputation in Latin America, as one of the most important scientific publications in Civil Engineering. This recognition is also observed worldwide over the recent years and the participation of a respectable number of international Associate Editors reflects this aspect.

During the early life of our journal, the dedication and enthusiasm of our now *Editor-in-Chief Emeritus*, Prof. José Luiz Antunes de Oliveira e Sousa, have been crucial for the success of our journal. Years ago, Prof. José Luiz gladly embraced the challenge to consolidate the periodical even with the financial and management limitations of that time. He should be honored and credited, in the name of all our collaborators, for all the accomplishments we have been observing in the recent yeas under the competent leadership of our current *Editor-in-Chief*.

Prof José Luiz is much more than a colleague for me. He has been a fraternal and loyal friend over all my professional and personal life. I am very grateful to him for all he has taught me, as a friend, a professor, a professional and as a human being, since our old times at Cornell University. Lots of good memories from that time. My sincere thanks to you, Mr. Super! It has been a pleasure to share with you my dreams, challenges, problems, solutions, and accomplishments all this time.

Of course, the constant support provided by the IBRACON Board of Directors, and all the past and future Presidents is deeply appreciated and is key for the future of our now well established periodical. *ISMJ* is included in the *SciELO* collection and is expected soon to be part of the Scopus database, as well.

As part of the 2022 celebrations, we are proud to announce one more issue of our *IBRACON Structures and Materials Journal (ISMJ)*.

Enjoy your reading

*Túlio Nogueira Bittencourt*
*Associate Editor*
*Past President of IBRACON*

ISSN 1983-4195
Volume 15, Number 3
June 2022

# IBRACON Structures and Materials Journal
## Revista IBRACON de Estruturas e Materiais

## Contents

*Experimental analysis of steel fiber reinforced concrete beams in shear*........15301
A. K. L. L. NZAMBI, D. R. C. OLIVEIRA, M. V. S. MONTEIRO and L. F. A. SILVA

*Optimum design of a composite floor system considering environmental and economic impacts*........15302
P. A. T. ARPINI, M. C. LOUREIRO, B. D. BREDA, A. F. CALENZANI and E. C. ALVES

*Ultrasonic wave propagation in thermally treated concrete up to 400ºC*........15303
A. C. C. VIANA, P. D. MORAES and I. J. PADARATZ

*RC-INSANE – an interactive environment for nonlinear analysis of reinforced concrete structures*........15304
P. D. N. REGES, R. L. S. PITANGUEIRA and L. L. SILVA

*Global analysis of DEF damage to concretes with and without fly-ash*........15305
N. P. HASPARYK, D. SCHOVANZ, F. TIECHER and S. C. KUPERMAN

*Experimental study of shear transfer in slim floor systems using precast concrete hollow core slabs and steel beam with web circular opening*........15306
G. COLDEBELLA, S. E. PEREIRA JR and S. DE NARDIN

*Correlation between diffusion coefficient values of chloride ions obtained through column and ion migration tests in cementitious matrices with varying contents of silica fume and mortar*........15307
S. A. PINTO, S. L. MACHADO and D. V. RIBEIRO

*Reliability analysis of slender columns using the general method with linear creep theory*........15308
K. RIBEIRO, D. D. LORIGGIO and M. V. REAL

*Short columns composed of concrete-filled steel tubes in a fire situation – Numerical model and the "air-gap" effect*........15309
F. M. RODRIGUES, A. L. MORENO JR and J. MUNAIAR NETO

*Crestbond shear connector for load transfer on concrete filled composite columns in fire*........15310
L. F. P. PRADO, L. G. J. MIRANDA and R. B. CALDAS

**Cover:** Parametric Tower

**Courtesy:** Marcela Noronha P. de O. e Sousa

IBRACON

**Ibracon Structures and Materials Journal** is published bimonthly
(February, April, June, August, October, and December) by IBRACON.

**IBRACON**
Instituto Brasileiro do Concreto Founded in 1972

Av. Queiroz Filho, nº 1700 — sala 407/408
Torre D — Villa Lobos Office Park
CEP 05319-000 — São Paulo, SP — Brazil
Phone: +55 11 3735-0202
Fax: +55 11 3733-2190
**E-mail:** riem@ibracon.org.br
**Website:** http://www.ibracon.org.br

**Cover design & Layout:** Editora Cubo
www.editoracubo.com.br

# Aims and Scope

## Aims and Scope

The IBRACON Structures and Materials Journal (in Portuguese: Revista IBRACON de Estruturas e Materiais) is a technical and scientific divulgation vehicle of IBRACON (Brazilian Concrete Institute), published every two months. Each issue has 12 to 15 articles and, possibly, a technical note and/or a technical discussion regarding a previously published paper. All contributions are reviewed and approved by professionals with recognized scientific competence in the area. The IBRACON Structures and Materials Journal is an open access Journal, free of charges for authors and readers.

## Objectives

The IBRACON Structures and Materials Journal´s main objectives are:

- Present current developments and advances in concrete structures and materials.
- Make possible the better understanding of structural concrete behavior, supplying subsidies for a continuous interaction among researchers, producers, and users.
- Stimulate the development of scientific and technological research in the areas of concrete structures and materials, through papers peer-reviewed by a qualified Editorial Board.
- Promote the interaction among researchers, constructors and users of concrete structures and materials and the development of Civil Construction.
- Provide a vehicle of communication of high technical level for researchers and designers in the areas of concrete structures and materials.

## Submission Procedure

The procedure to submit and revise the contributions, as well as the formats, are detailed in the Journal Website (ismj.org).

The papers and the technical notes are revised by at least two reviewers indicated by the editors. Discussions and replies are accepted for publication after a review by the editors and at least one member of the Editorial Board. In case of disagreement between the reviewer and the authors, the contribution will be sent to a specialist in the area, not necessarily linked to the Editorial Board. Conflict of interests is carefully handled by the Editors.

## Contribution Types

The Journal will publish original papers, short technical notes, and paper discussions. Original papers will be accepted if they are in accordance with the objectives of the Journal and present quality of information and presentation. A technical note is a brief manuscript. It may present a new feature of research, development, or technological application in the areas of Concrete Structures and Materials, and Civil Construction. This is an opportunity to be used by industries, companies, universities, institutions of research, researchers, and professionals willing to promote their works and products under development.

A discussion is received no later than 3 months after the publication of the paper or technical note. The discussion must be limited to the topic addressed in the published paper and must not be offensive. The right of reply is granted to the Authors. The discussions and the replies are published in the subsequent issues of the Journal.

The submission file should be in accordance with the paper template available at the Journal Website. It is recommended that the length of the papers does not exceed 25 pages. Where available, URLs for the references should be provided.

The IBRACON Structures and Materials Journal will conduct the review process for manuscripts submitted in English. Titles, abstracts, and keywords are presented in English, and in Portuguese or Spanish. Articles and technical notes are peer-reviewed and only published after approval of the reviewers and the Editorial Board.

Once accepted, an article is typeset according to the journal layout. The author will be required to review and approve the galleys before publishing. At this stage only typesetting errors will be considered.

## Internet Access

The IBRACON Structures and Materials Journal Webpage is available at http://ismj.org.

## Sponsors

The funds for the maintenance of the Journal are currently obtained from the IBRACON. The Journal is not supposed to be maintained with funds from private sponsorship, which could diminish the credit of the publications.

## Photocopying



## Copyright



## IBRACON

Av. Queiroz Filho, 1700 – sala 407/408 – Torre D
Villa Lobos Office Park
05319-000 – Vila Hamburguesa
São Paulo – SP
Phone: +55 (11) 3735-0202
E-mail: riem@ibracon.org.br

## Disclaimer

Papers and other contributions and the statements made, or opinions expressed therein are published on the understanding that the authors of the contribution are the only responsible for the opinions expressed in them and that their publication does not necessarily reflect the views of IBRACON or of the Journal Editorial Board.

# Editorial Board

# Direction

## Board of Direction 2021/2023 Biennium

**President**
Paulo Helene
**1st Vice-President Director**
Júlio Timerman
**2nd Vice-President Director**
Enio José Pazini Figueiredo
**Presidency Advisors**
Arnaldo Forti Battagin
Eduardo Antonio Serrano
Gilberto Antonio Giuzio
Iria Lícia Oliva Doniak
Jaques Pinto
João Luis Casagrande
Jorge Batlouni Neto
José Marques Filho
Mario William Esper
Ronaldo Tartuce
Rubens Machado Bittencourt
Selmo Chapira Kuperman
Simão Priszkulnik
Túlio Nogueira Bittencourt
Wagner Roberto Lopes
**1st Director-Secretary**
Cláudio Sbrighi Neto
**2nd Director-Secretary**
Carlos José Massucato
**1st Treasurer Director**
Júlio Timerman
**2nd Treasurer Director**
Hugo S. Armelin
**Marketing Director**
Alexandre Britez
**Marketing Director Advisor**
Guilherme Covas
**Publications Director**
Guilherme Parsekian
**Publications Director Advisor**
Túlio Nogueira Bittencourt
**Event Director**
Rafael Timerman
**Event Director Advisor**
Luis César De Luca
**Technical Director**
Carlos Britez
**Technical Director Advisor**
Emílio Takagi
**Institutional Relations Director**
César Henrique Daher
**Institutional Relations Director Advisor**
José Vanderley de Abreu
**Course Director**
Jéssica Pacheco
**Course Director Advisor**
André Mendes
**Student Activities Director**
Jéssica Andrade Dantas
**Student Activities Director Advisor**
Patrícia Bauer
**Personnel Certification Director**
Adriano Damásio Soterio
**Personnel Certification Director Advisor**
Paula Baillot
**Research and Development Director**
Bernardo Tutikian
**Research and Development Director Advisor**
Roberto Christ

## Council 2021/2023 Biennium

**Individual Members**
Alio Ernesto Kimura
Antônio Carlos dos Santos
Antônio Domingues de Figueiredo
Arnaldo Forti Battagin
Bernardo Fonseca Tutikian
Carlos José Massucato
César Henrique Sato Daher
Claudio Sbrighi Neto
Enio José Pazini Figueiredo
Geraldo Cechella Isaia
Iberê Martins da Silva
Inês Laranjeira da Silva Battagin
Iria Lícia Oliva Doniak
Jéssika Mariana Pacheco Misko
José Tadeu Balbo
Leandro Mouta Trautwein
Luiz Prado Vieira Júnior (*in memoriam*)
Mário William Esper
Rafael Timerman
Rubens Curti
Vladimir Antonio Paulon

**Past President Members**
Eduardo Antônio Serrano
José Marques Filho
Júlio Timerman
Paulo Roberto do Lago Helene
Ronaldo Tartuce
Rubens Machado Bittencourt
Selmo Chapira Kuperman
Simão Priszkulnik
Túlio Nogueira Bittencourt

**Corporate Members**
ABCIC - Associação Brasileira da Construção Industrializada de Concreto – Iria Lícia Oliva Doniak

ABCP - Associação Brasileira de Cimento Portland – Paulo Camilo Penna

ABECE - Associação Brasileira de Engenharia e Consultoria Estrutural – João Alberto de Abreu Vendramini

ABESC - Associação Brasileira das Empresas de Serviços de Concretagem – Wagner Roberto Lopes

EPUSP - Escola Politécnica da Universidade de São Paulo – Túlio Nogueira Bittencourt

IPT - Instituto de Pesquisas Tecnológicas do Estado de São Paulo – José Maria de Camargo Barros

MC-BAUCHEMIE BRASIL INDÚSTRIA E COMÉRCIO LTDA – Jaques Pinto

PhD Engenharia Ltda – Douglas de Andreza Couto

TQS Informática Ltda – Nelson Covas

VOTORANTIM Cimentos S/A – Mauricio Bianchi

IBRACON Structures and Materials Journal
Revista IBRACON de Estruturas e Materiais
ISSN 1983-4195 ismj.org

ORIGINAL ARTICLE

# Experimental analysis of steel fiber reinforced concrete beams in shear

*Análise experimental de vigas de concreto armado com fibra de aço ao cisalhamento*

Aaron Kadima Lukanu Lwa Nzambi[a]
Dênio Ramam Carvalho de Oliveira[a]
Marcus Vinicius dos Santos Monteiro[a]
Luiz Felipe Albuquerque da Silva[a]

[a]Universidade Federal do Pará – UFPA, Departamento de Engenharia Civil, Belém, PA, Brasil

Received 03 December 2020
Accepted 10 September 2021

**Abstract:** Some normative recommendations are conservative in relation to the shear strength of reinforced concrete beams, not directly considering the longitudinal reinforcement rate. An experimental program containing 8 beams of (100 x 250) mm$^2$ and a length of 1,200 mm was carried out. The concrete compression strength was 20 MPa with and without 1.00% of steel fiber addition, without stirrups and varying the longitudinal reinforcement ratio. Comparisons between experimental failure loads and main design codes estimates were assessed. The results showed that the increase of the longitudinal reinforcement ratio from 0.87% to 2.14% in beams without steel fiber led to an improvement of 59% in shear strength caused by the dowel effect, while the corresponding improvement was of only 22% in fibered concrete beams. A maximum gain of 109% in shear strength was observed with the addition of 1% of steel fibers comparing beams with the same longitudinal reinforcement ratio (1.2%). A significant amount of shear strength was provided by the inclusion of the steel fibers and allowed controlling the propagation of cracks by the effect of stress transfer bridges, transforming the brittle shear mechanism into a ductile flexural one. From this, it is clear the shear benefit of the steel fiber addition when associated to the longitudinal reinforcement and optimal values for this relationship would improve results.

**Keywords:** shear strength, concrete with steel fibers, beams without stirrups.

**Resumo:** Algumas recomendações normativas são conservadoras em relação à resistência ao cisalhamento de vigas de concreto armado, não levando diretamente em consideração a taxa de armadura longitudinal. Assim, foi realizado um experimento contendo 8 vigas de (100 x 250) mm$^2$ e comprimento de 1.200 mm, com concreto de resistência à compressão de 20 MPa com e sem adição de 1,00% de fibra de aço, sem estribos e variando-se a taxa de armadura de flexão. As capacidades de cisalhamento experimentais em comparação com as estimativas das principais normas foram analisadas. Os resultados mostraram que o aumento da taxa de armadura longitudinal de 0,87% para 2,14% em vigas sem fibra de aço levou a uma melhoria de 59% na resistência ao cisalhamento causada pelo efeito de pino, enquanto a melhoria correspondente foi de apenas 22% em vigas de concreto fibroso. Um ganho máximo de 109% na resistência ao cisalhamento foi observado com a adição de 1% de fibras de aço comparando vigas com a mesma taxa de armadura longitudinal (1,2%). Uma quantidade significativa de resistência ao cisalhamento foi fornecida pela inclusão das fibras de aço e permitiu controlar a propagação de fissuras pelo efeito de pontes de transferência de tensão, transformando o mecanismo de cisalhamento frágil em um mecanismo de flexão dúctil. Assim, fica claro o benefício da adição de fibra de aço para o cisalhamento quando associada à armadura longitudinal e valores ótimos para essa relação podem melhorar os resultados.

**Palavras-chave:** resistência ao cisalhamento, concreto com fibras de aço, vigas sem estribos.

**How to cite:** A. K. L. L. Nzambi, D. R. C. Oliveira, M. V. S. Monteiro, and L. F. A. Silva, "Experimental analysis of steel fiber reinforced concrete beams in shear" *Rev. IBRACON Estrut. Mater.*, vol. 15, no. 3, e15301, 2022, https://doi.org/10.1590/S1983-41952022000300001

**Corresponding author:** Aaron Kadima Lukanu Lwa Nzambi. E-mail: aaronkadima@email.com
**Financial support:** None.
**Conflict of interest**: Nothing to declare.
**Data Availability:** The data that support the findings of this study are available from the corresponding author, AKLLN, upon reasonable request.

## 1 INTRODUCTION

Reinforced concrete (RC) is widely used in several structures around the world. Owing to environmental issues in the steel production chain and its associated high costs, several alternatives and technically viable solutions have been proposed in civil construction applications worldwide, such as the use of new composite materials in structural reinforcement, the production chain of which is ecologically friendly using less expensive and more environmentally friendly manufacturing techniques [1]. Therefore, it is essential to understand the various aspects related to the structural capacity of these elements, as well as the properties of the materials that constitute them.

As far as the use of new materials is concerned, the use of steel fiber reinforced concrete (SFRC) has been increasingly used in structures around the world due to its various structural capacity benefits, which according to Yakoub [2], Amin and Foster [3], Nzambi et al. [1] are the increase in shear strength, tensile strength, flexure and ductility. According to Sahoo and Sharma [4], the correct dosage of steel fiber concrete with a minimum steel fiber content of 1% (78.5 kg/m$^3$), can change the beams failure behavior from fragile to ductile, allowing the partial replacement of stirrups in concrete beams and speed in the execution of structures.

Several studies have been developed with SFRC beams without stirrup reinforcement [5], [6], with the objectives of determining the main variables that control the shear behavior. Among these variables are the influence of steel fiber with different longitudinal reinforcement rates, Yavas and Goker [7] and the variation of the fiber volume, Resende et al. [8]. According to Yakoub [2] increasing the steel fibers content may generate an increase in the shear strength and improve the beam ductility.

Experimental results are presented here considering SFRC beams without stirrups tested to failure, varying the reinforcement ratio, thus intending to assess the SFRC beams behavior under shear forces.

## 2 DESIGN CODES SPECIFICATIONS

This section discusses the design models to determine the shear strength of RC and SFRC beams proposed in Model Code 10 [9], ACI 318 [10], ACI 544.4R [11], NBR 16935 [12], NBR 6118 [13], JSCE [14], and to determine the beams flexural strength proposed by Model Code 10 [9].

### 2.1 Shear strength design

The calculation the concrete shear strength capacity of reinforced concrete beams without stirrups and with steel fiber ($V_{MC10,f}$), according to Model Code 10 [9], are given by Equations 1 to 5, where $k_v$ is a parameter that depends on the level of approximation (LoA). The Model Code 10 [9] contains four levels of shear strength approximation (LoA I to LoA IV) consisting of increasing levels of calculation complexity to obtain the most accurate results. The LoA II has been analyzed in this study, recommended for design cases and general evaluation of an existing element. The approach used in this level of approximation is based on the Simplified Modified Compression Field Theory (SMCFT).

$$V_{MC10} = V_{c0} = k_v \cdot \sqrt{f_{ck}} \cdot z \cdot b_w \quad \text{(concrete shear strength capacity)} \tag{1}$$

$$k_v = \frac{0.4}{1+1500 \cdot \varepsilon_x} \cdot \frac{1300}{1000 + k_{dg} \cdot z} \quad \text{(accuracy level, LoA II)} \tag{2}$$

$$k_{dg} = \frac{32}{16 + d_g} \geq 0.75 \tag{3}$$

$$V_{MC10,f} = \left\{ 0.18 \cdot k \cdot \left[ 100 \cdot \frac{A_s}{b_w \cdot d} \cdot \left( 1 + 7.5 \cdot \frac{f_{Ftuk}}{f_{ctk}} \right) \cdot f_{ck} \right]^{\frac{1}{3}} + 0.15 \cdot \sigma_{cp} \right\} \cdot b_w \cdot d \tag{4}$$

(fibers contribution)

$$f_{Ftuk} = f_{Fts} - 0.6 \cdot \left( f_{Fts} - 0.5 \cdot f_{R3} + 0.2 \cdot f_{R1} \right) \geq 0 \tag{5}$$

Where $z$ is the internal lever arm between the flexural tensile and compressive forces ( $z \approx 0.9 \cdot d$ ); $\varepsilon_x$ is the longitudinal strains calculated at distance $z/2$; $k_{dg}$ is an aggregate size influence parameter; $d_g$ is the maximum aggregate size ($d_g$ = 9.5 mm); $k$ is a factor that takes into account the size effect calculated as $k = 1 + \sqrt{200/d} \leq 2.0$ for the effective depth of cross-section ($d$); $f_{Ftuk}$ is the characteristic value of the residual strength in the ultimate limit state (ULS), 0.6 takes into account the ultimate crack opening ($w_u$ = 1.5) over $CMOD_3$ (2.5). It is possible to avoid the use of conventional shear reinforcement (stirrups) if the limitation of $f_{Ftuk} \geq \sqrt{f_{ck}}/20$ is respected; $f_{ctk}$ is the characteristic tensile strength of concrete given as $0.3 \cdot (f_{ck})^{\frac{2}{3}}$ ; $f_{Fts}$ is the value of the residual tensile strength in the service limit state and can be taken as $0.45 \cdot f_{R1}$ ; $\sigma_{cp}$ is average normal stress acting on concrete cross section due to loading or prestressing. In this paper, the normal stress is zero.

The values of $f_{R1}$ and $f_{R3}$ represent residual flexural strength parameters and can be obtained from the load vs CMOD (CMOD = *Crack Mouth Opening Displacement*) diagram. In this paper, the empirical approach proposal of Moraes-Neto et al. [15] to determine the residual flexural strengths $f_{R1}$ and $f_{R3}$ given by Equations 6 and 7 is considered. The empirical equations of Moraes-Neto et al. [15] were established from the fiber reinforcement index ( $RI = C_f \cdot l_f / d_f$ ) that considers the fiber content ($C_f$) and the fiber aspect ratio ($l_f / d_f$) as the most influential parameters on $f_{Ri}$ values. The authors reported a statistical analysis with the data collected from the characterization of the post-cracking behavior of SFRC, notched beams subjected to three-point bending tests. Being aware that it is a rather simple approach to simulate the mechanisms of fiber reinforcement since other variables, such as the fiber-matrix bond strength, fiber inclination and fiber embedment length, influence the $f_{Ri}$ result values, but this information are often not available in the literature on SFRC of beams or slabs. And according to the authors, a relatively large scatter of results is naturally expected, but this approach is the only possibility to consider the fiber reinforcement in design with the absence of experimental data to predict the theoretical shear strength according to the Model Code 10 [9].

$$f_{R1} = 7.5 \cdot RI^{0.8} \tag{6}$$

$$f_{R3} = 6.0 \cdot RI^{0.7} \tag{7}$$

From ACI 318 [10], the shear strength of reinforced concrete beams without stirrups is obtained by Equation 8. The effect of steel fiber addition is considered by ACI 544.4R [11] which consider the same Equation 1 as Model Code 10 [9] for SFRC. The same procedures were also adopted by NBR 16935 [12], $V_{NBR,f} = V_{ACI,f} = V_{MC10,f}$ , while the shear contribution of concrete without steel fiber is calculated according to NBR 6118 [13], Equation 9.

$$V_{ACI} = V_{c0} = \left( \frac{\lambda \cdot \sqrt{f_{ck}}}{6} \right) \cdot b_w \cdot d \tag{8}$$

Where, $V_{c0}$ = concrete contribution to shear capacity (MPa); $\lambda$ is the reduction factor of the mechanical properties of the type of concrete, equal to 1 for normal weight concrete; $f_{ck}$ = concrete compressive strength (MPa); $b_w$ = cross section width (mm); and $d$ = effective height (mm).

$$V_{NBR} = V_{c0} = 0.126 \cdot f_{ck}^{2/3} \cdot b_w \cdot d \tag{9}$$

JSCE [6] recommends Equations 10 and 11 for calculating the shear strength of reinforced concrete beams without stirrups and with steel fiber. The shear strength resisted by the steel fiber ( $V_f$ ) is given by Equation 12. For the calculation of $f_{tyd}$ corresponding to the tensile yield strength of the concrete, Equation 13 was used, proposed by Choi et al. [16], which considers the fiber content ( $C_f$ ) and the shape factor of the steel fiber ( $l_f / d_f$ ).

$$V_{JSCE} = V_{c0} = \beta_d \cdot \beta_p \cdot f_{vcd} \cdot b_w \cdot d \text{ (concrete contribution)} \tag{10}$$

$$V_{JSCE,f} = \beta_d \cdot \beta_p \cdot f_{vcd} \cdot b_w \cdot d + V_f \text{ (fibers contribution)} \tag{11}$$

$$V_f = \frac{f_{tyd} \cdot b_w \cdot d}{1.15 \cdot tg45^{o}} \tag{12}$$

$$f_{tyd} = 0.292 \cdot \left(f_{ck}\right)^{1/2} \cdot \left[1 + C_f \cdot \left(0.1 \cdot \frac{l_f}{d_f} - 1\right)\right] \tag{13}$$

Where, $\beta_d = min\left(\sqrt[4]{\frac{1000}{d}};1.5\right)$ ; $\beta_p = min\left(\sqrt[3]{\frac{1000 \cdot A_s}{b_w \cdot d}};1.5\right)$; $f_{vcd} = min\left(0.20 \cdot \sqrt[3]{f_{ck}};0.72\right)$ and $A_s$ is area of longitudinal tension reinforcement.

## 2.2 Flexural strength

For the calculation of the flexural strength (Equation 14) of conventional and fiber concrete beams, the simplified model proposed by Model Code 10 [9] was adopted, as in Figure 1. The flexural strength parcel due to steel fiber addition is given by $f_{Ftuk}$ , which is previously calculated in Equation 5. The process of calculating the resistant moment, $m_R$ (Equation 15) was carried out via an interactive process after reaching the resultant forces balance ( $\Sigma F_i = 0$ ). According to Model Code 10 [9], the minimum material ductility for structural application, is guaranteed when $f_{R1,k} / f_{L,k} \geq 0.4$ and $f_{R3,k} / f_{R1,k} \geq 0.5$ .

$$V_{flex} = \frac{2 \cdot m_R}{a} \tag{14}$$

$$m_R = F_c \cdot y_c + F_t \cdot y_t + F_s \cdot y_s + F'_s \cdot y'_s \tag{15}$$

Where, $a$ is the shear span; $F_i$ and $y_i$ , respectively, are resultant forces and lever arms.

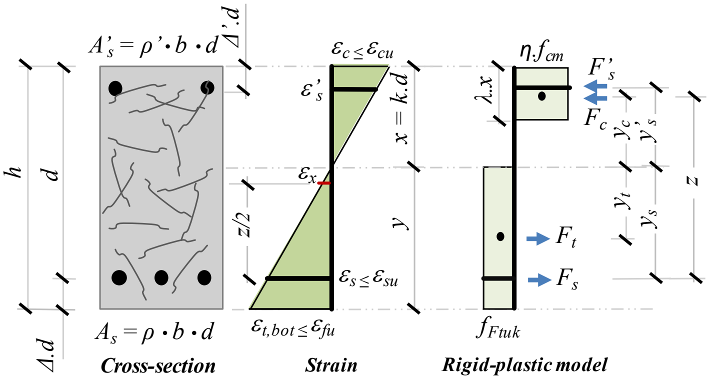


**Figure 1.** Flexure model of Model Code 10 [9].

## 3 EXPERIMENTAL PROGRAM

The experimental program consisted of the testing to failure two series of 4 beams with cross section of (100 x 200) mm$^2$ and length of 1200 mm. The beams were cast without stirrups and with approximately 20-MPa concrete was, with and without the addition of 1% steel fiber. The variables analyzed were the addition of steel fiber and the variation on the longitudinal reinforcement rate.

### 3.1 Materials properties

The concrete constituent materials used in the beams are presented in Table 1. The ABCP-method [17] was adopted for the concrete mix design using CPII - Z cement and rolled pebble with a maximum diameter of 9.5 mm. In addition, for the SFRC, superplasticizer was used to maintain a good workability and the same ratio w/c. The steel fibers used were type C according to the classification of the NBR 15530 [18], the *flat crimped* type (Figure 2a) with length ( $l_f$ ) of 31 mm, equivalent diameter ( $d_f$ ) of 1.2 mm and aspect ratio ( $l_f / d_f$ ) of 25.8. The characteristics of the reinforcing steel bars (Figure 2b) used in this research were obtained from the axial tensile test, according to NBR 6892 [19], and are presented in Table 2.

**Table 1.** Mixture Design.

| Materials | Consumption (Kg/m$^3$) | |
|---|---|---|
| | RC | SFRC |
| Portland CPII-Z32RS Cement | 310.61 | |
| Coarse aggregate (pebble, $d_{max}$ = 9.5 mm) | 1078.53 | |
| Fine aggregate (fine sand) | 781.49 | |
| Water | 205 | |
| w/c | 0.64 | |
| Steel Fiber | - | 78.6 |
| Superplasticizer Admixture | - | 0.95 |

**Table 2.** Steel bars' mechanical properties.

| Location | Ø (mm) | $f_{ys}$ (MPa) | $\varepsilon_{ys}$ (‰) | $E_s$ (GPa) |
|---|---|---|---|---|
| Stirrups | 4.2 | 651 | 5.20 | 203 |
| Longitudinal reinforcement | 6.3 | 540 | 4.40 | 225 |
| | 8.0 | 532 | 2.53 | 210 |
| | 10.0 | 521 | 2.45 | 212 |
| | 12.5 | 560 | 2.48 | 225 |

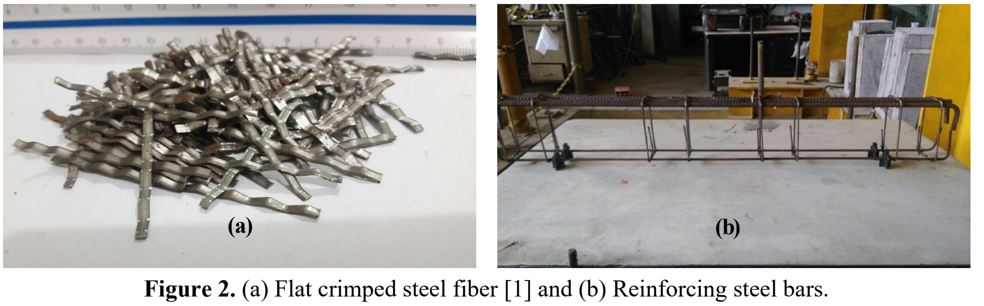


**Figure 2.** (a) Flat crimped steel fiber [1] and (b) Reinforcing steel bars.

### 3.2 Characteristics of beams

Eight reinforced concrete beams without stirrups were tested to failure, divided into two series with 4 beams each: the RC (VS) series, which does not have the addition of steel fiber, and the SFRC (VF) series, which has the addition of 1% steel fiber. The longitudinal reinforcement ratio varied from 0.87% to 2.14%. To measure the strains in the concrete and in the longitudinal reinforcement, electric strength strain gauges (EERs) were used. EXCEL brand sensors that were fixed on the central top surface of the beams to measure the strains in the concrete ($EER_c$ - model PA-06-1500BA-120L), and in the middle of the length of the steel bars to measure the strains in the longitudinal reinforcement ($EER_s$ - model PA-06-125AA-120L). The reading and recording of the data were performed through the Ahlborn ALMEMO ®5690-2M data acquisition equipment, with AMR *WinControl* software. The EERS application locations and typical test system details are shown in Figure 3 The EERS models used in concrete and steel are shown respectively in Figures 4a and 4b. The section properties are shown in Figure 4c. The beams were moulded and cured for 28 days in the laboratory with 85% relative air humidity. Three cylindrical concrete specimens (100 mm diameter and 200 mm height) from each mixture were tested to determine the concrete experimental compressive strength. Table 3 presents the summary of the main characteristics of the tested beams.

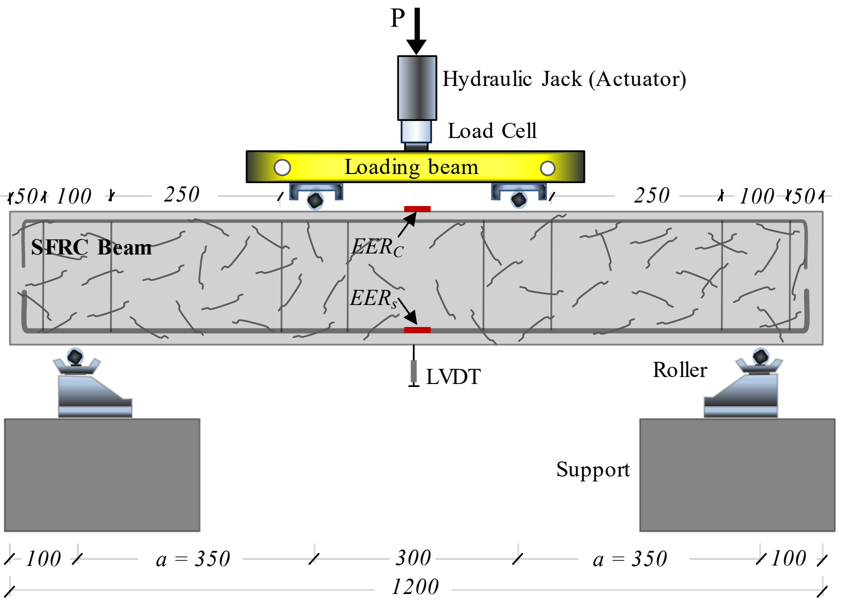


**Figure 3.** Test schema.

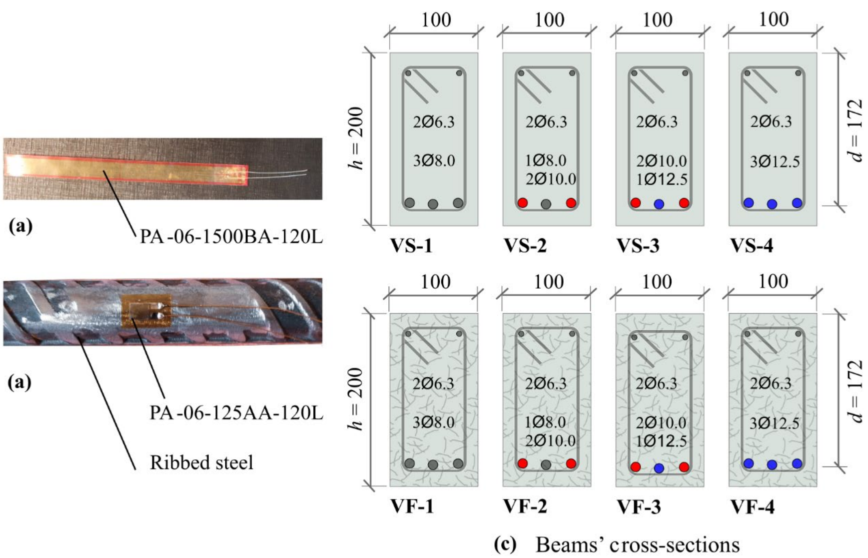


**Figure 4.** (a) Strain gauges model used for the concrete ($EER_c$), (b) Strain gauge on steel bar ($EER_s$) and (c) Detailing of beam sections.

**Table 3.** Characteristics of beams.

| Series | Beams | $d$ (mm) | $a/d$ | $\rho$ (%) | $C_f$ (%) | $f_c$ (MPa) |
|---|---|---|---|---|---|---|
| RC | VS-1 | 172 | 2 | 0.87 | - | **24.0** |
| | VS-2 | | | 1.20 | | **23.1** |
| | VS-3 | | | 1.62 | | **24.7** |
| | VS-4 | | | 2.14 | | **24.2** |
| SFRC | VF-1 | | | 0.87 | 1 | **22.8** |
| | VF-2 | | | 1.20 | | **21.5** |
| | VF-3 | | | 1.62 | | **21.7** |
| | VF-4 | | | 2.14 | | **22.0** |

### 3.3 Test setup and procedure

The test was performed on a TIME brand Hydraulic Universal Testing Machine (HUTM) with 1,000-kN capacity of and closed-loop displacement control. The beams were positioned so that they were loaded in four points (Figure 5) The distance between each the load application point to the support was 350 mm. The load consisted of two concentrated loads 300 mm apart. During the load application process, the test machine monitored the applied displacement and load while the data acquisition equipment recorded the strains in concrete and steel.

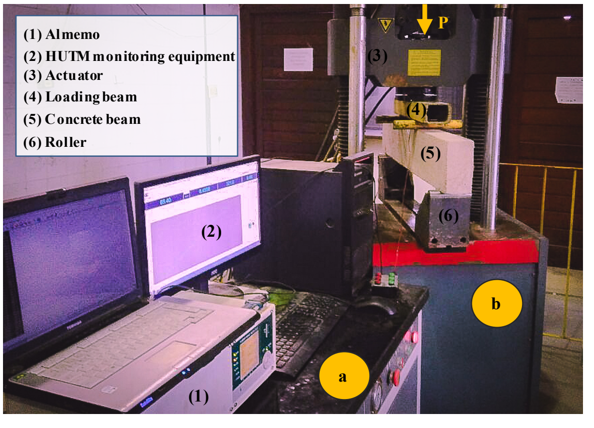


**Figure 5.** (a) Data acquisition equipment and (b) HUTM assembled test system.

## 4 RESULTS AND DISCUSSIONS

Table 4 shows the summary of the experimental results, including the experimental shear strength ($V_{Exp}$), the ultimate shear force ($V_{cort,u} = V_{Exp}/2$), the ultimate shear stress ( $v_u = V_{cort,u}/b \cdot d$), and the beam failure modes. All beams failed by shear and the SFRC beam series showed higher strength and consequently higher shear strength capacity (Figure 6).

**Table 4.** Loads and failure modes of the beams.

| Series | Beam | $\rho$ (%) | $f_c$ (MPa) | $V_{Exp}$ (kN) | $V_{cort,u}$ (kN) | $v_u$ (MPa) | Failure mode |
|---|---|---|---|---|---|---|---|
| RC | VS-1 | 0.87 | **24.0** | **35.5** | **17.8** | **1.0** | **Shear** |
| | VS-2 | 1.20 | **23.1** | **36.2** | **18.1** | **1.1** | |
| | VS-3 | 1.62 | **24.7** | **48.9** | **24.5** | **1.4** | |
| | VS-4 | 2.14 | **24.2** | **56.6** | **28.3** | **1.7** | |
| SFRC | VF-1 | 0.87 | **22.8** | **63.5** | **31.8** | **1.9** | |
| | VF-2 | 1.20 | **21.5** | **75.7** | **37.9** | **2.2** | |
| | VF-3 | 1.62 | **21.7** | **76.3** | **38.2** | **2.2** | |
| | VF-4 | 2.14 | **22.0** | 77.7 | 38.9 | 2.3 | |

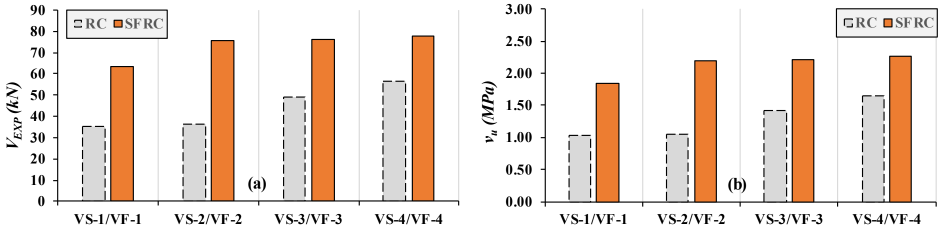


**Figure 6.** (a) Shear strength and (b) Shear stress.

### 4.1 Failure modes

The beams failure modes were all the same, shear with diagonal tensile, as expected, since the beams had no conventional shear reinforcement. Figure 7 shows the failure pattern of the VS-2 and VF-2 beams, which was similar for all beams. Sudden failures with large openings of diagonal cracks were observed in RC beams, while SFRC beams had ductile failures, keeping smaller widths openings cracks as shown in Figure 8. This behaviour is like that reported by Amin and Foster [3]. The shear stress transfer capacity in SFRC generated high failure loads strengths. According to Nzambi et al. [1], the introduction of steel fibers has a significant effect on improving the bond stress performance in terms of the failure load strength, resulting in a more ductile bonding behaviour of reinforcing bars with smaller diameters and the contribution of stress redistribution in the cracked cross-section through the steel fiber bridging effect. Also, concrete peeling was observed more expressively in RC beams, a typical characteristic of dowel effect.

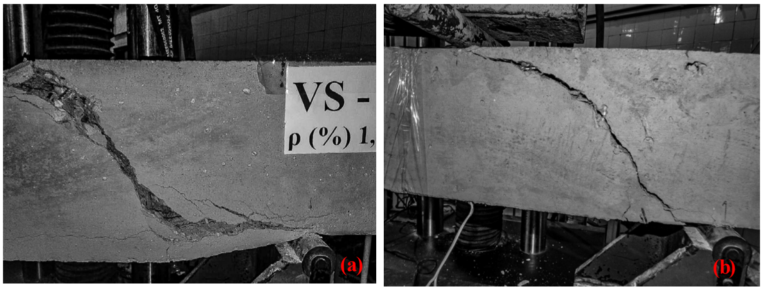


**Figure 7.** Failure pattern: (a) RC e (b) SFRC.

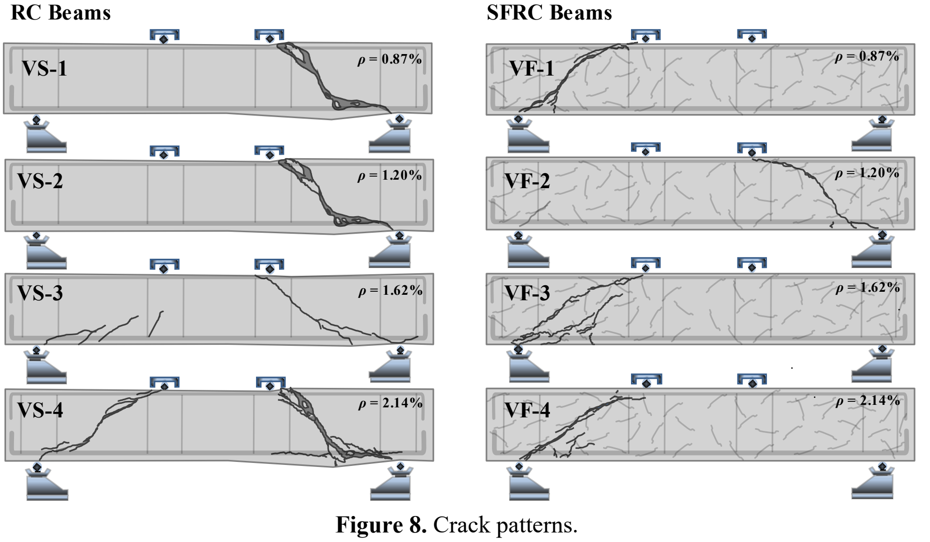


**Figure 8.** Crack patterns.

## 4.2 Strains and failure loads

In general, all beams showed similar strains patterns, with ultimate strains lower than 3.5‰, indicating that there was no concrete crushing. Figure 9 shows the concrete strains for the RC and SFRC series beams, respectively. For the RC beam series, all strains in the longitudinal reinforcement were less than 2.3‰, indicating that there was no yielding of longitudinal reinforcement, which was expected since the beams had no stirrups. In the SFRC series beams, all the beams had strains in the longitudinal reinforcements higher than in the RC series beams due to the addition of 1% steel fiber. In this series it was also observed a decrease in the strains of the longitudinal reinforcement with the increase of the rate of longitudinal reinforcement. Figure 10 shows the strains of the rebar for the RC and SFRC series beams.

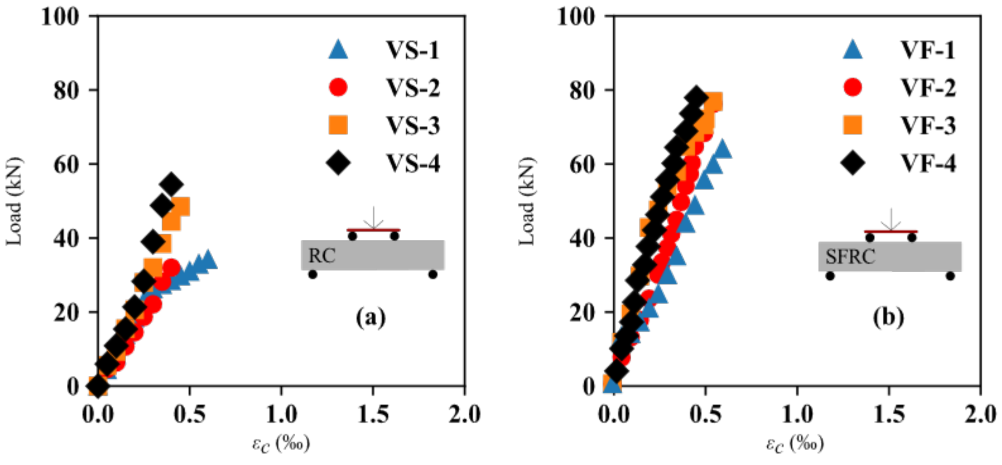


**Figure 9.** Concrete strains for RC and SFRC series.

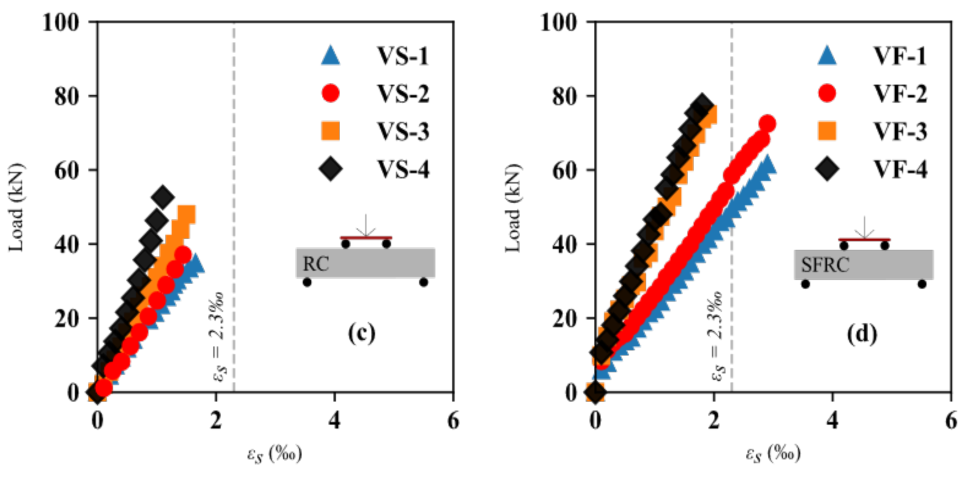


**Figure 10.** Strains in the longitudinal reinforcement for RC and SFRC series.

## 4.3 Effect of longitudinal reinforcement

The SFRC series beams showed, on average, an increase in strength of 70% compared to the RC series beams. The influence of the increase in longitudinal reinforcement was evident in the two beams series, as shown in Figure 11. For the RC beams series this influence was evident by the progressive increase in shear strength with the increase in the longitudinal reinforcement rate. This increase in strength was on average approximately equal to 25% and confirms that the longitudinal reinforcement rate provides a relevant contribution in the shear strength of concrete beams without steel fiber. It was evident that the reinforcement ratio over 1% allowed an increase up to 20% in the shear strength in SFRC, as observed in beams VF-1 and VF-2.

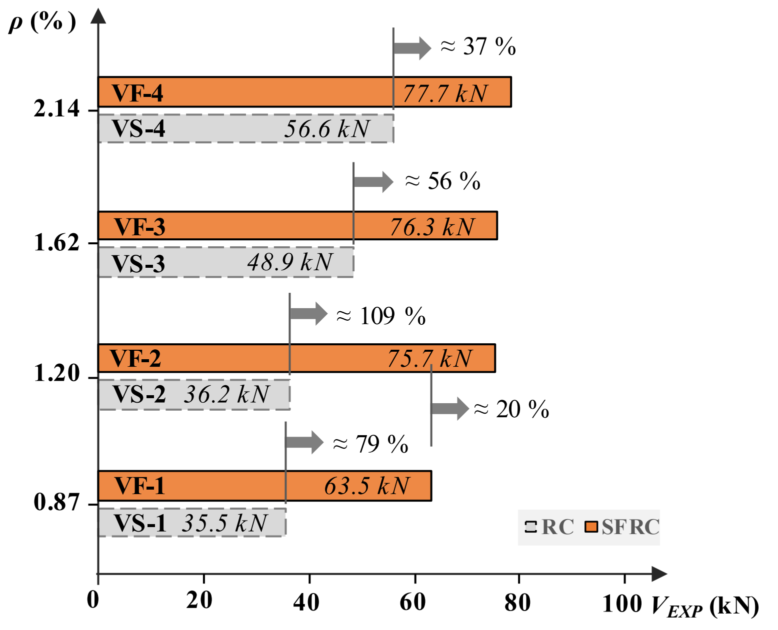


**Figure 11.** Shear strength of the beams and strength gain.

### 4.4 Comparison between experimental and estimates

Table 5 presents the estimates of flexural and shear strength by Model Code 10 [9] compared with the experimental strength ( $V_{Exp}$ ). The Table also presents the relationship $V_{flex}/V_{MC10}$ [20], which represents an estimate for the failure modes of the beams, which can be by shear with $V_{flex}/V_{MC10}$ > 1.0 or by flexure with $V_{flex}/V_{MC10}$ < 1.0. The results presented by the ratio $V_{flex}/V_{MC10}$ indicated that all beams presented shear failure, as observed in the tests. Figures 12a and 12b clearly show the behavior of the flexural reinforcement influence in the failure mode, a similar linear behavior for both the RC beams and the SFRC beams. With the increase in the reinforcement rate, the beams tend to fail more by shear and the addition of 1% of fiber volume in the concrete influenced the reduction on the results dispersion [1], and provided the lowest values of the $V_{flex}/V_{Exp}$ ratio in comparison with the RC beam series.

**Table 5.** Failure mode evaluation.

| Type | Beam | $V_{flex}$ (Eq. 15) (kN) | $V_{Exp}$ (kN) | $V_{MC10}$ (kN) | $V_{flex}/V_{Exp}$ | $V_{flex}/V_{MC10}$ | Failure mode |
|---|---|---|---|---|---|---|---|
| RC | VS-1 | 71.1 | 35.5 | 57.0 | 2.0 | 1.2 | Shear |
| | VS-2 | 94.5 | 36.2 | 55.7 | 2.6 | 1.7 | |
| | VS-3 | 122.8 | 48.9 | 55.4 | 2.5 | 2.2 | |
| | VS-4 | 153.5 | 56.6 | 56.9 | 2.7 | 2.7 | |
| SFRC | VF-1 | 76.2 | 63.5 | 52.0 | 1.2 | 1.6 | |
| | VF-2 | 100.0 | 75.7 | 57.2 | 1.3 | 1.8 | |
| | VF-3 | 128.4 | 76.3 | 63.1 | 1.7 | 2.1 | |
| | VF-4 | 158.9 | 77.7 | 69.5 | 2.0 | 2.3 | |

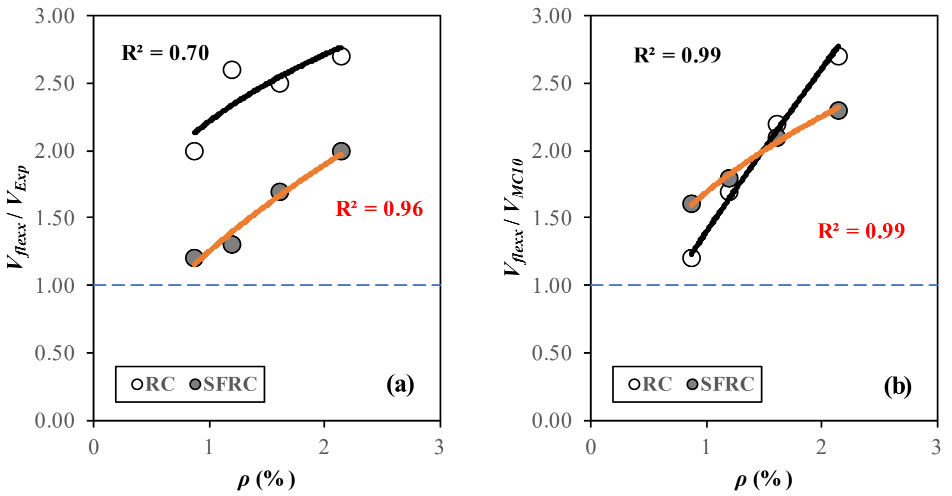


**Figure 12.** Influence of the flexural reinforcement rate on the failure mode: (a) Comparison with the $V_{flex}/V_{Exp}$ relationship and (b) Comparison with the $V_{flex}/V_{MC10}$ relationship.

Table 6 presents the relationship between the experimental loads and the loads estimated by Model Code 10 [9], ACI 318 [10], ACI 544.4R [11], NBR 16935 [12], NBR 6118 [13], and JSCE [14]. In general, the effect of fiber in SFRC tends to reduce the variability of results by around 6% compared to RC which was between 11% for JSCE [14], 23% for Model Code 10 [1] and ACI 318 [10], and 24% for NBR 6118 [13], while figures 13a and 13b clearly show the variability of this comparison of experimental ($V_{Exp}$) and normative shear strength.

It was observed that for the RC beam series, the Model Code 10 [9] overestimated the shear strength of the beams by approximately 40% with a reinforcement rate of 0.87% and 1.2%. The most conservative results were obtained with ACI 318 [10], which presented on average strength values 60% lower than the experimental results. The most accurate results for this series of beams were calculated with JSCE [14], obtaining average strength values 32% lower in relation to the experimental results, but it was observed that the Japanese standard was not able to predict the strength gain of 60% occurred between beams VS-1 and VS-4, provided by the increased rate of longitudinal reinforcement. The lowest coefficient of variation (11%) was also observed with the JSCE [14].

**Table 6.** Results estimated by the standards.

| Beam | $V_{Exp}$ (kN) | $V_{Exp}$ / $V_{MC10}$ | $V_{Exp}$ / $V_{ACI}$ | $V_{Exp}$ / $V_{NBR}$ | $V_{Exp}$ / $V_{JSCE}$ |
|---|---|---|---|---|---|
| | | | **RC** | | |
| VS-1 | 35.5 | 0.62 | 1.25 | 0.97 | 1.24 |
| VS-2 | 36.2 | 0.65 | 1.31 | 1.00 | 1.16 |
| VS-3 | 48.9 | 0.88 | 1.78 | 1.35 | 1.42 |
| VS-4 | 56.6 | 0.99 | 2.01 | 1.57 | 1.48 |
| **Mean** | | **0.79** | **1.59** | **1.22** | **1.32** |
| **Standard deviation** | | **0.18** | **0.37** | **0.29** | **0.15** |
| **Coef. of variation (%)** | | **23** | **23** | **24** | **0.11** |
| | | | **SFRC** | | |
| VF-1 | 63.5 | 1.22 | 1.22 | 1.22 | 0.87 |
| VF-2 | 75.7 | 1.33 | 1.33 | 1.33 | 1.01 |
| VF-3 | 76.3 | 1.21 | 1.21 | 1.21 | 0.98 |
| VF-4 | 77.7 | 1.12 | 1.12 | 1.12 | 0.95 |
| **Mean** | | **1.22** | **1.22** | **1.22** | **0.95** |
| **Standard deviation** | | **0.08** | **0.08** | **0.08** | **0.06** |
| **Coef. of variation (%)** | | **7** | **7** | **7** | **6** |

Note: $V_{MC10,f} = V_{ACI,f} = V_{NBR,f}$ for SFRC according to Model Code 10 [9], ACI 544.4R [11], and NBR 16935 [12], respectively.

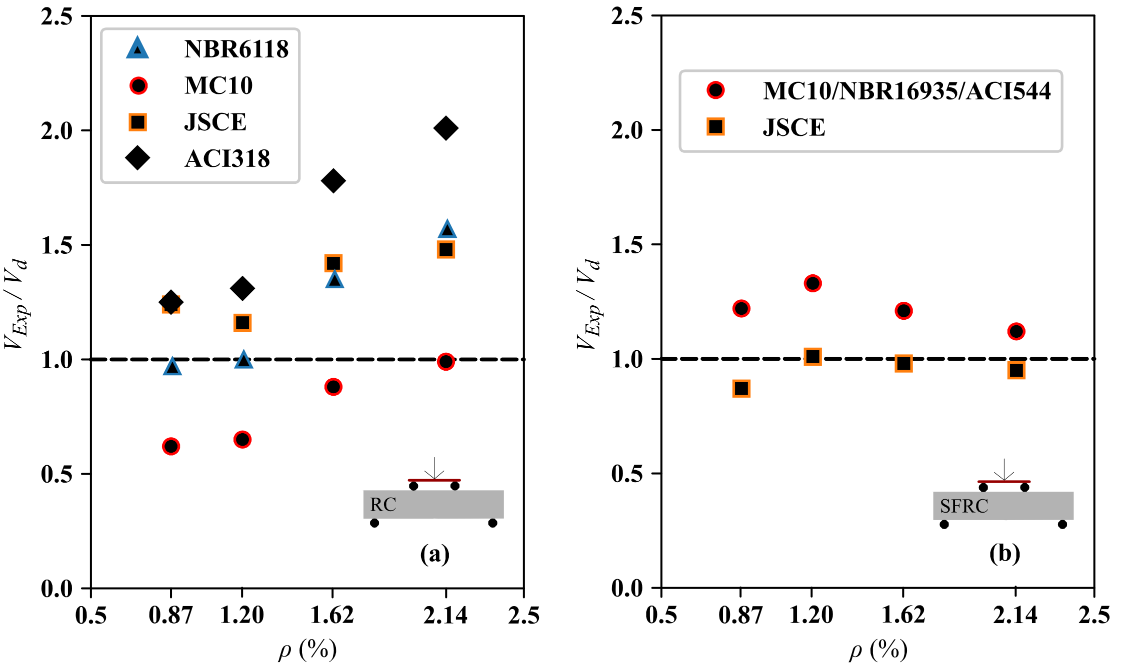


**Figure 13.** Relationship between experimental and shear strength estimates: (a) With the series of beams without fiber and (b) With the series of beams with fiber.

In the analysis of the SFRC series beams, the most accurate results were obtained by JSCE standards [14], which presented average strength values very close to those obtained experimentally, but for the reinforcement rate of 0.86%, the standards overestimated the results by approximately 15%. The most conservative results were obtained by NBR 16935 [12], Model Code 10 [9] and ACI 544.4R [11], which presented, on average, results 22% lower than the experimental results, showing the imprecision of the standard in predicting the shear strength of SFRC beams.

### 4.5 Characterization of the material class and classification

The stress-crack opening relationship in uniaxial tensile characterizes the post-cracking behavior of the material. According to Model Code 10 [9], the $f_{R1,k}$ strength values indicate the material classes, ranging from 1 MPa to 8 MPa. Whereas the $f_{R3,k}/f_{R1,k}$ ratio is denoted by the letters a, b, c, d, e, corresponds to the classification presented in Table 7, softening or hardening materials.

Table 8 presents the residual stresses at flexure ($f_{R1,d}$ and $f_{R3,d}$) and at tensile ($f_{FTS}$ and $f_{Ftu}$) obtained from the material class, indicating a softening behavior (Figure 14a). Two simplified stress-crack opening constitutive laws may be deduced from the tensile results with the Model Code 10 [9], a linear post-cracking model or a rigid-plastic model, as shown in Figures 14b and 14c. It is interesting to note that the empirical models for calculating residual stresses proposed by Moraes-Neto et al. [15] were satisfactory in predicting the failure mode and material behavior with the Model Code 10 [1].

**Table 7.** Classification according to Model Code 10 [9]

| Class | $f_{R3,k} / f_{R1,k}$ | Behavior |
|---|---|---|
| a | 0.5 | Softening |
| b | 0.7 | |
| c | 0.9 | |
| d | 1.1 | Hardening |
| e | 1.3 | |

**Table 8.** Residual stresses at SFRC flexure and tensile (Model Code 10) [9]

| Type | Beam | Class | Flexure | | Tensile | | Classification | |
|---|---|---|---|---|---|---|---|---|
| | | | $f_{R1,d}$ (MPa) | $f_{R3,d}$ (MPa) | $f_{Fts}$ (MPa) | $f_{Ftuk,k}$ (MPa) | $f_{R3,d} / f_{R1,d}$ | Behavior |
| SFRC | VF-1<br>VF-2<br>VF-3<br>VF-4 | 2.5c | 2.5 | 2.3 | 1.1 | 0.65 | 0.92* | Softening |

Note: * value obtained empirically [15].

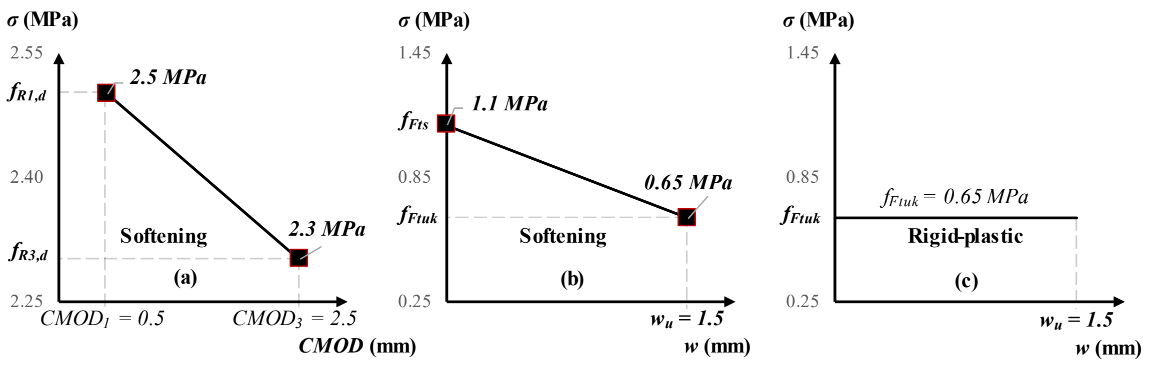


**Figure 14.** (a) Flexural response, (b) Softening Tensile response and (c) Rigid-plastic Tensile response

## 5 CONCLUSIONS

In this work the shear strength of beams with and without the addition of steel fiber were analyzed. A total of 8 beams without stirrups were tested, having as variables the addition of 1% of steel fiber and the variation of the longitudinal reinforcement rate. The results showed that the increase of the longitudinal reinforcement ratio from 0.87% to 2.14% in beams without steel fiber led to an improvement of 59% in shear strength caused by the dowel effect [8], observed between VS-1 and VS-4 beams, while the corresponding improvement was of only 22% in fibered concrete beams. A maximum gain of 109% in shear strength was observed with the addition of 1% of steel fibers comparing beams (VS-2 and VF-2) with the same longitudinal reinforcement ratio (1.2%). A significant amount of shear strength was provided by the inclusion of the steel fibers and allowed controlling the propagation of cracks by the effect of stress transfer bridges, transforming the brittle shear mechanism into a ductile flexural one.

Regarding the estimates of the standards for the RC beams, the results of NBR 6118 [13], JSCE [14] and ACI 318 [10] were conservative, while the Model Code 10 [9] was against safety in concrete with low compressive strength ($f_c$ ≤ 25 MPa), but the ACI 318 [10] was inaccurate in predicting the increase in strength when the rate of longitudinal reinforcement was varied, comparing VS-1 and VS-4, the JSCE [14] had an increase of 33% against 60% of experimental results.

For SFRC beams, the most accurate standards were JSCE [14] with a coefficient of variation of only 6%. For this series of beams the Model Code 10 [9], ACI 544.4R [11] and NBR 16935 [12] were the most conservative, recommending strength values lower than the JSCE [14] and the experimental results. Although 1% of fiber volume was insufficient to provide flexural failure, the results obtained show the potential possibility of using fibers to reduce the rate of longitudinal reinforcement in flexural strength.

## NOTATION

$a$ = shear span;

$A_s$ = area of longitudinal tension reinforcement;

$A'_s$ = area of longitudinal compression reinforcement;

$b_w$ = width of the beam cross section;

$C_f$ = fiber content;
$d$ = effective depth of the beam;
$d_f$ = fiber diameter;
$d_g$ = maximum aggregate size;
$\varepsilon_x$ = is the longitudinal strain;
$f_{ck}$ = characteristic concrete cylinder compressive strength;
$f_{cm}$ = average measured concrete cube compressive strength;
$f_{ctk}$ = characteristic tensile strength of concrete;
$f_{Fts}$ = residual tensile strength in the service limit state;
$f_{Ftuk}$ = residual strength characteristic to last limit state;
$f_{tyd}$ = corresponds to the tensile strength of the concrete, Equation 12, proposed by CHOI et al. (2007);
$f_{ys}$ = yield strength of the steel stirrups;
$f_{R1}$ e $f_{R3}$ = residual flexural strengths [15];
$k_{dg}$ = coefficient that depends on the maximum aggregate size;
$l_f$ = fiber length;
$m_R$ = strength moment;
$V_{c0}$ = concrete contribution to shear capacity;
$V_d$ = design shear capacity;
$V_f$ = design shear capacity of the steel fiber contribution;
$V_{flex}$ = flexural strength;
$V_{ACI}$ = shear capacity calculated by ACI 318 and ACI544.4R;
$V_{Exp}$ = ultimate experimental shear capacity;
$V_{JSCE}$ = shear capacity calculated by JSCE;
$V_{MC10}$ = shear capacity calculated by Model Code10;
$w_u$ = maximum crack opening accepted in structural design;
z = internal lever arm;
$\varepsilon_c$ = concrete compressive strain;
$\varepsilon_s$ = strain in steel reinforcement;
$\lambda$ = reduction factor of the mechanical properties of the type of concrete;
$\rho$ = tensile reinforcement ratio;
$\rho'$ = compressive reinforcement ratio;
$\sigma_{cp}$ = average normal stress acting on concrete cross section due to loading.


## ACKNOWLEDGEMENTS

The authors thank to CNPq and CAPES for the financial support.


## REFERENCES


[1] A. K. L. L. Nzambi, D. R. C. Oliveira, A. M. Oliveira, and M. S. Picanço, "Pull-out tests of ribbed steel reinforcing bars embedded in concrete with steel fibres," *Proc. Inst. Civ. Eng., Struct. Build.*, vol. 174, no. 3, pp. 181–189, 2021, http://dx.doi.org/10.1680/jstbu.17.00180.

[2] H. E. Yakoub, "Shear stress prediction: steel fiber-reinforced concrete beams without stirrups," *ACI Struct. J.*, vol. 103, no. 3, pp. 304–444, 2011, http://dx.doi.org/10.14359/51682346.

[3] A. Amin and S. J. Foster, "Shear strength of steel fibre reinforced concrete beams with stirrups," *Eng. Struct.*, vol. 111, pp. 323–332, 2016, http://dx.doi.org/10.1016/j.engstruct.2015.12.026.

[4] D. R. Sahoo and A. Sharma, "Effect of steel fiber content on behavior of concrete beams with and without stirrups," *ACI Struct. J.*, vol. 111, no. 5, pp. 1157–1167, 2014, http://dx.doi.org/10.14359/51686821.

[5] G. J. Parra-Montesinos, "Shear strength of beams with deformed steel fibers," *Concr. Int.*, vol. 28, no. 11, pp. 57–66, 2006.

[6] N. D. Tung and N. V. Tue, "Shear resistance of steel fiber-reinforced concrete beams without conventional shear reinforcement on the basis of the critical shear band concept," *Eng. Struct.*, vol. 168, pp. 698–707, 2018, http://dx.doi.org/10.1016/j.engstruct.2018.05.014.

[7] A. Yavas and C. O. Goker, "Impact of reinforcement ratio on shear behavior of I-shaped UHPC beams with and without fiber shear reinforcement," *Materials*, vol. 13, no. 7, pp. 1525, 2020, http://dx.doi.org/10.3390/ma13071525.

[8] T. L. Resende, D. C. T. Cardoso, and L. C. D. Shehata, "Influence of steel fibers on the dowel action of RC beams without stirrups," *Eng. Struct.*, vol. 221, pp. 111044, 2020, http://dx.doi.org/10.1016/j.engstruct.2020.111044.

[9] International Federation for Structural Concrete, *Model Code for Concrete Structures*. Wilhelm Ernst & Sohn, 2013.

[10] American Concrete Institute, *Building Code Requirements for Structural Concrete*, ACI 318, 2014, 524 p.

[11] American Concrete Institute, *Design Considerations for Steel Fiber Reinforced Concrete*, ACI 544.4R, 2018, 44 p.

[12] Associação Brasileira de Normas Técnicas, *Design of Fiber Reinforced Concrete Structures – Procedure*, NBR 16935, 2021 (in Portuguese).

[13] Associação Brasileira de Normas Técnicas, *Design of Concrete Structures – Procedure*, NBR 6118, 2014 (in Portuguese).

[14] Japanese Society of Civil Engineers, *Recommendations for Design and Construction of High-Performance Fiber Reinforced Cement Composites with Multiple Fine Cracks (HPFRCC)*. Concrete Committee, 2008.

[15] B. N. Moraes-Neto, J. A. O. Barros, and G. S. S. A. Melo, "A model for the prediction of the punching resistance of steel fibre reinforced concrete slabs centrically loaded," *Constr. Build. Mater.*, vol. 46, pp. 211–223, 2013, http://dx.doi.org/10.1016/j.conbuildmat.2013.04.034.

[16] K.-K. Choi, M. M. Reda Taha, H.-G. Park, and A. K. Maji, "Punching shear strength of interior concrete slab-column connections reinforced with steel fibers," *Cement Concr. Compos.*, vol. 29, no. 5, pp. 409–420, 2007, http://dx.doi.org/10.1016/j.cemconcomp.2006.12.003.

[17] P. P. F. Rodrigues, "*Parâmetros de Dosagem do Concreto*," 2. ed. São Paulo: ABCP, 1995.

[18] Associação Brasileira de Normas Técnicas, *Concrete Steel Fibers – Specification*, NBR 15530, 2007 (in Portuguese).

[19] Associação Brasileira de Normas Técnicas, *Metallic Materials — Tensile Testing Part 1: Method of Test at Room Temperature*, NBR 6892, 2013 (in Portuguese).

[20] L. D. S. Gomes, D. R. C. Oliveira, B. N. Moraes-Neto, A. B. Medeiros, A. N. Macedo, and F. A. C. Silva, "Experimental analysis of the efficiency of steel fibers on shear strength of beams," *Lat. Am. J. Solids Struct.*, vol. 15, no. 7, Jul 2018, http://dx.doi.org/10.1590/1679-78254710.

**Author contributions:** DRC: conceptualization, funding acquisition, supervision, writing; AKLL: conceptualization, data curation, formal analysis, methodology, writing; AKLL, MVS and LFA: data curation, formal analysis.

**Editors:** Ricardo Carrazedo, Guilherme Aris Parsekian.

**IBRACON Structures and Materials Journal**
Revista IBRACON de Estruturas e Materiais
ISSN 1983-4195 *ismj.org*

ORIGINAL ARTICLE

# Optimum design of a composite floor system considering environmental and economic impacts

## *Otimização de sistema de piso misto de aço e concreto considerando o impacto ambiental e econômico*

Paulo Augusto T. Arpini[a]
Mayane C. Loureiro[a]
Breno D. Breda[a]
Adenílcia F. Calenzani[a]
Élcio C. Alves[a]

[a]Universidade Federal do Espírito Santo – UFES, Departamento de Engenharia Civil, Vitória, ES, Brasil

Received 15 April 2021
Accepted 16 September 2021

**Abstract:** The composite floor system, composed of steel deck and concrete slab, generates more efficient and economical structures. On the other hand, the design of this type of structure has a high complexity level due to the consideration of several variables. In this respect, the objective of this paper is to present the formulation of the optimization problem for a composite floor system (steel and concrete) considering such environmental as economic impacts. To formulate the optimization problem, the reduction of environmental impact was adopted as an objective function - assuming the $CO_2$ emission and the finance cost as parameters. The restrictions were taken by the limiting states imposed in standard NBR 8800:2008. The computer program was developed via Matlab R2016a and the optimization process was carried out using the Genetic Algorithm toolbox existing in this platform. Two application examples of the formulation at hand are presented: the first from the literature and the second from an existing building - in both situations the influences of different concrete compressive characteristic strengths were analyzed. The results of the optimization problem show a reduction in geometry and, consequently, in its weight. The solution found by the program reduces by up to 17.70% of $CO_2$ emissions and 17.47% of the finance cost. When was applying different concrete compressive strengths, the optimal solution for environmental impact did not get the lowest cost. In general, the steel deck formwork obtained the highest percentage of environmental impact, while the beams and girders, with the same shape configuration, had the highest finance cost. Therefore, it is shown that the optimal design solution to $CO_2$ emissions is not always the better solution for the finance cost.

**Keywords:** steel-concrete composite floor system, cost and environmental impact, genetic algorithm.

**Resumo:** O sistema de piso misto, composto por *steel deck* e laje de concreto, gera estruturas mais eficientes e econômicas. Por outro lado, o dimensionamento deste tipo de estrutura apresenta um elevado nível de complexidade devido à consideração de várias variáveis. Nesse sentido, o objetivo deste trabalho é apresentar a formulação de um problema de otimização para um sistema de piso misto (aço e concreto) considerando os impactos ambientais e econômicos. Para formular o problema, a redução do impacto ambiental foi adotada como função objetivo - assumindo como parâmetros da otimização a emissão de $CO_2$ e o custo financeiro. As restrições foram atendidas pelos estados limitadores impostos na norma NBR 8800:2008. A rotina foi desenvolvida via Matlab R2016a e o processo de otimização foi realizado utilizando o Algoritmo Genético existente na plataforma. São apresentados dois exemplos de aplicação da formulação em questão: o primeiro da literatura e o segundo de um edifício existente - em ambas as situações foram analisadas as influências de diferentes resistências características à compressão do concreto. Os resultados do problema de otimização mostram uma redução na geometria e, consequentemente, no seu peso. A solução encontrada pelo programa reduz em até 17.70% as emissões de $CO_2$ e até 17.47% o custo financeiro. Quando se aplicou diferentes

**Corresponding author:** Paulo Augusto T. Arpini. E-mail: paulo.a.arpini@edu.ufes.br
**Financial support:** None.
**Conflict of interest:** Nothing to declare.
**Data Availability:** The data that support the findings of this study are available from the corresponding author, PATA, upon reasonable request.

resistências à compressão do concreto, a solução ótima de impacto ambiental não obteve o menor custo. Em geral, a fôrma de *steel deck* obteve o maior percentual de impacto ambiental, enquanto as vigas secundárias e principais, com a mesma configuração de forma, tiveram o maior custo financeiro. Portanto, mostra-se que a solução de projeto ideal para as emissões de $CO_2$ nem sempre é a melhor solução para o custo financeiro.

**Palavras-chave:** sistema de piso misto de aço-concreto, custo e impacto ambiental, algoritmo genético.

**How to cite:** P. A. T. Arpini, M. C. Loureiro, B. D. Breda, A. F. Calenzani, and E. C. Alves, "Optimum design of a composite floor system considering environmental and economic impacts", *Rev. IBRACON Estrut. Mater.*, vol. 15, no. 3, e15302, 2022, https://doi.org/10.1590/S1983-41952022000300002

## 1. INTRODUCTION

During the conception of a structural system, several different variables must be considered (dimension of structural elements, materials, cost, constructive process, among others), to define the most adequate design solution from technical, cost, and environmental perspectives. The latter is of great importance for the current worldwide scenario, and it is considered a strategic advantage, paramount for the sustainable development of civil construction.

On the quest for perfecting engineering processes, design optimization is a tool capable of offering good results for the solution of problems concerning the analysis and design of structures. As such, metaheuristic methods are studied, inspired in nature and its biological processes.

Optimization problems in civil construction usually involve finding the most financially viable solution. Recently, Öztürk et al. [1] used the TLBO and Jaya algorithms, while Kalemci et al. [2] used the Gray Wolf Optimization algorithm (GWO) to optimize the ideal design of a reinforced concrete retaining wall, to minimize the cost and weight of the structure, respectively.

Genetic Algorithms (GA) were proposed by John Holland in the 1960s. Those are models inspired by the principles of natural selection proposed by Charles Darwin. Considered one of the most consolidated metaheuristic methods, the application of GA's is observed in numerous areas, since this method presents high efficiency for finding globally optimized solutions [3].

Examples of GA applied to structural engineering include the optimization of reinforced concrete beams [4], [5], steel-concrete composite girders [6], spatial steel frames [7], railway viaducts [8] and bridges [9], [10].

It is worth noting that the optimized solution is not always the best alternative when problem variables are subjected to a specific type of constraint. Kripakaran et al. [11] developed a decision-making support system based on GA for the structural optimization of rigid steel frames and used the Modelling to Generate Alternatives (MGA) technique to determine structural solutions as close as possible to the optimized alternative. The ideal solution was chosen from a set of options that presented the best results.

From financial and environmental standpoints, the use of steel-concrete composite structures gained notoriety in civil construction for presenting performance improvements because of combining the use of both materials.

The presence of different materials increases the number of variables involved in the design of composite structures, making a more complex calculations and time-consuming if the conventionally used trial and error approach is adopted [12]. However, manufacturers usually provide design tables for specific structural elements such as steel decks, which are ideal tools for implementing optimization techniques featuring discrete variables.

Numerous studies using different methods for the design optimization of steel-concrete composite structures are observed in scientific literature, such as Žula et al. [13], Matos et al. [14], Dede [15] and Shariati et al. [16], Kaveh and Abadi [17].

Kravanja et al. [18] presented the optimal designs of different steel-concrete composite floor systems connected to a welded "I" section. The study was conducted by implementing structural optimization via nonlinear programming.

Pedro et al. [19] studied the optimization of "I" section steel-concrete composite bridges in two steps. On the first, a model commonly adopted by bridge engineers was implemented, followed by a finite element analysis on the second to improve the optimization

Silva and Rodrigues [20] implemented the iterative method of linear sequential programming associated with the Simplex method for the design of steel-concrete composite girders, with the objective of reducing the cost of materials.

Silva et al. [21] used the sequential linear programming algorithm to optimize mixed steel and concrete beams with partial interaction. The method proved to be efficient in the optimization of the composite beams when considering different design variables.

Gervásio [22] classifies steel as an environmentally friendly material due to its recycling potential. However, the author stresses that 1 kg of steel produced in a blast furnace generates 2494 g of $CO_2$, while the same weight of steel produced with an electric arc furnace generates 462 g of $CO_2$.

Paya-Zaforteza et al. [23] study the optimization of the cost and $CO_2$ emissions of 6 reinforced concrete plane frames via Simulated Annealing algorithm. Results indicated that the most environmentally friendly solution is only 2.77% more expensive than the cheapest solution, while the latter presented an increase of 3.80% in $CO_2$ emissions.

Tormen et al. [6] and Santoro and Kripka [12] presented studies on composite girders and, in addition to assessing the cost optimization of these elements, the authors state that the environmental impacts of using this type of girder are directly related to the degree of mechanical interaction between girders and slabs.

Despite the large number of studies on the optimization of steel-concrete composite structures available in scientific literature, research presenting both cost and environmental optimizations of systems featuring composite girders and slabs simultaneously are not observed. It is worth noting that, according to the International Energy Agency [24], civil construction accounted for 39% of total carbon dioxide ($CO_2$) emissions in 2018.

This paper presents the formulation for optimizing floor systems featuring steel-concrete composite girders and slabs, with the objective of determining the structure with the lowest financial and environmental costs. The problem was solved using Genetic Algorithms implemented with the toolbox provided by the software MATLAB [25], considering structural safety criteria prescribed in ABNT NBR 8800:2008 [26]. The formulation proposed here was validated with the example presented by Fakury et al. [27] and a composite floor system of an existing structure designed by conventional methods is analyzed.

## 2. THE PROBLEM FORMULATION

This section presents the proposed formulation for minimizing $CO_2$ emissions and other environmental costs of manufacturing the composite floor system shown in Figure 1, according to safety requirements for the structural materials used. The floor system is comprised of a composite slab supported by beams, a girder that supports the secondary beams parallel to the primary beams. The composite slab is molded on a trapezoidal steel deck and primary beam, girder and beams feature solid "I" sections. The shear connections are performed via stud bolts and for the structural model, the linear elastic behavior was considered.

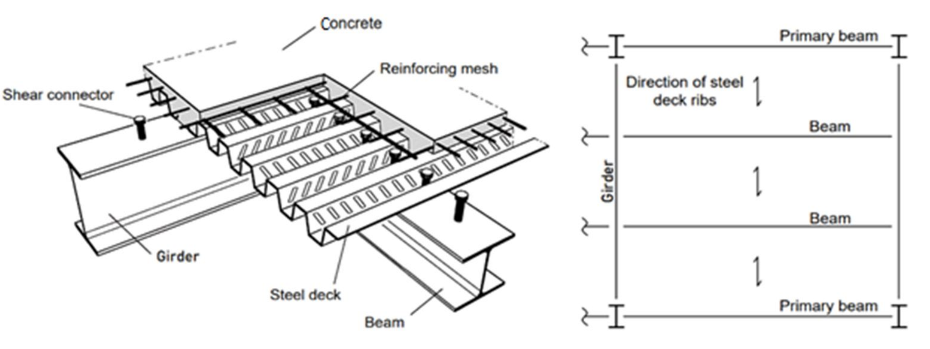


**Figure 1.** Composite floor with steel profiled sheeting (Adapted from Crisinel and Marimon 2004)

The design of the composite structural elements followed the standardized procedures provided by ABNT NBR 8800:2008 [26], based on limit-state design. It's Annex O of the standard prescribes the guidelines for the design of steel-concrete composite beams, while the design procedure for steel-concrete composite slabs is shown in Annex Q. Breda et al. [28] presented a formulation for the optimization problem analyzed here. However, the analysis performed by the authors was limited to cost optimization of the slabs and primary beams.

### 2.1 Choice variables

The decisions variables are the individuals that change during the optimization process. In the computer program, they are inserted using a 1×7 vector, whose data are:

$x_1$ : Profile determination of the Gerdau [29] catalog from where the dimensions for the parallel, secondary, and main beams are obtained. The range ranges from 1 to 88 for laminated profile and 1 to 174 for welded profiles of the VS series;

$x_2$ : The degree of beam-slab interaction of the secondary and main beam with values from $\alpha_{min}$ to 1;

$x_3$ : The total height of the slab and the thickness of the formwork according to the Metform [30] catalog.

$x_4$ : The maximum span of the slab according to the Metform [30] catalog.

$x_5$ : The type of formwork according to the Metform [30] catalog. The value of 1 was assigned to MF-50 and 2 to MF-75.

The values for the thickness of the steel deck are defined in accordance with the table provided by the company Metform. That are three thicknesses for the steel sheet (0.8, 0.95 and 1.25 mm) and eight total heights for each type of geometry: for MF-50, the height varies from 100 mm to 170 mm and for MF-75 from 130 mm to 200 mm. Thus, choosing one of the three steel deck thicknesses and one the eight available total heights result in twenty-four combinations.

The steel profiles are limited to the values given in table from Gerdau [29], the smallest profile is the W 150 × 13 and the largest, W 610 × 217. The steel wire mesh is defined according to stipulations from the steel deck manufacturer, and the diameter. The wires varying from Q-75 (ø3.8×ø3.8 - 150×150) to Q-138 (ø4.2×ø4.2 - 100×100). Transverse reinforcements were designed with 8 mm reinforcement bars and welded wire mesh Q-75 (ø3.8×ø3.8 - 150×150) to ensure that the minimum steel area is provided when necessary.

Figure 2 shows the cross section of the system indicating the dimensions of the profile and slab geometry that are obtained through the Gerdau [29] and Metform [30] catalog, respectively. $h$ corresponds to the height of the web, $b_f$ the width of the flanges, $t_w$ the thickness of the web, $t_f$ the thickness of the flanges, $t_c$ the height of the concrete slab, $b$ the effective width of the concrete slab and $h_f$ the height of the ribs of the shaped slab steel incorporated.

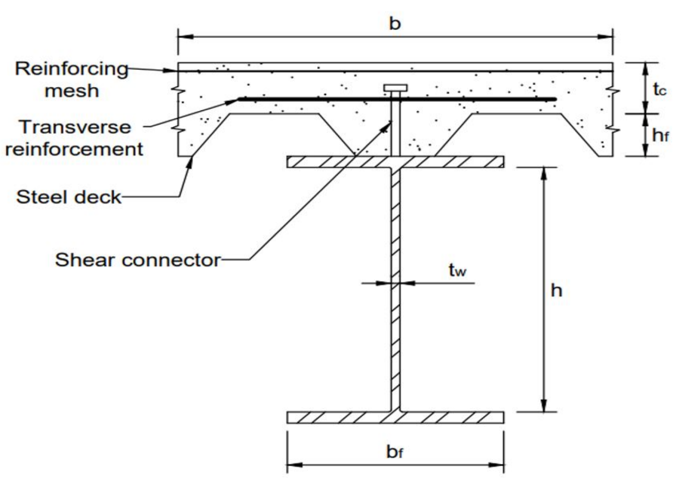


**Figure 2.** Cross-section of the composite girder and composite slab.

## 2.2 Objective function

The objective function for optimizing environmental impact, given in kg of $CO_2$ emission, is presented in Equation 1.

$$Minimize\, CO_2 = CO_{2(beam)} + CO_{2(formwork)} + CO_{2(concrete)} + CO_{2(mesh)} \tag{1}$$

where $CO_{2(beam)}$ corresponds to the $CO_2$ emissions of the steel profile, transverse reinforcement and shear connector of the primary beam and beams given by the sum of Equation 2 and 3.

$$CO_{2(beam)VSP} = (2 + n_{beam}) \cdot \left[ (\rho_{steel} \cdot A_a \cdot L \cdot E_{steel}) + (n \cdot \rho_{steel} . V_c \cdot E_{steel}) + (A_s \cdot l_b \cdot \rho_{steel} \cdot E_{steel}) \right] \tag{2}$$

with the first term of the equation corresponding to the sum of beams, represented by $n_{beams}$, and two parallel primary beams, while $\rho_{steel}$ is the specific mass of the steel from the profile in kg/m$^3$, $A_a$ is the cross-sectional area of profiled steel (m$^2$), L is the length of the beam (m), $E_{steel}$ is the $CO_2$ emission of steel (kg$CO_2$/kg), n is the number of stud bolt connectors, $V_c$ is the volume of the stud bolt connector (m$^3$), $A_s$ is the area of transverse reinforcement (m$^2$) and $l_b$ is the anchorage length of the transverse reinforcement (m).

$$CO_{2(beam)VP} = \left(V_{steel} \cdot E_{steel} \cdot \rho_{steel}\right) + \left(n_p \cdot V_c \cdot \rho_{steel} \cdot E_{steel}\right) + \left(A_{sp} \cdot l_{bp} \cdot \rho_{steel} \cdot E_{steel}\right) \tag{3}$$

where $V_{steel}$ is the volume of the girder, perpendicular to the beams (m$^3$), $n_p$ is the number of stud bolt connectors on the girder, $A_{sp}$ is the area of transverse reinforcement of the girder (m$^2$) and $l_{bp}$ the anchorage length of the transverse reinforcement on the girder (m).

$CO_{2concrete}$, is the $CO_2$ emission of concrete determined with Equation 4.

$$CO_{2(concrete)} = E_{conc} \cdot A_{slab} \cdot v_{conc} \tag{4}$$

where $E_{conc}$, is the $CO_2$ emission of concrete (kg$CO_2$/m$^3$), $A_{slab}$ is the rectangular area of the slab covered by the steel deck (m$^2$) and $v_{conc}$ is usage of concrete (m$^3$/m$^2$).

$CO_{2(formwork)}$ is the emission of the steel deck determined by Equation 5.

$$CO_{2(formwork)} = A_{slab} \cdot p_{formwork} \cdot E_{sd} \tag{5}$$

where $p_{formwork}$ is the weight of the steel deck (kg/m$^2$) and $E_{sd}$ the $CO_2$ emission of the steel deck (kg$CO_2$/kg).

$CO_{2(mesh)}$ represents the emission of the reinforcing mesh given by Equation 6.

$$CO_{2(mesh)} = A_{slab} \cdot p_{mesh} \cdot E_{mesh} \tag{6}$$

where $p_{mesh}$ is the weight of the mesh (kg/m$^2$) and $E_{tela}$ is the corresponding $CO_2$ emission (kg$CO_2$/kg).

### 2.3 Constraints

The constraint functions are based on ABNT NBR 8800:2008 [26] Annex O design recommendations, given by Equation 7:

$$C = \begin{cases} \dfrac{h_w / t_w}{5.7\sqrt{E / f_{yk}}} - 1 \le 0 \\ \dfrac{\alpha_{min}}{\alpha} - 1 \le 0 \\ \dfrac{M_{sd}}{M_{rd}} - 1 \le 0 \\ \dfrac{V_{sd}}{V_{rd}} - 1 \le 0 \\ \dfrac{q_{sd}}{q_{rd}} - 1 \le 0 \\ \dfrac{(M_{Ga,Sk} / W_{a,i}) + (M_{L,Sk} / W_{ef,i})}{f_{yk}} - 1 \le 0 \\ \dfrac{\delta_t}{\delta_{adm}} - 1 \le 0 \\ \dfrac{H_{v,Sd}}{H_{v.Rd}} - 1 \le 0 \end{cases} \tag{7}$$

where $h_w$ is the height of the profile web (m), $t_w$ is the web thickness (m), E is the modulus of elasticity of steel (kN/m$^2$), $f_{yk}$ the characteristic yield strength of steel of the profiles (kN/m$^2$), $\alpha_{min}$ minimum allowable interaction between beam and slab according to ABNT NBR 8800:2008 [26], $\alpha$ the degree of interaction between beam and slab, $M_{sd}$ the design bending moment acting on the beam (kN · m), $M_{rd}$ the design resistance to bending moment (kN · m), $V_{sd}$ is the design shear force acting on the structure (kN), $V_{rd}$ the design resistance of shear force (kN), $q_{sd}$ the uniformly distributed live load on the slab (kN/cm$^2$), $q_{rd}$ is the live-load capacity of the slab (kN/m$^2$), obtained from design tables provided by Metform [30], $M_{Ga,Sk}$ and $M_{L,Sk}$ are the design bending moments on the structure before and after concrete curing, respectively (kN · m), $W_{ef,i}$ is the inferior elastic section modulus of the transformed section (m$^3$), $W_{a,i}$ is the inferior elastic section modulus of the steel profile (m$^3$), $\delta_t$ is the total deflection (mm) and $\delta_{adm}$ is the maximum allowable deflection (mm), $H_{v,Sd}$ is the design shear force acting on the slab (kN/m), $H_{v,Rd}$ is the corresponding design resistance to shear force (kN/m).

## 3. RESULTS AND DISCUSSIONS

Two numerical examples are presented to verify the efficiency of the formulation proposed in this paper, one of which extracted from Fakury et al. [27] and the other corresponds to an existing structure featuring composite floor systems. The material properties common to both examples are Modulus of elasticity of steel ($E$): 200 GPa; Tensile strength of steel of the beams ($f_{yk}$): 345 MPa; Diameter of shear connectors ($d_{cs}$): 1.9 cm; Tensile strength of steel of the shear connectors ($f_{ucs}$): 415 MPa; Coefficient for consideration of connector grouping ($R_g$): 1; Coefficient for considering the position of connectors ($R_p$): 0.6. It is worth mentioning that, for simplicity, $R_p$ was considered in the most unfavorable situation, that is, connectors welded on a mixed slab with ribs perpendicular to the steel profile and the distance from the half height of the web of the form rib to the face of the connector shaft less than 50 mm. The parameter chosen to measure the environmental impact was the $CO_2$ emission resulting from construction processes, considering the total carbon footprint generated from raw material extraction to the final product. Table 1 presents the reference values of $CO_2$ emissions used in this study.

**Table 1.** $CO_2$ emission of materials

| Material | Unit | $CO_2$ emissions (kgCO$_2$) | Reference | Material | Unit | $CO_2$ emissions (kgCO$_2$) | Reference |
|---|---|---|---|---|---|---|---|
| Concrete 20 MPa | m$^3$ | 130.68 | Santoro and Kripka [12] | Steel deck | kg | 26.38 | Worldsteel Association [31] |
| Concrete 25 MPa | m$^3$ | 139.88 | | Steel profile | kg | 11.16 | |
| Concrete 30 MPa | m$^3$ | 148.28 | | Studbolt shear connector | | | |
| Concrete 35 MPa | m$^3$ | 162.36 | | Reinforcing steel mesh | kg | 19.24 | |
| Concrete 40 MPa | m$^3$ | 172.77 | | Steel CA50, ø 8 mm, reinforcement bar | | | |
| Concrete 45 MPa | m$^3$ | 185.32 | | | | | |
| Concrete 50 MPa | m$^3$ | 216.40 | | | | | |

The cost of the materials was obtained by consulting manufacturers or from other scientific studies, indicated in Table 2. The prices of concrete, steel profiles and reinforcing steel mesh were reproduced from SINAPI [32]. The cost of stud bolt connectors was obtained from Cordeiro [33] and the cost of the steel decks was provided by the MS Estruturas Metálicas (2020) company.

**Table 2.** Cost of materials

| Material | Unit | Cost (R$) | Reference | Material | Unit | Cost (R$) | Reference |
|---|---|---|---|---|---|---|---|
| Concrete 20 MPa | $m^3$ | 295.00 | | Steel CA-50, ø 8 mm, reinforcement bar | kg | 5.34 | SINAPI [32] |
| Concrete 25 MPa | $m^3$ | 307.42 | | Stud bolt shear connector | un | 11.40 | Cordeiro [33] |
| Concrete 30 MPa | $m^3$ | 317.11 | | Steel deck MF-50, thickness 0.80 mm | $m^2$ | 72.36 | |
| Concrete 35 MPa | $m^3$ | 329.15 | | Steel deck MF-50, thickness 0.95 mm | $m^2$ | 80.96 | |
| Concrete 40 MPa | $m^3$ | 341.57 | SINAPI [32] | Steel deck MF-50, thickness 1.25 mm | $m^2$ | 104.54 | |
| Concrete 45 MPa | $m^3$ | 384.01 | | Steel deck MF-75, thickness 0.80 mm | $m^2$ | 83.29 | MS Estruturas Metálicas [34] |
| Concrete 50 MPa | $m^3$ | 455.43 | | Steel deck MF-75, thickness 0.95 mm | $m^2$ | 93.18 | |
| Steel profile | kg | 9.47 | | Steel deck MF-75, thickness 1.25 mm | $m^2$ | 120.31 | |
| Reinforcing steel mesh | kg | 7.96 | | | | | |

### 4.1 Example 1 – Fakury, Silva and Caldas

The example from Fakury et al. [27] presents a floor system from a commercial building located in a moderate environmental aggressiveness zone. The system features a composite slab with steel deck MF-75 of 0.95 mm thickness, 15.0 cm of height, reinforcing mesh Q-75 (ø3.8×ø3.8 – 150×150) and concrete with a compressive strength of 25 MPa, manufactured using gneiss as aggregate. The beams V1 are simply supported and comprised of the laminated profile W 310 × 28,3, while the girder V3 features the monosymmetric welded profile VSM 450 × 59, with the narrowest flange in contact with the slab. The geometries of the floor and reference cross-section are given in Figure 3 and load factors for dead and live loads, considered here before and after concrete curing, are given in Table 3.

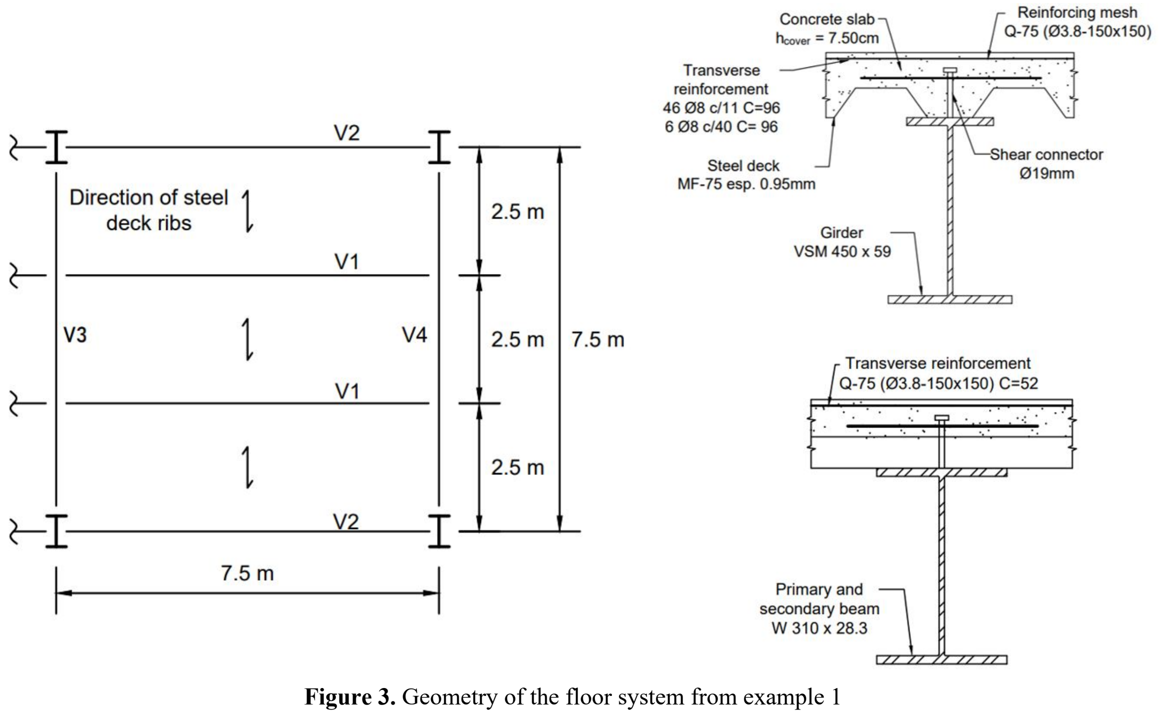


**Figure 3.** Geometry of the floor system from example 1

**Table 3.** Loads before concrete curing

| | Load type | Load | Characteristic value [kN/m$^2$] | Load factor |
|---|---|---|---|---|
| Before concrete curing | Dead | Weight of the steel structure | 0.25 | 1.15 |
| | Live | Construction live load | 1.00 | 1.30 |
| After concrete curing | Dead | Weight of the steel structure | 0.25 | 1.25 |
| | | Weight of the flooring | 1.35 | 1.50 |
| | Live | Serviceability live load | 5.00 | 1.50 |

Table 4 presents the results obtained by Fakury et al. [27] and results from the proposed formulation. The geometry and cross-section of the optimum solution indicated by the program are shown in Figure 4.

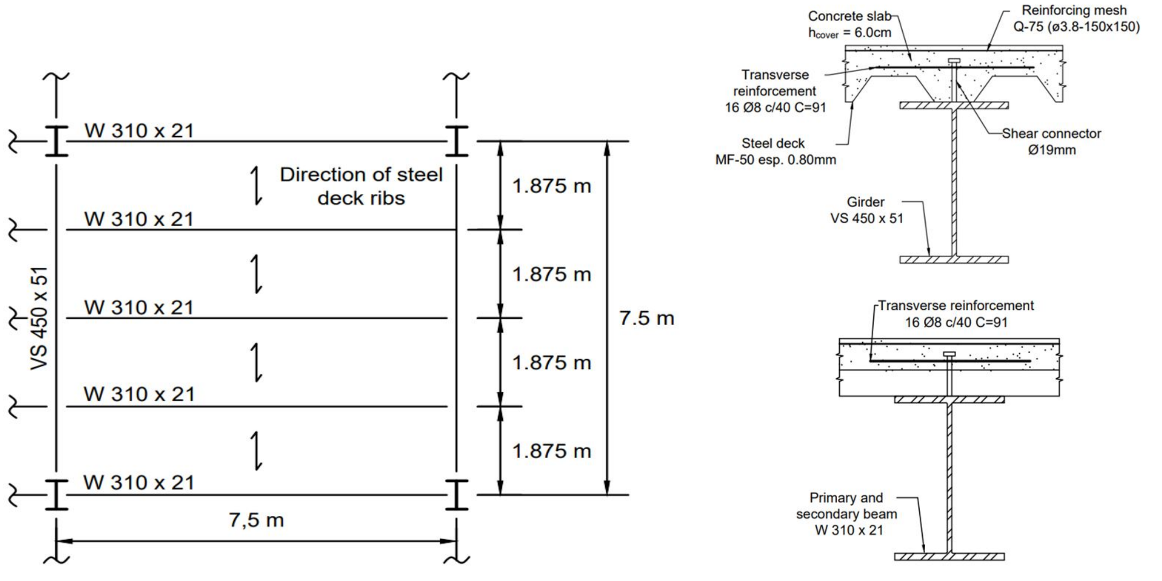


**Figure 4.** Optimal geometry of the floor system for example 1

**Table 4.** Results for example 1

| Information | Unit | Fakury et al. [27] | Optimized solution |
|---|---|---|---|
| Number of beams | un | 2 | 3 |
| Steel deck type | -- | MF-75 | MF-50 |
| Steel deck thickness | mm | 0.95 | 0.80 |
| Maximum span | m | 2.50 | 2.20 |
| Total height of the slab | cm | 15.00 | 11.00 |
| Thickness of the concrete layer | cm | 7.50 | 6.00 |
| Reinforcing steel mesh | -- | Q-75 (ø3.8-150 × 150) | Q-75 (ø3.8-150 × 150) |
| Profile of the beam V1 | -- | W 310 × 28.3 | W 310 × 21 |
| Degree of composite interaction V1 | -- | 0.47 | 0.54 |
| Total number of connectors V1 | un | 32 | 48 |
| Transverse reinforcementV1 | | Q-75 (ø3.8 150 × 150) C=52 | 16 ø8 c/40 C=91 |
| Profile of the primary beam V2 | -- | W 310 × 28.3* | W 310 × 21 |
| Degree of composite interaction V2 | un | 0.47* | 0.51 |
| Total number of connectors V2 | -- | 32* | 32 |
| Transverse reinforcementV2 | | Q-75 (ø3.8-150×150) C=52* | 16 ø8 c/40 C=91 |
| Profile of the girder V3 | -- | VSM 450 × 59 | VS 450 × 51 |
| Degree of composite interaction V3 | -- | 0.65 | 0.71 |
| Total number of connectors V3 | un | 32 | 28 |
| Transverse reinforcement V3 | -- | 46 ø8 c/11 C=96<br>6 ø8 c/40 C= 96 | 16 ø8 c/40 C=91 |

*Adopted Information

Results from Table 4 shows that, despite the optimized solution indicating a larger number of shear connectors and beams, the profile section selected for said beams presents a lower linear weight in comparison with the reference example, while maintaining the same height.

The slab selected for the optimized solution presents a smaller height, with reductions of height for the steel deck and the concrete layer. Since the composite beam V2 are primary and internal, the optimization procedure selected the same profile used for the beams.

Table 5 shows a comparison between $CO_2$ emission and cost obtained from the optimization program and from Fakury et al. [27].

**Table 5.** $CO_2$ emission and cost for example 1

| Information | Fakury et al. [27] | | Optimization program | |
|---|---|---|---|---|
| | Environmental impact ($kgCO_2$) | Cost (R$) | Environmental impact ($kgCO_2$) | Cost (R$) |
| Beams V1 | 481.77 | 4434.9 | 517.52 | 4960.56 |
| Primary beam V2 | 481.77 | 4434.9 | 345.016 | 3307.04 |
| Girder V3 | 494.71 | 4535.2 | 436.07 | 3951.78 |
| Transverse reinforcement | 35.7 | 123.7 | 31.52 | 102.36 |
| S*teel deck* | 1661.9 | 5241.38 | 1390.39 | 4685.06 |
| Concrete | 885.18 | 1945.39 | 806.5 | 1772.47 |
| Reinforcing steel mesh | 130.95 | 541.78 | 130.95 | 541.78 |
| TOTAL | 4171.98 | 21257.25 | 3657.966 | 19321.05 |

As shown in Table 5, the environmental impact resulting from $CO_2$ emission, indicates reductions in this parameter for the steel deck (16.34%), concrete (8.89%), Transverse reinforcement (11.71%), girder V3 (11.85%) and primary beam V2 (28.39%). These results may be explained by reductions of the linear weight of the girders, number of connectors, along with steel deck and concrete layer thicknesses, which tends to reduce material consumption and consequently the rate of de $CO_2$ emission. Since the reinforcing steel mesh used was the same for both approaches, no changes are observed for this material.

Furthermore, Table 5 also shows considerable reduction of cost when the optimized solution is implemented. The percentual reductions of cost were primary beam V2 (25.43%) and girder V3 (12.86%), transverse reinforcement (17.25%), steel deck (10.61%) and concrete (8.89%). In a general perspective, the environmental optimization program presents a reduction in cost of 10.51%.

A comparison between both responses reveals that, although the optimized alternative features a greater number of beams, the results correspond to a reduction of 12.32% and 9.11% of total cost and $CO_2$ emission, respectively. Table 6 shows the compressive strength influences of concrete on the environmental impact of the optimized results.

**Table 6.** Results from example 1 for different values of $f_{ck}$

| Information | Unit | 20 MPa | 25 MPa | 30 MPa | 35 MPa | 40 MPa | 45 MPa | 50 MPa |
|---|---|---|---|---|---|---|---|---|
| Number of V1* | un | 3 | 3 | 3 | 3 | 3 | 3 | 3 |
| Steel deck type | -- | MF-50 | MF-75 | MF-75 | MF-75 | MF-50 | MF-50 | MF-75 |
| Steel deck thickness | mm | 0.80 | 0.80 | 0.80 | 0.80 | 0.80 | 0.80 | 0.80 |
| Maximum span | m | 2.10 | 2.20 | 2.20 | 2.20 | 2.10 | 1.90 | 2.20 |
| Total height of the slab | cm | 11.00 | 14.00 | 14.00 | 14.00 | 11.00 | 11.00 | 14.00 |
| Thickness of the concrete layer | cm | 6.00 | 6.50 | 6.50 | 6.50 | 6.00 | 6.00 | 6.50 |
| Reinforcing steel Mesh | -- | Q-75 (ø3.8 – 150 × 150) | Q-75 (ø3.8 – 150 × 150) | Q-75 (ø3.8 – 150 × 150) | Q-75 (ø3.8 – 150 × 150) | Q-75 (ø3.8 – 150 × 150) | Q-75 (ø3.8 – 150 × 150) | Q-75 (ø3.8 – 150 × 150) |
| Profile V1 and V2* | -- | W 310 × 21 | W 310 × 21 | W 310 × 21 | W 310 × 21 | W 310 × 21 | W 310 × 21 | W 310 × 21 |
| Degree of composite interaction V1 and V2 | -- | 0.53 | 0.54 | 0.52 | 0.61 | 0.54 | 0.49 | 0.5 |
| Total number of connectors V1 | un | 48 | 48 | 48 | 54 | 48 | 48 | 48 |
| Number of connectors V2 | un | 32 | 32 | 32 | 36 | 32 | 32 | 32 |
| Transverse reinforcement V1 and V2 | -- | 16 ø8 c/40 C=106 | 16 ø8 c/40 C=91 | 16 ø8 c/40 C=80 | 16 ø8 c/40 C=73 | 16 ø8 c/40 C=66 | 16 ø8 c/40 C=61 | 16 ø8 c/40 C=56 |
| Profile V3* | -- | VS 450 × 59 | VS 450 × 51 | VS 450 × 51 | VS 450 × 51 | VS 450 × 51 | VS 450 × 51 | VS 450 × 51 |
| Degree of composite interaction | -- | 0.5 | 0.66 | 0.69 | 0.78 | 0.48 | 0.86 | 0.78 |
| number of connectors | un | 20 | 28 | 30 | 34 | 22 | 38 | 34 |
| Transverse reinforcement V3 | -- | 16 ø8 c/40 C=109 | 30 ø8 c/23 C=91 | 38 ø10 c/18 C=80 | 46 ø8 c/8 C=73 | 16 ø8 c/40 C=70 | 46 ø8 c/8 C=61 | 46 ø8 c/8 C=56 |
| TOTAL $CO_2$ emission | kg | 3403.84 | 3671.32 | 3718.71 | 3800.69 | 3529.68 | 3600.44 | 4102.14 |
| TOTAL cost | R$ | 18780.85 | 19321.05 | 19399.16 | 19622.19 | 18459.14 | 18862.50 | 20209.63 |

Results show that an increase in the compressive strength of concrete initially results in more $CO_2$ emission. However, at 40 MPa there is a reduction of environmental impact, followed by a tendency to increase for larger values of compressive strength. The most environmentally friendly solution corresponds to an $f_{ck}$ of 20 MPa. As such, it is plausible to conclude that increases in $f_{ck}$ interferes with improvements in $CO_2$ emission up to a limit value.

Furthermore, the lowest cost is obtained for $f_{ck}$ equal to 40 MPa, implying that the financially optimal solution does not necessarily correspond to the environmentally optimal alternative. If limitations related to environmental aggressiveness are imposed, as stated by Kripakaran et al. [11] concerning the decision-making support system and the application of MGA, a more comprehensive analysis of the results reveals that the best solution from a financial and environmental standpoint is obtained for $f_{ck}$ equal to 40 MPa. Figures 5a and 5b present percentages of $CO_2$ emission and cost for each analyzed alternative. It is observed that the steel deck presents the highest percentage of $CO_2$ emission for all resistance classes of concrete, followed in most cases by profiles V1 and V2, except for $f_{ck}$ values of 35 MPa, 45 MPa and 50 MPa, in which concrete presents the second highest percentage. Alternatively, Figure 5b shows the contribution of each material to the total cost of the structural system. Beams V1 and primary beam V2 figured as the most financially burdensome, followed by an alternation between girder V3 and the steel deck.

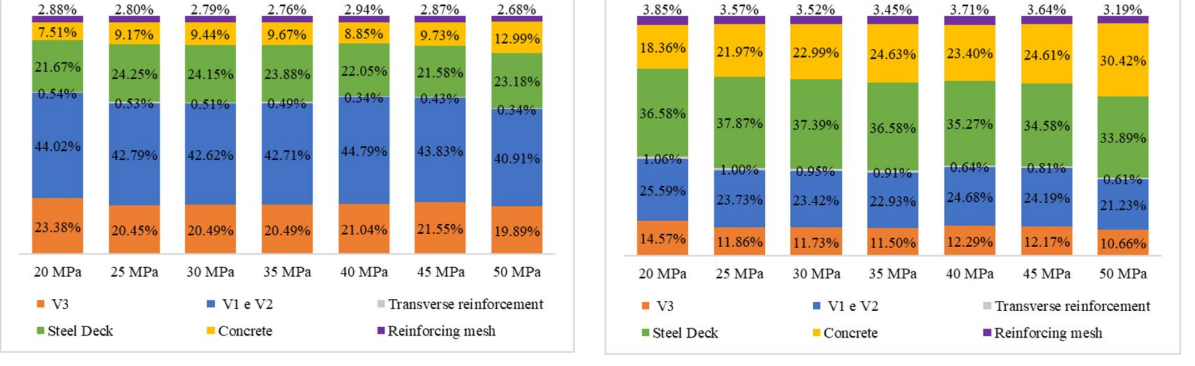


(a) $CO_2$ emission for each element from the optimized solution for example 1

(b) Cost for each element from the optimized solution for example 1

**Figure 5.** Optimized solution for example 1

The least expensive solution is only 1.71% cheaper than the solution corresponding to the smallest $CO_2$ emission, which presents a reduction of 3.57% for this parameter. As such, if a financial limit is imposed, the best possible solution features a compressive strength of concrete equal to 20 MPa.

Given the analysis of Figure 5, it is noted that a large portion of $CO_2$ emission is attributed to the steel from secondary beams, girders, and steel deck, reaching up to 85% of total emissions of the structure for lower $f_{ck}$ values. As the compressive strength of concrete increases, emissions from this material also increase, while emissions from steel are reduced to values around 65%. Furthermore, the largest cost results from steel elements, reaching up to 90% of the total value for smaller concrete compressive strengths.

The way constraints are imposed by the program indicates the percentage of optimization attributed to each variable, such as the ratios between maximum deflection and allowable deflection ($\Delta\delta$), applied loads and resistance to shear force ($\Delta V$) and bending moment ($\Delta M$). Figures 6a and 6b presents these ratios to SLS and ULS of the beam, primary beam, and girder profiles for example 1. The imposed constraints show that the smallest ratio corresponds to $\Delta M$, especially for girder V3 if a compressive strength of 40 MPa is adopted for concrete. This indicated that the applied load is close to the resistance stipulated by the ULS.

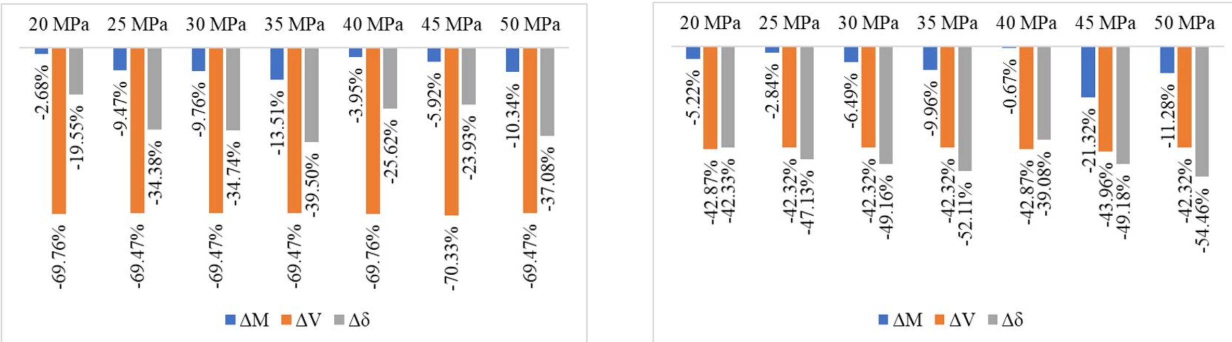


(a) Beam V1 and primary beam V2 (b) Girder V3

**Figure 6.** Verification of SLS and ULS

### 4.2 Example 2 – Case study of the Nexem building

This example presents an application of the methodology proposed herein to the Nexem building – Nucleous of Excelence in Metallic Structures (direct translation from Portuguese), shown in Figure 7. This example is also analyzed by Breda et al. [28]. The structure is located at Goiabeiras campus of the Federal University of Espírito Santo (UFES) and features a composite girder and slab system with a constructed area of 264.98 m$^2$.

According to field measurements performed by Breda et al. [28], the system selected for analysis is the classroom located on the first floor, featuring steel deck MF-50 with 0.80 mm thickness, 15.0 cm of total height, reinforcing mesh Q-113 (ø 3.8 × ø 3.8 – 100 × 100) and concrete with an $f_{ck}$ of 30 MPa. The internal composite beams V1 are simply supported and feature cross-section W 200 × 31.3, as shown in Figure 8.

**Figure 7.** Nexem (Breda et al. [28])

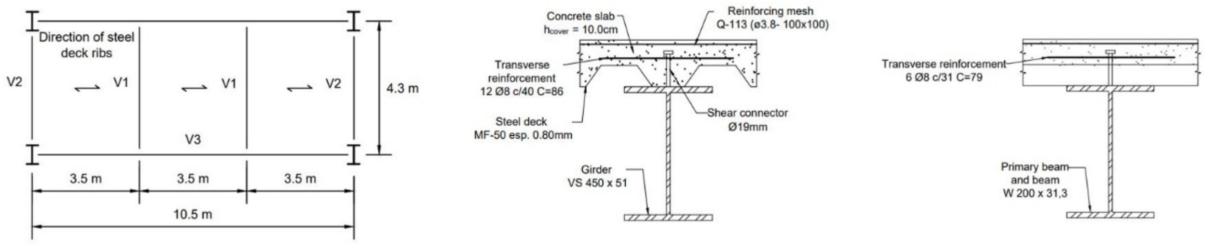


**Figure 8.** Geometry of the floor system from example 2

The construction was propped, and the characteristic values of dead and live loads, along with the corresponding load factors are given in Table 7.

**Table 7.** Loads after concrete curing

| Load type | Load | Characteristic value [kN/m$^2$] | Load factor |
|---|---|---|---|
| Dead loads | Weight of the steel structure | 0.40 | 1.40 |
| | Weight of the flooring | 1.35 | 1.40 |
| Live loads | Serviceability live load | 3.00 | 1.50 |

Table 8 shows results for the conventional and optimized design of Nexem. Regardless of the optimized design indicating the use of two additional beams V1, a reduction of cross-section geometry is observed for all profiles, resulting in less linear weight and a smaller height. The presence of additional beams also reduced the thickness of the slab.

**Table 8.** Results for example 2

| Information | Unit | NEXEM | Optimized solution |
|---|---|---|---|
| Number of beams V1 | un | 2 | 4 |
| Steel deck type | -- | MF-50 | MF-50 |
| Steel deck thickness | mm | 0.80 | 0.80 |
| Maximum span | m | 3.50 | 2.10 |
| Total height of the slab | cm | 15.00 | 11.00 |
| Thickness of the concrete layer | cm | 10.00 | 6.00 |
| Reinforcing steel mesh | -- | Q-113 (ø3.8- 100×100) | Q-75 (ø3.8-150×150) |
| Profile of the beam V1 | -- | W 200 × 31.3 | W 200 × 15 |
| Degree of composite interaction V1 | -- | 0.40 | 0.43 |
| Total number of connectors V1 | un | 24 | 40 |
| Transverse reinforcementV1 | | 6 ø8 c/31 C=79* | 10 ø8 c/38 C=72 |
| Profile of the primary beam V2 | -- | W 200 × 31.3* | W 200 × 15 |
| Degree of composite interaction V2 | un | 0.40* | 0.43 |
| Total number of connectors V2 | -- | 24* | 20 |
| Transverse reinforcementV2 | | 6 ø8 c/31 C=79** | 10 ø8 c/38 C=72 |
| Profile of the girder V3 | -- | VS 450 × 51** | VS 400 × 44 |
| Degree of composite interaction V3 | -- | 0.85** | 0.69 |
| Total number of connectors V3 | un | 38** | 26 |
| Transverse reinforcementV3 | -- | 12 ø8 c/40 C=86** | 22 ø8 c/40 C=87 |

*Adopted information **Information obtained with the program developed

Results show a reduction in financial and environmental cost for most elements designed with de optimization program. The topology indicated by the program features the same steel deck type adopted for the original design of the building, but remaining components of the slab system are the major contributors for optimizing the design, namely 32% for concrete and 32.78% for the reinforcing steel mesh. Even with an increase in the number of beams V1, the program reduces the weight and cost of primary beams V2 and girder V3, by 24.16% and 15.29%, respectively.

Table 9 shows a comparison between greenhouse gas emission and cost of the optimized program and the existing structural design.

**Table 9.** $CO_2$ emission and cost for example 2

| Information | NEXEM | | Optimization program | |
|---|---|---|---|---|
| | Environmental impact ($kgCO_2$) | Cost (R$) | Environmental impact ($kgCO_2$) | Cost (R$) |
| Beam V1 | 298.97 | 2797.02 | 281.33 | 2828.23 |
| Primary beams V2 | 298.97 | 2797.02 | 140.66 | 1414.12 |
| Girder V3 | 609.41 | 5518.81 | 522.92 | 4675.17 |
| Transverse reinforcement | 8.52 | 23.69 | 22.25 | 61.74 |
| Steel deck | 999.3 | 3267.05 | 999.3 | 3267.05 |
| Concrete | 836.86 | 1793.41 | 569.06 | 1219.52 |
| Reinforcing steel mesh | 156.36 | 646.91 | 105.11 | 434.87 |
| TOTAL | 3208.39 | 16843.91 | 2640.63 | 13900.70 |

It must be noted that, except for beams V1, which presented reduction in $CO_2$ emission (5.9%), every component that contributed to cost reduction also reduced environmental impact by the following percentages: 29.43% (V2), 14.19% (V3), 32% (concrete) and 32.78% (reinforcing steel mesh). Overall, the optimization program reduced environmental impact by 17.7% and cost by 17.47%. Geometries of the floor plan and the cross-section obtained with the optimized procedure are presented in Figure 9.

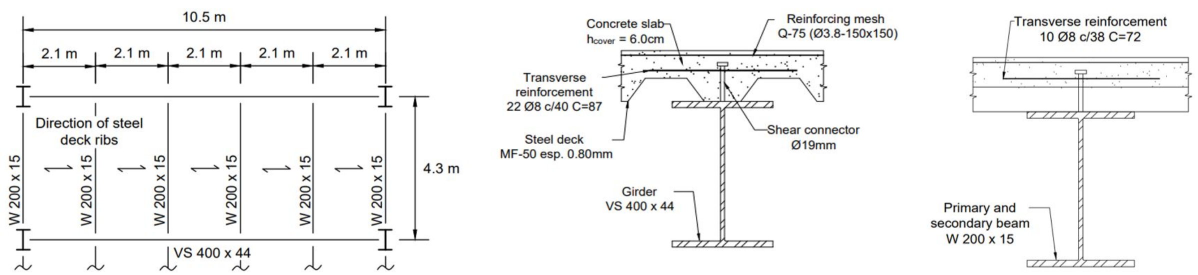


**Figure 9.** Optimal floor geometry for example 2

Table 10 and Figures 10a and 10b show the influence of concrete strength on the environmental impact of the composite system analyzed here.

**Table 10.** Results from example 2 for different values of $f_{ck}$

| Information | Unit | 20 MPa | 25 MPa | 30 MPa | 35 MPa | 40 MPa | 45 MPa | 50 MPa |
|---|---|---|---|---|---|---|---|---|
| Number of V1* | un | 4 | 4 | 4 | 4 | 5 | 5 | 4 |
| Steel deck type | -- | MF-50 | MF-75 | MF-50 | MF-50 | MF-50 | MF-50 | MF-50 |
| Steel deck thickness | mm | 0.80 | 0.80 | 0.80 | 0.80 | 0.80 | 0.80 | 0.80 |
| Maximum span | m | 210.00 | 210.00 | 210.00 | 240.00 | 200.00 | 200.00 | 230.00 |
| Total height of the slab | cm | 12.00 | 11.00 | 11.00 | 11.00 | 11.00 | 11.00 | 11.00 |
| Thickness of the concrete layer | m | 7.00 | 6.00 | 6.00 | 6.00 | 6.00 | 6.00 | 6.00 |
| Reinforcing steel mesh | -- | Q-75 (ø3.8 – 150 × 150) | Q-75 (ø3.8 – 150 × 150) | Q-75 (ø3.8 – 150 × 150) | Q-75 (ø3.8 – 150 × 150) | Q-75 (ø3.8 – 150 × 150) | Q-75 (ø3.8 – 150 × 150) | Q-75 (ø3.8 – 150 × 150) |
| Profile V1 and V2* | -- | W 150 × 13 | W 150 × 13 | W 200 × 15 | W 200 × 15 | W 150 × 13 | W 200 × 15 | W 150 × 13 |
| Degree of composite interaction V1 e V2 | -- | 0.45 | 0.67 | 0.43 | 0.58 | 0.78 | 0.52 | 0.4 |
| Total number of connectors V1 | un | 32 | 48 | 40 | 48 | 70 | 60 | 32 |

**Table 10.** Continued...

| Information | Unit | 20 MPa | 25 MPa | 30 MPa | 35 MPa | 40 MPa | 45 MPa | 50 MPa |
|---|---|---|---|---|---|---|---|---|
| Number of connectors V2 | un | 16 | 24 | 20 | 24 | 28 | 24 | 16 |
| Transverse reinforcement V1 e V2 | -- | 10 ø8 c/38 C=103 | 10 ø8 c/38 C=90 | 10 ø8 c/38 C=79 | 10 ø8 c/38 C=72 | 10 ø8 c/38 C=66 | 10 ø8 c/38 C=60 | 10 ø8 c/38 C=55 |
| Girder V3* | -- | VS 400 × 44 | VS 400 × 44 | VS 400 × 44 | VS 400 × 44 | VS 400 × 38 | VS 400 × 37 | VS 400 × 44 |
| Degree of composite interaction | -- | 0.67 | 0.74 | 0.69 | 0.68 | 0.8 | 0.88 | 0.64 |
| Number of connectors | un | 32 | 30 | 26 | 26 | 26 | 28 | 24 |
| Transverse reinforcementV3 | -- | 22 ø8 c/40 C=114 | 22 ø8 c/40 C=100 | 22 ø8 c/40 C=87 | 22 ø8 c/40 C=78 | 22 ø8 c/40 C=71 | 22 ø8 c/40 C=66 | 22 ø8 c/40 C=61 |
| TOTAL $CO_2$ emission | kg | 2576.40 | 2549.68 | 2640.63 | 2693.10 | 2659.88 | 2767.10 | 2830.83 |
| TOTAL cost | R$ | 13357.91 | 13513.32 | 13900.70 | 14075.37 | 13791.62 | 14328.19 | 13711.98 |

*V1: Beams; V2: Primary beam; V3: Girder

The table indicates the smallest environmental impact for an $f_{ck}$ of 25 MPa and the cheapest solution for a compressive strength of 20 MPa. Therefore, increases in the compressive strength of concrete do not improve the optimized solution and the most financially optimum alternative does not correspond to the lowest environmental impact. The optimization program arrived at the same solution of steel deck as the original design of NEXEM, given that the steel sheet from the table used already presented the minimum dimensions.

An assessment of optimized solution concerning environmental impact and cost indicates that the difference of $CO_2$ emission for finding the best cost is 1.04%, smaller than what is observed for the cost of 1.15%.

Based on Figure 10a, the largest portion of $CO_2$ emission stems from the steel deck, with an average of 37.57%, while the most expensive item is the girder V3, corresponding, on average, to 33.64% of the total cost (see Figure 10b).

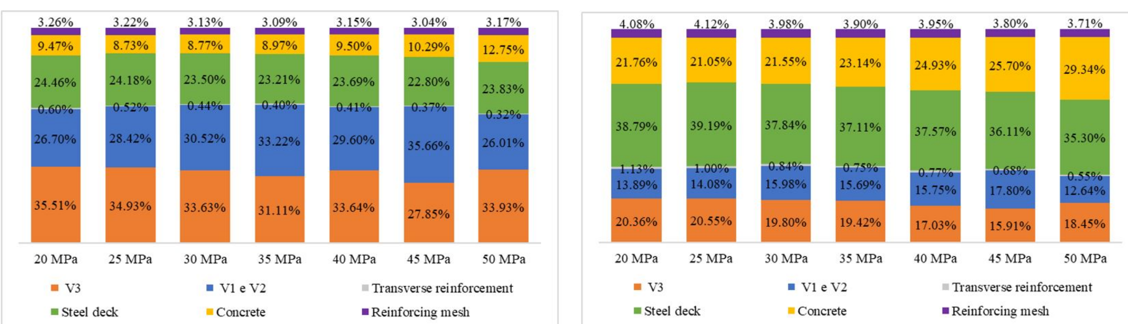


(a) $CO_2$ emission for each element from the optimized solution for example 2 (b) Cost for each element from the optimized solution for example 2

**Figure 10.** Optimized solution for example 2

Further, steel generates the largest material consumption of the global floor system, which represents the equivalent of 76.06% of $CO_2$ emission and 90.22% of the total cost.

Figures 11a and 11b present the SLS and the ULS for the beam V1, primary beam V2 and girder V3. It is noted that percentages for SLS and ULS are large for the design of beam V1 and primary beam V2. Girder V3, however, presents smaller values for each limit state, especially for $\Delta\delta$, that is, the design value is close to the allowable limit prescribed by the SLS.

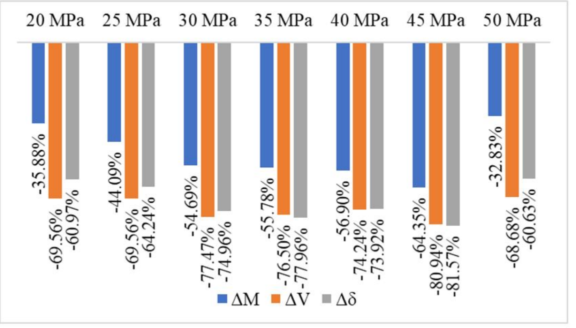


(a) Beam V1 and primary beam V2

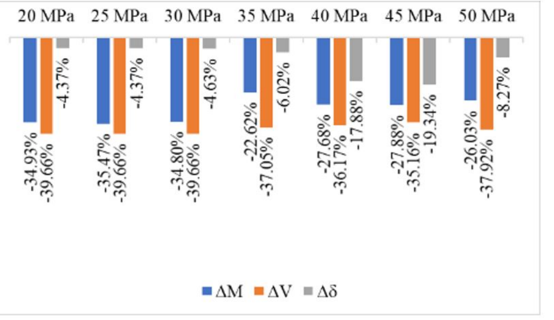


(b) Girder V3

**Figure 11.** Verification of SLS and ULS

## 4. CONCLUSIONS

This present study proposed a formulation for optimizing the design of a floor system featuring steel-concrete composite girders and slabs, with the objective of determining a structural system of minimal financial and environmental costs.

The formulation was validated by two numerical examples, the first of which originally presented by Fakury et al. [27] and the second corresponding to an existing structure featuring the same composite floor system in its structure, Nexem.

The first example showed that, despite the optimized design increasing the number of beams, amplifying financial and environmental costs attributed to these elements, the solution presents lighter girders and reduced the geometry of the composite slab. Overall, the solution reduced $CO_2$ emission by 12.32% and cost by 9.11%. If limits according to the class of environmental aggressiveness are imposed on the values of concrete strength, alternatives in accordance to studies conducted by Kripakaran et al. [11] on a decision making support system and application of MGA, indicate an optimal solution corresponding to an $f_{ck}$ of 40MPa.

In similar fashion to the first case study, results from the second example present an increase in the number of beams and lighter profiles. Consequently, the typology of the composite slab was subjected to reductions in all components except the steel deck. Overall, the optimized design reduced environmental impact by 17.7% and cost by 17.47%.

Both examples indicated a reduction in environmental impact in comparison with the original solution, since most elements adopted for the optimized design presented reductions in geometry, and consequently, in weight. It is also noted that optimizing $CO_2$ emission reduced the cost of the structure, indicating that structural weight is related to cost and environmental parameters.

The detailing of the cost and $CO_2$ emission of the materials included in the optimization shows a larger environmental impact attributed to steel elements, with more than 75% in both examples. Likewise, the largest costs also result from steel elements, reaching a value of 90% in relation to the cost of the concrete used. As such, the materials that generate the largest $CO_2$ emission also represent the largest portion of global costs.

In closure, both examples showed that the steel deck presents the largest percentage of environmental impact for the entire system, while primary beam and beam profiles with the same cross-section presented the largest cost. Furthermore, it was seen that increasing $f_{ck}$ does not improve environmental factors, however, if standardized restrictions are imposed on this parameter, the solution corresponding to the lowest environmental impact is not necessarily the same.

## ACKNOWLEDGEMENTS

The authors would like to thank Capes and Fapes for the support given to the postgraduate program in civil engineering at UFES and CNPq for the research grant provided.

## REFERENCES

[1] H. T. Öztürk, T. Dede, and E. Türker, "Optimum design of reinforced concrete counterfort retaining walls using TLBO, Jaya algorithm," *Structures*, vol. 25, pp. 285–296, 2020, http://dx.doi.org/10.1016/j.istruc.2020.03.020.

[2] E. N. Kalemci, S. B. İkizler, T. Dede, and Z. Angın, "Design of reinforced concrete cantilever retaining wall using Grey wolf optimization algorithm," *Structures*, vol. 23, pp. 245–253, 2020, http://dx.doi.org/10.1016/j.istruc.2019.09.013.

[3] H. R. Maier, S. Razavi, Z. Kapelan, L. S. Matott, J. Kasprzyk, and B. A. Tolson, "Introductory overview: Optimization using evolutionary algorithms and other metaheuristics," *Environ. Model. Softw.*, vol. 114, pp. 195–213, 2019, http://dx.doi.org/10.1016/j.envsoft.2018.11.018.

[4] M. Shahnewaz, A. Rteil, and M. S. Alam, "Shear strength of reinforced concrete deep beams: a review with improved model by genetic algorithm and reliability analysis," *Structures*, vol. 23, pp. 494–508, 2020, http://dx.doi.org/10.1016/j.istruc.2019.09.006.

[5] E. Zhu et al., "Optimizing reinforced concrete beams under different load cases and material mechanical properties using genetic algorithms," *Steel Compos. Struct.*, vol. 34, pp. 467–485, 2020. https://doi.org/http://dx.doi.org/10.12989/scs.2020.34.4.467.

[6] A. F. Tormen, Z. M. C. Pravia, F. B. Ramires, and M. Kripka, "Optimization of steel-concrete composite beams considering cost and environmental impact," *Steel Compos. Struct.*, vol. 34, pp. 409–421, 2020. https://doi.org/http://dx.doi.org/10.12989/scs.2020.34.3.409.

[7] M.-B. Prendes-Gero, A. Bello-García, J.-J. del Coz-Díaz, F.-J. Suárez-Domínguez, and P.-J. García Nieto, "Optimization of steel structures with one genetic algorithm according to three international building codes," *Rev. Constr.*, vol. 17, pp. 47–59, 2018, http://dx.doi.org/10.7764/RDLC.17.1.47.

[8] J. Malveiro, D. Ribeiro, C. Sousa, and R. Calçada, "Model updating of a dynamic model of a composite steel-concrete railway viaduct based on experimental tests," *Eng. Struct.*, vol. 164, pp. 40–52, 2018, http://dx.doi.org/10.1016/j.engstruct.2018.02.057.

[9] M. H. Ha, Q. A. Vu, and V. H. Truong, "Optimum design of stay cables of steel cable-stayed bridges using nonlinear inelastic analysis and genetic algorithm," *Structures*, vol. 16, pp. 288–302, 2018, http://dx.doi.org/10.1016/j.istruc.2018.10.007.

[10] M. Z. Abd Elrehim, M. A. Eid, and M. G. Sayed, "Structural optimization of concrete arch bridges using Genetic Algorithms," *Ain Shams Eng J*, vol. 10, no. 3, pp. 507–516, 2019, http://dx.doi.org/10.1016/j.asej.2019.01.005.

[11] P. Kripakaran, B. Hall, and A. Gupta, "A genetic algorithm for design of moment-resisting steel frames," *Struct. Multidiscipl. Optim.*, vol. 44, no. 4, pp. 559–574, 2011, http://dx.doi.org/10.1007/s00158-011-0654-7.

[12] J. F. Santoro and M. Kripka, "Minimizing environmental impact from optimized sizing of reinforced concrete elements," *Comput. Concr.*, vol. 25, pp. 111–118, 2020.

[13] T. Žula, S. Kravanja, and U. Klansek, "MINLP optimization of a composite I beam floor system," *Steel Compos. Struct.*, vol. 22, no. 5, pp. 1163–1192, 2016, http://dx.doi.org/10.12989/scs.2016.22.5.1163.

[14] J. C. Matos, I. B. Valente, P. J. S. Cruz, and V. N. Moreira, "Probabilistic-based assessment of composite steel-concrete structures through an innovative framework," *Steel Compos. Struct.*, vol. 20, no. 6, pp. 1345–1368, 2016, http://dx.doi.org/10.12989/scs.2016.20.6.1345.

[15] T. Dede, "Jaya algorithm to solve single objective size optimization problem for steel grillage structures," *Steel Compos. Struct.*, vol. 26, pp. 163–170, 2018. https://doi.org/http://dx.doi.org/10.12989/scs.2018.26.2.163.

[16] M. Shariati et al., "Application of Extreme Learning Machine (ELM) and Genetic Programming (GP) to design steel-concrete composite floor systems at elevated temperatures," *Steel Compos. Struct.*, vol. 33, pp. 319–332, 2019. https://doi.org/https://doi.org/10.12989/scs.2019.33.3.319.

[17] A. Kaveh and A. S. M. Abadi, "Cost optimization of a composite floor system using an improved harmony search algorithm," *J. Construct. Steel Res.*, vol. 66, no. 5, pp. 664–669, 2010, http://dx.doi.org/10.1016/j.jcsr.2010.01.009.

[18] S. Kravanja, T. Žula, and U. Klanšek, "Multi-parametric MINLP optimization study of a composite I beam floor system," *Eng. Struct.*, vol. 130, pp. 316–335, 2017, http://dx.doi.org/10.1016/j.engstruct.2016.09.012.

[19] R. L. Pedro, J. Demarche, L. F. F. Miguel, and R. H. Lopez, "An efficient approach for the optimization of simply supported steel-concrete composite I-girder bridges," *Adv. Eng. Softw.*, vol. 112, pp. 31–45, 2017, http://dx.doi.org/10.1016/j.advengsoft.2017.06.009.

[20] A. R. Silva and T. A. Rodrigues, "Optimized dimensioning of steel-concrete composite beams," *Rev. IBRACON Estrut. Mater.*, vol. 12, no. 6, pp. 1428–1453, 2019, http://dx.doi.org/10.1590/s1983-41952019000600012.

[21] A. R. Silva, F. A. Neves, and J. B. M. Sousa, "Optimization of partially connected composite beams using nonlinear programming," *Structures*, vol. 25, pp. 743–759, 2020, http://dx.doi.org/10.1016/j.istruc.2020.03.007.

[22] H. Gervásio, “The sustainability of steel and metallic structures” in *Construmetal - Lat. Am. Met. Constr. Congr.*, São Paulo, 2008.

[23] I. Paya-Zaforteza, V. Yepes, A. Hospitaler, and F. González-Vidosa, "$CO_2$-optimization of reinforced concrete frames by simulated annealing," *Eng. Struct.*, vol. 31, no. 7, pp. 1501–1508, 2009, http://dx.doi.org/10.1016/j.engstruct.2009.02.034.

[24] International Energy Agency, *Global Status Report for Buildings and Construction*. 2019.

[25] Mathworks, Inc., *Mathworks R2015a*. 2015.

[26] Associação Brasileira de Norma Técnicas, *Projeto de Estruturas de Aço e de Estruturas Mistas de Aço e Concreto de Edifícios – Procedimento*, ABNT NBR 8800:2008, 2008.

[27] R. Fakury, A. Silva, and R. Caldas, *Dimensionamento de Elementos Estruturais de Aço e Mistos de Aço e Concreto*. São Paulo: Pearson Education do Brasil, 2016.

[28] B. D. Breda, T. C. Pietralonga, and É. C. Alves, "Optimization of the structural system with composite beam and composite slab using Genetic Algorithm," *Rev. IBRACON Estrut. Mater.*, vol. 13, no. 6, pp. e13602, 2020, http://dx.doi.org/10.1590/s1983-41952020000600002.

[29] GERDAU. “Perfil estrutural.” https://www2.gerdau.com.br/produtos/perfil-estrutural (accessed May. 17, 2020).

[30] METFORM. “Steel Deck: a solução definitiva em lajes.” http://www.metform.com.br/ wordpress/wpcontent/ uploads/2015/05/steel_deck_metform.pdf (accessed May 17, 2020).

[31] Worldsteel Association, *LCI Data for Steel Products*, 2019.

[32] Sistema Nacional de Pesquisa de Custos e Índices da Construção Civil. http://www.caixa.gov.br/poder-publico/apoio-poder-publico/sinapi/Paginas/default.aspx (accessed Mar. 20, 2020).

[33] F. C. R. Cordeiro, “Análise de produtividade da mão-de-obra e composição de custos do serviço de execução da laje steel deck,” Undergraduate thesis, UFSC, Florianópolis, 2016.

[34] M. S. Estruturas Metálicas. “Painel steel deck.” https://rms-estruturas-metalicas.webnode.com.pt/products/painel-steel-deck-apartir-de-r%24-46%2C35-m%C2%B2/ (accessed Mar. 19, 2020).

**Author contributions:** PATA: conceptualization, data curation, formal analysis, methodology, writing; MC: conceptualization, data curation, formal analysis, methodology, writing; BDB: data curation, formal analysis, methodology, writing; AFGC: conceptualization, data curation, formal analysis, methodology, supervision, writing ECA: conceptualization, data curation, formal analysis, methodology, supervision, writing.

**Editors:** Mark Alexander, Guilherme Aris Parsekian

IBRACON Structures and Materials Journal
Revista IBRACON de Estruturas e Materiais
ISSN 1983-4195 ismj.org

ERRATUM

# Erratum

Paulo Augusto T. Arpini[a]
Mayane C. Loureiro[a]
Breno D. Breda[a]
Adenílcia F. Calenzani[a]
Élcio C. Alves[a]

[a]Universidade Federal do Espírito Santo – UFES, Departamento de Engenharia Civil, Vitória, ES, Brasil

In the article **"Optimum design of a composite floor system considering environmental and economic impacts"**, DOI number https://doi.org/10.1590/S1983-41952022000300002, published in IBRACON Structures and Materials Journal ISSN 1983-4195, v.15, n.3, e 15302, 2022, on page 1-17:

## 3. RESULTS AND DISCUSSIONS

Where it reads:

**Table 1.** $CO_2$ emission of materials

| Material | Unit | $CO_2$ emissions (kg$CO_2$) | Reference | Material | Unit | $CO_2$ emissions (kg$CO_2$) | Reference |
|---|---|---|---|---|---|---|---|
| Concrete 20 MPa | $m^3$ | 130.68 | Santoro and Kripka [12] | Steel deck | kg | 26.38 | Worldsteel Association [31] |
| Concrete 25 MPa | $m^3$ | 139.88 | | Steel profile | kg | 11.16 | |
| Concrete 30 MPa | $m^3$ | 148.28 | | Studbolt shear connector | | | |
| Concrete 35 MPa | $m^3$ | 162.36 | | Reinforcing steel mesh | kg | 19.24 | |
| Concrete 40 MPa | $m^3$ | 172.77 | | Steel CA50, ø 8 mm, reinforcement bar | | | |
| Concrete 45 MPa | $m^3$ | 185.32 | | | | | |
| Concrete 50 MPa | $m^3$ | 216.40 | | | | | |

It should be read:

**Table 1.** $CO_2$ emission of materials

<table>
<tr><th rowspan="2">Material</th><th rowspan="2">Unit</th><th>$CO_2$ emissions</th><th rowspan="2">Reference</th><th rowspan="2">Material</th><th rowspan="2">Unit</th><th>$CO_2$ emissions</th><th rowspan="2">Reference</th></tr>
<tr><th>($kgCO_2$)</th><th>($kgCO_2$)</th></tr>
<tr><td>Concrete 20 MPa</td><td>$m^3$</td><td>130.68</td><td rowspan="7">Santoro and Kripka [12]</td><td>Steel deck</td><td>kg</td><td>2.638</td><td rowspan="5">Worldsteel Association [31]</td></tr>
<tr><td>Concrete 25 MPa</td><td>$m^3$</td><td>139.88</td><td>Steel profile</td><td rowspan="2">kg</td><td rowspan="2">1.116</td></tr>
<tr><td>Concrete 30 MPa</td><td>$m^3$</td><td>148.28</td><td>Studbolt shear connector</td></tr>
<tr><td>Concrete 35 MPa</td><td>$m^3$</td><td>162.36</td><td>Reinforcing steel mesh</td><td rowspan="2">kg</td><td rowspan="2">1.924</td></tr>
<tr><td>Concrete 40 MPa</td><td>$m^3$</td><td>172.77</td><td>Steel CA50, ø 8 mm, reinforcement bar</td></tr>
<tr><td>Concrete 45 MPa</td><td>$m^3$</td><td>185.32</td><td></td><td></td><td></td><td></td></tr>
<tr><td>Concrete 50 MPa</td><td>$m^3$</td><td>216.40</td><td></td><td></td><td></td><td></td></tr>
</table>

Rev. IBRACON Estrut. Mater., vol. 15, no. 3, e15303, 2022

IBRACON Structures and Materials Journal
Revista IBRACON de Estruturas e Materiais
ISSN 1983-4195 ismj.org

ORIGINAL ARTICLE

# Ultrasonic wave propagation in thermally treated concrete up to 400 ºC

*Propagação de ondas ultrassônicas em concreto termicamente tratado até 400 ºC*

Ana Carolina Costa Viana[a]
Poliana Dias de Moraes[a]
Ivo José Padaratz[a]

[a]Universidade Federal de Santa Catarina – UFSC, Departmento de Engenharia Civil, Florianópolis, SC, Brasil

Received 06 November 2020
Accepted 21 September 2021

**Abstract:** The ultrasonic pulse velocity, obtained by ultrasonic non-destructive testing, has been applied to evaluate the concrete integrity. The attenuation parameters have shown more sensitivity to damage detection in the microstructure of concrete since they consider the entire ultrasonic waveform. However, it is still necessary to evaluate the sensitivity of those parameters to thermally damaged concrete. This work aims to assess the behavior and the sensitivity of the following ultrasonic parameters: pulse and group velocities, maximum amplitude, total energy, accumulated energy, and time instants corresponding to 25%, 50%, and 75% of the energy, in detecting changes due to thermal degradation of the concrete. A sample of 39 cylindrical concrete specimens with 100 mm in diameter and 300 mm in length and C25 strength class was used. The sample was distributed into 5 groups heated between 20 and 400 ºC until the internal temperature of the specimens became homogeneous. The groups were cooled inside a muffle furnace until reaching 150 ºC. Subsequently, they were exposed to the ambient temperature and humidity of the laboratory environment for, at least, 24 hours prior to the tests of mass loss, ultrasound, and compressive strength. The results show that the ultrasonic parameters are sensitive to the thermal degradation of the concrete. The pulse velocity, the accumulated energy, and the time instants corresponding to percentages of the energy decrease monotonically as the temperature increases. The group velocity shows significant dispersions, while the maximum amplitude and the total energy increase at 200 ºC. The results led to the conclusion that the pulse velocity is the least sensitive parameter, while the time instants corresponding to 25%, 50%, and 75% of the energy are the most sensitive parameters in detecting changes due to thermal degradation of the concrete.

**Keywords:** ultrasound, attenuation parameters, sensitivity, concrete, high temperatures.

**Resumo:** A velocidade de pulso ultrassônico, obtida por meio do ensaio não destrutivo do ultrassom, tem sido usada para avaliar a integridade do concreto. Os parâmetros de atenuação têm apresentado maior sensibilidade na detecção de danos na microestrutura do concreto, visto que consideram todo o formato da onda ultrassônica. Porém, ainda é necessária a avaliação da sensibilidade desses parâmetros ao concreto danificado termicamente. Este trabalho tem como objetivo avaliar o comportamento e a sensibilidade dos seguintes parâmetros ultrassônicos: velocidades de pulso e de grupo, amplitude máxima, energia total, energia acumulada e tempos de propagação correspondentes a 25%, 50% e 75% da energia, na detecção de mudanças devidas à degradação térmica do concreto. Uma amostra de 39 corpos de prova cilíndricos de concreto de 100 mm de diâmetro e 300 mm de comprimento e de classe de resistência C25 foi usada. Ela foi distribuída em 5 grupos aquecidos entre 20 e 400 ºC, até que a temperatura interna dos corpos de prova se tornasse homogênea. Os grupos foram resfriados dentro do forno elétrico até 150 ºC. Em seguida, eles foram expostos à temperatura e à umidade do laboratório por, no mínimo, 24 horas antes dos ensaios de perda de massa, de ultrassom e de resistência à compressão. Os resultados mostram que os parâmetros do ultrassom são sensíveis à degradação térmica do concreto. A velocidade de pulso, a energia acumulada e os tempos correspondentes às porcentagens de energia decrescem monotonicamente conforme a temperatura aumenta. A velocidade de grupo apresenta dispersões significativas, enquanto a amplitude máxima e a energia total aumentam aos 200 ºC. Os resultados permitem concluir que a velocidade de pulso é o parâmetro que possui menor sensibilidade, enquanto os tempos correspondentes a 25%, 50% e 75% da energia são considerados os parâmetros de maior sensibilidade na detecção de mudanças devido à degradação térmica do concreto.

**Palavras-chave:** ultrassom, parâmetros da atenuação, sensibilidade, concreto, altas temperaturas.

**How to cite:** A. C. C. Viana, P. D. Moraes, and I. J. Padaratz, "Ultrasonic wave propagation in thermally treated concrete up to 400 ºC," *Rev. IBRACON Estrut. Mater.*, vol. 15, no. 3, e15303, 2022, https://doi.org/10.1590/S1983-41952022000300003

**Corresponding author:** Ana Carolina Costa Viana. E-mail: anacarolviana@outlook.com
**Financial support:** Coordination for the Improvement of Higher Education Personnel (CAPES).
**Conflict of interest:** Not applicable.
**Data Availability:** The data that support the findings of this study are available from the corresponding author, ACCV, upon reasonable request.

## 1 INTRODUCTION

Ultrasonic testing is a non-destructive method based on the propagation of stress waves, which has been used in the analysis of concrete quality. It detects superficial and internal damage using a fast and simple procedure. Since it is a non-destructive method, it allows monitoring the internal structure of the concrete. Therefore, ultrasonic testing can help in selecting appropriate procedures for the repair and rehabilitation of concrete structures and in the concrete integrity assessment, even in cases of fire damage [1], [2].

The ultrasonic pulse velocity (UPV) is commonly used to indicate the damage degree, since velocities are generally lower in damaged concrete [3], [4]. However, according to Santhanam [5] and Shiotani and Aggelis [6], this parameter does not give a complete evaluation of the concrete damage since ultrasonic pulse velocity (UPV) is measured from the first detectable wave disturbance. Signal processing applied to the ultrasound method made feasible the analysis of attenuation parameters, such as group velocity, maximum amplitude, and energy, by analyzing the ultrasonic waveforms [7]. Ultrasound attenuation is the result of energy loss due to scattering from the concrete microstructure, which redirects the energy beam, and due to dissipation from the viscoelastic water/cement matrix, which is related to the energy absorption [8].

According to Hauwaert [7], the attenuation parameters are more sensitive to damage since they include information from the ultrasonic signal in an entire time window. Research has shown the sensitivity of attenuation parameters to the presence of cracks and non-homogeneities in concrete specimens with compressive strength of 20 to 70 MPa and 28 days to 4 years old [5], [9], [10]. Santhanam [5], Moradi-Marani [11], Carelli [12], Hofmann [13] and Silva [14] studied the behavior of attenuation parameters in cubic concrete specimens and reinforced concrete beams subjected to loading. The results have shown that attenuation parameters are more sensitive than pulse velocity to the presence of damage. Hauwaert [7] analyzed cubic concrete specimens with saw-cut and reported that the maximum amplitude and the energy are more sensitive to the presence of microcracks. Camara [15] analyzed cubic concrete specimens with non-homogeneities and observed that the group velocity and the time instants corresponding to percentages of the energy are more sensitive to the presence of non-homogeneities. In addition, Aggelis et al. [16] and Souza and Pinto [10] simulated a repair process using epoxy for filling cracks in concrete specimens and reported that the maximum amplitude and the total energy increase, as the epoxy fills the crack.

In concrete structures subjected to fire, the damage detected by the ultrasound method is related to physicochemical changes in the cement paste and the aggregates, as well as their thermal incompatibility [17], [18]. The first effects of the temperature rise occur when concrete is heated around 100 ºC. The cement paste starts to lose the free water present in the pores, followed by capillary, adsorbed, and interlayer waters, contributing to the porosity and the calcite increase [17], [19], [20]. In addition, ettringite starts to decompose [20], [21]. Between 105 and 110 ºC, chemically bound water from the calcium silicate hydrate (CSH) starts to be released [18], [22]. At 180 ºC, CSH gel starts to dissociate and, consequently, the cement paste loses its binding property, and its porosity increases [21]. Between 200 and 300 ºC, capillary water evaporates completely [19]. Above 300 ºC, the siliceous aggregates lose their strength more expressively, resulting in the shrinkage, the appearance of microcracks, and the reduction in the mechanical properties of the concrete [22-24]. At 350 ºC, calcium hydroxide starts to decompose into lime and water [18]. From 400 ºC, Portlandite crystals start to dehydroxylate, contributing to shrinkage and microcracks in the cement paste [17], [23]. Above 500 ºC, most changes in concrete are considered irreversible [22].

Studies that use ultrasonic testing to assess the integrity of heated concrete usually limit their analysis to the ultrasonic pulse velocity (UPV) [4], [25], [26]. However, Yamada et al. [27] stressed the importance of detailed waveform analysis. Therefore, they also evaluated the behavior of the maximum amplitude and the total energy of the ultrasonic signal in concretes heated up to 600 ºC. They verified that, in most cases, these parameters decrease as the temperature increases and reported that an accurate evaluation of their sensitivity to temperature changes is required. The authors are not aware of studies that assess the behavior of group velocity, accumulated energy, and time instants corresponding to percentages of the energy in heated concrete.

This work aims to assess the behavior and the sensitivity of the following ultrasonic parameters: pulse and group velocities, maximum amplitude, total energy, accumulated energy, and time instants corresponding to 25%, 50%, and 75% of the energy, in detecting changes due to thermal degradation of the concrete.

## 2 MATERIALS AND EXPERIMENTAL PROGRAM

In this section, the methodologies applied to the casting and curing of concrete specimens, the ultrasonic testing and the calculation of ultrasonic parameters, the compressive strength testing, and the statistical analysis of the data are presented.

### 2.1 Concrete mixture

A conventional concrete with a C25 strength class was used. It was produced with: Brazilian Portland cement CP II-Z-32, natural fine sand (sand 1), natural medium sand (sand 2), natural siliceous coarse aggregate, and water from the city of Florianópolis/SC main water supply. The particle size distribution and the physical characteristics of the sands and the coarse aggregate are presented in Figure 1 and Table 1, respectively. They were determined according to the Brazilian standard NBR 7211:2009 [28]. The mix proportions and the characteristics of the concrete are presented in Table 2.

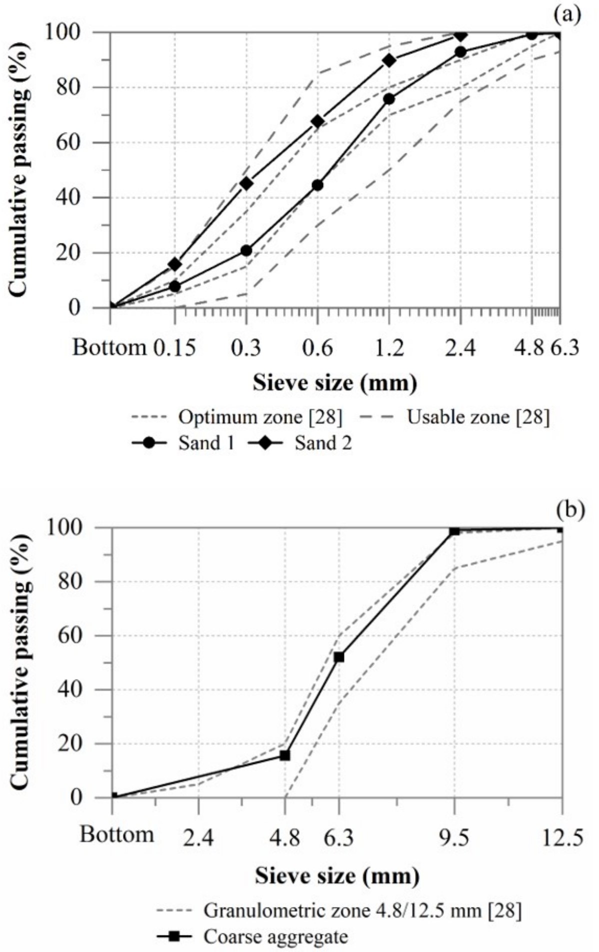


**Figure 1.** Particle size distribution (a) sands (logarithmic scale); (b) coarse aggregate.

**Table 1.** Physical characteristics of the sands and the coarse aggregate.

| | **Sand 1** | **Sand 2** | **Coarse aggregate** |
|---|---|---|---|
| *Fineness modulus* | *1.83* | *2.59* | *0.88* |
| *Maximum characteristic dimension (mm)* | *2.36* | *4.75* | *9.50* |
| *Minimum characteristic dimension (mm)* | *< 0.15* | *< 0.15* | *< 4.80* |
| *Specific mass (g/cm³)* | *2.61* | *2.52* | *2.91* |

**Table 2.** Concrete mixture and characteristics.

| ***Constituent materials (kg/m³)*** | ***Cement*** | ***Sand 1*** | ***Sand 2*** | ***Coarse aggregate*** | ***Water*** |
|---|---|---|---|---|---|
| | *400.16* | *428.17* | *428.17* | *948.38* | *256.41* |
| ***Characteristics of the concrete*** | ***Dry material content (kg)*** | | ***Mortar content (%)*** | ***Water/cement ratio*** | ***Slump test (cm)*** |
| | *4.51* | | *56.99* | *0.64* | *6.50* |

## 2.2 Sample and specimens

The sample consisted of 47 cylindrical concrete specimens with 100 mm in diameter and 300 mm in length, as recommended by RILEM TC 129 MHT [29] for concrete specimens exposed to high temperatures. They were cast and compacted according to the Brazilian standard NBR 5738:2015 [30]. During this process, type K thermocouples were inserted in the geometric centers of 5 specimens to measure their internal temperature throughout the preliminary heating tests.

After 24 hours of casting, the concrete specimens were demolded and stored in a humid chamber for 6 days, as recommended by RILEM TC 129 MHT [29]. Following the curing period, they were exposed to the ambient temperature and humidity of the laboratory environment for another 56 days, to simulate a concrete aging process close to the real and to decrease the interference that late hydration reactions of cement could cause during the concrete heating process [31], [32].

After 28 days of curing, 7 specimens were subjected to compressive strength tests and showed an average compressive strength of 29 MPa, with a standard deviation of 1.2 MPa. After 63 days of curing, the concrete specimens were divided into 6 groups and exposed to temperatures between 20 and 500 °C, as specified in Table 3. Once the specimens had cooled, they were subjected to the following tests: mass loss, ultrasound, and compressive strength, as presented in the flow chart illustrated in Figure 2.

**Table 3.** Number of specimens.

| Group | Temperature (°C) | Number of specimens | |
|---|---|---|---|
| | | Preliminary heating tests | Heating test, ultrasonic test, and compressive strength test |
| *I* | *20* | - | *7* |
| *II* | *100* | *1* | *7* |
| *III* | *200* | *1* | *7* |
| *IV* | *300* | *1* | *7* |
| *V* | *400* | *1* | *7* |
| *VI* | *500* | *1* | - |

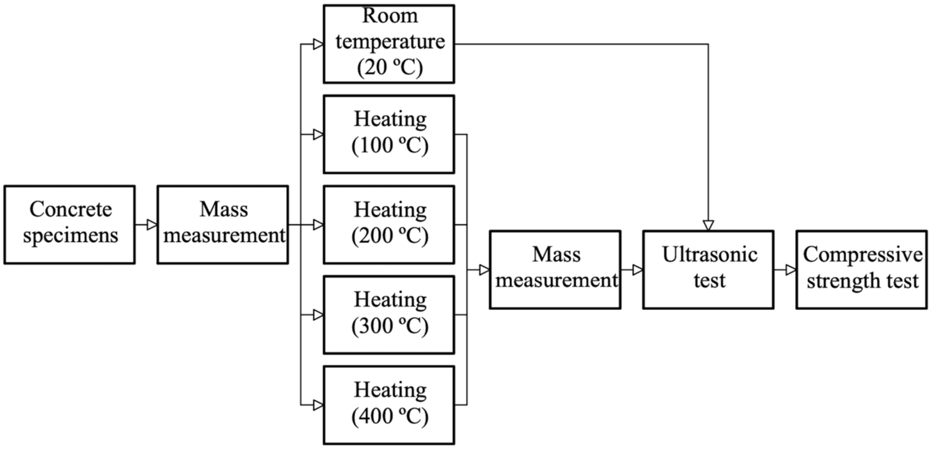


**Figure 2.** Tests sequence

## 2.3 Heating tests

A muffle furnace with internal dimensions of 460 mm × 610 mm × 590 mm, 12 kW power, and heating capacity up to 1340 °C was used. Preliminary heating tests were performed using one cylindrical concrete specimen (groups II to VI), with an inserted type K thermocouple, for each temperature level (100, 200, 300, 400, and 500 °C). They were heated at a rate of 10 °C/min to avoid internal stresses caused by the thermal gradient between the outer and inner parts of the concrete specimens.

During the preliminary heating tests, the internal temperature of the concrete specimens was measured by connecting the thermocouples to a data acquisition system. The obtained data allowed to determine the time required to achieve a homogeneous temperature throughout the specimens. The specimens heated up to 500 °C suffered an explosive spalling precluding the application of the ultrasonic test. Therefore, the following heating tests were performed up to 400 °C.

Groups II to V, composed of 7 concrete specimens each, were heated according to the heating cycles determined based on the preliminary tests, shown in Table 4. After the thermal treatment, the groups were cooled inside the muffle furnace, until they had reached 150 °C. Subsequently, they were exposed to the ambient temperature and humidity of the laboratory environment for, at least, 24 hours prior to the tests of mass loss, ultrasound, and compressive strength.

**Table 4.** Heating cycles.

| Group | Temperature (°C) | Time 1 (h-min) | Time 2 (h-min) |
|---|---|---|---|
| *II* | *100* | *00:10* | *03:50* |
| *III* | *200* | *00:20* | *04:50* |
| *IV* | *300* | *00:30* | *03:10* |
| *V* | *400* | *00:40* | *02:30* |

Time 1: time for the muffle furnace to reach the testing temperature; Time 2: time for the entire specimen to reach the testing temperature.

## 2.4 Mass loss measurements

The mass loss of the specimens was determined by Equation 1. The specimens of Group I were weighed once, while the specimens of groups II to V were weighed before the heating tests and after the cooling process.

$$ML = [(m_i - m_f) / m_f].100 \,, \tag{1}$$

where $ML$ is the mass loss (%), $m_i$ is the mass of the concrete specimen before the heating test (g), and $m_f$ is the mass of the concrete specimen after the heating test and the cooling process (g).

## 2.5 Ultrasonic testing

The ultrasonic tests were conducted with two piezoelectric transducers, a source, and a receiver of 20 mm diameter, coupled to the opposite faces of the specimen in a direct transmission arrangement. They excite longitudinal (P) waves with a frequency band of 200 kHz. The electric impulses generated by the ultrasonic instrument had a pulse amplitude of 500 V and a pulse width of 2.5 µs. The signal response was sampled with a sampling rate of 2 MHz and a recording time window of 5 ms.

Before starting the tests, the specimens of groups I to V were prepared according to the Brazilian standard NBR 8802:2019 [33]. Subsequently, the ultrasonic instrument was calibrated through the coupling of the transducers to the calibration rod, using a coupling gel between the surfaces. Twenty measurements were performed for each specimen, to ensure sufficient data and to reduce the variability in the results. Based on the average of the data signals obtained for each specimen, the following parameters were analyzed: pulse and group velocities, maximum amplitude, total energy, accumulated energy, and time instants corresponding to 25%, 50%, and 75% of the energy (Figure 3).

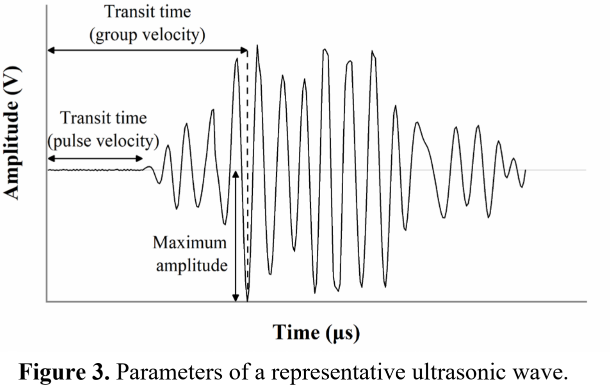


**Figure 3.** Parameters of a representative ultrasonic wave.

### 2.5.1 Ultrasonic parameters

The pulse velocity and the maximum amplitude parameters were obtained directly from the ultrasonic signal data, while the group velocity, the total energy, the accumulated energy, and the time instants corresponding to percentages of energy were calculated. The group velocity of the waveforms was calculated using Equation 2, according to Washer et al. [34]. The distance between the transducers, which is the specimen length (300 mm), and the transit time for the maximum amplitude of the waveform were considered [12], [13].

$$V_g = L / t_{am} , \tag{2}$$

where $V_g$ is the group velocity (m/s), $L$ is the distance between the two transducers (m), and $t_{am}$ is the transit time for the maximum amplitude of the waveform (s).

The total energy of the waveform was calculated by the module of the area under the signal [6], [10], as shown in Equation 3.

$$E = \int_{t0}^{ti} \left| A(t) \right| dt, \tag{3}$$

where $E$ is the total energy (V.ms), $A(t)$ is the amplitude of the signal at time t (V), $t$ is the time (ms), $t_0$ is the starting time of the first wave group (ms), and $t_i$ is the time corresponding to the end of the first wave group (ms).

The accumulated energy of the waveforms, within the time window of 5 ms, was calculated as the sum of percentages of the energy at intervals of 0.5 μs [6]. The slope of the curves was calculated by Equation 4. A range of 0.1% to 50% of the energy was considered.

$$m = y_2 - y_1 / x_2 - x_1 , \tag{4}$$

where $m$ is the slope of the curve, $y_2$ is 50% of the energy (%), $y_1$ is 0.1% of the energy (%), $x_2$ is the time corresponding to 50% of the energy (ms), and $x_1$ is the time corresponding to 0.1% of the energy (ms).

The time instants corresponding to 25%, 50%, and 75% of the energy were obtained by verifying the time that these percentages of energy occurred.

## 2.6 Compressive strength measurements

After the ultrasonic tests, the specimens of groups I to V were tested with at least 63 days old, according to the Brazilian standard NBR 5739:2018 [35]. The compressive strength of the concrete was calculated by Equation 5.

$$\sigma = F_{max} / A, \tag{5}$$

where $\sigma$ is the compressive strength of concrete (MPa), $F_{max}$ is the maximum force applied to the specimen during the test (N), and $A$ is the cross-section area of the specimen (mm$^2$).

After obtaining the concrete average compressive strength, the characteristic compressive strength of Group I (20 °C) was calculated according to the Brazilian standard NBR 12655:2015 [36]. Then, the reduction coefficients of the compressive strength were calculated by Equation 6.

$$k_{c,\theta} = f_{c,\theta} / f_{ck} , \tag{6}$$

where $k_{c,\theta}$ is the reduction coefficient of the concrete compressive strength, $f_{c,\theta}$ is the compressive strength (MPa) at temperature θ (°C), and $f_{ck}$ is the characteristic compressive strength (MPa) at ambient temperature.

### 2.7 Statistical analysis methods

The influence of temperature on the mass loss, ultrasonic and compressive strength data was statistically analyzed, using a software package. Firstly, the occurrence of outliers was verified, and these data were eliminated [37]. Subsequently, the Kolmogorov-Smirnov normality test was performed, at 5% significance [38]. For data normality, the analysis of variance test (ANOVA) and Tukey's tests were performed at 5% probability of error [38]. When the assumption of normality was violated, Kruskal-Wallis and multiple comparisons tests were performed at 5% probability of error [38].

## 3 RESULTS AND DISCUSSIONS

In this section, the following results are presented and discussed: mass loss, residual compressive strength, ultrasonic pulse velocity (UPV), group velocity, maximum amplitude, total energy, accumulated energy, and time instants corresponding to 25%, 50%, and 75% of the energy.

### 3.1 Mass loss

The mass losses of the concrete specimens due to thermal treatment are illustrated in Figure 4. Groups II to V present an average mass loss of 1%, 6%, 7%, and 7%, respectively. The Tukey test revealed statistically significant differences among group means, except between the following groups: I and II (20-100 ºC), III and IV (200-300 ºC), III and V (200-400 ºC), IV and V (300-400 ºC).

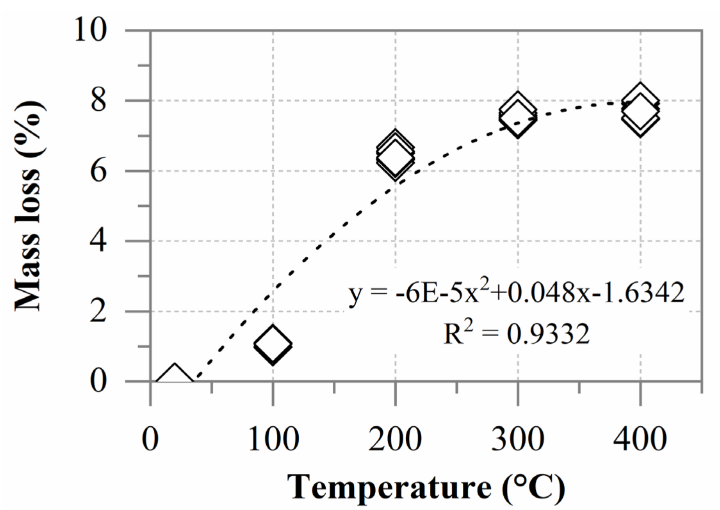


**Figure 4.** Mass losses of the concrete specimens.

The mass loss increases non-linearly as the temperature increases. Similar results were obtained by Malik [39] and Silva [40], which analyzed concretes with a compressive strength between 40 and 50 MPa. The data show that, up to 100 °C, the average mass loss is 1%, since at this temperature the water starts to change its phase from liquid to gaseous [19]. At 200 °C, the average mass loss is more significant, corresponding to 6%, since the physically adsorbed and free waters have already completely evaporated and the chemically bound water starts to be released [18], [19], [39]. Also, the CSH gel starts to dissociate and, consequently, the cement paste porosity increases [21]. At 300 °C, all types of water start to evaporate, and the mass loss is 7%.

Regarding the mass loss measurement, the thermal treatment caused changes in the mass of concrete specimens. The results indicate that the concrete porosity increases, and the chemical compounds were decomposed. These alterations change the compressive strength and the ultrasonic waveform of the concrete. However, a thermogravimetric analysis might be done to verify the chemical changes due to the mass loss.

### 3.2 Compressive strength of the concrete

The compressive strengths of the concrete specimens are illustrated in Figure 5. Groups I to V exhibit an average compressive strength and a coefficient of variation of 35 (15%), 28 (17%), 27.5 (15%), 28 (5%), and 24 (6.5%) MPa, respectively. The Tukey test revealed statistically significant differences between the following groups: I and II (20- 100 °C), I and III (20-200 °C), I and IV (20-300 °C), I and V (20-400 °C), indicating that the thermal treatment affects the compressive strength of the concrete.

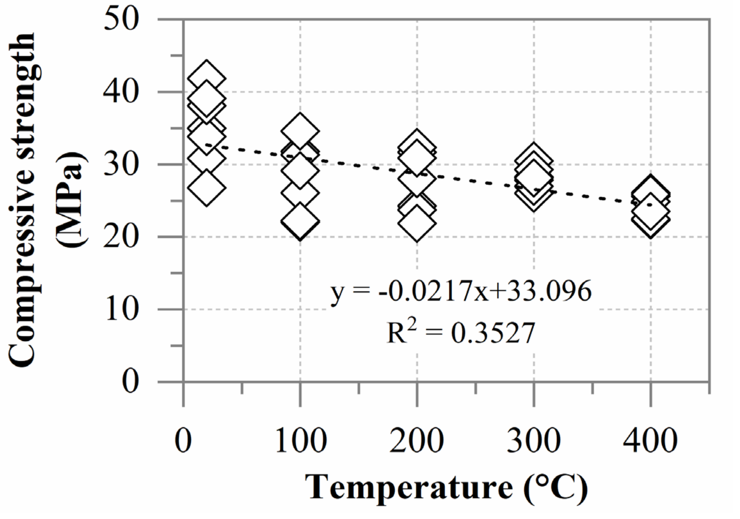


**Figure 5.** Compressive strength of the concrete specimens.

The data show that the compressive strength decreases as the temperature increases, as observed by Handoo et al. [4], Silva [40], and Ergün et al. [41]. This behavior results from the evaporation of all types of water present in the concrete, the dissociation of the CSH gel, the dehydroxylation of the Portlandite, the shrinkage of the cement paste, and the thermal incompatibility between the cement paste and the aggregates [17-23]. At 400 °C, the compressive strength reduces 30%, due to the chemical transformations of the cement paste, the breakup of some siliceous aggregates, and the presence of cracks in the transition zone [17], [18].

The reduction coefficients of the compressive strength of thermally treated concrete are shown in Table 5. Between 100 and 300 °C, the reduction coefficients of concrete specimens decrease more expressively, when compared to the reduction coefficients of Brazilian standard NBR 15200:2014 [42]. These differences are probably related to several choices used in this research, especially the rate of heating, the time of exposure to heat, and the cooling process since these factors lead to concrete degradation.

**Table 5.** The reduction coefficients of the compressive strength of concrete.

| Group | Temperature (ºC) | Reduction coefficients (tests) | Reduction coefficients (ABNT NBR 15200:2012) |
|---|---|---|---|
| *I* | *20* | *1.00* | *1.00* |
| *II* | *100* | *0.80* | *1.00* |
| *III* | *200* | *0.79* | *0.95* |
| *IV* | *300* | *0.80* | *0.85* |
| *V* | *400* | *0.70* | *0.75* |

### 3.3 Ultrasonic waveforms

The ultrasonic waveforms on a single concrete specimen of each group (I to V), in a time window of 1.5 ms, are illustrated in Figure 6. The specimen of group I (20 °C) exhibits higher amplitudes when compared to those of groups II to V (100, 200, 300, and 400 °C). As the temperature increases, the delay increases, and the amplitudes decrease. This behavior is evident from 300 °C. The observed changes on the waveforms are related to the signal attenuation caused by the presence of microcracks and by the increase in the concrete porosity, due to heating [9]. Carelli [12] and Hofmann [13] identified a similar behavior when comparing reinforced concrete beams before and after the presence of cracks.

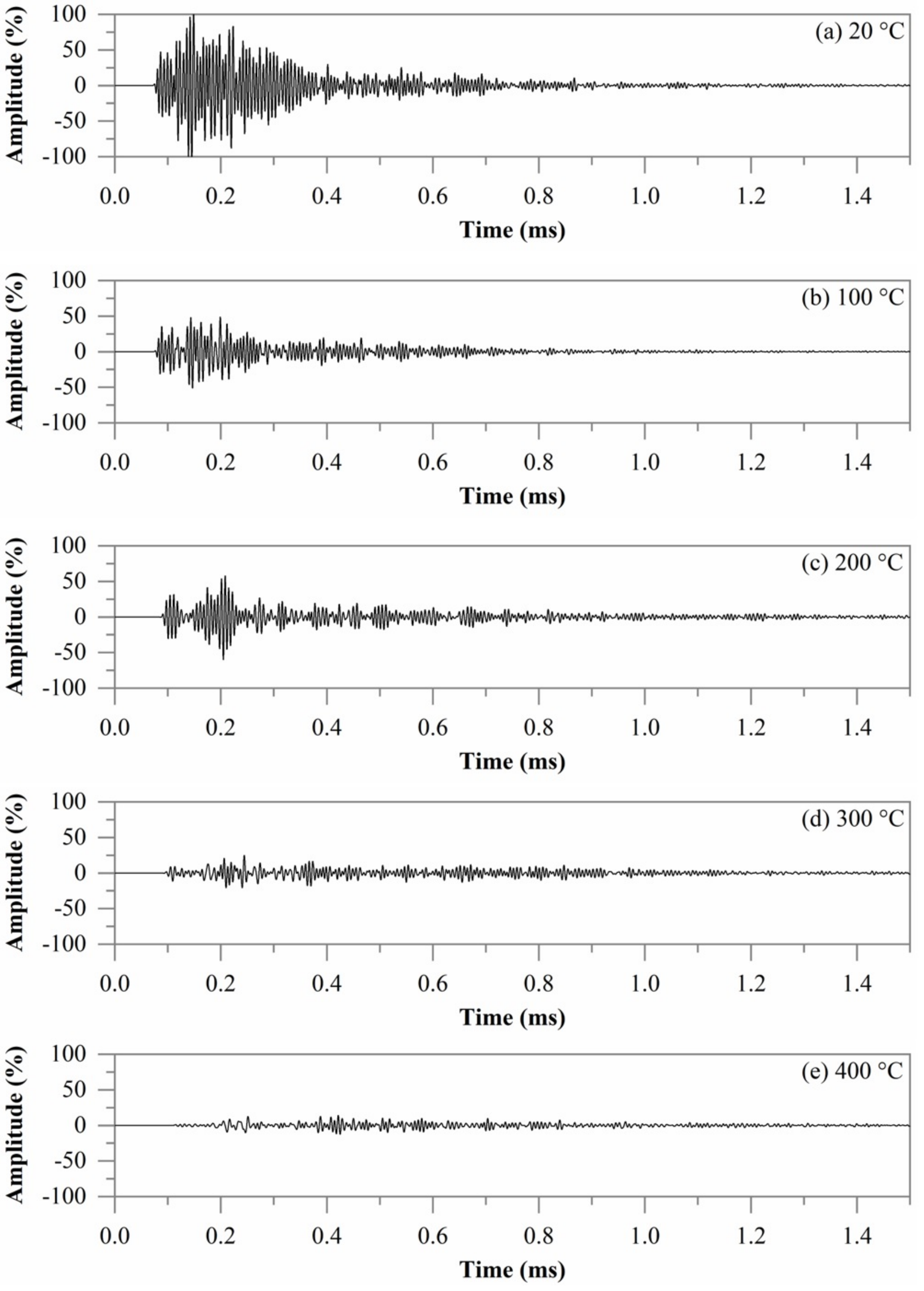


**Figure 6.** Ultrasonic waveform between 20 °C and 400 °C.

## 3.4 Average pulse velocities

The average pulse velocities are illustrated in Figure 7. Groups I to V have an average pulse velocity and a coefficient of variation of 4464 (1.1%), 4299 (1.8%), 3835 (1.0%), 3427 (2.8%), and 2872 (2.5%) m/s, respectively. The Tukey test revealed statistically significant differences among group means.

The data show that the average pulse velocity decreases linearly as the temperature increases. An average decrease of 4% (100 °C), 14% (200 °C), 23% (300 °C), and 36% (400 °C) is observed. Similar results were obtained by Handoo et al. [4], which analyzed cubic concrete specimens heated for 5 hours. They verified that the average pulse velocity of the concrete group heated at 400 ºC decreased 33% compared to the average obtained for the unheated group. This is an expected behavior, since high temperatures cause physicochemical changes in the concrete, such as water evaporation, the dehydration of chemical compounds, and the thermal incompatibility between the cement paste and the aggregates [17-23], [43-44]. These cause mass changes, as observed by the mass loss results, also porosity and microcracks, which increase the time to the first detectable disturbance of the wave, consequently, the UPV values decrease [45].

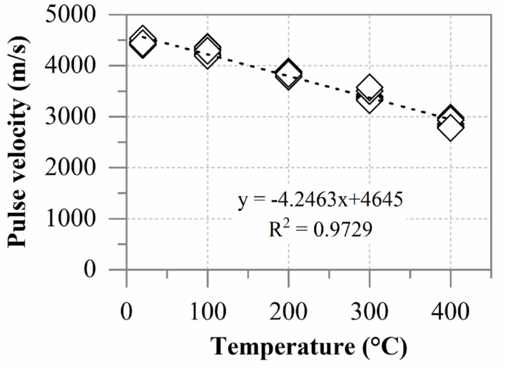


**Figure 7.** Average pulse velocities.

## 3.5 Average group velocities

The average group velocities are illustrated in Figure 8. After the elimination of outliers [37], groups I to V present an average group velocity and a coefficient of variation of 2320 (19%), 1854 (8%), 1444 (21%), 1826 (37%), and 1025 (38%) m/s, respectively. The Tukey test revealed statistically significant differences between the following groups: I and III (20-200 °C), I and V (20-400 °C), II and V (100-400 °C), IV and V (300-400 °C). Therefore, the group velocity can capture the changes undergone by the thermally treated concrete specimens.

The data show that the average group velocity decreases as the temperature increases. However, the average of Group IV (300 °C) is higher than the average obtained for Group III (200 °C). Also, this parameter decreases significantly in the presence of damage when compared to pulse velocity, as evidenced by the reductions of 20% (100 °C), 38% (200 °C), 21% (300 °C), and 56% (400 °C). Similar results were reported by Carelli [12] and Shiotani and Aggelis [6], which analyzed concrete and mortar specimens with artificially induced cracks and cubic mortar specimens containing artificial damage, respectively.

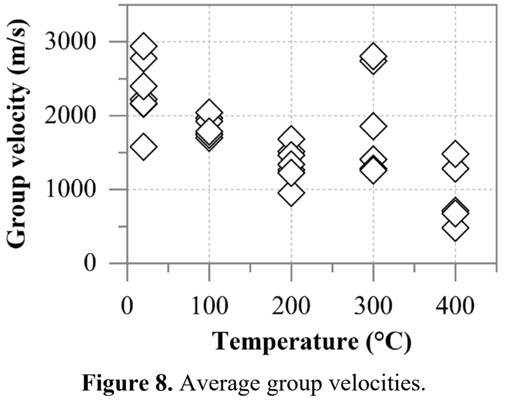


**Figure 8.** Average group velocities.

The data also show significant dispersions like those obtained by Camara [15] when analyzing cubic concrete specimens, with and without non-homogeneities. This behavior is probably due to the dependence of the group velocity on the time corresponding to the maximum amplitude of the waveforms, which can vary among concrete specimens due to their heterogeneity [12], [15]. Further studies are required to assess the behavior of group velocity in thermally degraded concrete, evaluating different approaches for its calculation.

### 3.6 Average maximum amplitudes

The average of the maximum amplitudes of the waveforms are illustrated in Figure 9. After the elimination of outliers [37], groups I to V show an average maximum amplitude and a coefficient of variation of 500 (0%), 273 (20%), 319 (14%), 139 (14%), and 80 (28%) V, respectively. The multiple comparisons test revealed statistically significant differences among group means, denoting that the maximum amplitude can capture the changes undergone by concrete specimens heated up to 400 °C.

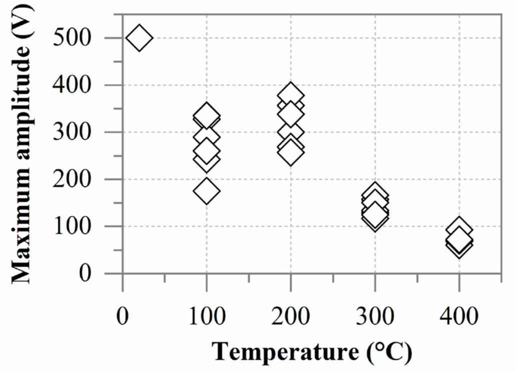


**Figure 9.** Average maximum amplitudes.

The unheated concrete specimens show waveforms with greater maximum amplitudes. At 100 °C, the average maximum amplitude decreases around 45% and a relative minimum of 176 V is verified. This result is probably associated with the greater porosity of this concrete specimen [45]. At 200 °C, the average maximum amplitude reduces only 36% when compared to the unheated group. At 300 and 400 °C, there is an even more significant decrease in the maximum amplitude due to the intensive attenuation of the signal. Yamada et al. [27] observed similar behavior in concrete specimens with a water/cement ratio of 0.7 heated up to 600 °C.

The heating up to 100 ºC causes the evaporation of free water and the increase of cement paste porosity, which decreases the maximum amplitude of the waveform. Above 100 ºC, the loss of free water in the pores, the decomposition of ettringite and the dissociation of CSH gel, contribute to increasing the concentration of calcite [20- 21]. Ngala and Page [46] and Shi et al. [47] states that calcite fills the pores and the voids of cement paste. Therefore, this reaction is probably responsible for the amplitude recovery at 200 ºC. Between 300 and 400 ºC, the chemically bound and capillary waters have already evaporated, increasing the porosity [19]. Also, the thermal incompatibility between the cement paste and the aggregate increases the number of microcracks in the transition zone [17-18]. Consequently, the maximum amplitude of the waveform continues to decrease.

### 3.7 Average total energies

The average total energies of the waveforms are illustrated in Figure 10. After the elimination of outliers [37], groups I to V show an average total energy and a coefficient of variation of 61 (4%), 29 (4%), 42 (11%), 25 (13%), and 15 (6%) V·ms, respectively. The Tukey test revealed statistically significant differences among group means, except between groups II and IV (100-300 °C). This demonstrates that the total energy can capture the changes undergone by the thermally treated concrete.

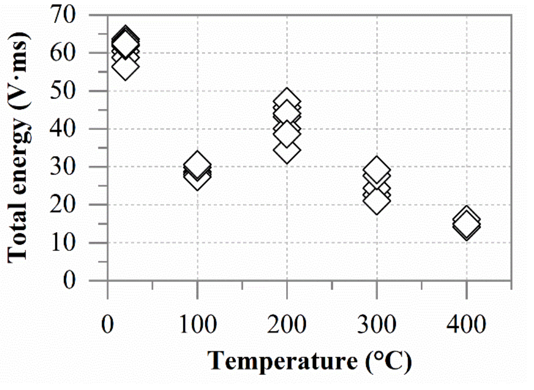


**Figure 10.** Average total energies.

The data show that the average total energy decreases linearly as the temperature increases, except for Group II (100 ºC), which presents a relative minimum. This behavior is like the one presented by the average maximum amplitude, since the energy is related to the amplitudes of the waveform, as observed in Equation 3.

An average decrease of 52% (100 °C), 31% (200 °C), 59% (300 °C), and 75% (400 °C) is observed when compared to the average at 20 ºC. Yamada et al. [27] reported similar results when analyzing concrete prisms with water/cement ratios of 0.5, 0.6, and 0.7 heated up to 600 °C. According to Anugonda et al. [8], the loss of energy is due to the combination of scattering and dissipation of the ultrasonic waves, which was observed in Figure 6. In thermally treated concrete, the energy is absorbed by microcracks, and voids developed due to high temperatures [17], [48].

### 3.8 Average accumulated energies

The average accumulated energies of waveforms are illustrated in Figure 11. The transmitted energy reduces gradually as the temperature increases. The average slopes of the curves decrease 3% (100 °C), 39% (200 °C), 55% (300 °C), and 65% (400 °C). The curves of groups I (20 °C) and II (100 °C) show similar behavior. However, the groups heated above 100 °C show low-sloped curves. Also, at 0.25 ms, Group I reach 50% of the energy, while groups II to V reach 48%, 34%, 23%, and 13% of the energy, respectively. Therefore, accumulated energy can capture the changes undergone by concrete specimens heated up to 400 °C.

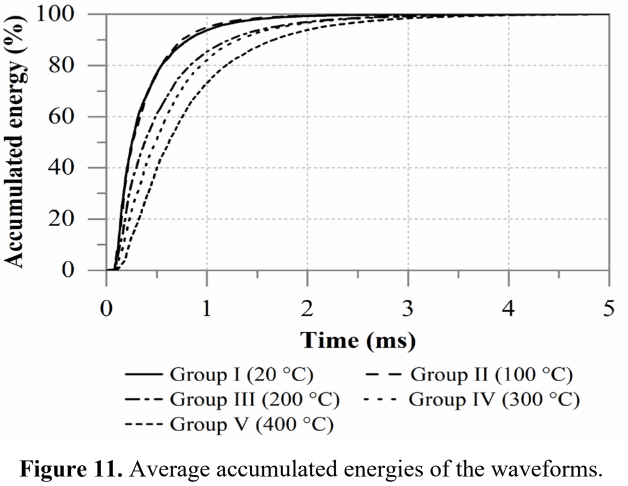


**Figure 11.** Average accumulated energies of the waveforms.

At the beginning of the time window, groups without or with small damage show greater amplitudes, as observed in Figure 6. As the damage increases, the amplitude of the waveforms reduces since the energy accumulates more gradually over time. Consequently, the slopes of the curves are lower [12]. Similar results were reported by Santhanam [5] and Shiotani and Aggelis [6] when analyzing cubic concrete specimens subjected to different load levels and cubic mortar specimens containing artificial damage.

### 3.9 Average time instants corresponding to 25%, 50%, and 75% of the energy

The average time instants corresponding to 25%, 50%, and 75% of the energy waveforms are illustrated in Figure 12. The time instants corresponding to percentages of the energy increases monotonically as the temperature increases. The Tukey test revealed statistically significant differences among group means, except between groups I and II (20-100 °C). Therefore, the time corresponding to percentages of the energy can capture the changes undergone by the thermally treated concrete specimens.

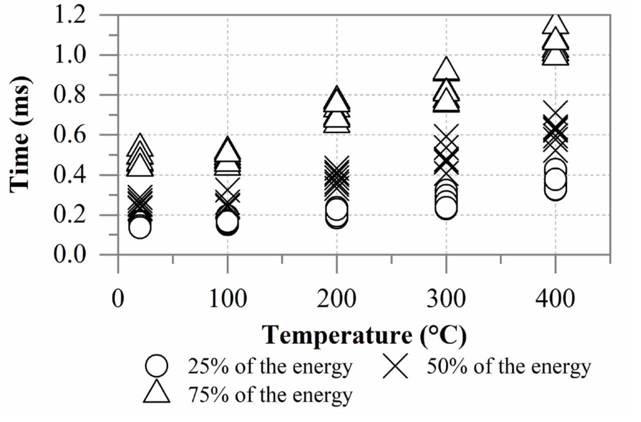


**Figure 12.** Averages time instants corresponding to percentages of the energy.

The average time instants to reach those energy levels increase significantly above 100 °C. They increase 3% between 20 and 100 ºC and 45%, 79% and 132% between the room temperature and 200, 300 and 400 °C, respectively. This is caused by signal attenuation, due to the presence of microcracks and voids in the thermally treated concrete specimens [45]. This behavior was also reported by Hofmann [13] and Silva [14] when analyzing reinforced concrete beams before and after the appearance of cracks.

### 3.10 Ultrasonic parameters sensitivity

To evaluate the sensitivity of the ultrasonic parameters to temperature changes, they were normalized from the values obtained at room temperature, as shown in Table 6. All parameters are sensitive to temperatures changes. The pulse and group velocities, the maximum amplitude, the total energy, and the slope of the accumulated energy curve decrease as the temperature increases, while the time instants corresponding to percentages of the energy increase.

**Table 6.** Normalized ultrasonic parameters.

| Group | Temperature (°C) | Ultrasonic parameters | | | | | | | |
|---|---|---|---|---|---|---|---|---|---|
| | | *Pulse velocity* | *Group velocity* | *Maximum amplitude* | *Total energy* | *Slope of the curve* | *T25%* | *T50%* | *T75%* |
| *I* | *20* | *1.00* | *1.00* | *1.00* | *1.00* | *1.00* | *1.00* | *1.00* | *1.00* |
| *II* | *100* | *0.96* | *0.80* | *0.55* | *0.48* | *0.97* | *1.05* | *1.04* | *1.01* |
| *III* | *200* | *0.86* | *0.62* | *0.64* | *0.69* | *0.61* | *1.31* | *1.52* | *1.52* |
| *IV* | *300* | *0.77* | *0.79* | *0.28* | *0.41* | *0.45* | *1.71* | *1.93* | *1.74* |
| *V* | *400* | *0.64* | *0.44* | *0.16* | *0.25* | *0.35* | *2.33* | *2.43* | *2.21* |

T25%: time instant corresponding to 25% of the energy; T50%: time instant corresponding to 50% of the energy; T75%: time instant corresponding to 75% of the energy.

The attenuation parameters change more significantly in the presence of thermal damage when compared to pulse velocity, especially the time instants corresponding to percentages of the energy and the maximum amplitude, since these parameters consider the information from the ultrasonic waveform in the entire time window [5], while pulse velocity is measured by the first detectable disturbance of the wave [6]. According to Aggelis and Shiotani [48], even though the wave energy scattering affects the amplitudes, some energy remains scattered in the forward direction. This explains why non-homogeneities, have a limited influence on the pulse velocity, when compared to the attenuation parameters.

The pulse velocity, the slope of the accumulated energy curves and the time instants corresponding to percentages of the energy show a characteristic behavior. The group velocity increases at 300 °C, probably, due to its dependence on the time corresponding to the maximum amplitude, which varies between concrete specimens. The total energy and the maximum amplitude increase at 200 °C, probably due to the presence of calcite [20]. Further research should be undertaken to investigate these topics.

Regarding the ultrasonic parameters, the pulse velocity is the least sensitive parameter, followed by the group velocity, which shows significant dispersions. The slope of the accumulated energy curve, the maximum amplitude and the total energy detects the thermal damage, since the first decreases monotonically as the temperature increases, while the second and the third are very sensitive to thermal damage. However, the time instants corresponding to 25%, 50%, and 75% of the energy are the most sensitive parameters, denoting that they can be the best indicator of thermally damaged concrete. Despite these promising results, further studies are recommended before field applications.

## 4 CONCLUSIONS

In this research, the behavior of pulse and group velocities, maximum amplitude, total energy, accumulated energy, and time instants corresponding to percentages of the energy were analyzed in concrete groups heated at five temperature levels in a range of 20 to 400 ºC. The sample consisted of 39 cylindrical concrete specimens measuring 100 mm in diameter and 300 mm in length, distributed into five groups, with an average compressive strength of 29 MPa at room temperature. The results lead to the following conclusions:

- the pulse velocity decreases as the temperature increases, however, it is the least sensitive parameter;
- the group velocity is more sensitive than pulse velocity, but shows significant dispersions;
- the maximum amplitude and the total energy are very sensitive to thermal damage, but further studies must be done to investigate the increase of these parameters at 200 °C;
- the slope of the accumulated energy curve is sensitive to changes in heated concrete since it decreases as the temperature increases;
- the time instants corresponding to 25%, 50%, and 75% of the energy are the most sensitive parameters in detecting changes due to thermal degradation of the concrete.

## ACKNOWLEDGEMENTS

The authors thank the Coordination for the Improvement of Higher Education Personnel (CAPES) for sponsoring this research.

## CITATIONS

[1] International Atomic Energy Agency, *Guidebook on non-destructive testing of concrete structures*. Vienna: IAEA, 2002.

[2] T. R. Naik, V. M. Malhotra, and J. S. Popovics, *Nondestructive testing of concrete*, 2nd ed. Florida: CRC, 2004.

[3]

S. A. Kumar and M. Santhanam, “Detection of concrete damage using ultrasonic pulse velocity method,” in *Proc. National Seminar on Non-Destructive Evaluation*, 2006.

[4] S. K. Handoo, S. Agarwal, and S. K. Agarwal, "Physicochemical, mineralogical, and morphological characteristics of concrete exposed to elevated temperatures," *Cement Concr. Res.*, vol. 32, pp. 1009–1018, 2002.

[5] M. Santhanam, "Ultrasonic characterization of damage in concrete," *Tech Sci. Press*, vol. 3, no. 2, pp. 111–125, 2010.

[6] T. Shiotani and D. G. Aggelis, "Wave propagation in cementitious material containing artificial distributed damage," *Mater. Struct.*, vol. 42, pp. 377–384, 2009.

[7] A. V. Hauwaert, J. F. Thimus, and F. Delannay, "Use of ultrasonics to follow crack growth," *Ultrasonics*, vol. 36, pp. 209–217, 1998.

[8] P. Anugonda, J. S. Wiehn, and J. A. Turner, "Diffusion of ultrasound in concrete," *Ultrasonics*, vol. 39, pp. 429–435, 2001.

[9] T. P. Phillipidis and D. G. Aggelis, "Experimental study of wave dispersion and attenuation in concrete," *Ultrasonics*, vol. 43, pp. 584–595, 2005.

[10] F. C. Souza and R. C. A. Pinto, "Ultrasonic investigation on the effectiveness of crack repair in concrete," *Rev. IBRACON Estrut. Mater.*, vol. 13, no. 5, 2020.

[11] F. Moradi-Marani, P. Rivard, C. P. Lamarche, and S. A. Kodjo, "Evaluating the damage in reinforced concrete slabs under bending test with the energy of ultrasonic waves," *Constr. Build. Mater.*, vol. 73, pp. 663–673, 2014.

[12] J. M. Carelli, "Análise do comportamento de ondas ultrassônicas em elementos fissurados de concreto e argamassa," M.S. thesis, Universidade Federal de Santa Catarina, Florianópolis, 2014.

[13] M. A. Hofmann, "Atenuação da energia do sinal ultrassônico na detecção de danos por fissuração no concreto," M.S. thesis, Universidade Federal de Santa Catarina, Florianópolis, 2015.

[14] P. M. Silva, "Análise da perda de rigidez em vigas de concreto armado devido à fissuração por esforços de flexão utilizando ensaio de ultrassom," M.S. thesis, Universidade Federal de Santa Catarina, Florianópolis, 2017.

[15] R. M. Camara, "Estudo do efeito da variação de pressão de acoplamento no comportamento dos parâmetros ultrassônicos," M.S. thesis, Universidade Federal de Santa Catarina, Florianópolis, 2017.

[16] D. G. Aggelis, T. Shiotani, and D. Polyzos, "Characterization of surface crack depth and repair evaluation using Rayleigh waves," *Cement Concr. Compos.*, vol. 31, pp. 77–83, 2009.

[17] B. Fernandes, A. M. Gil, F. L. Bolina, and B. F. Tutikian, "Microstructure of concrete subjected to elevated temperatures: Physico-chemical changes and analysis techniques," *IBRACON Struct. Mater. J.*, vol. 10, no. 4, pp. 838–863, 2017.

[18] Q. Ma, R. Guo, Z. Zhao, Z. Lin, and K. He, "Mechanical properties of concrete at high temperature—A review," *Constr. Build. Mater.*, vol. 93, pp. 371–383, 2015.

[19] R. C. A. Lima, L. F. Caetano, and L. S. Filho, "Microstructural changes in high density concretes exposed to high temperatures," *IBRACON Mater. J.*, vol. 10, no. 1, pp. 7–14, 2005.

[20] M. Castellote, C. Alonso, C. Andrade, X. Turrillas, and J. Campo, "Composition and microstructural changes of cement pastes upon heating, as studied by neutron diffraction," *Cement Concr. Res.*, vol. 34, pp. 1633–1644, 2004.

[21] M. Malik, S. K. Bhattacharyya, and S. V. Barai, "Thermal and mechanical properties of concrete and its constituents at elevated temperatures: A review," *Constr. Build. Mater.*, vol. 270, pp. 121398, 2021.

[22] O. Arioz, "Effects of elevated temperatures on properties of concrete," *Fire Saf. J.*, vol. 42, no. 8, pp. 516–522, 2007.

[23] B. Georgali and P. E. Tsakiridis, "Microstructure of fire damaged concrete. A case study," *Cement Concr. Compos.*, vol. 27, pp. 255–259, 2005.

[24] G. A. Khoury, "Effect of fire on concrete and concrete structures," *Prog. Struct. Eng. Mater.*, vol. 2, no. 4, 2000.

[25] H. W. Chung, "Ultrasonic testing of concrete after exposure to high temperatures," *NDT Int.*, vol. 18, no. 5, pp. 275–278, 1985.

[26] D. S. Silva, "Propriedades mecânicas residuais após incêndio em concretos usados na construção civil na grande Florianópolis," M.S. thesis, Universidade Federal de Santa Catarina, Florianópolis, 2009.

[27] K. Yamada, H. Tsuchiya, and Y. Kosaka, "Quality evaluation of concrete exposed to high temperature by ultrasonic spectroscopy," *J. Soc. Mater. Sci.*, vol. 38, no. 431, pp. 959–965, 1989.

[28] Associação Brasileira de Normas Técnicas, *Agregados para concreto - Especificação NBR 7211 2009*, 2009.

[29] International Union of Laboratories and Experts in Construction Materials, *Systems and structures, test methods for mechanical properties of concrete at high temperatures Rilem TC 129 MHT Part 3-9*, 1995.

[30] Associação Brasileira de Normas Técnicas, *Moldagem e cura de corpos de prova cilíndricos ou prismáticos de concreto NBR 5738 2015*, 2015.

[31] P. K. Mehta and P. J. M. Monteiro *Concreto - estrutura, propriedades e materiais*, 2nd ed. São Paulo: Ibracon, 2014.

[32] Laboratoire Central des Ponts et Chaussées, *Recommendations for preventing disorders due to Delayed Ettringite Formation*. Descartes: Ifsttar, 2009. Accessed: Nov. 06, 2020. [Online]. Available: https://www.ifsttar.fr/fileadmin/user_upload/editions/ifsttar/guidetechnique/2018-GTI5.A-guidetechnique-Ifsttar.pdf

[33] Associação Brasileira de Normas Técnicas, *Concreto endurecido – Determinação da velocidade de propagação de onda ultrassônica NBR 8802 2015*, 2019.

[34] G. A. Washer, R. E. Green, and R. B. Pond, "Velocity constants for ultrasonic stress measurement in prestressing tendons," *Res. Nondestruct. Eval.*, vol. 14, pp. 81–94, 2002.

[35] Associação Brasileira de Normas Técnicas, *Concreto – Ensaio de compressão de corpos de prova cilíndricos NBR 5739 2018*, 2018.

[36] Associação Brasileira de Normas Técnicas, *Concreto de cimento Portland — Preparo, controle, recebimento e aceitação — Procedimento NBR 12655 2015*, 2015.

[37] R. M. Bethea and R. R. Rhinehart, *Applied engineering statistics*, 1st ed. New York: Marcel Dekker, 1991.

[38] D. C. Montgomery and G. C. Runger, *Applied statistics and probability for engineers*, 3rd ed. New York: Wiley, 2003.

[39] M. Malik, S. K. Bhattacharyya, and S. V. Barai, "Microstructural changes in concrete: Postfire scenario," *J. Mater. Civ. Eng.*, vol. 33, no. 2, 2021.

[40] D. S. Silva, "Propriedades mecânicas residuais após incêndio em concretos usados na construção civil na grande Florianópolis," M.S. thesis, Universidade Federal de Santa Catarina, Florianópolis, 2009.

[41] A. Ergün, G. Kürklü, B. M. Serhat, and M. Y. Mansour, "The effect of cement dosage on mechanical properties of concrete exposed to high temperatures," *Fire Saf. J.*, vol. 55, pp. 160–167, 2013.

[42] Associação Brasileira de Normas Técnicas, *Projeto de estruturas de concreto em situação de incêndio NBR 15200 2012*, 2012.

[43] I. Hager, "Behavior of cement concrete at high temperature," *Bull. Pol. Acad. Sci.*, vol. 61, no. 1, 2013.

[44] S. A. Hassan, "Effect of high elevated temperatures on the compressive strength and ultrasonic pulse velocity of high strength concrete," *J. Eng. Dev.*, vol. 11, no. 1, pp. 58–69, 2007.

[45] J. H. Bungey, S. G. Millard, and M. G. Grantham, *Testing of concrete in structures*, 4th ed. New York: Taylor & Francis, 2006.

[46] V. T. Ngala and C. L. Page, "Effects of carbonatation on pore structure and diffusional properties of hydrated cement pastes," *Cement Concr. Res.*, vol. 27, no. 7, pp. 995–1007, 1997.

[47] C. Shi, Y. Li, J. Zhang, W. Li, L. Chong, and Z. Xie, "Performance enhancement of recycled concrete aggregate," *J. Clean. Prod.*, vol. 112, pp. 466–472, 2016.

[48] D. G. Aggelis and T. Shiotani, "Effect of inhomogeneity parameters on wave propagation in cementitious material," *ACI Mater. J.*, vol. 105, no. 2, pp. 187–193, 2008.

**Author's contributions:** ACCV: conceptualization, data curation, formal analysis, methodology, writing; PDM: conceptualization, formal analysis, methodology, writing and supervision; IJP: formal analysis, methodology and writing.

**Editors:** Lia Pimentel, Guilherme Aris Parsekian.

Rev. IBRACON Estrut. Mater., vol. 15, no. 3, e15304, 2022

IBRACON Structures and Materials Journal
Revista IBRACON de Estruturas e Materiais
ISSN 1983-4195 ismj.org

ORIGINAL ARTICLE

# RC-INSANE – an interactive environment for nonlinear analysis of reinforced concrete structures

*RC-INSANE – um ambiente interativo para análise não-linear de estruturas de concreto armado*

Pâmela Daniela Nogueira Reges[a]
Roque Luiz da Silva Pitangueira[a]
Leandro Lopes da Silva[a]

[a]Universidade Federal de Minas Gerais – UFMG, Programa de Pós-graduação em Engenharia de Estruturas - PROPEEs, Belo Horizonte, MG, Brasil

Received 23 April 2021
Accepted 21 September 2021

**Abstract:** The development of numerical and computational resources that can present reliable models for the analysis of reinforced concrete structures is mainly driven by its widespread use. Considering that reinforced concrete is a composite material and bond is the load-carrying mechanism, these models must consider that the structural behavior is affected by the interaction between concrete and reinforcement. On this basis, the Finite Element Method (FEM) is a well-established method able to provide consistent results for reinforced concrete modeling through reinforcement and bond models. Nevertheless, to simplify the analysis, the hypothesis of strain compatibility between concrete and reinforcement is usually considered. Under certain loads and specific geometries, this hypothesis is not valid, and the bond-slip phenomenon must be considered to fully characterize the structural behavior. To fulfill this need, this paper presents a graphic interface that enables the modeling of reinforced concrete structures through discrete and embedded reinforcement models, with the possibility to include the bond-slip phenomenon based on several constitutive laws proposed in the literature. The computational implementations were held in the INSANE (INteractive Structural ANalysis Environment), an open-source software based on the Object-Oriented Programming paradigm, which enclosures several constitutive models for nonlinear concrete modeling and different numerical techniques, and a post-processing application able to represent the results by way of a friendly-user graphic interface.

**Keywords:** reinforced concrete, finite element method, reinforcement models, bond models, nonlinear analysis.

**Resumo:** O desenvolvimento de recursos numéricos e computacionais capazes de apresentar modelos confiáveis para a análise de estruturas de concreto armado é impulsionado principalmente pelo seu uso generalizado. Considerando que o concreto armado é um material composto e a ligação entre eles é o mecanismo de transmissão de carga, estes modelos devem levar em conta que o comportamento estrutural é afetado pela interação entre concreto e armadura. Neste sentido, o Método dos Elementos Finitos (MEF) é um método bem estabelecido capaz de fornecer resultados consistentes para modelagem de concreto armado através de modelos de armadura e aderência. No entanto, a fim de simplificar a análise, a hipótese de compatibilidade de deformação entre concreto e aço é geralmente considerada. Sob certas cargas e geometrias, esta hipótese não é válida, e o fenômeno de escorregamento da armadura deve ser considerado para caracterizar plenamente o comportamento estrutural. Para atender a essa necessidade, este artigo apresenta uma interface gráfica que permite a modelagem de estruturas de concreto armado por meio de modelos de armadura discreta e embutida, com a possibilidade de incluir a perda de aderência com base em uma série de leis constitutivas propostas na literatura. A implementação computacional foi realizada no sistema INSANE (*INteractive Structural ANalysis Environment*), um programa de código aberto baseado no paradigma da programação orientada a objetos, que engloba vários modelos constitutivos para modelagem não-linear de

**Corresponding author:** Pâmela Daniela Nogueira Reges. E-mail: pamelanogueira@ufmg.br
**Financial support:** The authors gratefully acknowledge the support from the Brazilian research agencies CAPES (Coordenação de Aperfeiçoamento de Pessoal de Nível Superior), FAPEMIG (Fundação de Amparo à Pesquisa do Estado de Minas Gerais; grant PPM-00747-18), and CNPq (Conselho Nacional de Desenvolvimento Científico e Tecnológico; grant 309515/2017-3).
**Conflict of interest:** Nothing to declare.
**Data Availability:** The data that support the findings of this study are available from the corresponding author, PDNR, upon reasonable request.

estruturas de concreto, diferentes métodos numéricos e também uma aplicação de pós-processamento capaz de representar os resultados por meio de uma interface gráfica amigável.

**Palavras-chave:** concreto armado, método dos elementos finitos, modelos de armadura, modelos de aderência, análise não-linear.

**How to cite:** P. D. N. Reges, R. L. S. Pitangueira, and L. L. Silva, "RC-INSANE – an interactive environment for nonlinear analysis of reinforced concrete structures," *Rev. IBRACON Estrut. Mater.*, vol. 15, no. 3, e15304, 2022, https://doi.org/10.1590/S1983-41952022000300004

## 1 INTRODUCTION

The extensive application of concrete structures in the engineering field is a well-known fact. Its utility lies in the combination of concrete, strong in compression, and steel, strong in tension. Hence, assessing the structural response to loads is fundamental for the safe and economical design of reinforced concrete structures. This response may be predicted through experimental research, which provide a firm basis for design equations and the basic parameters required for finite element models, e.g., material properties. However, they tend to be costly, time-consuming, and involve many test specimens to fully characterize the structural behavior.

Given these limitations, the development of reliable computational tools that can enclosure the structural behavior of reinforced concrete structures is a necessity. Numerical models must be able to consider that reinforced concrete (RC) is a composite material, comprising two materials with different physical and mechanical behavior. Furthermore, reinforcement steel and concrete interact in a complex manner through bond, which is essential to the development of the required performance of RC structures. In this connection, bond is the term of the load-carrying mechanism. This bond action becomes evident, for example, in the regions near cracks or at the end anchorages of straight bars (Figure 1).

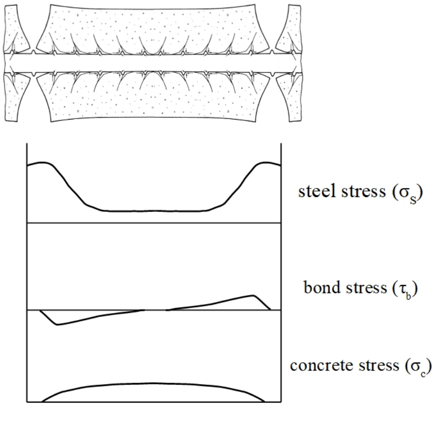


**Figure 1.** Reinforced concrete tensile member with crack formation and corresponding stress distribution [1], [2]

In most nonlinear analysis of reinforced concrete structures in engineering practice, one of the basic working hypotheses is the strain compatibility between concrete and reinforcement (i.e., perfect bond) to simplify the analysis. However, in certain situations wherein the bond stress demands are large, the bond-slip phenomenon must be considered so the complete structural behavior is characterized.

Furthermore, the fact that the concrete is a heterogeneous material that exhibits a complex nonlinear behavior must also be considered in analyses of reinforced concrete structures. Hence, the association of constitutive models capable of accurate predict the material response of concrete with reinforcement models able to enclosure the bond-slip phenomenon enables nonlinear analysis of reinforced concrete structures in a variety of loading situations.

The purpose of this work is to provide an interactive graphical interface able to perform nonlinear analysis of reinforced concrete structures with different reinforcement models and bond-slip laws considering a variety of constitutive models for concrete. Thus, extending the flexibility of FEM simulation tools.

The work here presented was implemented in the INSANE (INteractive Structural ANalysis Environment) system, an open-source software for computational mechanics, developed at the Structural Engineering Department (DEES) of the Federal University of Minas Gerais (UFMG). The detailed description of the INSANE system as well as its theoretical formulation is not the purpose of this paper as the current organization of the software is the result of several contributions by different research [3].

## 2 THE INSANE SYSTEM

The INSANE project (acronym first conceived for INteractive Structural ANalysis Environment) was designed as a computational system for the Finite Element Method (FEM). However, as it was developed, numerous changes were made to generalize the problem-solving process, enabling its application to various fields as well as its expansion to different numerical models (e.g., mesh-free, Generalized Finite Element Method (GFEM), and Boundary Element Method (BEM) models). The elevated level of generalization of the software enables its expansion and the simultaneous collaboration of different research.

The software includes an interactive graphical interface with preprocessing, processing (numerical core responsible for the analysis of discrete models), and postprocessing applications. In the preprocessing phase, the input required to solve the problem is generated through the graphical application or read in using an XML file (eXtensible Markup Language). In the solution (processing) part of the model, a set of linear or nonlinear equations is solved to obtain the results, such as displacements values. Lastly, the postprocessing application enables the visualization of the results, e.g. stress and strain fields. The use of the system and its graphical interface applied to the modelling of reinforced concrete structures will be explained in the following sections.

As previously mentioned, the development of the system involves several studies, being Simão [4], Castro [5], and Wolenski et al. [6] the ones more strictly related to this work, which dealt with the implementation of reinforcement models in the numerical core of the INSANE system. This work was focused on adding specific resources into the existing graphical interface of INSANE for accessing the available tools for RC modeling previously implemented in the numerical core by means of a user-friendly interface. Due to its generality, most part of the resources available in the system, as constitutive models for concrete and the postprocessing application, required small interventions to enable their use combined with reinforcement and bond models.

## 3 INTERACTIVE GRAPHICAL APPLICATION FOR MODELING REINFORCED CONCRETE STRUCTURES

When formulating a finite element model that can accurately predict the behaviour of a reinforced concrete structure, three aspects must be considered, the most adequate reinforcement model, the foreseen bond-slip behaviour, and the appropriate constitutive model. These three aspects are detailed in this section, focusing on the models available in the system.

### 3.1 Reinforcement models

In the classical modeling of rebars in a reinforced concrete structure, two different approaches may be considered: the *discrete* model and the *embedded* model [7].

In the discrete model [8] the reinforcement is modeled with one-dimensional bar elements (truss or beam elements) which are assumed to be pin connected and are superimposed on the two-dimensional concrete element mesh, as seen in Figure 2. The advantage of this model, besides its simplicity, is that it can include the slip of reinforcement steel with respect to the surrounding concrete (the modeling of bond is introduced in the next section). One limitation of this model is the bar positioning, which is limited to the interface between concrete elements, leading to an increase in the number of elements to fully discretize the reinforcement.

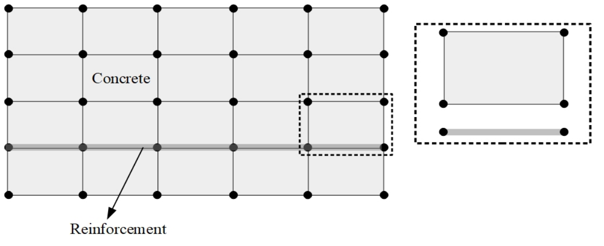


**Figure 2.** Discrete reinforcement model

Another possibility for the modeling of reinforcement is to introduce the bar as a one-dimensional element embedded in the concrete element, i.e., the *embedding of reinforcement*. The embedded approach introduces displacement constraints as far as nodes of the reinforcement and the concrete coincide [9]. In this model, illustrated in Figure 3, the embedded reinforcement may have an arbitrary position. For further discussion see, for example, Balakrishna and Murray [10], Allwood and Bajarwan [11], and Elwi and Hrudey [12]. Variations of these models can be found in the literature to accommodate different materials as reinforced fiber-reinforced polymer (FRP) concrete structures [13].

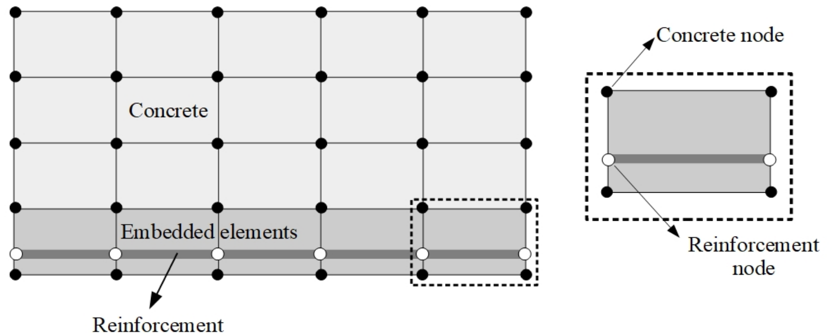


**Figure 3.** Embedded reinforcement model

### 3.2 Bond models

To simulate reinforced concrete structures, besides the modeling of the reinforcement covered in the last section, the modeling of the bond is also fundamental considering that steel and concrete interacts via bond. In this sense, two approaches may be distinguished with respect to the finite element models: *rigid bond* and *flexible bond*.

When the hypothesis of a rigid bond is considered, the slip between concrete and reinforcement is disregarded. Hence, finite elements for reinforcement and for concrete may share the same nodes, enforcing displacement compatibility, as illustrated in Figure 4a.

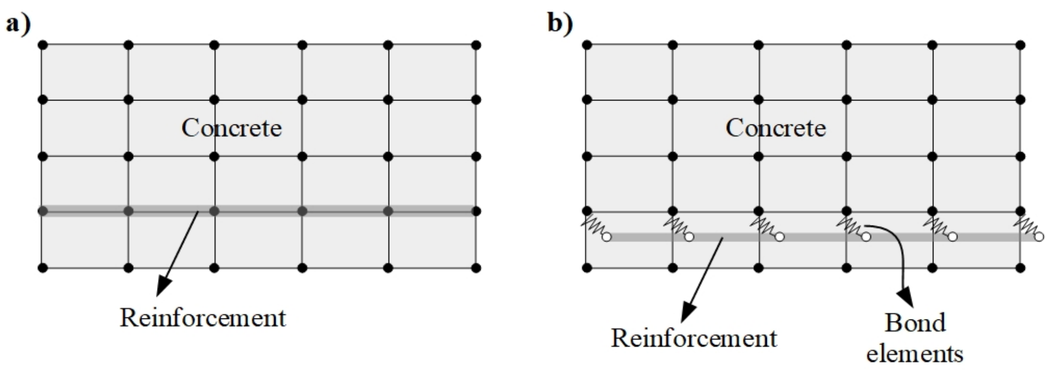


**Figure 4.** Bond (a) Rigid. (b) Flexible. (Adapted from Häussler-Combe [9]).

For the flexible bond, slip between concrete and reinforcement is regarded, and, consequently, finite elements for the reinforcement and for the concrete should have their own nodes, as depicted in Figure 4b. Concrete nodes and reinforcement nodes are connected through special elements, i.e., *bond elements*, which present an adequate *bond law*.

For the case of the embedded reinforcement model, the flexible bond is included in the model formulation, thus requiring a bond law. For the discrete reinforcement model, the user may opt between simulating the bond through *contact elements* or *bond-link elements*.

The bond-link element is the simplest type of bond elements, and was developed by Ngo and Scordelis [8]. This bond element possesses no physical dimensions and may be conceptually thought of as two orthogonal springs (in 2D case) connecting two nodes with identical coordinates, as shown in Figure 5. The user must specify the bond law for each direction.

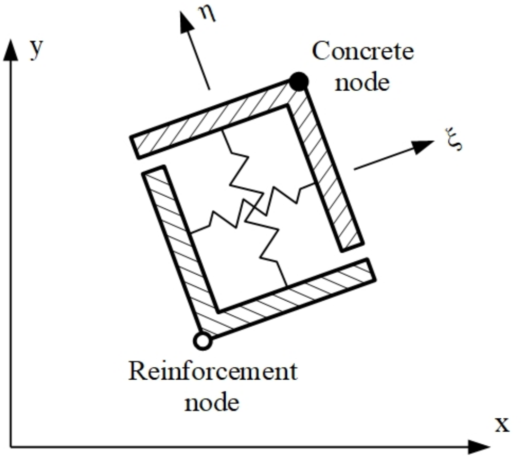


**Figure 5.** Bond-link element (Adapted from Keuser and Mehlhorn [2])

The contact element, initially proposed by Hoshino [14] and Schäfer [15] and later modified by Dinges et al. [16], represents the bond by a continuous element connecting concrete and reinforcement (Figure 6), which may present a linear or high-order approximation for the displacement field, whose parameters are defined by the user. The bond-law associated may be linear or nonlinear [17]–[19].

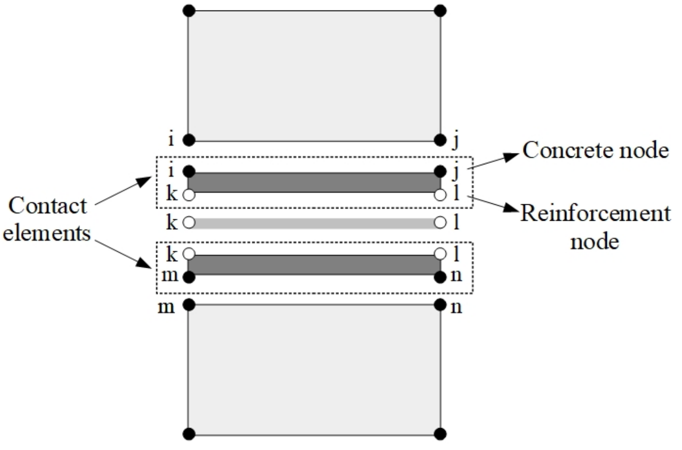


**Figure 6.** Schematic representation of bond simulation using contact elements.

Independently of the bond element chosen, a bond law must be associated to characterize the behavior in the interface between concrete and reinforcement. In recent years, numerous research have been devoted to the study of bond models able to enclosure the bond-slip phenomenon under different load situations, as cyclic, thermal and confining loads [20]–[24], as well as different materials, e.g., fiber reinforced concrete [25], [26] and fiber reinforced polymer rebars [27], [28]. The introduction of such new bond models could be easily implemented into the system due to its high level of generalization with few changes in the graphical interface.

In the INSANE system numerous bond laws are already available (Linear Bond Law, Dörr Bond Law [29], Eligehausen Bond Law [30], and Hawkins Bond Law [31]). however, for brevity, only the one proposed by Eligehausen et al. [30], labeled in the system as *Eligehausen Bond La*w, will be here presented.

To predict the local bond stress-slip relationship of deformed reinforcing bars under generalized excitations, Eligehausen et al. [30] performed numerous pull-out tests and analytical investigations, proposing the bond law graphically represented in Figure 7. In the figure, $\tau$ is the bond stress for a given slip $w_b$, $\tau_{max}$ is the maximum bond stress, $\tau_f$ is the final bond stress, $w_{b1}$ is the slip for the maximum bond stress, $w_{b2}$ is the maximum slip for the maximum bond stress, and $w_{b3}$ the slip for the final bond stress. The Eligehausen Bond Law may describe the behavior of smooth and ribbed rebars if appropriated parameters for the law are adopted.

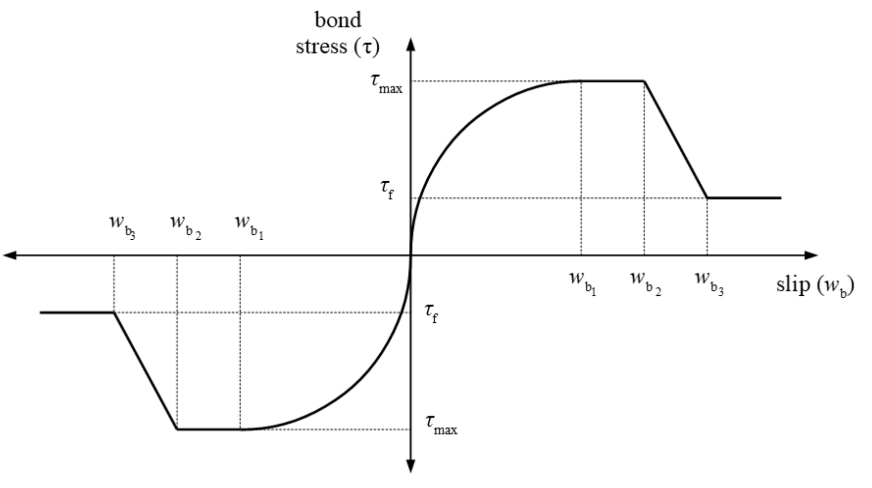


**Figure 7.** Bond stress-slip law proposed by Eligehausen et al. [30].

## 4 MODELING EXAMPLE IN THE INTERACTIVE GRAPHICAL APPLICATION

To illustrate the analysis process through the graphical application and the use of the reinforcement and bond models presented, a quarter ring problem with one curved reinforcing layer under constant pressure proposed by Elwi and Hrudey [12] is modeled, as seen in Figure 8a. The modeling process and the results for both the discrete (Figure 8b) and embedded reinforcement models (Figure 8c) are presented in the following section.

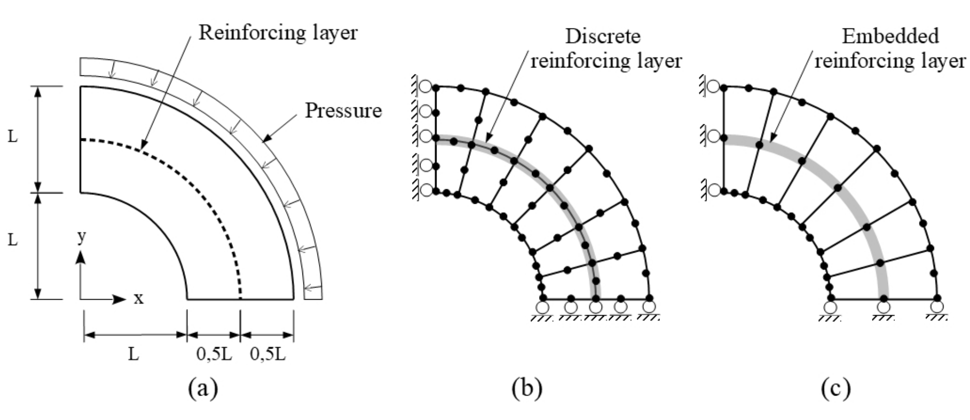


**Figure 8.** Quarter ring problem with one curved reinforcing layer: (a) geometry; (b) mesh for the discrete reinforcement model; (c) mesh for the embedded reinforcement model.

### 4.1 Modeling with the discrete reinforcing model

Initially, the test was conducted disregarding bond-slip and, subsequently, including a linear bond law modeled with spring and contact elements. The quarter ring was modeled with a mesh composed of twelve Q8 plane stress elements, as depicted in Figure 8b, and linear elastic materials.

To model the test proposed through the INSANE system, the user is initially requested to choose the analysis type (for this specific case, the user should choose the *plane analysis*) and the folder in which the files generated during the analysis will be saved. After, the first module of the system is displayed, the *Geometry* module, illustrated in Figure 9. In this example, L was considered as 1 m (see Figure 8a). The second module is the *Mesh* module where the mesh of twelve plane elements is defined, as seen in Figure 10.

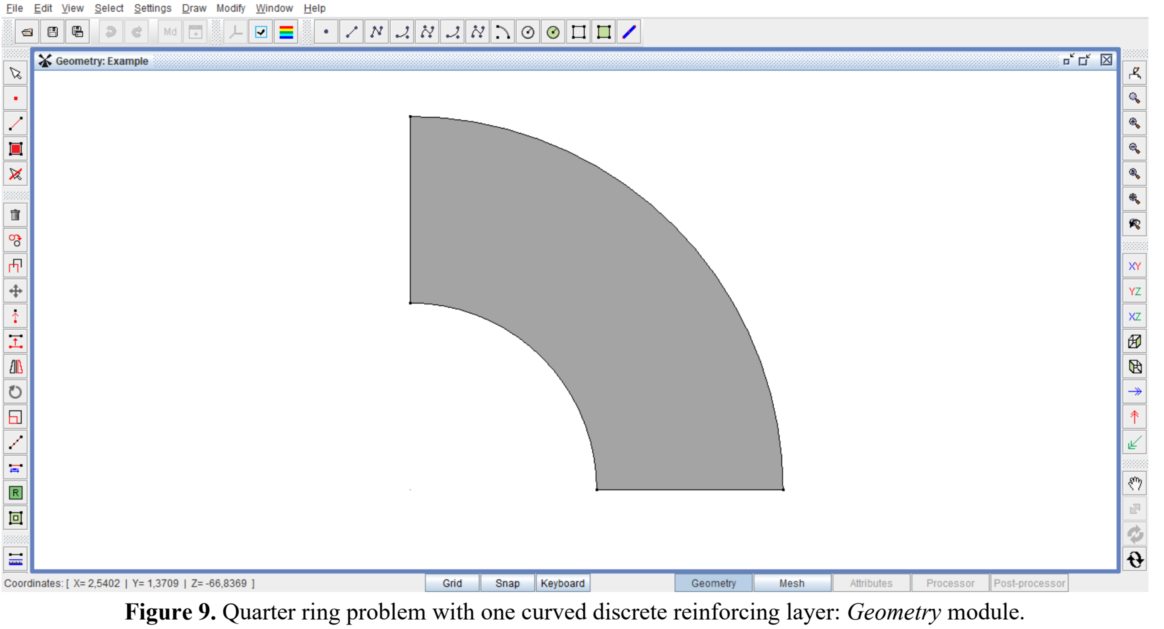


**Figure 9.** Quarter ring problem with one curved discrete reinforcing layer: *Geometry* module.

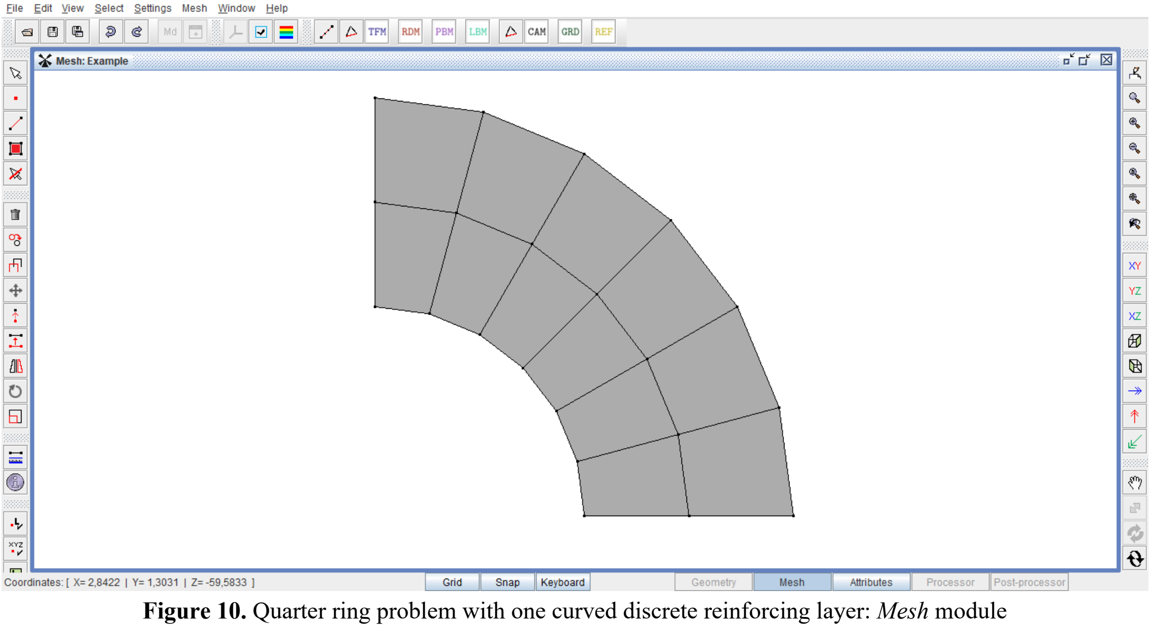


**Figure 10.** Quarter ring problem with one curved discrete reinforcing layer: *Mesh* module

After this stage, the analysis is defined in plane stress and the element as quadrilateral with eight nodes (Q8). Following, in the *Attributes* module, the constitutive model, the materials, the sections and the restraints are defined. An overview of this module is shown in Figure 11. In this module, the possibility to insert reinforcement in the analysis was implemented and the process of including the bars will be detailed in the following paragraphs. For the remaining parameters that must be defined for the analysis and are not related to the reinforcement inclusion, the reader may refer to the INSANE user manual for plane models (in Portuguese) available at [3].

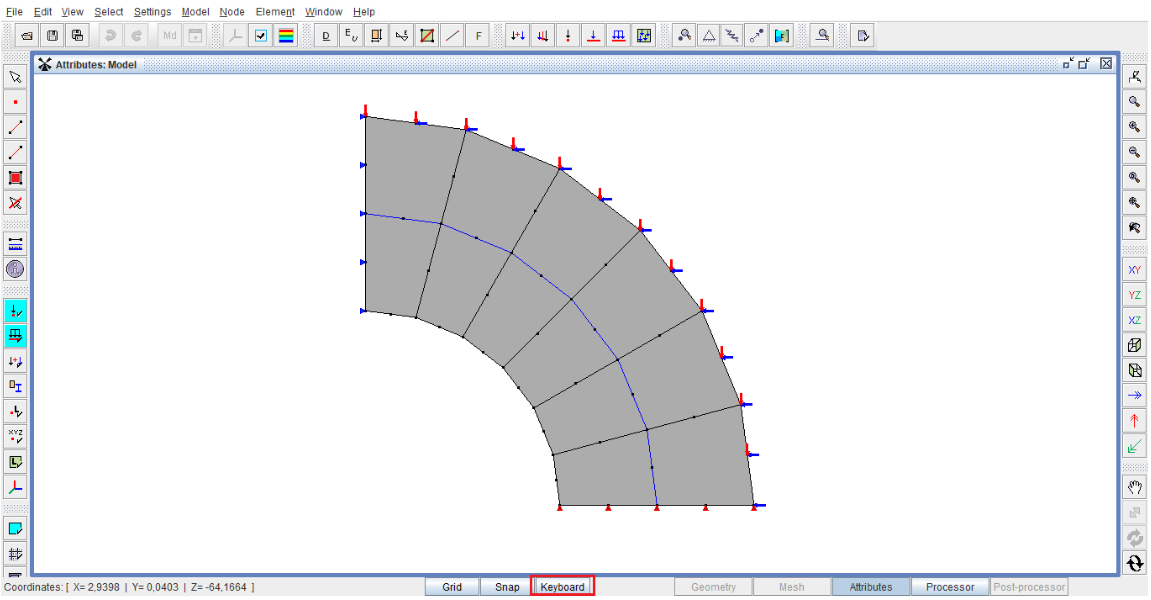


**Figure 11.** Quarter ring problem with one curved discrete reinforcing layer: *Attributes* module

The first step is to determine the position of the reinforcing layer as depicted in Figure 8b. The user may introduce the bars specifying the coordinates through the keyboard or drawing directly, using mouse device.

For the first alternative, the user must select the keyboard option available at the bottom of the Attributes module, as highlighted in Figure 11. Next, the user can introduce the reinforcement using the button "Create reinforcing bars" or the corresponding item from the drop-down menu "Model" (Figure 12). Following this procedure, the dialog "Create Steel Reinforcing Bars" (see Figure 13) is displayed, and the user may draw the reinforcement specifying the vertices that define the origin and the end of the bar or identifying an existent edge in which the bar will be inserted. The creation of the reinforcement based on an existing edge is exclusively for the discrete model, in which the bars have their position restricted to the interface between two elements, as discussed in Section 3.1.

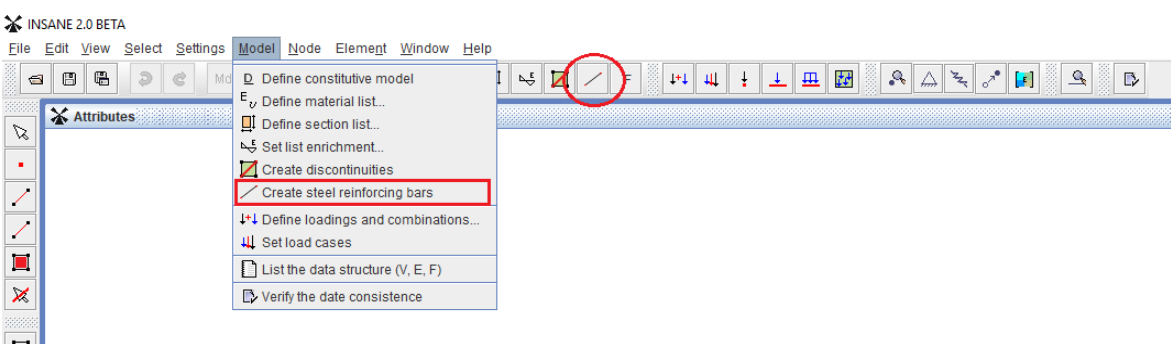


**Figure 12.** Options for the creation of the reinforcing layer available in the system

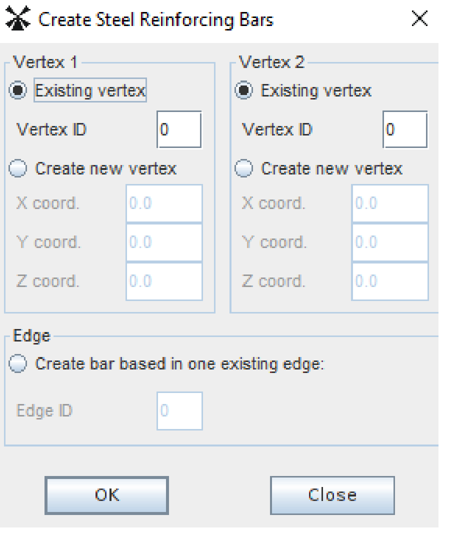


**Figure 13.** "Create Steel Reinforcing Bars" dialog

If the user chooses to draw the reinforcement directly using the mouse, the desired edge needs to be selected and, subsequently, click in the button for the creation of bars (Figure 12). The discrete bar created is now displayed in blue for its better visualization, as shown in Figure 11.

For the definition of the bond model, a specific material should be created through the "Material" popping dialog (Figure 14), where all the materials used in the analysis are specified. For the modeling with bond-link elements (springs) the corresponding option "BondSlipBySpring" must be selected from the drop-down menu and the concerning characteristics defined, as the reinforcement Young's modulus (ELASTICITY), and the spring orientation (SPi_ANGLE) and area of influence (SPi_INFLUENCE_AREA), as illustrated in Figure 15. The number of required springs for the analysis is related to the number of nodes for each edge, defined by the plane element used in the analysis. For the present example, quadrilateral elements with eight nodes were used, hence each edge has three nodes, and an orientation and area of influence must be specified for the corresponding three bond-link elements. In addition to the parameters discussed, the bond laws and their associated variables should be defined. For this analysis, the linear option was selected.

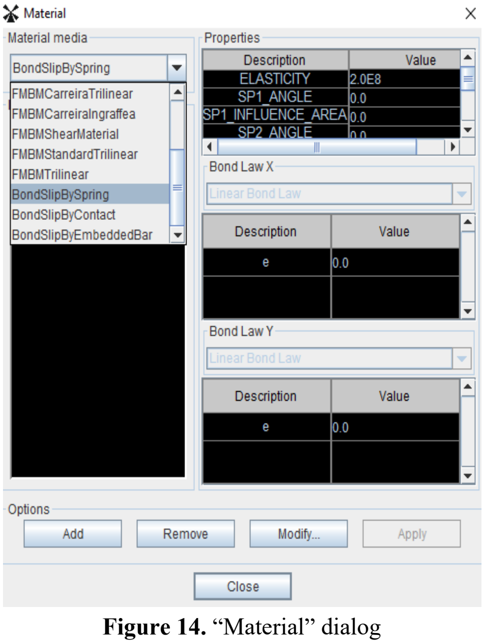


**Figure 14.** "Material" dialog

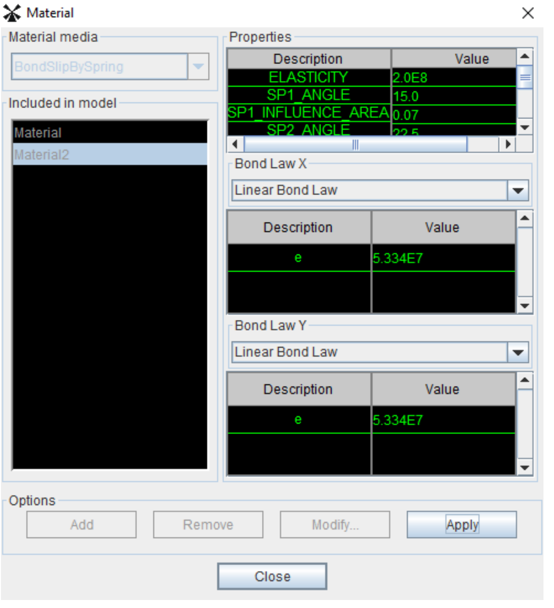


**Figure 15.** "Material" dialog: definition of the parameters for bond-link elements

If the user opts for bond modeling with contact elements, the procedure is like the one described for bond-link elements and the option "BondSlipByContact" should be chosen. In this case, in addition to the elastic modulus, the user must enter the perimeter of the reinforcement (Figure 16). Like bond-link elements, bond-laws need to be set. Similarly to the model with spring elements, linear bond-laws were used.

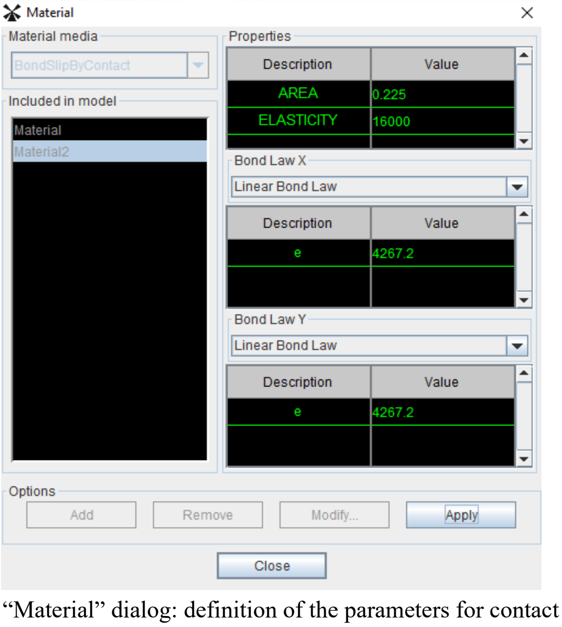


**Figure 16.** "Material" dialog: definition of the parameters for contact elements

Finally, after the definition of all parameters required for the analysis, the user may pass to the next stage of processing and visualize the results in the post-processor application (Figure 17). For a nonlinear analysis, the parameters for the numerical strategy must be defined before processing the model. More details in the INSANE user manual.

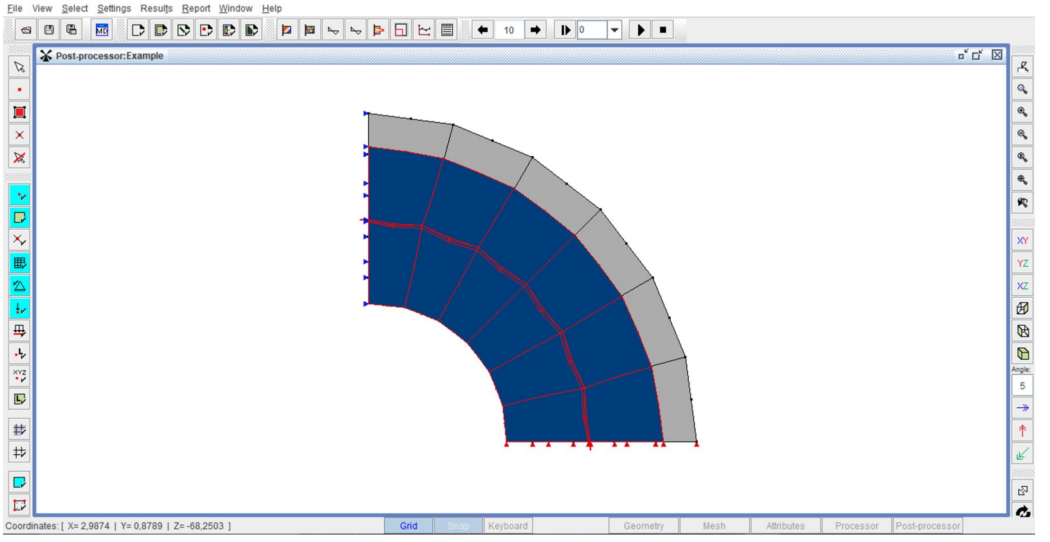

Figure 17. Quarter ring problem with one curved discrete reinforcing layer: *Post-processor* module

## 4.2 Modeling with the embedded reinforcing model

A similar procedure as described in the last section should be followed when modeling with the embedded reinforcing model. For this case, a different mesh, with fewer elements, was used for modeling the same problem of the quarter ring previously discussed, as illustrated in Figure 8c. This to emphasize that, for this specific reinforcement model, the position of the layer is not restricted to the interface between elements, allowing the same analysis with less refined meshes compared to the discrete model. The creation of the elements associated to the reinforcing layer follows the same steps as for the discrete model. However, to differentiate a discrete model from an embedded model, the user must enter coordinates for the extremities of the bar so that it does not coincide with existing edges of the model. After providing the location of the layer, the program identifies which elements are being intersected by the reinforcement and associates each bar to the corresponding embedded element. As for the discrete model, in the “Material” dialog information as the surface area and elastic modulus of the layer, and the bond-law must be defined (Figure 18).

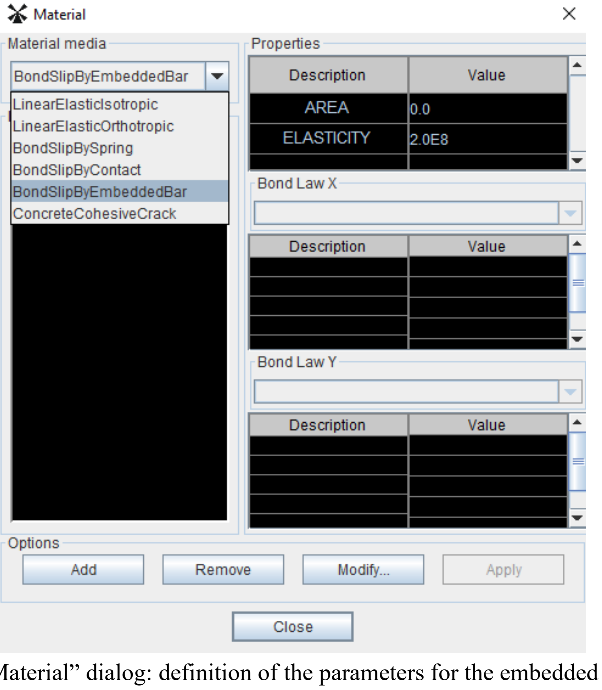


Figure 18. “Material” dialog: definition of the parameters for the embedded reinforcing model.

For the example here presented, considering initially the discrete reinforcement model, three models were adopted. The first disregarding bond-slip, followed by an analysis with bond-link elements, and lastly with contact elements. Following, an analysis with the embedded model was also conducted. Numerical values used for the various parameters are as follows: $A_S/L = 0.025$, $E_S/E_C = 8$, $\nu = 0.25$, $E_bL/E_S = 0.2667$, and $O_S = 0.45$, where $A_S$ is the cross-section area of the layer per unit thickness, $E_S$, $E_C$ and $E_b$ are the initial tangential moduli for the normal stress-strain relation for the reinforcement, the concrete, and the bond stress-slip relation, respectively, and $O_S$ the perimeter of the layer per unit thickness. Figure 19 shows the stress in the curved steel layer for each model.

The predicted behavior for the four models is as expected: with no bond-slip, the layer is submitted to a constant stress and, when the bond-slip is activated, the steel pushes out of the quarter and there is a reduction of the layer stress at the edges. The difference in the result obtained for spring elements compared to contact and embedded elements is due to their different formulations.

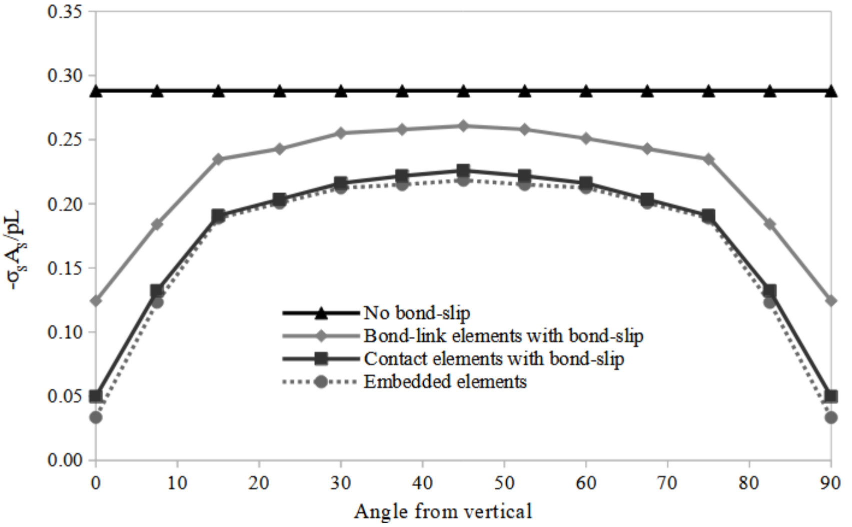


**Figure 19.** Quarter ring problem with one curved discrete reinforcing layer: steel stress

Figure 20 illustrates the visualization of the results presented in Figure 19 in the postprocessing application for the embedded model. As it may be noticed, the steel layer is entirely under compression with lower stress at the edges due to the bond-slip that pushes the steel out of the quarter leading to a reduction of the layer stress.

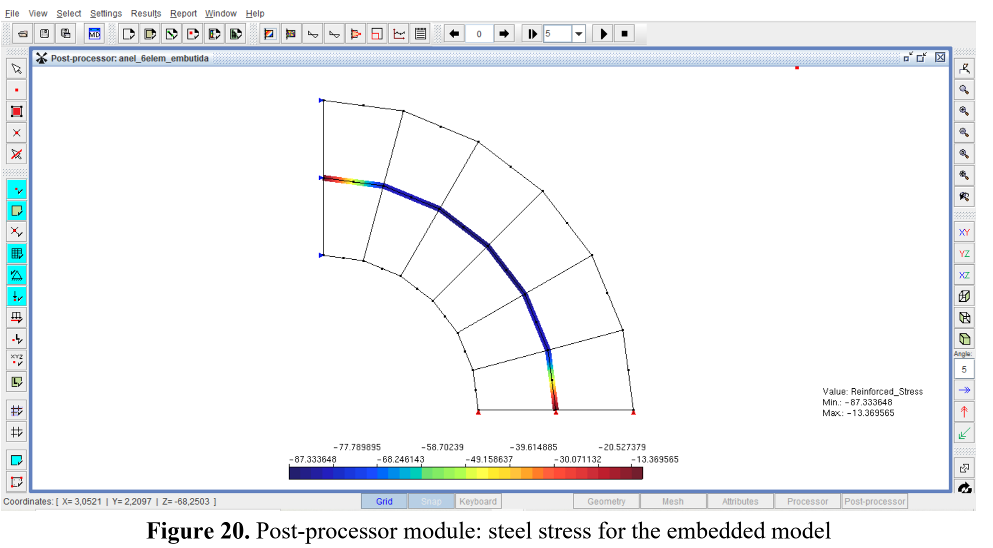


**Figure 20.** Post-processor module: steel stress for the embedded model

## 5 MODELING REINFORCED CONCRETE STRUCTURES

To validate the models presented, two reinforced concrete beams submitted to bending tests are modeled using the graphical application detailed in Section 4 and the results are discussed in the following sections.

### 5.1 Reinforced concrete beam – Mazars and Pijaudier-Cabot [32]

The results for tests conducted on bending beams are presented by Mazars and Pijaudier-Cabot [32] and these results are here compared to a simulation carried out by means of the graphical application of the INSANE system. Figure 21 illustrates the geometry of the adopted model as well as the mesh used.

The material parameters, as specified by Mazars and Pijaudier-Cabot [32], are as follows: Young's modulus for the concrete $E_0 = 3\times10^4$ MPa; Poisson's ratio for the concrete $\nu_0 = 0.2$; Young's modulus for the steel ribbed bars $E_S = 2.1\times10^5$ MPa. The smeared crack model was adopted for modeling the concrete associated to the stress-strain relationships proposed by Carreira and Chu [33] in compression and Boone and Ingraffea [34] in tension with the following parameters: maximum stress in compression $f_c = 25.0$ N/mm$^2$, maximum stress in tension $f_t = 2.5$ N/mm$^2$, fracture energy $G_f = 0.1$ N/mm, characteristic length h = 50 mm, and shear retention factor $\beta_r = 0.05$.

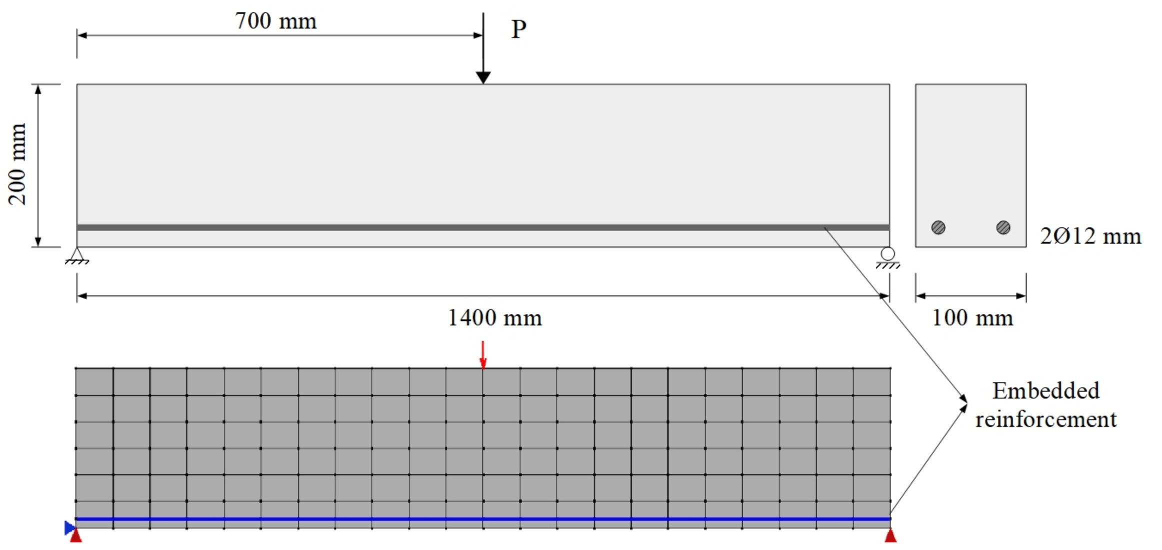


**Figure 21.** Reinforced concrete beam – Mazars and Pijaudier-Cabot [32]: model and mesh

For the nonlinear analysis, the generalized displacement control method was adopted with tolerance of $1\times10^{-3}$ and P = 1 N (Figure 21). For the representation of the steel ribbed bars the embedded model was chosen associated to the bond stress-slip relationship proposed by Eligehausen et al. [30]: $w_{b1} = 0.5$ mm; $w_{b2} = 1.0$ mm; $w_{b3} = 5.0$ mm; $\tau_{max} = 22$ MPa; $\tau_f = 9$ MPa (Figure 7).

The result obtained for deflection of the mid-span versus load is presented in Figure 22 and there is a satisfactory agreement with the experimental results observed by Mazars and Pijaudier-Cabot [32]. The results for the various variables of the problem can be visualized in the Post-processor application in a user-friendly interface. Figure 23 illustrates the damage profile and the bond stress for a load of 28 kN, where in the symmetric aspect of the problem is noticed. Considering the bond stress, for the first half of the beam, the bond slip is directed in the positive direction of the axis, leading to a stress also positive. In the second half, however, there is the development of a negative bond stress, in accordance with the expected behavior for a reinforced concrete beam in bending. The region where damage is more prominent, there are spikes in the bond stress related to the load transfer between damage and undamaged zones.

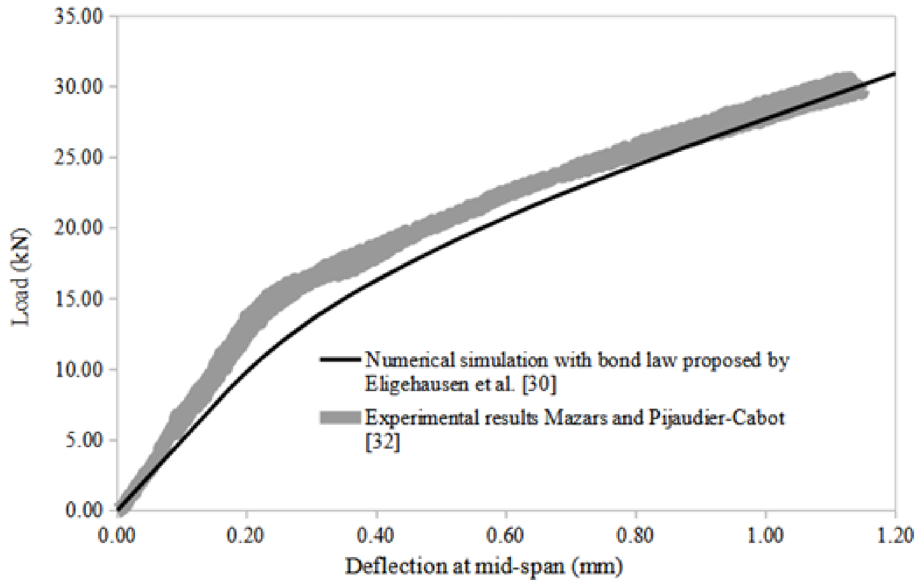


**Figure 22.** Reinforced concrete beam – Mazars and Pijaudier-Cabot [32]: deflection versus load.

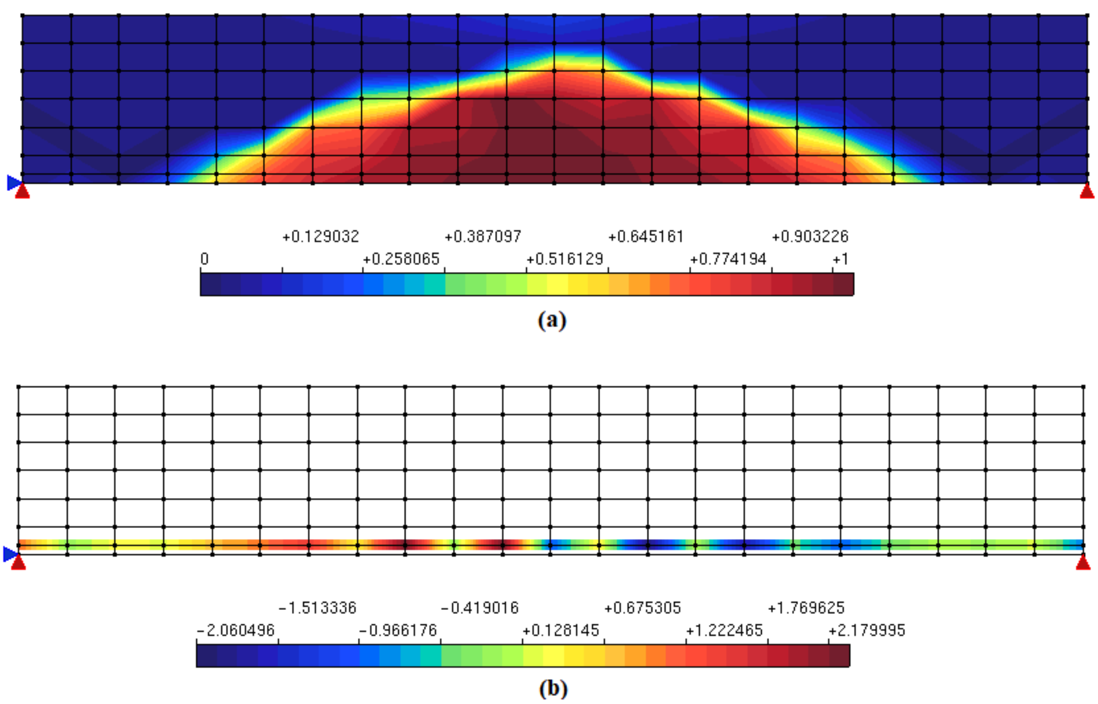


**Figure 23.** Reinforced concrete beam – Mazars and Pijaudier-Cabot [32]: visualization of damage (a) and bond stress (b) (MPa) in the post-processor module.

## 5.2 Reinforced concrete beam – Álvares [35]

For this example, the reinforced concrete beam studied by Álvares [35] is modeled following the geometric parameters and the mesh illustrated in Figure 24. A plane stress analysis was carried out with quadrilateral elements of four nodes and the slip between concrete and reinforcement was disregarded. The concrete was modeled with a volumetric damage model [36] associated to a polynomial damage law with the following parameters: $f_e = 0.945$ N/mm$^2$, $k_0 = 0.000094$ and $\bar{E} = 16222.22$ N/mm$^2$ in tension; $f_e = 11.2$ N/mm$^2$, $k_0 = 0.0017$ and

$\bar{E}$ = 16222.22 N/mm$^2$ in compression, where $f_e$ is the equivalent stress related to the material strength limit, $k_0$ is the strain threshold that marks the elastic limit, and $\bar{E}$ is the equivalent Young's modulus.

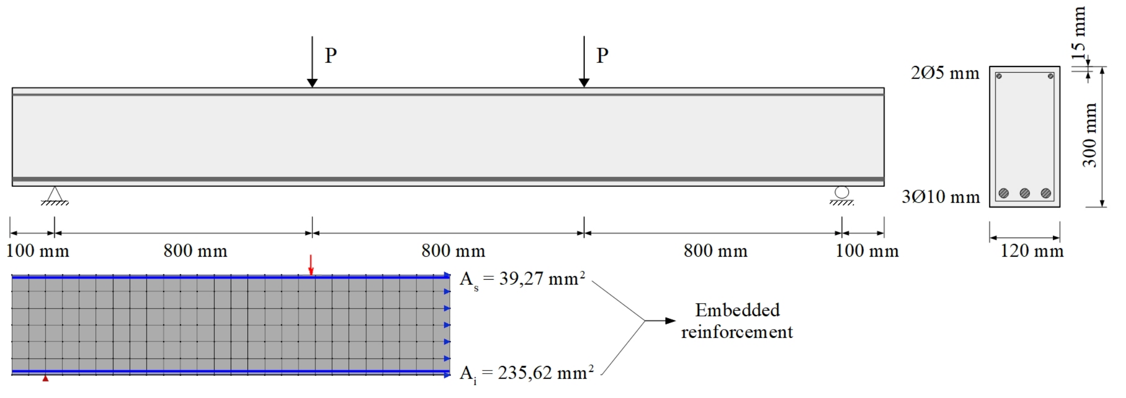


**Figure 24.** Reinforced concrete beam – Álvares [35]: model and mesh

The generalized displacement control method was used with an initial load factor of 1125, tolerance of $1\times10^{-3}$ and P = 1 N (Figure 24). The results for the deflection in the mid-span versus the applied load are displayed in Figure 25 in comparison to the experimental and numerical results obtained by Álvares [35]. The model here proposed was able to satisfactorily describe the behavior of the beam.

As an example of the use of the post-processor application, Figure 26 represents the damage when the beam is subjected to a load of 13 kN and the corresponding reinforcement stress. As expected for the model, the damage is more prominent in the mid-span, where the tensile stress is higher as noticed in the stress distribution for the reinforcement.

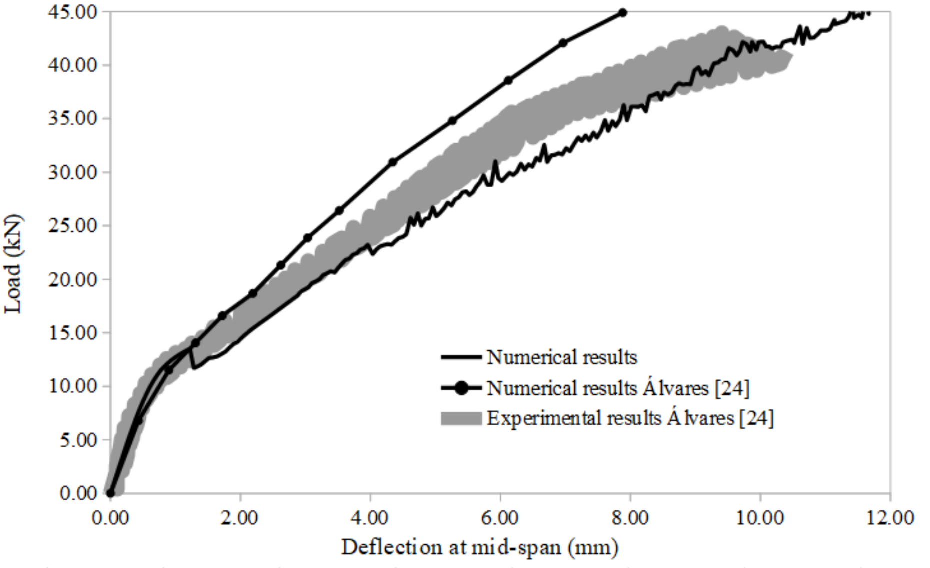


**Figure 25.** Reinforced concrete beam – Álvares [35]: deflection versus load

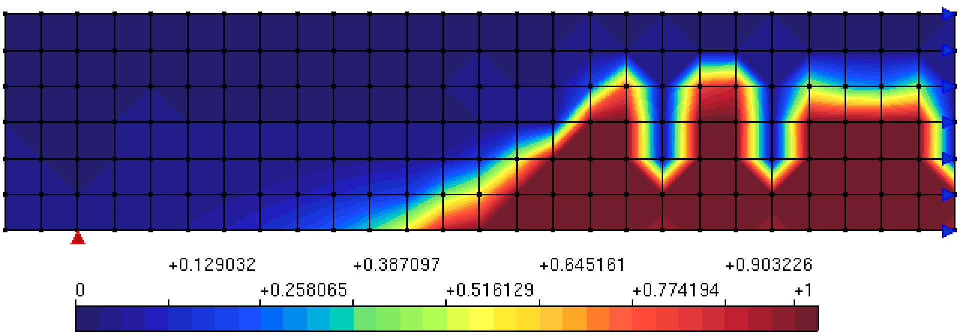


**(a)**

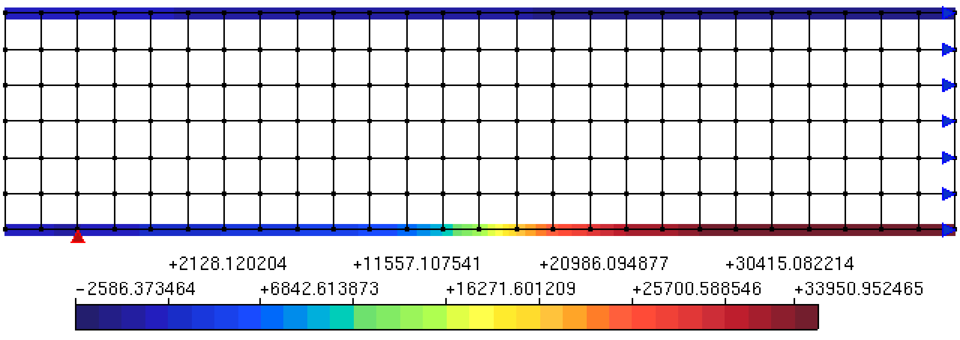


**(b)**

**Figure 26.** Reinforced concrete beam – Álvares [35]: visualization of the damage (a) and the reinforcement stress (b) in the post-processor module.

## 6 CONCLUSIONS

This work introduced the interactive environment for nonlinear analysis of reinforced concrete structures, which allows the analysis of structures with different reinforcement and bond models associated to a wide range of constitutive models able to describe the behavior of concrete. With such free open-source application, structural engineers can better understand the behavior of reinforced concrete structures through nonlinear analyses, going beyond the scope of reinforced concrete design practices and enabling better designs and procedures in construction.

The modeling examples here presented illustrate the use of the INSANE system for reinforced concrete analyses and the user-friendly visualization of the obtained results, providing an instrument for structural analysis with more extensive hypotheses, disregarded in engineering practice. The examples here presented attest the system capacity to simulate and predict the behavior of RC structures in accordance with experimental data.

## ACKNOWLEDGMENTS

The authors gratefully acknowledge the support from the Brazilian research agencies CAPES (Coordenação de Aperfeiçoamento de Pessoal de Nível Superior), FAPEMIG (Fundação de Amparo à Pesquisa do Estado de Minas Gerais; grant PPM-00747-18), and CNPq (Conselho Nacional de Desenvolvimento Científico e Tecnológico; grant 309515/2017-3).

## REFERENCES

[1] Y. Goto, "Cracks formed in concrete around deformed tension bars," *ACI-Journal*, vol. 68, no. 4, pp. 244–251, 1971.

[2] M. Keuser and G. Mehlhorn, "Finite element models for bond problems," *J. Struct. Eng.*, vol. 113, no. 10, pp. 2160–2173, Oct. 1987, http://dx.doi.org/10.1061/(ASCE)0733-9445(1987)113:10(2160).

[3] INSANE. "INSANE Project" https://www.insane.dees.ufmg.br/ (accessed Apr., 2021).

[4] W. I. S. Simão, "Modelos de armadura e aderência para análise não-linear de estruturas de concreto armado", M.S. thesis, Struc. Dept., UFMG, Belo Horizonte, MG, Brazil, 2003. [Online]. Available: http://www.pos.dees.ufmg.br/defesas/197M.PDF

[5] S. S. Castro "Framework teórico e computacional para estruturas de concreto armado: implementação de modelos de armadura e aderência", M.S. thesis, Struc. Dept., UFMG, Belo Horizonte, MG, Brazil, 2013. [Online]. Available: http://www.pos.dees.ufmg.br/defesas/724M.PDF

[6] A. R. V. Wolenski, S. S. Castro, S. S. Penna, and R. L. S. Pitangueira, "Experimental and finite element analysis of bond-slip in reinforced concrete," *RIEM*, vol. 8, pp. 787–799, 2015.

[7] H. G. Kwak and F. Filippou, *Finite Element Analysis of Reinforced Concrete Structures Under Monotonic Loads*, Report No. UCB-SEMM-90/14. University of California, Berkeley, California, 1990.

[8] D. Ngo and A. C. Scordelis, "Finite element analysis of reinforced concrete beams," *ACI-Journal*, vol. 64, no. 3, pp. 152–163, 1967.

[9] U. Häussler-Combe, *Computational Methods for Reinforced Concrete Structures*, Germany: Ernst & Sohn, 2015.

[10] S. Balakrishna and D. Murray, *Prediction of Response of Concrete Beams and Panels by Nonlinear Finite Element Analysis*, IABSE Reports, pp. 393–404, 1987.

[11] R. J. Allwood and A. A. Bajarwan, "A new method for modeling reinforcement and bond in finite element analysis of reinforced concrete," *Int. J. Numer. Methods Eng.*, vol. 28, pp. 883–844, 1989.

[12] A. E. Elwi and T. M. Hrudey, "Finite element model for curved embedded reinforcement," *J. Eng. Mech.*, vol. 115, pp. 740–754, 1989.

[13] X. Lin and Y. X. Zhang, "Novel composite beam element with bond-slip for nonlinear finite-element analyses of steel/FRP-reinforced concrete beams", *J. Struct. Eng.*, vol. 139, no. 12, 2013. https://doi.org/10.1061/(ASCE)ST.1943-541X.0000829.

[14] M. Hoshino "Ein Beitrag zur Untersuchung des Spannungszustandes an Arbeitsfugen mit Spannglied-Kopplungen von abschnittsweise in Ortbeton hergestellten Spannbetonbriicken", Ph.D. thesis, Technischeltoch Schale, Darmstadt, Germany, 1974.

[15] H. Schäfer, "Contribution to the solution of contact problems with the aid of bond elements", in *Computer Methods in Applied Mechanics and Engineering*, T. J. R. Hughes, M. Papadrakakis, J. T. Oden, Eds., Amsterdam: North-Holland Publishing Company, vol. 6, pp. 335–354, 1989.

[16] D. Dinges et al. "Untersuchung verschiedener Elementsteifigkeitsmatrizen auf ihre Eignung zur Berechnung von Stahlbetonkonstruktionen", in *Proc. of the 2nd Interimreport, Darmstadt, 3rd Interimreport*, Kassel/Darmstadt, 1982.

[17] N. Dominguez, D. Brancherie, L. Davenne and A. Ibrahimbegović, "Prediction of crack pattern distribution in reinforced concrete by coupling a strong discontinuity model of concrete cracking and a bond-slip of reinforcement model", *Int. J. Computer-Aid Eng. Softw.*, vol. 22, pp. 558–582, 2005.

[18] L. Lowes, J. P. Moehle, and S. Govindjee, "Concrete-steel bond model for use in finite element modeling of reinforced concrete structures," *ACI Struct. J.*, vol. 101, pp. 501–511, 2004.

[19] B. Richard et al., "'A three-dimensional steel/concrete interface model including corrosion effects," *Eng. Fract. Mech.*, vol. 77, pp. 951–973, 2010.

[20] H. Zhou et al., "Experimental study of bond-slip performance of corroded reinforced concrete under cyclic loading", *Adv. in Mechanical Eng.*, vol. 7, 2015.

[21] H. Lin et al., "The bond behavior between concrete and corroded steel bar under repeated loading", *Eng. Struc.*, vol. 140, pp. 390–405, 2017.

[22] J. Khalaf, Z. Huang, and M. Fan, "Analysis of bond-slip between concrete and steel bar in fire," *Comput. Struc.*, vol. 162, pp. 1–15, 2016.

[23] Z. Wang et al., "Bond-slip model considering freeze-than damage effect of concrete and its application", *Eng. Structures*, vol. 201, no. 3, 2019.

[24] S. Coccia, E. Maggio and Z. Rinaldi, "Bond slip model in cylindrical reinforced concrete elements confined with stirrups," *Int. J. Adv. Struct. Eng.*, vol. 7, pp. 365–375, 2015.

[25] X. Lin and Y. X. Zhang, "Bond-slip behavior of FRP-reinforced concrete beams," *Constr. Build. Mater.*, vol. 44, pp. 110–117, 2013.

[26] I. Vilanova et al., "Numerical simulation of bond-slip interface and tension stiffening in GFRP RC tensile elements," *Compos. Struct.*, vol. 153, pp. 504–513, 2016.

[27] A. Qasem, Y. S. Sallam, H. H. Eldien and B. H. Ahangarn, "Bond-slip behavior between ultra-high-perfomance concrete and carbon fiber reinforced polymer bars using a pull-out test and numerical modelling", *Constr. Build. Materials,* vol. 260, pp. 119857, 2020.

[28] L. Huang, J. Chen, J. Qu and Q. Dai, "Modeling for bond-constitutive relationships of FRP rebars to concrete matrix," *Constr. Build. Materials,* vol. 263, pp. 120654, 2020.

[29] K. Dörr "Bond behavior of ribbed reinforcement under transverse pressure", in *IASS Symp. on Nonlinear Behavior of Reinforced Concr. Spatial Struct.*, vol. 1, Preliminary Report. Werner Verlag, Dusseldorf, 1978.

[30] R. Eligehausen, E. Popov, and V. Bertero, *Local Bond Stress Slip Relationship of Deformed Bars Under Generalized Excitations*, Earthquake Engineering Research Center, report to the National Science Foundation, University of California, Berkeley, 1983.

[31] N. Hawkins, I. J. Lin and F. L. Jeang, *Local Bond Strength of Concrete for Cyclic Reversed Loadings*, University of Washington, 1982.

[32] J. Mazars and G. Pijaudier-Cabot, "Continuum damage theory – application to concrete," *J. Eng. Mech.*, vol. 115, no. 2, pp. 345–365, 1989.

[33] D. J. Carreira and K. Chu, "Stress-strain relationship for plain concrete in compression," *ACI J.*, vol. 82, pp. 797–804, 1985.

[34] T. Boone and A. R. Ingraffea “Simulation of the fracture process at rock interfaces”, in *Proc. of the fourth Int. Conf. in Numerical Methods in Fract. Mech.*, 1987, pp. 519-531.

[35] M. S. Álvares, “Estudo de um modelo de dano para o concreto: formulação, identificação paramétrica e aplicação com o emprego do método dos elementos finitos”, Master thesis, Univ. São Paulo, São Carlos, Brazil, 1993.

[36] L. Gori, S. S. Penna, and R. L. S. Pitangueira, "A computational framework for constitutive modelling," *Comput. Struc.*, vol. 187, pp. 1–23, 2017.

**Author contributions:** PDNR: implementation, formal analysis, writing. LLS and RLSP: methodology, supervision.

**Editors:** Bernardo Horowitz, Guilherme Aris Parsekian.

IBRACON Structures and Materials Journal
Revista IBRACON de Estruturas e Materiais
ISSN 1983-4195 ismj.org

ORIGINAL ARTICLE

# Global analysis of DEF damage to concretes with and without fly-ash

*Análise global dos danos da DEF em concretos com e sem cinza volante*

Nicole Pagan Hasparyk[a]
Dioice Schovanz[b]
Francieli Tiecher[b]
Selmo Chapira Kuperman[c]

[a]Furnas Centrais Elétricas S.A., Departamento de Segurança de Barragens e Tecnologia, Goiânia, GO, Brasil
[b]IMED Campus Passo Fundo, Programa de Pós-graduação em Engenharia Civil, Passo Fundo, RS, Brasil
[c]Desek Ltda., São Paulo, SP, Brasil

Received 15 February 2021
Accepted 01 October 2021

**Abstract:** Delayed Ettringite formation (DEF) is an internal expansive reaction that can damage concrete. DEF is strongly influenced by the temperature, above about 60-65°C, and other factors involving cement chemistry especially, but also its physical characteristics. The exposure environment over time also promotes a condition to increase deterioration from DEF. Expansions results from secondary ettringite formation are progressive and can lead concrete to microcracking impacting its performance and durability over time. Several concrete structures are pointed to be severely attacked by DEF, and test method as well a better comprehension on this pathology is necessary to promote specific and proper preventive measures to avoid future damages. Furthermore, compared to alkali-silica reaction, DEF occurs more readily and aggressively, and sometimes prematurely, depending on several factors, such as type of cement, concrete mix design, exposure conditions, among others. This paper involves an overall analysis of the behavior of concretes with two types of Portland cements (High early-strength cement and a Portland pozzolanic cement, with fly-ash) in relation to DEF process. Several data from a laboratory study where DEF was induced through a specific thermal curing procedure are presented and discussed. The analyses involved the assessment of physical, mechanical, and expansive properties besides microstructural monitoring of samples from concretes over time. These experiments allowed detecting high values of expansions from DEF (up to 1.2%) in the concrete without fly ash. The mechanical properties were severely impacted from this deleterious process; as expansions increased, losses in the mechanic and elastic properties were verified. Expansion levels in the order of 0.5% prompted remarkably high reductions and, at about 1% the losses were relevant for both strengths (tensile and compressive) and modulus of elasticity, of 60% and 80%, respectively, in the presence of cement without fly-ash. Concrete microstructure has indicated massive formations of ettringite as well as micro-cracking and the fragility of the cement matrix because of DEF. On the other hand, expansion up to 0.2% did not promote important negative effects on the properties of concrete, especially with the pozzolanic cement tested. Furthermore, an overall approach with several correlations between physical and mechanical properties was taken to obtain different levels of deterioration for a concrete presenting DEF.

**Keywords:** concrete, delayed ettringite formation (DEF), expansion, mechanical and physical properties, microstructure, fly-ash, damage.

**Resumo:** A formação da etringita tardia (DEF) é uma reação expansiva que ocorre no interior do concreto já endurecido, podendo danificá-lo. A DEF é fortemente influenciada pela temperatura, quando acima de 60-65°C, e outros fatores envolvendo a química do cimento, principalmente, características físicas e os materiais constituintes do cimento. O ambiente de exposição ao longo do tempo também promove uma condição propícia para aumentar a deterioração por DEF. As expansões resultantes da formação da etringita tardia são progressivas e podem levar o concreto a microfissuras, afetando seu desempenho e durabilidade ao longo do tempo. Diversas estruturas de concreto são apontadas como severamente atacadas por DEF, sendo necessário

**Corresponding author:** Nicole Pagan Hasparyk. E-mail: nicole@furnas.com.br
**Financial support:** This work had financial and infrastructure support from Furnas Centrais Elétricas S.A./ANEEL, P&D 0394-1504-2015. D. Schovanz benefits from a partial scholarship financed by the Research Foundation of the State of Rio Grande do Sul - FAPERGS by the FAPERGS Grant.
**Conflict of interest:** Nothing to declare.
**Data Availability:** The data that support the findings of this study are available from the corresponding author, NPH, upon reasonable request.

um melhor entendimento desta patologia a fim de promover medidas preventivas específicas e adequadas para evitar danos futuros. Além disso, em comparação com a reação álcali-sílica, a DEF ocorre de forma mais rápida e agressiva, e muitas vezes de modo prematuro, dependendo de vários fatores, como tipo de cimento, concreto, condição de exposição, entre outros. Este trabalho envolve uma análise geral do comportamento de concretos com dois tipos de cimentos Portland (cimento de alta resistência e outro cimento pozolânico, com cinza volante) em relação ao processo DEF. Várias informações de estudo laboratorial são apresentadas e discutidas após a indução de DEF por um procedimento específico com cura térmica. As análises envolveram a avaliação das propriedades físicas, mecânicas e expansivas, além do monitoramento microestrutural de amostras de concretos ao longo do tempo. Esses experimentos permitiram detectar altos valores de expansões de DEF (até 1,2%), principalmente no concreto sem pozolana. As propriedades mecânicas foram severamente afetadas por esse processo deletério; com o aumento das expansões, foram constatadas perdas nas propriedades. Considerando níveis de expansão da ordem de 0,5%, a redução foi muito elevada e, em cerca de 1% as perdas foram relevantes tanto para as resistências (tração e compressão) e módulo de elasticidade, de 60% e 80%, respectivamente, na presença de cimento sem cinzas volantes. A microestrutura do concreto indicou formações maciças de etringita bem como microfissuras e a fragilidade da matriz de cimento como consequências da DEF. Por outro lado, a expansão de até 0,2% não promoveu efeitos negativos importantes nas propriedades do concreto, principalmente com o cimento pozolânico testado. Além disso, uma abordagem geral com várias correlações entre as propriedades físicas e mecânicas foi feita para obter diferentes níveis de deterioração do concreto por DEF.

**Palavras-chave:** concreto, formação da etringita tardia (DEF), expansão, propriedades físicas e mecânicas, microestrutura, cinza volante, deterioração.

**How to cite:** N. P. Hasparyk, D. Schovanz, F. Tiecher, and S. C. Kuperman, "Global analysis of DEF damage to concretes with and without fly-ash" *Rev. IBRACON Estrut. Mater.*, vol. 15, no. 3, e15305, 2022, https://doi.org/10.1590/S1983-41952022000300005

## 1 INTRODUCTION

Delayed ettringite formation (DEF) involves crystallization of ettringite in hardened cementitious matrix. In the presence of moisture, it can cause progressive expansions over time, leading to cracking. The increase of these expansions can affect the mechanical properties of concrete and accelerate the entry of aggressive agents, causing loss of performance and durability of structures.

DEF occurs when the aluminates are not completely consumed during the cement hydration, being the sulfated phase still present after the first hours of this process [1], [2]. Alterations during hydration process occurs due to high temperature levels, and above 65ºC. The mechanisms of DEF involve dissolution of calcium hydroxide and decalcification of C-S-H prior to ettringite production, according to Gu et al. [3]. The available aluminum is originated from the monosulfate itself since it is the main source of $Al_2O_3$ in Portland cement [4], [5]. In the early stages of the cement hydration process the characteristics of the cement, are among the main factors interfering in DEF [6], [7]. The use of pozzolanic admixtures can decrease the heat evolution during hydration because they react slower than the clinker [8]. The phases produced in the pozzolanic reaction also led to greater stability, improving the concrete resistance to acid attacks [9].

Nonetheless, the preventive measures involving mineral admixtures is far from conclusive. Several variables from admixtures, such as type, fineness, composition, optimum contents interfere in the mitigative process [10]–[14]. Some results also indicate a non-mitigative behavior for DEF, depending on the material and test method [15], [16].

The probability of DEF occurrence is associated with the amounts of sulfate and aluminum in the cement. If there is too much sulfate and too little aluminum, the sulfoaluminate phase will be ettringite, otherwise, it will be monosulfate [17]. Moreover, specific surface and alkalis play an important role in the DEF occurrence, besides the relation $(SO_3)^2/Al_2O_3$, that is suggested to be below 2 in order to reduce risks of DEF, according to Zhang et al. [14].

The high porosity in the interfacial transition zone (ITZ) due to the wall effect allows the beginning of the ettringite crystallization in this site. The speed of ettringite crystallization is higher compared to the cement matrix, even tough, the pressures generated in the ITZ may be not too high, according to Jebli et al. [18]. The DEF expansion can reach high levels, of the order of 2% and, according to some researchers it is also possible to detect, in laboratory tests, mass gains as expansions increases achieving levels higher than 1% due to ettringite crystal precipitations in the matrix [3].

These high levels of expansion affect the modulus of elasticity of concrete, which values can decrease up to 40% [19]–[21]. Brunetaud et al. [22] point, though, that even smaller expansions, next to 0.10%, can reduce the modulus of elasticity of concrete, which is a mechanical property widely affected by cracking. The reduction in the porosity as DEF fills the voids leads to pressure and cracking, decreasing modulus of elasticity as well as strengths [11]. According to Pichelin et al. [4], there is a latent period between expansions from 0.05% to 0.10% in which just the modulus is affected by DEF.

In general, the compressive strength is less sensitive to expansive reactions when compared to the modulus of elasticity. However, many studies have shown that the compressive strength can also be intensely affected by DEF, even increasing at early stages [19], [23], [24]. According to Pichelin et al. [4], this behavior can be explained by considering that the secondary ettringite crystallizes in the ITZ. DEF can also fill pre-existing cracks, besides voids. In consequence, it fills and densifies the cement matrix, increasing the compressive strength. However, if there is enough moisture, the DEF spreading speed will be greater than other expansive reactions, such as ASR (Alkali-Silica Reaction), for example [25]–[27]. Hence, there will be growth in expansion and cracking, decreasing the compressive strength, besides having a negative impact in other properties, such as tensile strength and modulus.

After diagnosing DEF-affected concrete structures in the field, many researchers have shown concern for the fact that it is not possible to interrupt the development of the reaction until now [28]–[30], similarly to ASR. The pressure caused by the expansions is affected by structural restraint and the process is like the one caused by ASR [31]. Among the existing gaps, the lack of standardized methods to assess the DEF-potential in laboratory studies can be highlighted. Some researchers have developed their methodologies, however, showing many divergences, such as Melo [32], Giannini et al. [19], Fu [33], Dayarathne et al. [10], Leklou et al. [13], Rashidi et al. [34], Duggan and Scot Test [35], Kchakech et al. [36], Martin et al. [37], Nguyen et al. [38].

In general, to assess concrete structures affected by DEF the properties that have been evaluated are modulus of elasticity, compressive strength, and tensile strength [1], [4], [39], [40]. More recently, two indexes obtained from the Stiffness Damage Test (SDT) have been suggested: The Stiffness Damage Index (SDI) and the Plastic Deformation Index (PDI). This trial was initially employed to assess ASR, but some promising initial results concerning to DEF were obtained [26], [37].

Based on this context, the main purpose of this research is to evaluate the levels of damage of concretes with and without fly-ash when subjected to DEF triggering conditions. The study presents data from several physical, mechanical, and microstructural analyses and correlations to different expansion levels over one year of monitoring.

## 2 EXPERIMENTAL PROGRAM

The mix proportioning adopted in the experimental program was 1:1.6:1.9 (by mass), water-cement (w/c) ratio of 0.46, and cement content of 470 kg/m$^3$. A polyfunctional admixture based on lignosulfonate and polycarboxylate was used in the proportion of 0.6% and 0.1% for ASTM cement type III and IP, respectively.

A thermal curing method, based on Fu [33], Kchakech et al. [36], and Rashidi et al. [34], was adapted by increasing the temperature in the first hours of cement hydration to create conditions for DEF occurrence, as shown in Figure 1.

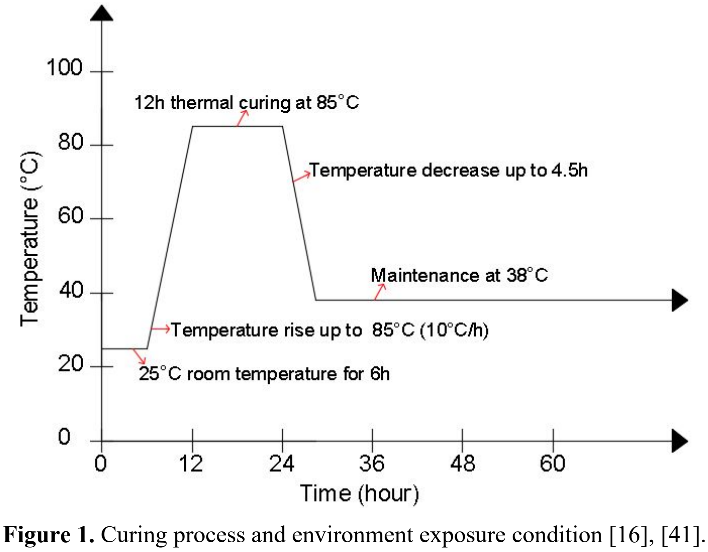


**Figure 1.** Curing process and environment exposure condition [16], [41].

### 2.1. Materials

In this study, two different types of Brazilian Portland cements were used: one like Type III Portland cement – with high early strength [42] (Table 1), and other like Type IP Portland cement [42], with Fly Ash Type F (Table 2) – a pozzolanic cement.

**Table 1.** Properties of the high early strength Portland cement, ASTM Type III.

| Chemical Properties (%) | | | | | | | | | | |
|---|---|---|---|---|---|---|---|---|---|---|
| $SiO_2$ | $Al_2O_3$ | $Fe_2O_3$ | CaO | MgO | $SO_3$ | $Na_2O$ | $K_2O$ | $Na_2Oeq$ | Loss on ignition | Insoluble Residue |
| 18.86 | 4.46 | 2.75 | 61.46 | 3.93 | 3.28 | 0.23 | 0.85 | 0.79 | 3.37 | 0.76 |
| **Hydration heat ($J.g^{-1}$) for 41h:** 328.30 | | | | | | | | | | |
| **Mechanical and Physical Properties** | | | | | | | | | | |
| **Compressive Strength (MPa)** | | | | **Specific Mass ($g/cm^3$)** | **Thermal expansion (mm)** | **Blaine Fineness ($cm^2/g$)** | | | | |
| **1 day** | **3 days** | **7 days** | **28 days** | | | | | | | |
| 25.6 | 38.6 | 44.4 | 54.1 | 3.09 | 0.50 | 4520 | | | | |

**Table 2.** Properties of the Portland-pozzolan cement, ASTM Type IP.

| Chemical Properties (%) | | | | | | | | | | |
|---|---|---|---|---|---|---|---|---|---|---|
| $SiO_2$ | $Al_2O_3$ | $Fe_2O_3$ | CaO | MgO | $SO_3$ | $Na_2O$ | $K_2O$ | $Na_2Oeq$ | Loss on ignition | Insoluble Residue |
| 29.47 | 10.24 | 4.12 | 45.02 | 2.98 | 2.25 | 0.18 | 1.34 | 1.10 | 3.55 | 26.21 |
| **Hydration heat ($J.g^{-1}$) for 41h:** 259.00 | | | | | | | | | | |
| **Mechanical and Physical Properties** | | | | | | | | | | |
| **Compressive Strength (MPa)** | | | | **Specific Mass ($g/cm^3$)** | **Thermal expansion (mm)** | **Blaine Fineness ($cm^2/g$)** | | | | |
| **1 day** | **3 days** | **7 days** | **28 days** | | | | | | | |
| 14.4 | 25.5 | 32.8 | 46.0 | 2.82 | 1.00 | 4180 | | | | |

The aggregates (fine and coarse) used are potentially innocuous to ASR occurrence, as established by ASTM C-1260:2018 [43] and Brazilian standard NBR 15577-1:2018 [44]. Table 3 shows the characteristics of the fine and coarse aggregates.

**Table 3.** Characteristics of the aggregates.

| Properties | Fine aggregate | Coarse aggregate |
|---|---|---|
| Origin | Natural Pit sand | Granite - Crushing |
| Maximum size | 4.75 mm | 19.00 mm |
| Fineness modulus | 2.56 | 6.72 |
| Specific Mass | 2.05 $g/cm^3$ | 2.68 $g/cm^3$ |
| Water absorption | 3.0% | 0.40% |
| Powdered material | 1.3% | 0.32% |

Figures 2 and 3 present the particle size distribution of fine and coarse aggregates, respectively.

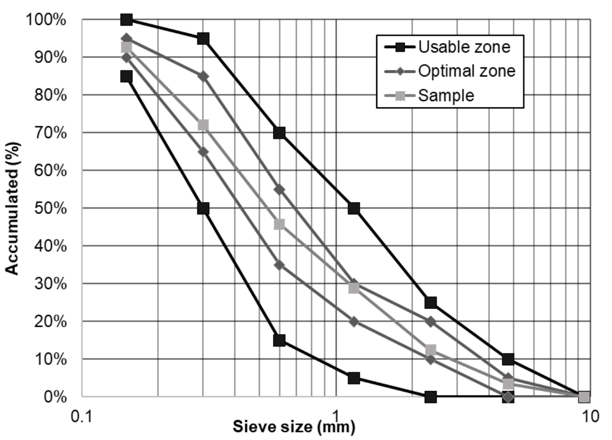


**Figure 2.** Particle size distribution of fine aggregate.

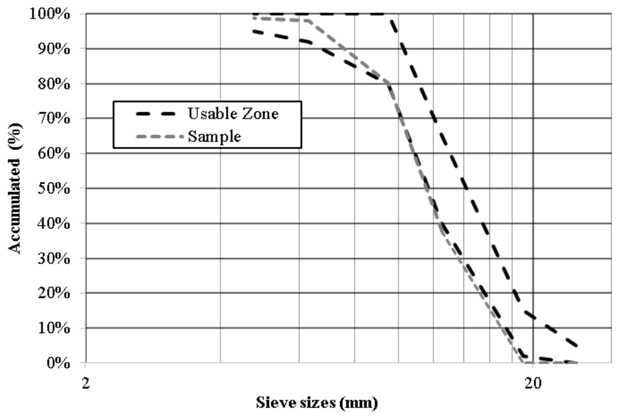


**Figure 3.** Particle size distribution of coarse aggregate.

## 2.2 Evaluation of concrete characteristics and properties

The physical characteristics of concretes were assessed by measuring the dimensional variation and mass variation of prismatic specimens with dimensions (75 × 75 × 285) mm. Measurements of five samples were carried out weekly over 12 months. The methodology of ASTM C-1260:2018 [43] was adopted to assess the dimensional variation. The mass variation was measured on a digital scale with an accuracy of 0.001 g.

Visual inspection of the specimens was also carried out, which consisted of verifying and photographing anomalies indicative of the occurrence of DEF.

The mechanical properties of concrete were evaluated by measuring compressive strength, splitting tensile strength, and modulus of elasticity tests at the ages of 7, 28, 56, 84, 168, 252, and 365 days, using cylindrical specimens (100 x 200) mm. Three specimens were cast to be evaluated by physical and mechanical tests.

The test method known as SDT (Stiffness Damage Test) was performed to obtain the SDI (Stiffness Damage Index) and PDI (Plastic Deformation Index) parameters at the same ages of mechanical properties. This test followed the procedure proposed by some researchers, such as Giannini et al. [19], Sanchez et al. [26], and Martin et al. [37], in which the specimens are subjected to five cycles of loading/unloading at a controlled loading rate of 0.10 MPa/s, loading up to 40% of the 28-day concrete strength (Figure 4).

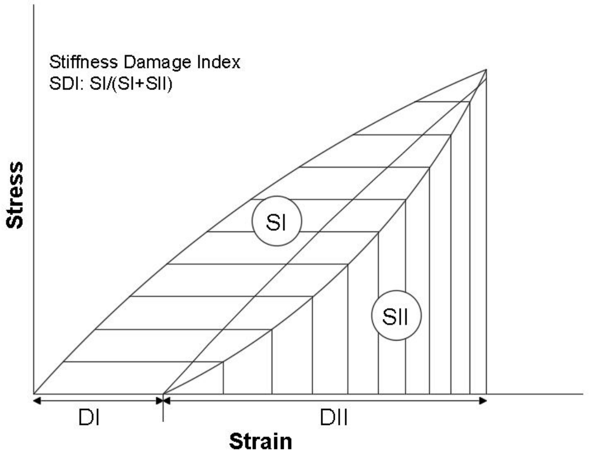


**Figure 4.** Stiffness Damage Test (SDT): Stiffness Damage Index (SDI) and Plastic Deformation Index (PDI) [19], [37].

The microstructure of some selected samples from concretes was assessed on fracture surfaces by a scanning electron microscope (SEM), using a secondary electron (SE) detector, and an Energy-dispersive X-ray spectroscopy (Double-EDS Detector). Samples were covered by a gold sputtering before SEM analyses.

## 3 RESULTS AND DISCUSSIONS

### 3.1. Evaluation of physical characteristics

Indeed, according to the visual inspections some features of chemical reactions, such as whitish precipitations related to DEF (considering further confirmation by SEM/EDS) were detected prematurely, and notably for the concretes cast with Type III cement. At 56 days, those whitish spots started to appear clearer, and, over time, these symptoms began to spread over the entire surface of the evaluated concretes. After 84 days, a white material filled the voids, and, at 196 days, some mapped micro-cracks were visible (when the concrete showed expansion next to 1%), presenting a gradual increase of white areas until the last age of evaluation (365 days), with a complete covering of the concrete surface. As for the concrete containing fly-ash, this incidence was less expressive and those symptoms became more evident later, and shortly after the age of 140 days, with some dissemination over the surface of concrete over time (Figure 5).

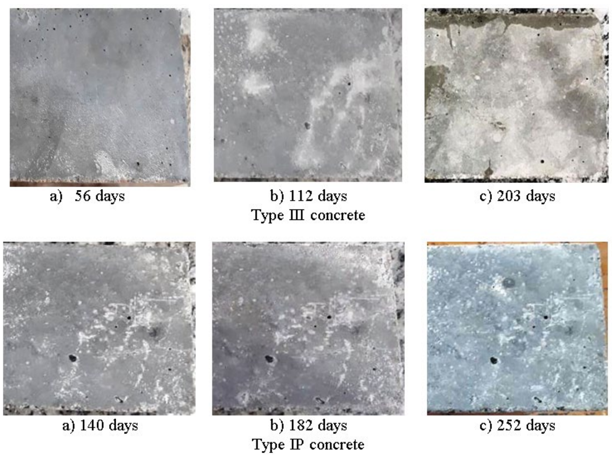


**Figure 5.** Visual inspection of concretes.

According to [1], [5], [45]–[48], the neoformations from sulfate attack and DEF may locate in sites like voids of the cementitious matrix, paste/aggregate transition zones, and pre-existing microcracks of concrete (Figure 6). The internal expansion is influenced by parameters of concrete microstructure, which are directly dependent on the characteristics of cement and concrete. Regarding the Portland-pozzolan cement (Type IP), the signs were not so clear, since the whitish material only could be found in some punctual areas, and with more evidence just after 140 days.

Several diagnoses of DEF from Blanco et al. [49], are registered for old dams for over 30 years. The main symptoms were white precipitations in the surface cracks of concretes at both directions of the spillway, upstream and downstream. To obtain a precise diagnosis, sometimes it is necessary a specific investigation involving mechanical tests as well as microstructural analyses of concrete cores drilled from the structure, especially when there is lack of information for old structures [49]–[51].

(a) Cracking of the base of a pylon (crack width >0.3 mm). (b) Longitudinal cracks in the middle of a prestressed precast concrete beam.

**Figure 6.** Cracking in the surface of concrete structures due to DEF [29].

Figure 7 shows the expansion behavior and mass gain over time of the tested concretes. It is observed that Type III cement presented for both expansion and gain mass of concretes the highest values compared to the pozzolanic one. The maximum values obtained for expansion rates and mass gain of the samples with Type III cement were high, next to 1.2% and 2.5%, respectively. For samples with Type IP cement, the values were next to 0.2% and 0.5%, respectively. Some expansion results close to 1% at 168 days of testing in samples with Type III cement, reported in the literature, corroborate the results obtained in this research, thus indicating a high probability of this expansion being due to DEF [26], [48], [52]. Sanchez et al. [26] also observed higher levels of DEF expansion, such as 1.87%.

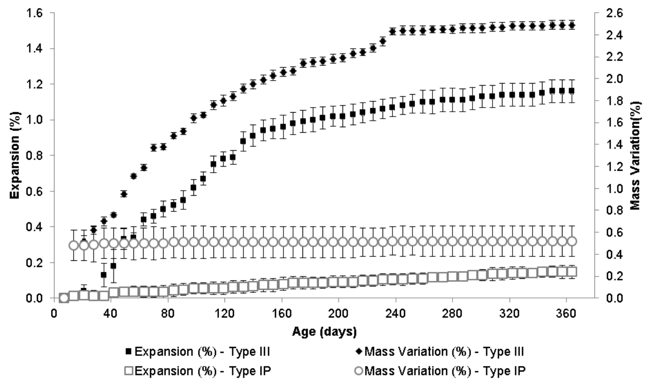


**Figure 7.** Expansion and mass variation of concretes over time.

The partial replacement of cement by fly ash leads to a reduction of the $SO_3/Al_2O_3$ ratio. The increase in $Al_2O_3$ induces greater precipitation of monosulfate, leading the sulfate concentration in the pore solution to decrease. This phenomenon results in a reduction of the sulfate absorption capacity by C-S-H gels and therefore reduces the potential for DEF expansion [7], [13], [53], [54]. Delayed ettringite formation occurs due to the conversion of monosulfate and mechanisms that reduces the amount of $Al_2O_3$, leading to a greater amount of monosulfate and of $SO_4^{2}$ ions free or weak bound to C-S-H, according to Melo [55]. This causes an increase in the neo-formed ettringite amount over time.

### 3.2. Assessment of mechanical properties

Figure 8 presents the results of the mechanical properties for both concretes. The behavior of the compressive and tensile strengths, and of the modulus of elasticity align with DEF- induced damage of concrete with Type III cement, over time. As both strengths decreased, the modulus dropped over time, and the maximum decrease occurred between three and six months. The mechanical behavior of the Portland pozzolanic concrete was different from the concrete with Type III cement. In general, a relation between compressive and tensile strengths can be observed (Figure 9). The data of tensile strength are situated between 5 and 10% of the compressive strength, presenting concrete with Type III cement a wider dispersion of values due to DEF occurrence.

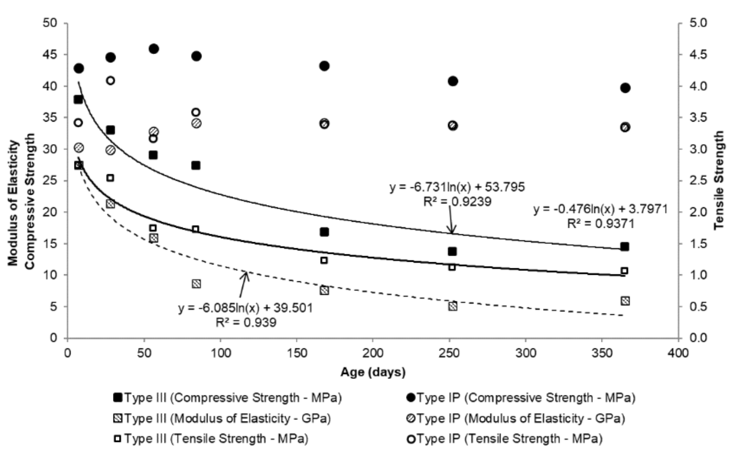


**Figure 8.** Evolution of mechanical properties over time.

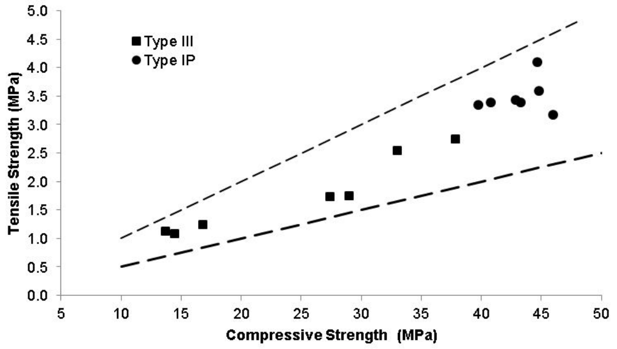


**Figure 9.** Relationship between tensile strength and compressive strength of concretes.

According to Figure 10, there is a good correlation between these mechanical properties. As stated by Price [54], when the value of the compressive strength is next to 18 MPa, the tensile strength represents about 10% of the compressive strength. However, for compressive strengths slightly higher, next to 25 MPa, this ratio drops to 8%-9%. When the compressive strength presents higher values, next to 40 MPa, the tensile strength represents about 7% of the compressive strength. Due to the concrete damaged conditions, it was not possible to make predictions of the modulus of elasticity based on the compressive strength data. As previously stated by Giannini et al. [19], there is no way to predict modulus of elasticity of affected concretes based on standard codes.

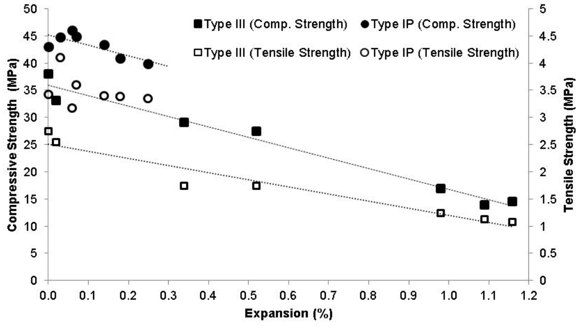


**Figure 10.** Relationship between the tensile and compressive strengths versus expansion.

Figure 11 shows the correlation of the results obtained experimentally to those obtained from the equations of Brazilian standard code ABNT NBR 6118: 2014 [56] ($E_{ci} = 5600\sqrt{fck}$) and ACI 318: 2014 [57] ($E_{ci} = 4730\sqrt{fc}$). It is possible to observe that DEF expansions caused negative effects on the mechanical properties (Figures 12, 13 and 14).

Even for the Portland pozzolanic concrete, both strengths decreased, although with less damage (bellow 10% for the maximum expansions detected) compared to concrete with Type III cement (next to 60% at higher expansion level above 1%).

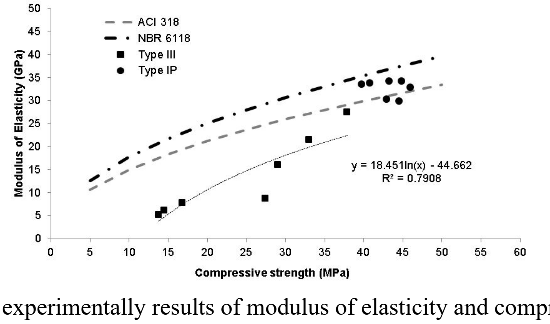


**Figure 11.** Correlation between the experimentally results of modulus of elasticity and compressive strength with the estimated results from Brazilian standard code ABNT NBR 6118:2014 [56] and ACI 318:2014 [57].

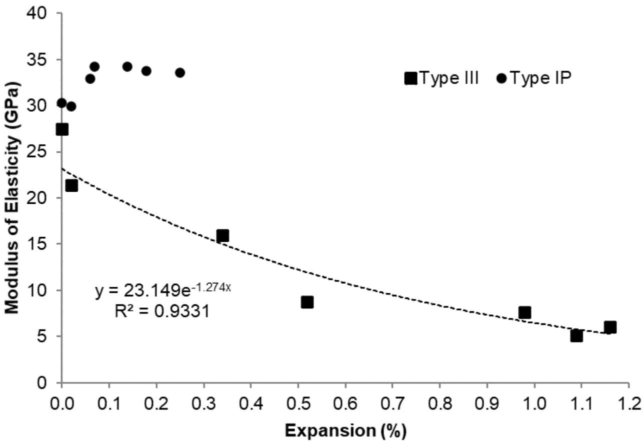


**Figure 12.** Relationship between modulus of elasticity versus expansion.

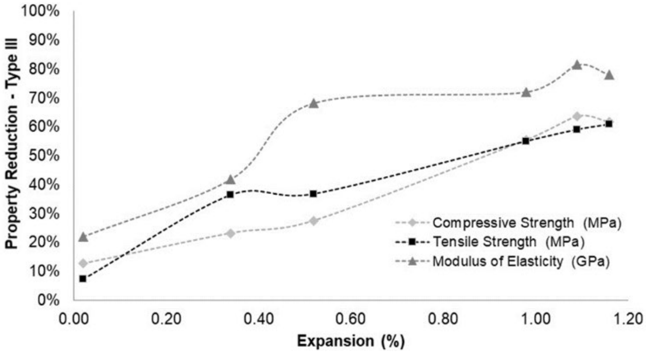


**Figure 13.** Correlation between the mechanical properties and expansion for Type III cement.

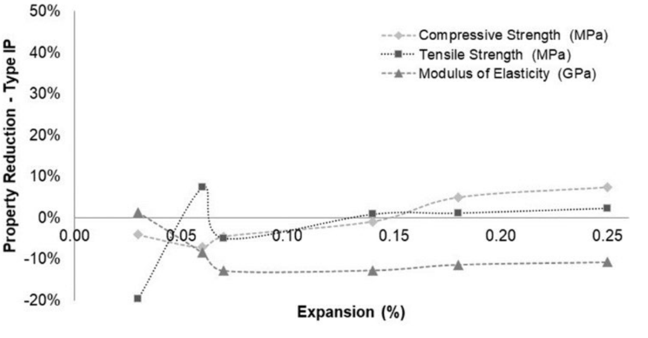


**Figure 14.** Correlation between the mechanical properties and expansion for Type IP cement.

For expansion levels of 0.20%-0.40%, the decrease of tensile strength was next to 40%. According to the literature [26], [54], some DEF-affected concrete structures showed a reduction of tensile strength next to 65%. The modulus of elasticity presented a drop of about 80% with the high DEF induced expansion (over 1%) for concrete with Type III cement (Figure 13) whereas expansions up to 0.25% did not impact this property in the presence of pozzolanic cement (Figure 14). According to [19], [58], deleterious effects on the modulus of elasticity can arise even before the occurrence of significant expansions.

In the literature, some researchers agree that DEF expansions negatively affect the mechanical properties of concrete [19], [24], [58]. However, some studies pointed to negative results of compressive strength (drop of 50%) when the expansion values are remarkably high, next to 1.50% [1], [3], [23].

### 3.3. Stiffness Damage Test (SDT)

Figures 15 and 16 show the stress-strain curves plot with SDT results for concretes with Type III cement and Type IP cement, respectively, considering the six evaluated ages. For concrete with Type III cement, a gradual increase in deformation is observed over time, as the expansions increase. This behavior is intrinsically related to the microcracking caused by DEF stresses, thus weakening the concrete. At 365 days, expansions above 1% caused very high deformations. The SDI at 365 days represents next to four times the deformation obtained at 28 days. So, with larger hysteresis areas in the stress-strain plots, there is dissipated energy and more plastic deformation accumulated, resulting in loss of stiffness. Similar behavior was observed by Giannini et al. [19], Sanchez et al. [26], Martin et al. [37] and Smaoui et al. [59].

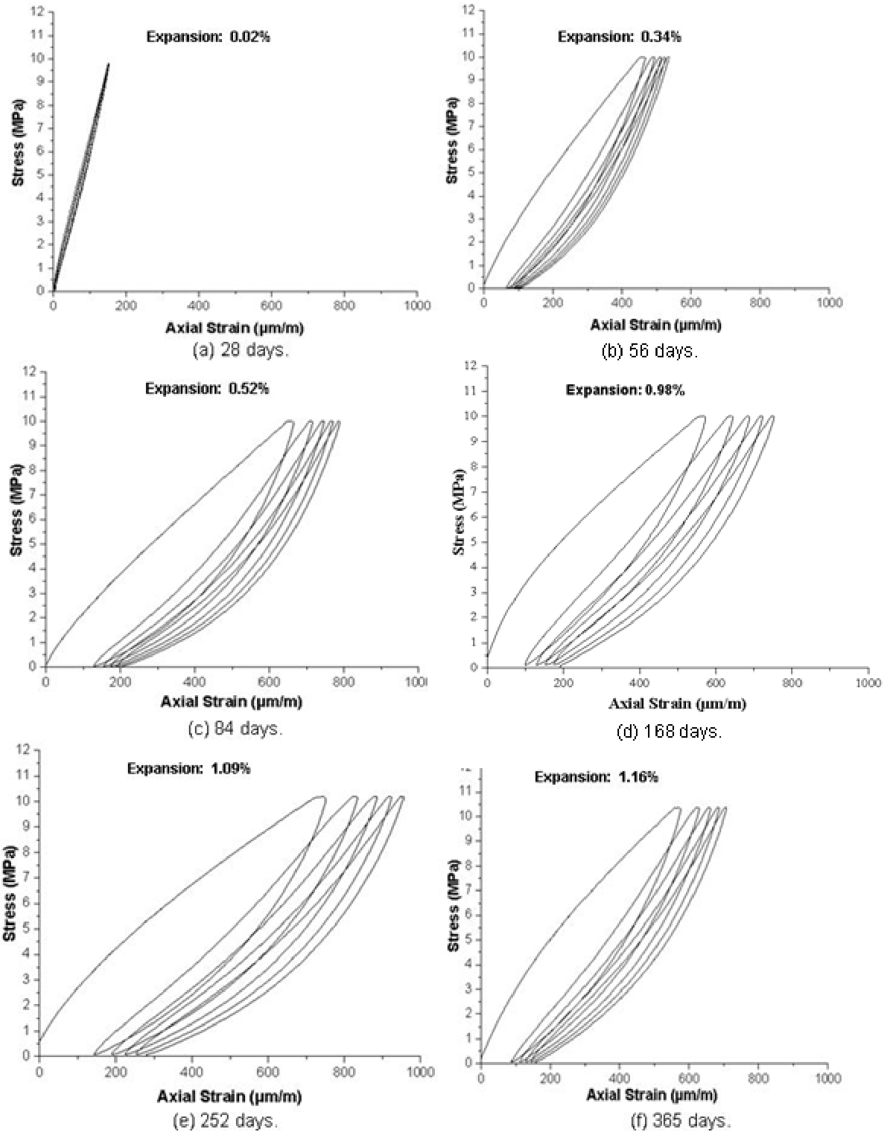


**Figure 15.** Results of Stiffness Damage Test (SDT) for Type III cement.

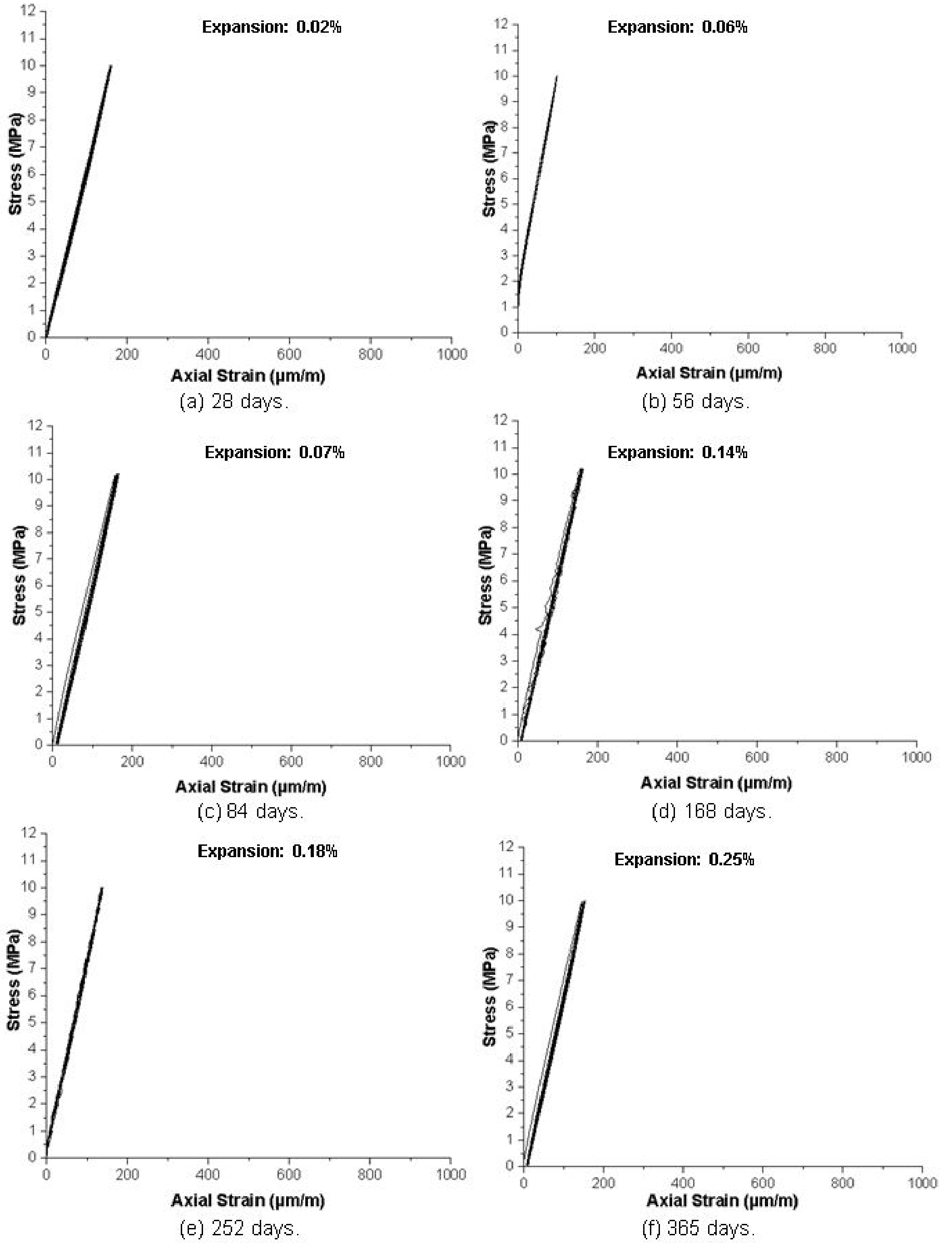


**Figure 16.** Results of Stiffness Damage Test (SDT) for Type IP cement.

Figures 17 and 18 show that after the second month of testing, when the expansions were already expressive and the values of the mechanical properties decreased, the SDT was not sensitive enough to detect the DEF progress over time, showing little variation until 365 days. Concretes with Type IP cement showed different behavior, the Stiffness Damage Index (SDI) and Plastic Deformation Index (PDI) were lower than for concretes with Type III cement. Besides, the maximum expansion achieved was next to 0.2%, indicating there were no important changes over time by using SDT.

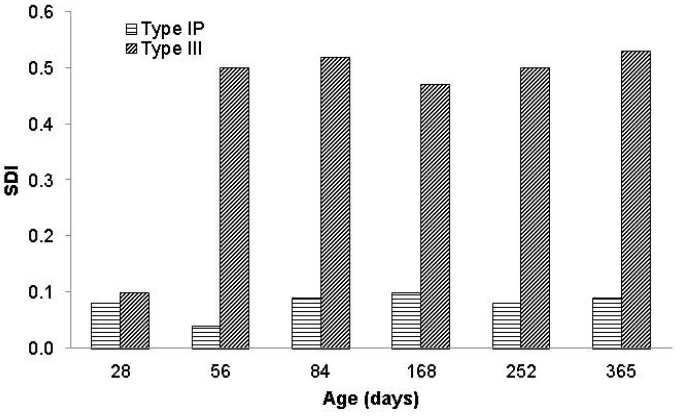


**Figure 17.** Stiffness Damage Index (SDI) of concretes over time.

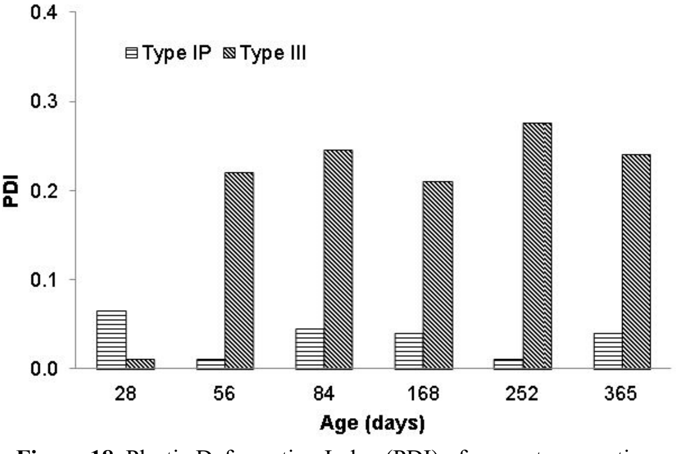


**Figure 18.** Plastic Deformation Index (PDI) of concretes over time.

Figure 19 presents a correlation between the modulus of elasticity and the Stiffness Damage Index (SDI). For concrete with Type III cement, when the modulus of elasticity decreases, the SDI increases. The same does not occur for concrete with pozzolanic cement.

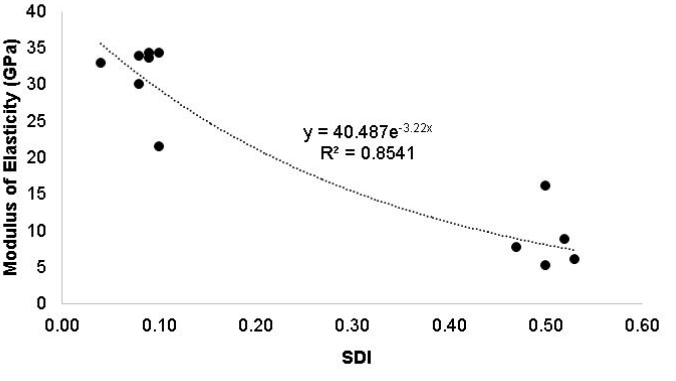


**Figure 19.** Correlation between Stiffness Damage Index (SDI) and modulus of elasticity.

Figure 20 shows the correlation between expansion, Stiffness Damage Index (SDI), and Plastic Deformation Index (PDI). Concrete with Type III cement presented SDI values in the range of 0.10 to 0.53, while the expansion values were in the range of 0.02% to 1.16%. For concrete with Type IP cement, the SDI values varied from 0.04 to 0.10 and the expansions from 0.02% to 0.25%. However, for concrete with Type III cement, the SDI did not show important variations for expansions above of 0.34%, being in the range of 0.47 to 0.53. The SDI value for concrete with pozzolanic cement did not increase when compared to the higher expansion values, since the level of expansions does not exceed 0.25%.

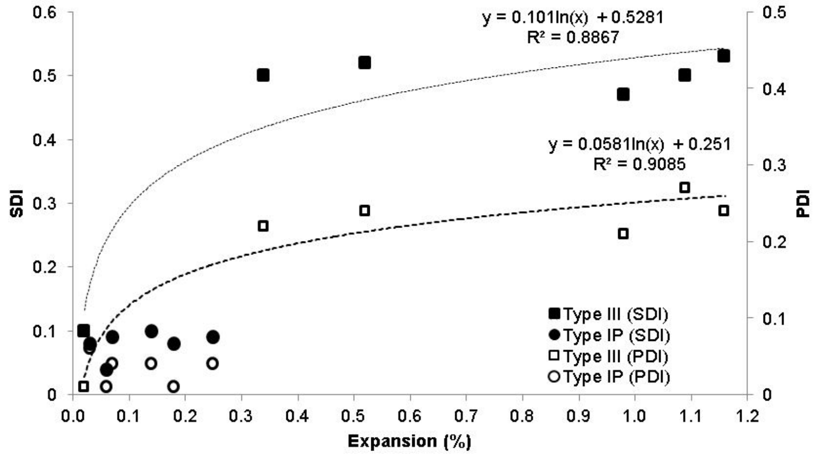


**Figure 20.** Correlation between expansion, Stiffness Damage Index (SDI), and Plastic Deformation Index (PDI).

In general, the behaviors of SDI and PDI were similar for the concretes with both types of cement. However, the Stiffness Damage Index (SDI) seems to have adhered better to the DEF behavior in the present study. Concerning the Plastic Deformation Index (PDI), this parameter can assist in damage identification of concrete, especially when studying pathological phenomena related to permanent dimensional change, that is, when exceeding the limits of elastic deformation [19]. In this sense, it is observed that the concrete with Type III cement presented permanent deformations due to the high level of triggered expansibility.

Concerning the results obtained in the present study for concrete with Type III cement, higher values were observed for SDI compared to PDI for similar expansion rates (of the order of 1.0%), when compared to the few data available and published in the international literature. In this study, the values obtained for SDI and PDI were 0.53 and 0.27, respectively, while for Giannini et al. [19], these values were in the order of 0.57 and 0.49, and, for Sanchez et al. [26], 0.38 and 0.33, respectively. In other words, for DEF affected concretes, in the range of 1% expansion, the concrete with Type III cement showed more stiffness damage.

### 3.4. Evaluation of microstructural characteristics

Figures 21 and 22 show the microstructural characteristics of the samples analyzed over time and up to 365 days by SEM/EDS. The first ettringite crystals neoformations were visualized at 28 days for concrete with Type III cement (Figure 21), filling the voids of the concrete. After 168 days, there were massive agglomerations of these neoformations. At this age, a weakened cement-aggregate transition zone and many ettringite crystals around the aggregates were observed. After 365 days, concrete was completely fragile, with relevant neoformations, indicating extreme deterioration. The analysis of the microstructure of concrete with Type III cement was consistent with the mechanical properties drop over time. It was also consistent with the high expansion levels, over 1%. On the other hand, the pozzolanic concrete (Figure 22) showed scarce voids with ettringite at 28 days. The deposition of ettringite crystals increased over time, but less intensely than for concrete with Type III cement. At 168 days, some massive formations in the cement matrix and voids filled with ettringite gave rise as it was detected by SEM, although there were still some preserved transition zones. At 365 days, the pozzolanic concrete had already obtained microstructural features linked to DEF development, although less intensely than for concrete with Type III cement. Even so, the microstructural and mechanical evaluations were also consistent for the pozzolanic concrete up to the evaluated age.

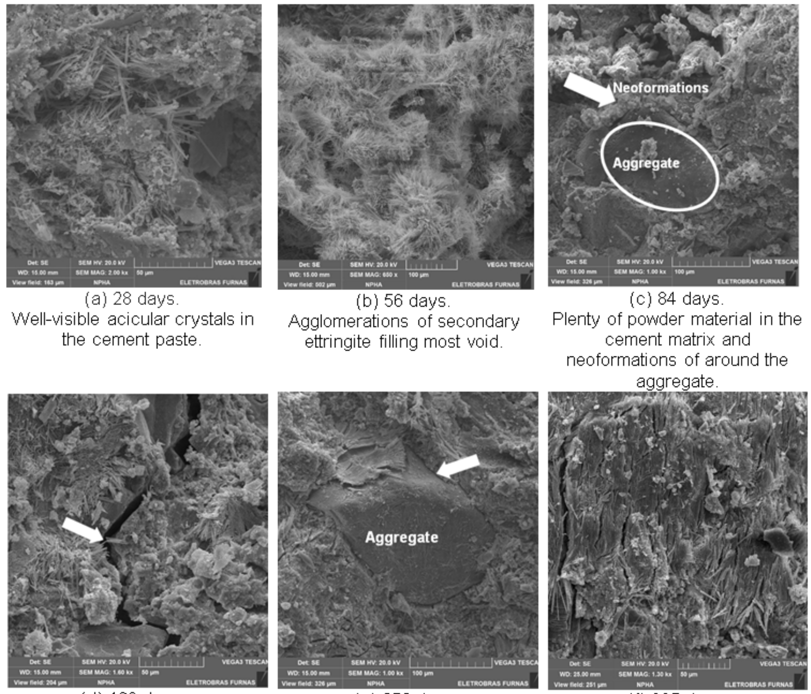


(a) 28 days.
Well-visible acicular crystals in the cement paste.

(b) 56 days.
Agglomerations of secondary ettringite filling most void.

(c) 84 days.
Plenty of powder material in the cement matrix and neoformations of around the aggregate.

(d) 168 days.
Interfacial Transition Zone (ITZ) weakened due to DEF-attacked, plenty of neoformations on the surrounding zone.

(e) 252 days.
Plenty of ettringite neoformations on the aggregate and surrounding zone.

(f) 365 days.
Cement matrix completely fragile due to the compacted ettringite.

**Figure 21.** Micrographs of concrete with Type III cement.

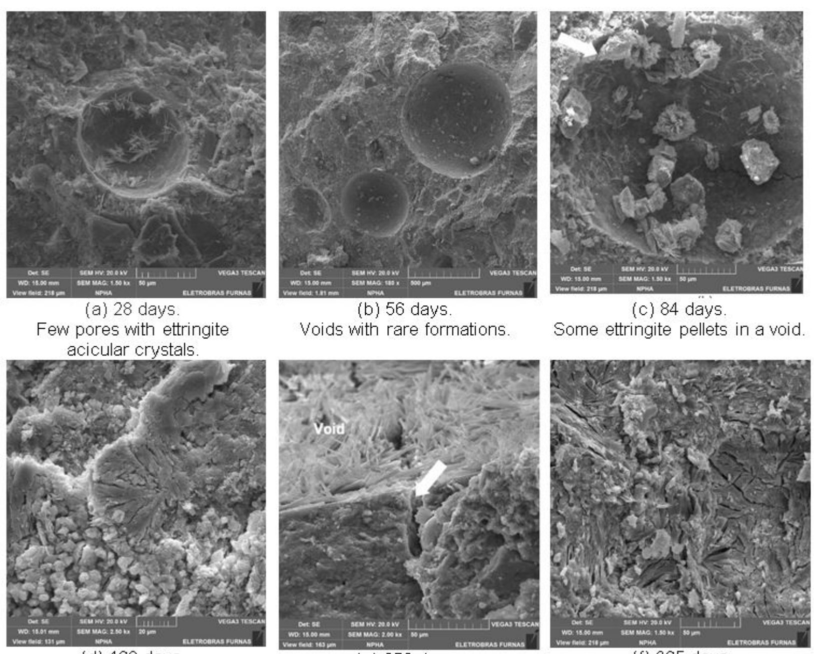


(a) 28 days.
Few pores with ettringite acicular crystals.

(b) 56 days.
Voids with rare formations.

(c) 84 days.
Some ettringite pellets in a void.

(d) 168 days.
Massive formations of ettringite compacted in the cement matrix.

(e) 252 days.
A radial micro-crack was observed on the edge of a pore fulfilled with secondary ettringite formations.

(f) 365 days.
Extensive growth of compacted ettringite in the cement matrix, indicating DEF.

**Figure 22.** Micrographs of concrete with Type IP cement.

The microstructural analyses performed by Bragança et al. [60], show some similarities in the microstructure of concrete affected from DEF, especially the presence of massive ettringite and microcracks, but the extent of expansions detected at one year was lower, and below 0.05%, and the tests were performed with mortars. In the present study, concrete specimens were evaluated and besides the characteristics mentioned before, it was possible to detect higher expansions (1.2% for Type III cement and 0.25% for Type IP cement) at one year, and the microstructural characteristics indicate a high level of concrete deterioration due to the intense massive formations as well as fragilities in the ITZ, for type III cement.

### 3.5 General Overview and Discussions

In order to perform a global analysis of the DEF damage considering the progress of expansive reactions and all data obtained from the mechanical behaviors of concretes without pozzolan, Table 4 summarizes data based upon the level of expansions, as previously performed by Sanchez et al. [26] for DEF and other expansive mechanisms.

**Table 4.** Global analyses of DEF damage for concretes without admixture.

| Level of damage | Level of expansion (%) | Maximum reduction (%) observed on the | | | Data for | |
|---|---|---|---|---|---|---|
| | | Compressive strength | Tensile strength | Modulus of elasticity | SDI | PDI |
| Moderate | 0.02-0.03 | 13 | 7 | 22 | 0.10 | 0.01 |
| High | 0.04-0.20 | 25 | 23 | 45 | - | - |
| Very High | 0.30-0.52 | 28 | 37 | 68 | 0.52 | 0.24 |
| Ultra high | 0.53-1.10 | 64 | 59 | 82 | 0.50 | 0.27 |
| | ≥1.10 | 62 | 61 | 78 | 0.53 | 0.24 |

According to data from Table 4, modulus of elasticity is the more affected property by the increasing expansions, and over time compared to both strengths, as expected. Considering the level "moderate damage" and expansion below 0.03%, the loss for modulus can achieve 22%, but the stiffness damage index indicates 0.10. Sanchez et al. [26] observed a similar SDI-value for DEF mechanism. In the "high level of damage", loss on the compressive strength duplicates as well as for modulus of elasticity (loss of 25 and 45%, respectively) and triplicates for the tensile strength (23% of loss), signing a high damage from 0.04% of DEF expansions. For higher levels of expansion (above 0.30%), damage is extremely high, and seriously reflecting in all mechanical properties as shown by a high level of both stiffness damage index as well as plastic deformation index. SDI in this study achieved 0.52, higher than those verified by Sanchez et al. Around 1% of expansions, about 80% of modulus can be reduced damaging severely the concrete, with losses of the order of 60% for both strengths; Sanchez et al. [26] verified similar mechanical behaviors for the expansive mechanisms studied. In this study the microstructural analyses by SEM were included to corroborate damages caused by the type of ettringite crystals formed as well as the places they were accommodated. Thus, it was possible to explain those high level of deteriorations. For example, after 56 days several ettringite crystals had already been produced in the cement matrix filling several voids, indicating a premature DEF process. Over time it was perceived a progress of those neoformations, with the presence of massive ettringite and microcracking at 6 months, with injuries to the interfacial transition zone (ITZ), justifying the losses for the mechanical properties, but specially for the modulus of elasticity, with expressive expansions of about 1%. From this point, there was a small increase in the expansions since the level of damage had been extremely high leading to a fragile cement matrix besides affecting completely the integrity of the concrete. In the studies from Bragança et al. [60], from levels of expansion of 0.015%, the elastic modulus tends to reduce as the expansions increases. The modulus was negatively influenced at about 35% of loss at one year.

In the case of pozzolanic cement, with fly ash, the behavior was different considering a global analyses of DEF damage since neither modulus of elasticity nor SDT indexes were affected by expansions up to 0.25%; SDI remained at 0.10 and PDI achieved 0.04 for this high level of expansion. On the other hand, in relation to the strengths, above 0.14% of expansion caused a decrease of about 18% for tensile strength, and considering expansions of 0.18%, a decrease of about 10% was detected for compressive strength, considering the reference age of 28 days. This behavior can suggest the long term of fly ash in acting as pozzolanic material and a self-healing effect over time. Nevertheless, it is important to perform internal microstructural analyses by SEM to check if pozzolan inhibited the expansive process from DEF or just promoted a delay on the expansion behavior and the damages. From this view, an alert must be registered since the internal integrity of this concrete was effectively impaired by DEF. Thus, the expansive process and damage was just delayed for this type of cement based upon the SEM analyses (Figure 22). Differently from the concrete without pozzolan, the first important microstructural signs were verified around six months, considering the massive formations dispersed along the cement matrix. At this point, expansions achieved 0.14%, justifying negative impacts in the tensile strength. Considering nine months, some cracks were identified in the cement paste, leading to losses in the compressive strength (with 0.18% of expansion), but no reduction neither in the modulus of elasticity nor in the SDT indices, yet. Injuries in the ITZ were not detected up to one year for this concrete. The fact is that the ettringite observed by SEM at 365 days seems that will take more time to induce modulus reductions by cracks in the ITZ. Thus, further ages are necessary to be monitored by SEM. The process for this type of concrete differs from the one without admixture. Some studies related to the use of SCMs and pozzolans indicate this behavior, such the one published by Silva et al. [61] and other research [12], [52], [55].

## 4 CONCLUSIONS

Delayed ettringite formation (DEF) was evaluated through physical, mechanical, and microstructural analyses and correlated to expansions of two concretes, with and without fly-ash, over time. The main purpose of this research was to perform a global analysis of DEF based on multiple analyses and the major conclusion is that both concretes with (Type IP cement) and without fly-ash (Type III cement) suffered from DEF, even though in different levels of deterioration. The mechanical properties were affected prematurely for concrete with Type III cement, achieving high levels of damage with expressive expansions, of about 1% at one year. As to concrete tested with Type IP cement it was noted just a time delay on the expansive and deterioration process caused by DEF, due to the presence of fly-ash. Notwithstanding, elasticity modulus and SDT indexes were not yet affected up to one year, the high level of expansions detected (0.25%) has already led this concrete to damages reflected in the strength at one year and important proofs of the presence of massive ettringite and microcracking associated to DEF by microstructural analysis indicating internal deterioration and the potential progress of DEF over time.

In brief, the performance and durability of concrete structures in the field depends on several factors, including the type of cement, and premature tests for DEF in the laboratory, even in concrete, can promote false-negative results and risks of high levels of damage due to the expansive behavior of this phenomenon. The expansive suppression mechanisms by fly-ash are complex and still limited for DEF phenomenon. A specific topic related to expansive mechanisms, such as DEF, must be included in the design phase and an appropriate technological control during the production, curing and placing of concretes are mandatory.

## ACKNOWLEDGEMENTS

This work had financial and infrastructure support from Furnas Centrais Elétricas S.A./ANEEL, P&D 0394-1504-2015. D. Schovanz benefits from a partial scholarship financed by the Research Foundation of the State of Rio Grande do Sul - FAPERGS by the FAPERGS Grant.

## REFERENCES

[1] H. F. W. Taylor, C. Famy, and K. L. Scrivener, "Delayed ettringite formation," *Cement Concr. Res.*, vol. 31, no. 5, pp. 683–693, 2001, http://dx.doi.org/10.1016/S0008-8846(01)00466-5.

[2] M. Collepardi, "A state-of-the-art review on delayed ettringite attack on concrete," *Cement Concr. Compos.*, vol. 25, no. 4-5, pp. 401–407, 2003, http://dx.doi.org/10.1016/S0958-9465(02)00080-X.

[3] Y. Gu, R.-P. Martin, O. Omikrine Metalssi, T. Fen-Chong, and P. Dangla, "Pore size analyses of cement paste exposed to external sulfate attack and delayed ettringite formation," *Cement Concr. Res.*, vol. 123, pp. 105766, 2019, http://dx.doi.org/10.1016/j.cemconres.2019.05.011.

[4] A. Pichelin, M. Carcassès, F. Cassagnabère, S. Multon, and G. Nahas, "Sustainability, transfer and containment properties of concrete subject to delayed ettringite formation (DEF)," *Cement Concr. Compos.*, vol. 113, pp. 103738, 2020, http://dx.doi.org/10.1016/j.cemconcomp.2020.103738.

[5] P. K. Mehta and P. J. M. Monteiro, *Concreto: Estrutura, Propriedades e Materiais.* 2. ed. São Paulo: IBRACON, 2014.

[6] L. F. M. Sanchez, T. Drimalas, B. Fournier, D. Mitchell, and J. Bastien, "Comprehensive damage assessment in concrete affected by different internal swelling reaction (ISR) mechanisms," *Cement Concr. Res.*, vol. 107, pp. 284–303, 2018, http://dx.doi.org/10.1016/j.cemconres.2018.02.017.

[7] L. F. M. Sanchez, T. Drimalas, and B. Fournier, "Assessing condition of concrete affected by internal swelling reactions (ISR) through the Damage Rating Index (DRI)," *Cement*, vol. 1-2, 100001, 2020, http://dx.doi.org/10.1016/j.cement.2020.100001.

[8] W. Deboucha, N. Leklou, A. Khelidj, and O. Plé, "Combination effect of limestone filler and slag on delayed ettringite formation in heat-cured mortar," *J. Mater. Civ. Eng.*, vol. 32, 04019365, 2020.

[9] C. S. Poon, L. Lam, and Y. L. Wong, "A study on high strength concrete prepared with large volumes of low calcium fly ash," *Cement Concr. Res.*, vol. 30, pp. 447–455, 2000.

[10] W. H. R. S. Dayarathne, G. S. Galappaththi, K. E. S. Perera, and S. M. A. Nanaykkra, “Evaluation of the potential for delayed ettringite formation in concrete,” in *Proc. 19th ERU Symp*., Moratuwa, Sri Lanka, 2013.

[11] V. H. Nguyen, N. Leklou, J.-E. Aubert, and P. Mounanga, "The effect of natural pozzolan on delayed ettringite formation of the heat-cured mortars," *Constr. Build. Mater.*, vol. 48, pp. 479–484, 2013., http://dx.doi.org/10.1016/j.conbuildmat.2013.07.016.

[12] Y. Amine, N. Leklou, and O. Amiri, "Effect of supplementary cementitious materials (SCM) on delayed ettringite formation in heat-cured concretes," *Energy Procedia*, vol. 139, pp. 565–570, 2017, http://dx.doi.org/10.1016/j.egypro.2017.11.254.

[13] N. Leklou, V. Nguyen, and P. Mounanga, "The effect of the partial cement substitution with fly ash on Delayed Ettringite Formation in heat-cured mortars," *KSCE J. Civ. Eng.*, vol. 21, no. 4, pp. 1359–1366, 2017., http://dx.doi.org/10.1007/s12205-016-0778-9.

[14] Y. Zhang, Y. Pan, and D. Zhang, "A literature review on delayed ettringite formation: mechanism, affect factors and suppressing methods," *Mag. Concr. Res.*, vol. 73, no. 7, pp. 325–342, 2021.

[15] J. L. Bronholo, “Estudo do ataque individual e misto de DEF e RAA e de seus efeitos deletérios nas propriedades físico-químicas e mecânicas de concretos e argamassas de cimento Portland pozolânico e de alta resistência,” M.S. thesis, Inst. Tecnol. Desenvolv – LACTEC, 2020.

[16] D. Schovanz, “Study on delayed ettringite formation (DEF) in concretes with Portland-pozzolan cement and high early strength Portland cement,” M.S. thesis, Fac. Meridional, Passo Fundo, 2019.

[17] Y. K. Ramu, V. Sirivivatnanon, P. Thomas, Y. Dhandapani, and K. Vessalas, "Evaluating the impact of curing temperature in delayed ettringite formation using electrochemical impedance spectroscopy," *Constr. Build. Mater.*, vol. 282, pp. 122726, 2021, http://dx.doi.org/10.1016/j.conbuildmat.2021.122726.

[18] M. Jebli, F. Jamin, C. Pelissou, E. Lhopital, and M. S. E. Youssoufi, "Characterization of the expansion due to the delayed ettringite formation at the cement paste-aggregate interface," *Constr. Build. Mater.*, vol. 289, pp. 122979, 2021, http://dx.doi.org/10.1016/j.conbuildmat.2021.122979.

[19] E. R. Giannini, L. F. M. Sanchez, A. Tuinukuafe, and K. J. Folliard, "Characterization of concrete affected by delayed ettringite formation using the stiffness damage test," *Constr. Build. Mater.*, vol. 162, pp. 253–264, 2018, http://dx.doi.org/10.1016/j.conbuildmat.2017.12.012.

[20] T. Ahmed, E. Burley, S. Rigden, and A. I. Abu-Tair, "The effect of alkali reactivity on the mechanical properties of concrete," *Constr. Build. Mater.*, vol. 17, no. 2, pp. 123–144, 2003.

[21] A. Pavoine, X. Brunetaud, and L. Divet, "The impact of cement parameters on Delayed Ettringite Formation," *Cement Concr. Compos.*, vol. 34, no. 4, pp. 521–528, 2012, http://dx.doi.org/10.1016/j.cemconcomp.2011.11.012.

[22] X. Brunetaud, L. Divet, and D. Damidot, "Impact of unrestrained Delayed Ettringite Formation-induced expansion on concrete mechanical properties," *Cement Concr. Res.*, vol. 38, no. 11, pp. 1343–1348, 2008, http://dx.doi.org/10.1016/j.cemconres.2008.05.005.

[23] L. F. M. Sanchez, B. Fournier, M. Jolin, M. J. Bastien, and D. Mitchell, "Practical use of the Stiffness Damage Test (SDT) for assessing damage in concrete infrastructure affected by alkali-silica reaction," *Constr. Build. Mater.*, vol. 125, pp. 1178–1188, 2016, http://dx.doi.org/10.1016/j.conbuildmat.2016.08.101.

[24] J. Jeong, H. Ramézani, and N. Leklou, "Porous-micro-dilatation theory for random crystallization: Monte Carlo simulation for delayed ettringite formation," *Acta Mech.*, vol. 228, no. 9, pp. 3223–3249, 2017., http://dx.doi.org/10.1007/s00707-017-1863-y.

[25] J. F. Seignol, O. Omikrine-Metalssi, N. Baghdadi, and F. Toutlemonde, “From AAR to DEF: numerical modeling of structures affected by expansive reactions in concrete,” in *Proc. 14th Int. Conf. on AAR Concr.*, 2012.

[26] L. F. M. Sanchez, T. Drimalas, B. Fournier, D. Mitchell, and J. Bastien, "Comprehensive damage assessment in concrete affected by different internal swelling reaction (ISR) mechanisms," *Cement Concr. Res.*, vol. 107, pp. 284–303, 2018, http://dx.doi.org/10.1016/j.cemconres.2018.02.017.

[27] M. M. Karthik, J. B. Mander, and S. Hurlebaus, "Simulating behaviour of large reinforced concrete beam-column joints subject to ASR/DEF deterioration and influence of corrosion," *Eng. Struct.*, vol. 222, pp. 111064, 2020, http://dx.doi.org/10.1016/j.engstruct.2020.111064.

[28] M. Thomas, K. Folliard, T. Drimalas, and T. Ramlochan, "Diagnosing delayed ettringite formation in concrete structures," *Cement Concr. Res.*, vol. 38, no. 6, pp. 841–847, 2008, http://dx.doi.org/10.1016/j.cemconres.2008.01.003.

[29] B. Godart and L. Divet, “Lessons learned from structures damaged by delayed ettringite formation and the French prevention strategy,” in *Proc. 5th Int. Conf. Forensic Eng.*, France, 2013.

[30] N. P. Hasparyk, S. C. Kuperman, and J. R. Torres Combined attack from ARS and DEF in the foundation,” in *Proc. 15th Int. Conf. Alkali Aggregate React. Concr.*, São Paulo, 2016.

[31] Y. Kawabata, N. Ueda, T. Miura, and S. Multon, "The influence of restraint on the expansion of concrete due to delayed ettringite formation," *Cement Concr. Compos.*, vol. 121, pp. 104062, 2021, http://dx.doi.org/10.1016/j.cemconcomp.2021.104062.

[32] S. K. Melo, "Study of delayed ettringite formation in Portland cement by hydration heat," M.S. thesis, Univ. Fed. Goiás, Goiânia, 2010.

[33] Y. Fu, "Delayed Ettringite Formation in Portland cement products," Ph.D. dissertation, Univ. Ottawa, Ottawa, 1996.

[34] M. Rashidi, A. Paul, J.-Y. Kim, L. J. Jacobs, and K. E. Kurtis, "Insights into delayed ettringite formation damage through acoustic nonlinearity," *Cement Concr. Res.*, vol. 95, pp. 1–8, 2017, http://dx.doi.org/10.1016/j.cemconres.2017.02.004.

[35] S. Bauer, B. Cornell, D. Figursky, T. Ley, J. Miralles, and K. Folliard, *Alkali-Silica Reaction and Delayed Ettringite Formation in Concrete: a Literature Review. Report: Project Performed in Cooperation with the Texas Department of Transportation and the Federal Highway Administration*. Austin: Center Transp. Res, Univ. Texas, 2006.

[36] B. Kchakech, R. P. Martin, O. O. Metalssi, J. C. Renaud, L. Baron, and F. Toutlemonde, "Effect of temperature and curing duration of early heat treatments on the risk of expansion associated with delayed ettringite formation," in *Proc. 15th Int. Conf. Alkali Aggregate React. Concr.*, São Paulo, 2016.

[37] R. P. Martin, L. F. M. Sanchez, B. Fournier, and F. Toutlemonde, "Evaluation of different techniques for the diagnosis and prognosis of Internal Swelling Reaction (ISR) mechanisms in concrete," *Constr. Build. Mater.*, vol. 156, pp. 956–964, 2017, http://dx.doi.org/10.1016/j.conbuildmat.2017.09.047.

[38] V. H. Nguyen, N. Leklou, and P. Mounanga, "The development of accelerated test method for internal sulfate attack by delayed ettringite formation," *Mater. Sci. Forum*, vol. 987, pp. 27–32, 2020, http://dx.doi.org/10.4028/www.scientific.net/MSF.987.27.

[39] N. P. Hasparyk, "Investigation of concretes affected by alkali-aggregate reaction and advanced characterization of exuded gel," Ph.D. dissertation, Univ. Fed. Rio Grande do Sul, Porto Alegre, 2005.

[40] J. Sun and Z. Chen, "Influences of limestone powder on the resistance of concretes to the chloride ion penetration and sulfate attack," *Powder Technol.*, vol. 338, pp. 725–733, 2018, http://dx.doi.org/10.1016/j.powtec.2018.07.041.

[41] N. P. Hasparyk, D. Schovanz, and S. C. Kuperman, *Instrução Técnica Furnas no GSTE004R0 – Método de Ensaio para a Avaliação do Potencial de Ocorrência da Etringita Tardia (DEF) em Concreto*. Ed. Furnas, 2020.

[42] American Society for Testing and Materials, *Standard Test Method for Chemical Analysis of Hydraulic Cement*, ASTM C 150, 2008.

[43] American Society for Testing and Materials, *Standard Test Method for Potential Alkali Reactivity of Aggregates (Mortar-Bar Method)*, ASTM C 1260, 2018.

[44] Associação Brasileira de Normas Técnicas, *Agregados – Reatividade Álcali-Agregado - Parte 1: Guia para Avaliação da Reatividade Potencial e Medidas Preventivas para Uso de Agregados em Concreto*, ABNT 15577-1, 2018.

[45] E. Adamopoulou, P. Pipilikaki, M. S. Katsiotis, M. Chaniotakis, and M. Katsioti, "How sulfates and increased temperature affect Delayed ettringite formation (DEF) in white cement mortars," *Constr. Build. Mater.*, vol. 25, no. 8, pp. 3583–3590, 2011, http://dx.doi.org/10.1016/j.conbuildmat.2011.03.051.

[46] K. Ma, G. Long, and Y. Xie, "A real case of steam-cured concrete track slab premature deterioration due to ASR and DEF," *Case Stud. Constr. Mater.*, vol. 6, pp. 63–71, 2017, http://dx.doi.org/10.1016/j.cscm.2016.12.001.

[47] D. G. Batista, "Investigation of concrete deterioration from HPPs by reactions involving aggregates," M.S. thesis, Univ. Fed. Goiás, Goiânia, 2013.

[48] Z. Zhang, Q. Wang, H. Chen, and Y. Zhou, "Influence of the initial moist curing time on the sulfate attack resistance of concretes with different binders," *Constr. Build. Mater.*, vol. 144, pp. 541–551, 2017, http://dx.doi.org/10.1016/j.conbuildmat.2017.03.235.

[49] A. Blanco, F. Pardo-Bosch, S. Cavalaro, and A. Aguado, "Lessons learned about the diagnosis of pathologies in concrete dams: 30 years of research and practice," *Constr. Build. Mater.*, vol. 197, pp. 356–368, 2019, http://dx.doi.org/10.1016/j.conbuildmat.2018.11.143.

[50] D. Schovanz et al., "Evaluation of delayed ettringite formation through physical, mechanical, and microstructural assays," *ACI Mater. J.*, vol. 118, no. 1, pp. 101–109, 2021, http://dx.doi.org/10.14359/51728282.

[51] B. Godart, "Pathology, assessment and treatment of structures affected by Delayed Ettringite Formation," *Struct. Eng. Int.*, vol. 27, no. 3, pp. 362–369, 2017., http://dx.doi.org/10.2749/101686617X14881932436771.

[52] M. Al Shamaa, S. Lavaud, L. Divet, J. B. Colliat, G. Nahas, and J. M. Torrenti, "Influence of limestone filler and of the size of the aggregates on DEF," *Cement Concr. Compos.*, vol. 71, pp. 175–180, 2016, http://dx.doi.org/10.1016/j.cemconcomp.2016.05.007.

[53] Y. Thiebaut et al., "Effects of stress on concrete expansion due to delayed ettringite formation," *Constr. Build. Mater.*, vol. 183, pp. 626–641, 2018, http://dx.doi.org/10.1016/j.conbuildmat.2018.06.172.

[54] W. H. Price, "Factors influencing concrete strength," *J. Proc.*, vol. 47, pp. 417–432, 1951.

[55] S. K. Melo, N. P. H. Hasparyk, H. Carasek, H. H. Silva, and C. Martins, "Influence of temperature on microstructure of pozzolanic Portland cement paste and the delayed ettringite formation (DEF)," in *An. 54º Cong. Bras. Concr.*, Alagoas, 2012.

[56] Associação Brasileira de Normas Técnicas, *Design of Concrete Structures – Procedure*, ABNT NBR 6118, 2014.

[57] American Concrete Institute, *Building Code Requirements for Structural Concrete*, ACI 318-14, 2014.

[58] E. R. Giannini, “Evaluation of concrete structures affected by alkali-silica reaction and delayed ettringite formation,” Ph.D. dissertation, Univ. Texas, Austin, 2012.

[59] N. Smaoui, M.-A. Bérubé, B. Fournier, B. Bissonnette, and B. Durand, "Evaluation of the expansion attained to date by concrete affected by alkali–silica reaction. Part I: experimental study," *Can. J. Civ. Eng.*, vol. 31, no. 5, pp. 826–845, 2004, http://dx.doi.org/10.1139/l04-051.

[60] M. O. G. P. Bragança, N. P. Hasparyk, J. L. Bronholo, A. S. Silva, K. F. Portella, and S. C. Kuperman, "Electrochemical impedance spectroscopy and ultrasound for monitoring expansive reactions and their interactions on cement composites," *Constr. Build. Mater.*, vol. 305, pp. 124726, 2021, http://dx.doi.org/10.1016/j.conbuildmat.2021.124726.

[61] A. S. Silva, A. B. Ribeiro, L. Divet, “Prevention of internal sulphate reaction in concrete: long-term results of the effect of mineral additions,” in *Proc. 16th Int. Conf. Alkali Aggregate React. Concr.* Lisboa, vol.1, 2021.

**Author contributions:** NPH: conceptualization, methodology, SDT and microstructural analyses, writing, global analyses, discussion, supervision, reviewing, funding acquisition; DS: formal analysis, methodology, writing; FT: conceptualization, formal analysis, methodology, writing, supervision; SCK: conceptualization, methodology, supervision, reviewing.

**Editors:** Bruno Briseghella, Guilherme Aris Parsekian.

IBRACON Structures and Materials Journal
Revista IBRACON de Estruturas e Materiais
ISSN 1983-4195 ismj.org

ORIGINAL ARTICLE

# Experimental study of shear transfer in slim floor systems using precast concrete hollow core slabs and steel beam with web circular opening

## *Estudo experimental da transferência de forças de cisalhamento em pisos mistos de pequena altura com lajes pré-fabricadas de concreto e viga em aço com abertura circular na alma*

Gustavo Coldebella[a]
Sineval Esteves Pereira Junior[a]
Silvana De Nardin[a]

[a]Universidade Federal de São Carlos – UFSCar, Programa de Pós-Graduação em Engenharia Civil – PPGECiv, São Carlos, SP, Brasil

Received 26/02/2021
Accepted 20/10/2021

**Abstract:** Steel-concrete slim flooring system using precast concrete hollow core slabs and steel beam with web openings is an innovative construction system designed to combine the high bending resistance of both precast prestressed hollow core slabs and steel beam with web openings. This system can provide floor systems with a minimum constructional depth in comparison with ordinary composite floors. The aim of this study was to evaluate in an exploratory way the shear transferring mechanism between the steel beam with circular web opening and the precast hollow-concrete slab. The shear connection is formed by in-situ concrete passes through the web openings and infill the voids of the precast slabs. One push-out test was conducted to investigate the shear transferring mechanism of shear connection and the experimental results were compared to analytical methods. The shear resistance of the shear connection was predicted with good accurate by analytical methods.

**Keywords:** slim floor, push-out test, concrete hollow core slabs, beam with web opening, shear connection.

**Resumo:** Piso misto de pequena altura com lajes alveolares e viga em aço com aberturas na alma é um tipo inovador de sistema construtivo projetado para aliar o alto desempenho estrutural das lajes pré-fabricadas de concreto protendido e das vigas em aço com aberturas na alma, proporcionando um pavimento de altura reduzida, comparado aos pisos convencionais. Este artigo tem como objetivo avaliar de forma exploratória a contribuição do efeito de pino de concreto como dispositivo mecânico de conexão entre a seção de aço e a laje de concreto. A análise foi realizada com base no resultado experimental de um ensaio de cisalhamento direto, que simula uma tipologia de conexão ao cisalhamento em pisos mistos com lajes alveolares de concreto e viga em aço com abertura circular na alma. Os resultados foram comparados com métodos analíticos. A capacidade resistente da conexão de cisalhamento apresentou boa aproximação com os valores previstos por métodos analíticos.

**Palavras-chave:** piso misto de pequena altura, ensaio de cisalhamento direto, lajes alveolares pré-moldadas de concreto protendido, viga com abertura na alma, estrutura mista.

**How to cite:** G. Coldebella, S. E. Pereira Junior, and S. De Nardin, "Experimental study of shear transfer in slim floor systems using precast concrete hollow core slabs and steel beam with web circular opening," *Rev. IBRACON Estrut. Mater.*, vol. 15, no. 3, e15306, 2022, https://doi.org/10.1590/S1983-41952022000300006

**Corresponding author:** Sineval E. Pereira Junior. E-mail: sineval@estudante.ufscar.br
**Financial support:** This study was financed in part by the Coordenação de Aperfeiçoamento de Pessoal de Nível Superior – Brasil (CAPES) Finance Code 001.
**Conflict of interest:** Nothing to declare.
**Data Availability:** The data that support the findings of this study are available from the author, SDN, upon request.

## 1 INTRODUCTION

Recently, multistorey buildings have demanded solutions that combine structural efficiency to overcome long spans, economical construction and high productivity of construction processes [1]. The slim floor system is an innovative steel-concrete composite floor where the slab is supported on the lower flange of the steel beam resulting in a floor system with a minimum depth. This type of floor system can be composed by precast hollow core slabs and steel beam with circular web openings. The circular web openings of both, steel beam and precast hollow core units offer passage for the in-situ concrete creating interaction between the components and resulting in a composite section. Among the several types of composite floor systems, it is possible to highlight two configurations whose main difference is the position of the slab in relation to the beam. In conventional composite floor (Fig. 1a), the slab is supported on the top flange of the steel beam and the composite behavior is created by shear connectors welded on the top flange. In the composite slim floor system, the slab is embedded in the height of the steel beam resulting in flat appearance. The slim floor system (Fig. 1b) has advantages as height lower than the conventional composite floor, building service passage and fast construction. Both composite floor, conventional and slim floor, can be used several types of steel beams and slabs. Monosymmetric steel section with sequential web openings can be used in slim floor system; the behavior of this steel section depends on the shape and size of the openings. The choose of the better shape and size of the openings is based on the structural performance and saving materials. Sections with castellated and cellular openings are made by cutting the original steel profile longitudinally resulting in two parts. Then, these parts are welding together in a new configuration where the flanges are farther apart. The castellated beams have repeating hexagonal web openings, and this can increase the height of the original profile by two thirds, depending on the dimensions of the opening. Cellular beams are characterized by circular web openings allowing greater variety of spacing and diameters of the openings [2]. Moreover, the circular opening shape are suitable to pass building services.

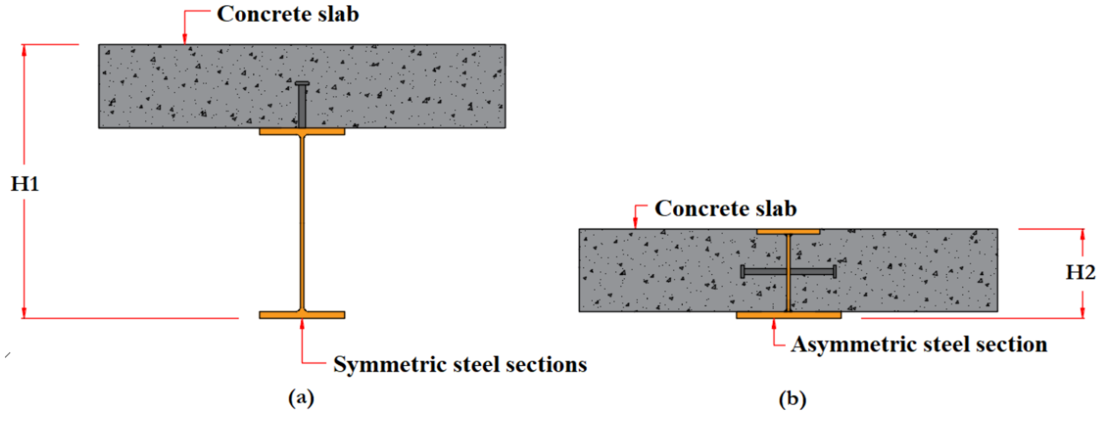


Fig. 1: Composite beam section – (a) conventional composite beam; (b) composite slim floor

The key feature of the composite slim floor system is that the steel cellular beam are contained within the concrete resulting in a system less susceptible to the local instabilities [3]. The concrete passing through the circular web openings of the steel profile provides the shear connection transferring the longitudinal forces between the components of the composite slim floor system. The infill concrete can be combined to with the additional steel reinforcing bar to increase the steel-concrete interaction. As the steel profile is embedded, partially or completely in the concrete, the steel-concrete shear connection is the result of concrete infill elements interact with web and steel reinforcing bar, associated with the bonding effect at the steel-concrete interface. The virtual shear connector to transfer the steel-concrete shear forces is different from conventional mechanisms [4].

In the composite slim floor system, the steel profile can be combines with several types of slabs. Solid concrete slabs, composite slabs with profiled steel decking (Fig. 2a) and prestressed hollow core slabs (Fig. 2b) are employed in slim floor systems. In comparison with the composite slim floor with composite slab, the use of pre-prestressed hollow core slabs increases the degree of industrialization and reduces the cast-in-place concrete.

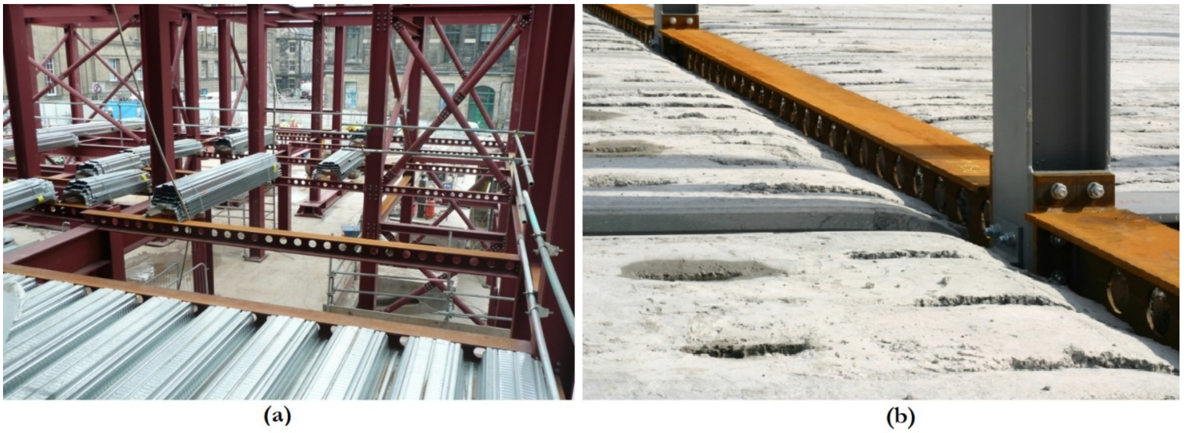


Fig. 2: Slim floor construction – (a) Steel decking [5]; (b) Precast hollow core slabs [6]

In summary, composite floor system formed by steel beam with web circular openings and precast hollow-core slabs can be an interesting structural solution. However, compared to conventional composite floor systems, there are several aspects of the structural behavior need to be investigated.

The main aim of this study is to analyze the shear connection provide by the through concrete in the large web opening of the steel beam, which forms an effect of concrete dowel. Studies of shear transfer mechanisms in composite slim floor systems with precast slabs often replace the precast slab by solid slabs. The innovation of this study is the precast slab that was included in the push out test. The exploratory study is based on experimental results of a push-out test. The geometry of specimen was developed taking account the Eurocode 4 [7]. The tested specimen represents a composite slim floor system formed by precast hollow-core slab and steel beam with web circular openings. The experimental results were compared with analytical methods developed to predict the shear resistance of shear connection.

## 2 SHEAR TRANSFERRING MECHANISM ON COMPOSITE SLIM FLOOR SYSTEM

The composite slim floor formed by precast hollow core slabs and steel beam with web circular openings takes advantage of the concrete filling the slab voids to shear forces transfer at the steel-concrete interface. The concrete passes through the web openings profile, completely filling the web openings and greatly contributing to the transfer of shear forces between the steel profile and the concrete slab. The steel beam with web circular openings is partially embedded in the concrete. Due this, the steel-concrete interaction is attributed to by concrete dowel effect (Fig. 3) or both, the concrete dowel and the steel bars immersed in the slab-beam opening. Different of shear transferring mechanisms promoted by the headed studs, in the composite slim floor the mechanism is formed by both, the concrete passing through the web openings of steel profile and tie bars.

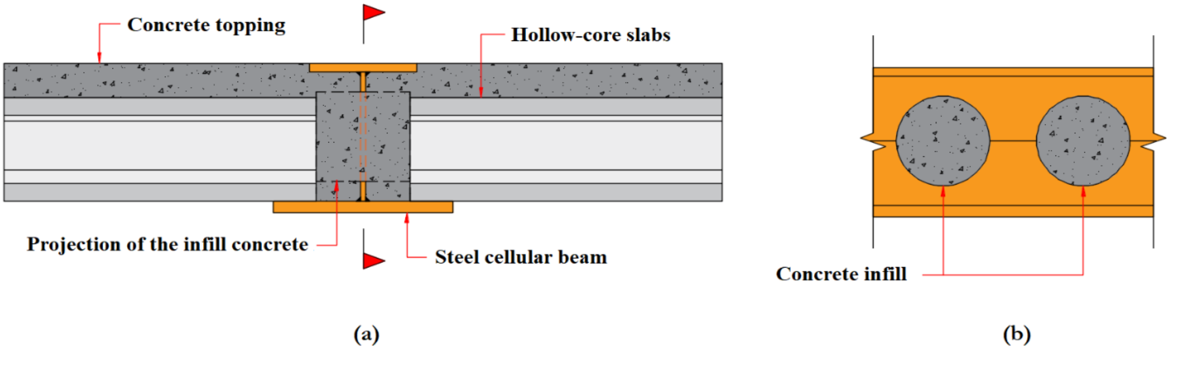


Fig. 3: Slim floor with precast hollow core slab and steel beam with web circular openings – (a) Cross section; (b) Section A - A

The shear transfer at the first stages of loading is due to mechanisms such as chemical adhesion, friction and local compression, which are generated in the contact zone between components [4]. The steel profile is subjected to a longitudinal shear stress that induces bending and shear stresses in the section. With the load is increased, the shear resistance of the infill concrete in the web opening will be reached, and there may be a large slip at the interface between the steel beam and the concrete slab (Fig. 4), followed by the start of concrete cracking [4]. The transverse reinforcement embedded in concrete can contribute to improving the steel-concrete connection after cracking the slab [4]. The load continues increasing and causes the crack evolution process. At this stage, the transverse reinforcement resists the internal tensile stresses increasing the strength capacity of the shear connection and contributing to the redistribution of internal forces between the concrete slab and the steel beam.

The transverse reinforcement embedded in the concrete contributes is significant to the steel-concrete shear connection, however its use is not mandatory. Within this system, in which most of the beam is embedded in concrete, the bond shear resistance is enhanced significantly with the virtual concrete dowel formed by in-situ concrete passes through the continuous void of the slab and the web opening and fills the voids.

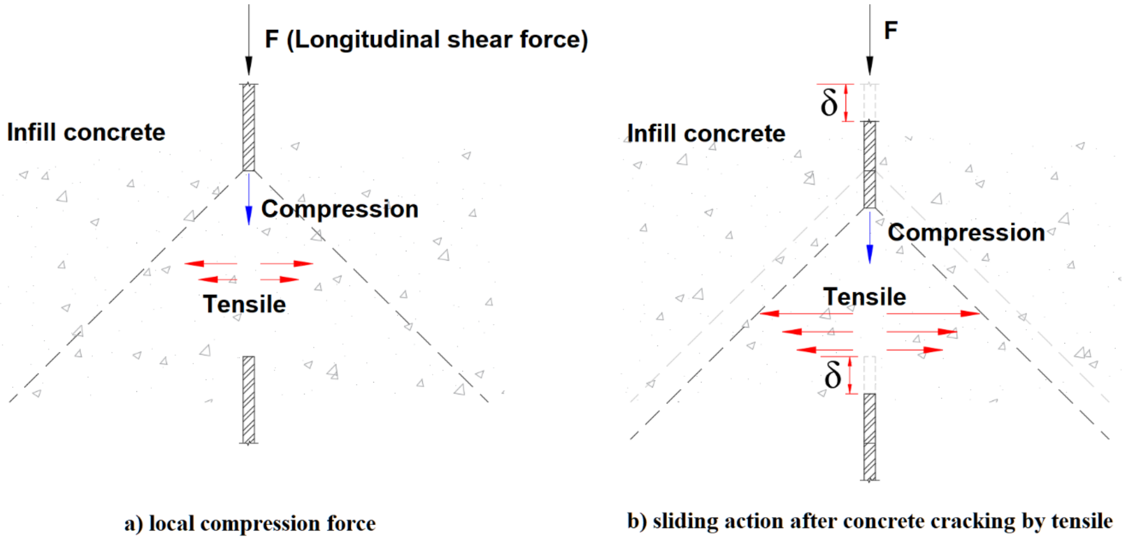


Fig. 4: Mechanism of transferring longitudinal force in shear connection – (a) Local compression force; (b) sliding action after concrete cracking by tensile

The push-out test [7] is the most common way to investigate the shear transferring mechanisms; the steel-concrete interface is evaluated under the direct longitudinal shear force. The ability of steel-concrete connection to transfer the longitudinal shear force and the contribution of mechanisms to controlling the slip at the steel-concrete interface can be evaluated in this type of test.

The Load vs. Slip response is very useful to evaluate the steel-concrete shear strength and connection ductility. Although the geometry of the specimen recommended by Eurocode 4 [7] is very different of the composite slim floor system, it was taken as the starting point to the present study. This is very common and employed for several researchers. For example, the shear transferring mechanisms in slim floor system comprising steel profile and prestressed concrete hollow core slabs was investigated by push-out tests [8]. The steel-concrete connection was provided by headed shear studs. The modified geometry was adequate to investigate the shear resistance and the ductility of the steel-concrete connection [8]. Regarding the steel-concrete transfer mechanism in composite slim floor formed by steel beam and solid slab between the profile flanges, several push-out test results were reported by Huo and D'Mello [9]. The chemical bond of steel-concrete was reduced applying grease on the surface of the steel profile in contact with the concrete. Two types of shear connection were investigated: concrete dowel (in-situ concrete completely fills the web openings) and the combination of concrete dowel and tie bars. The push-out test results had led to the development of a design method to estimate the shear resistance of the shear connection. This method is described in item 2.1.

In the present study the tested specimen is formed by a steel profile with circular web opening and precast hollow core concrete slabs. This difference in relation to the other studies introduces a series of complications in the assemblage of the specimen. Despite this, the specimen properly represents each component of the composite slim floor system.

This study is important because there is a lack of studies about composite slim floor system including the precast concrete slab and the steel profile with web opening.

### 2.1 Shear resistance capacity of shear connection

Huo and D'Mello [9] developed an analytical procedure to estimate the shear resistance of the concrete infill element based on the failure mechanisms founded in the push-out tests. The failure mechanism was thus described: the top section of concrete infill was crushed by the web in shear direction and the other part of the concrete infill was ruptured by tensile splitting in the transverse direction [9]. The procedure combines both the compressive and tensile resistance (Table 1). Chen et al. [10] also developed an analytical procedure whose coefficients applied on compressive and tensile resistance of concrete infill element are the main difference in relation to Huo and D'Mello [9].

According to Chen et al. [10], the values 1.68 and 1.44 suggested by Huo and D'Mello [9]should be replaced respectively, by 1.30 and 1.15 when the slim floor is formed by composite decking and steel beam with web circular openings. A summary of design procedures [9, 10] is shown in Table 1. The numerical coefficients (Table 1) on compressive and tensile resistance were determined from a set of tests carried out by Huo and D'Mello [9] and Chen et al. [10].

**Table 1:** Analytical procedures for shear longitudinal resistance

| **Huo and D'Mello [9]** | **Chen et al. [10]** |
|---|---|
| Resistance force for one concrete dowel | |
| $R_c = 1.68 \cdot (f_{cu} \cdot A_c) + 1.44 \cdot (f_{ctm} \cdot A_t)$ | $R_c = 1.30 \cdot (f_{cu} \cdot A_c) + 1.15 \cdot (f_{ctm} \cdot A_t)$ |

Where $R_c$ is Shear resistance of the shear connection, $f_{cu}$ and $f_{ctm}$ arethe concrete compressive cube strength of concrete and the concrete tensile splitting strength, , respectively; $A_c$ is the area of concrete infill in the compression ($A_c$=$t_w$.$d_o$), $A_t$ is the area of concrete infill in the tensile splitting ($A_t$= $\frac{\pi d_0{}^2}{4}$ ), $d_o$ is the diameter of circular web openings and $t_w$ is the web thickness.

A coefficient equal to 0.84 was obtained by Tran and Graubner [11] to convert the compressive strength from standard cylinder specimens to cube compressive strength and was applied in the present study.

## 3 EXPERIMENTAL PROGRAM

A specimen representing a composite slim floor system formed by a steel beam with one web circular opening and precast hollow core slabs was subjected to direct monotonic shear force. The Load *vs*. Slip behavior was obtained because of the push-out test. In the tested specimen the shear connection was only formed by the in-situ concrete completely fills the web opening without any additional steel bar. Therefore, the effect of concrete dowels was the main mechanism to resist the longitudinal shear.

### 3.1 Specimens

The tested specimen was composed by a steel profile with a circular web and precast hollow-core slabs. The circular opening was placed in the in the middle of the web height. (Fig. 5a). The geometry of the specimen was chosen taking the Eurocode 4 [7] as a reference. However, there are no specific recommendations for composite slim floor in Eurocode 4 [7].

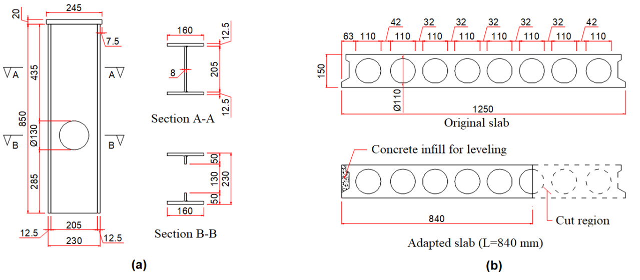


Fig. 5: Geometry of components – (a) Steel beam with web circular opening; (a) hollow core slab [mm]

For this reason, the geometry of specimen was adjusted according to the characteristics of the slim floor. The position of the voids in precast slab and the shear connection mechanism were decisive factors to define the geometry. Fig. 5 and Fig. 6 given the geometry of specimen and the test setup. Recommendations of Lawson and Hicks [12] and the catalogue of ArcelorMittal [13] helped to select the geometry of the steel profile, including the opening diameter. The size of web openings was taken equal to 130 mm (Fig. 5a). The precast hollow-core concrete units (Fig. 5b) were donated by the company CASSOL Pré-fabricados LTDA. Some adjustments in the precast concrete units were necessary to match one of the slab voids with the circular opening of the steel profile (Fig. 5b). To regularize the slab edges which act as support during the test, the cut end was performed with industrialized grout (Fig. 5b). The bond between the steel and concrete was reduced with the use of grease on the surface of the steel profile before casting with concrete. The contribution of the adhesion for the shear transferring mechanism was decreased using this procedure.

The slab voids were filled with high fluidity in-situ concrete, in which only gravel 0 (granulometry 4.8 mm to 9.5 mm) was used as coarse aggregate. All the voids of slabs were filled with in-situ concrete; however only one of them matches with the circular web opening of the steel profile. Hence, the shear resistance and behavior of the concrete dowel could be investigated.

The welded steel beam was fabricated by ASTM A36 and the main properties of the steel were determined by means of characterization tests carried out in accordance with ASTM E8/E8M-09 [14]. Mechanical properties of steel, concrete of precast slabs and in-situ concrete are given in Table 2. The elasticity modulus of steel was assumed equal to 200 GPa [15]. The concrete strength of the precast hollow-core slabs was provided by the manufacturer (Table 2). The other properties of the precast slabs were estimated from the prescriptions of ABNT NBR6118 [16].

**Table 2:** Material properties

| | **Steel beam** | | |
|---|---|---|---|
| **Component** | **Modulus of elasticity [GPa]** | **Yield strength [MPa]** | **Ultimate strength [MPa]** |
| Top and bottom flange | 200$^{(1)}$ | 298.85$^{(2)}$ | 421.52$^{(2)}$ |
| web | 200$^{(1)}$ | 309.25$^{(2)}$ | 428.99$^{(2)}$ |
| | **Concrete slab** | | |
| **Type** | **Modulus of elasticity [GPa]** | **Cylinder compressive strength [MPa]** | **Tensile strength [MPa]** |
| Hollow core slab | 35.42$^{(3)}$ | 40$^{(3)}$ | 3.51$^{(3)}$ |
| Infill concrete | 27.41$^{(2)}$ | 34.06$^{(2)}$ | 2.28$^{(2)}$ |

$^{(1)}$: theoretical values. $^{(2)}$: experimental values. $^{(3)}$: values provided by the manufacturer of the precast concrete slab

### 3.2 Instrumentation and test setup

The push-out test was performed on a static hydraulic jack of 1500kN capacity. A static vertical load was applied on the top end of the steel profile and vertical reactions on the base of the concrete slab allowed for the transfer of direct force to the shear connection by downward movement of the steel profile in load direction (Fig. 6d). The test was displacement-controlled, and the vertical load was continuously until the failure. The test was conducted in the Structures Laboratory of Engineering School at São Carlos/USP.

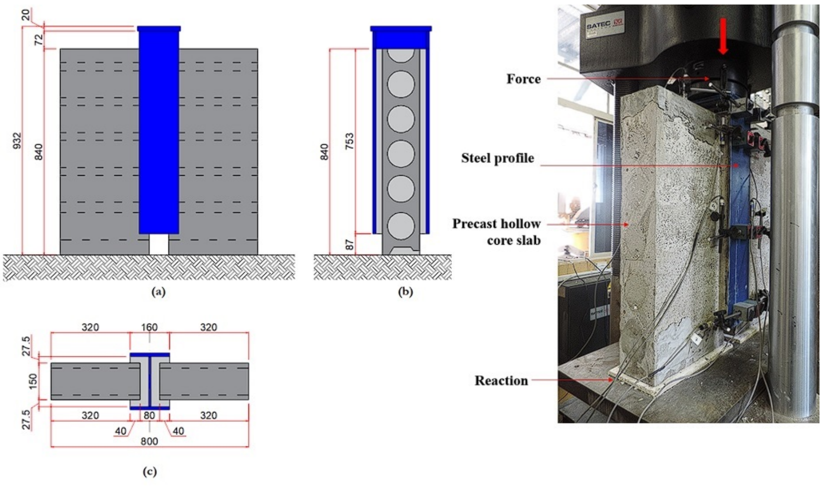


Fig. 6: Geometrical characteristics of composite cross-sections and setup of push out test - (a) Frontal view; (b) lateral view; (c) top view; (d) overview [mm]

Six displacement transducers were positioned along the specimen to measure the relative displacements at the steel profile in relation to the precast concrete slab (Fig. 7c). The relative displacements were measure at the upper and lower ends of the hollow-core slab, on both sides (Fig. 7a). In Fig. 7, S and I indicate upper and lower, respectively; E and D are the left and right faces of the vertical axis of the steel profile, respectively. The letter C refers to the half-height section and the numbers 1, 2 and 3 are the positions; 1: left, 2: center and 3: right (Fig. 7b).

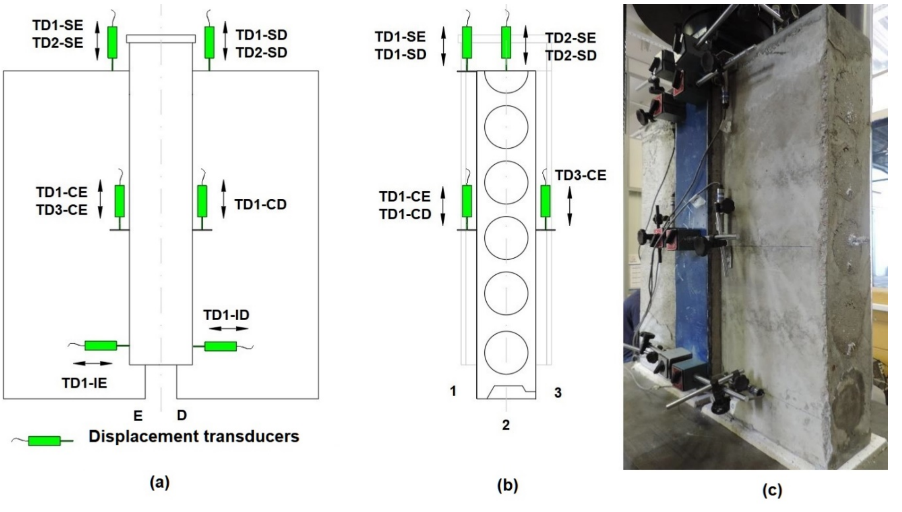


Fig. 7: Test setup and instrumentations of the push-out tests – (a) Frontal view; (b) lateral view; (c) Instrumented specimen

## 4 RESULTS AND DISCUSSIONS

### 4.1 Load vs. Slip response

To help, the Load vs. Slip curves of push-out test are presented in two ways for a better comprehension. First (Fig. 8a to Fig. 11a) the complete Load *vs*. Slip curves are presented. After, in Fig. 8b-11b are highlighted the portions of the curves until the rupture of the concrete dowel limiting the slipping to 0.25mm.

The Load *vs*. Slip behavior (Fig. 8-11) can be divided into three phases. Values of load and corresponding steel-concrete slip are given in Table 3:

- Phase I: there was almost no steel-concrete slip up to the rupture of the infill concrete that corresponding to vertical load of 73.63 kN (Fig. 8b). Thereafter, the load value immediately decreased to 60.80kN and the slip continues to increase.
- Phase II: the load increased again however slower than before, and large slips were recorded until the load was 76.09 kN. This load value was very similar to the concrete dowel rupture strength. Once again, slow decrease of the load was observed, and it reached 67.16 kN. The steel-concrete slip corresponding to the load decrease of Phase II was higher than in the Phase I (see Table 3).
- Phase III: the load becomes to increase, and the specimen carried maximum load of 80.44 kN. Large slips were induced after the ultimate load was reached.

According to Eurocode 4 [7], the slip should be measured at least until the load reaches to 20% below the ultimate load. However, this procedure was not performed because the load was kept almost constant while the steel-concrete slip was increased. Due this, the test was stopped after a long time in which the load was almost constant. Table 3 indicates the steel-concrete slip for three phases.

**Table 3:** Slip corresponding to the loading phases

| Load [kN] | | Slip [mm] | | | | | | |
|---|---|---|---|---|---|---|---|---|
| | | TD1-SE | TD1-SD | TD2-SE | TD2-SD* | TD1-CE | TD1-CD | TD3-CE |
| I | 73.63 | 0.05 | 0.01 | 0.12 | 0.00 | 0.03 | 0.03 | 0.03 |
| | 60.80 | 0.10 | 0.02 | 0.16 | 0.02 | 0.07 | 0.05 | 0.06 |
| II | 76.09 | 2.44 | 0.65 | 2.61 | 0.68 | 2.39 | 0.65 | 2.34 |
| | 67.16 | 6.33 | 4.46 | 6.49 | 4.51 | 6.32 | 4.30 | 6.25 |
| III | 80.44 | 12.23 | 10.36 | 12.36 | 10.45 | 12.25 | 9.95 | 12.17 |

* Corrected for absolute values

Similar slip behavior (Fig. 8a) was founded in all measured points (TD2-SE, TD1-SD, TD2-SD) at the top edge. The same was recorded in center line of the top edge (TD2-SE and TD2-SD, Fig. 9). Comparing the slip behavior on both, right and the left sides of the steel-concrete connection, nearly the same slip behavior were obtained in the test (Fig. 10). Therefore, the geometric imperfections of the specimen as well as the regularization of the model support base were insignificant for the slip.

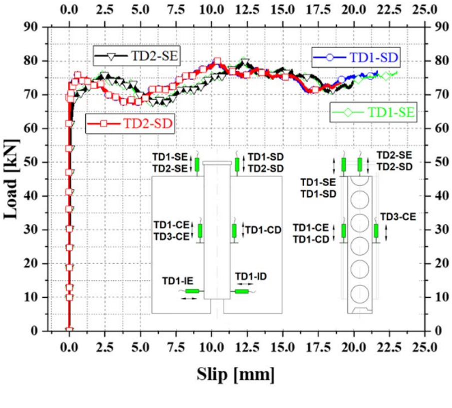


**(a) General**

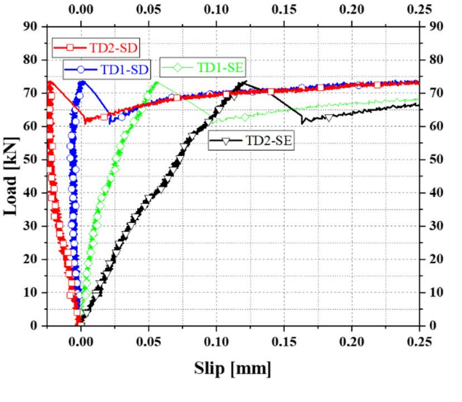


**(b) First phase**

Fig. 8: Load versus slip curves at the top of specimen

The slips recorded on TD1-SE and TD2-SE, both points on the upper left of the edge are very similar (Fig. 8a). Therefore, there was no significant asymmetry between the right and left sides of the specimen. Slips at the middle thickness of the slab were recorded by displacement transducers TD2-SE and TD2-SD (Fig. 7). The maximum values of slip recorded at left (TD2-SE) and right (TD2-SD) of the specimen were, respectively, 19.9 mm and 19.1 mm (Fig. 9). The slip values in all points are higher than 6 mm which indicates ductile behavior of the shear connection as outlined in the Eurocode 4 [7].

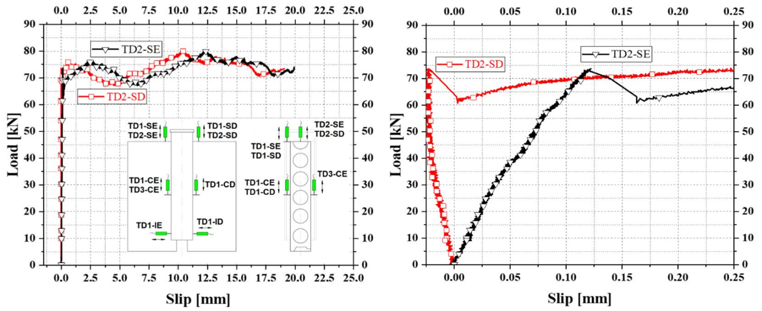


**(a) General** **(b) First phase**

Fig. 9: Load versus slip curves in point 2 at the top of specimen

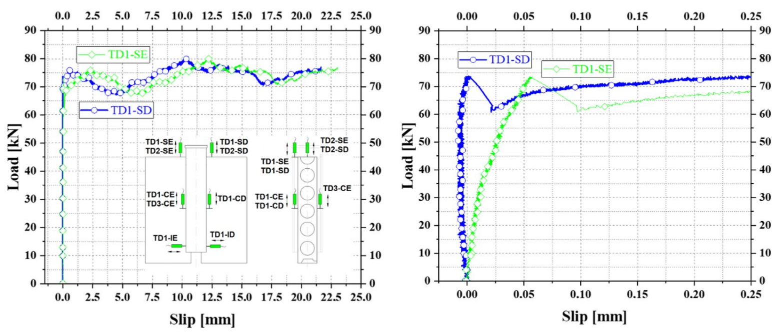


**(a) General** **(b) First phase**

Fig. 10: Load versus slip curves in point 1 at the top of specimen

The slip in half-length was also recorded by displacement transducers. Points TD1-CE and TD3-CE 1 (Fig. 11b) presented similar behavior until to the first peak load (limit of the Phase I). However, the slip values recorded in the point TD1-CD at right side of steel profile were lower than the others since the first peak load (limit of the Phase I). this can be observed in Fig. 11b and Table 3.

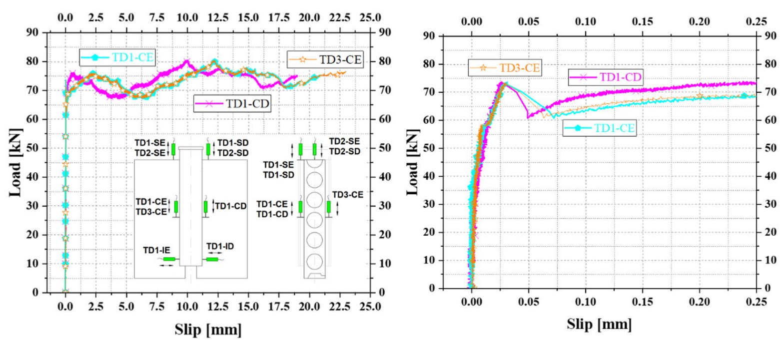


**(a) General** **(b) First phase**

Fig. 11: Load versus slip curves at the half length of the specimen

Displacement transducers TD1-ID and TD1-IE recorded the horizontal steel-concrete separation, and the results are given in Fig. 12. The separation was measured at the bottom of the steel profile. Horizontal separation and steel-concrete slip presented the similar behavior up to the rupture of the concrete dowel. Thereafter, the behavior of right (TD1-ID, Fig. 12) and left (TD1-IE, Fig. 12) sides were not similar behavior. The loss of shear transferring of connection maybe indicates a loss of symmetry of the precast concrete slabs in relation to the steel profile. The horizontal separation at right side continues to increase up to the test end.

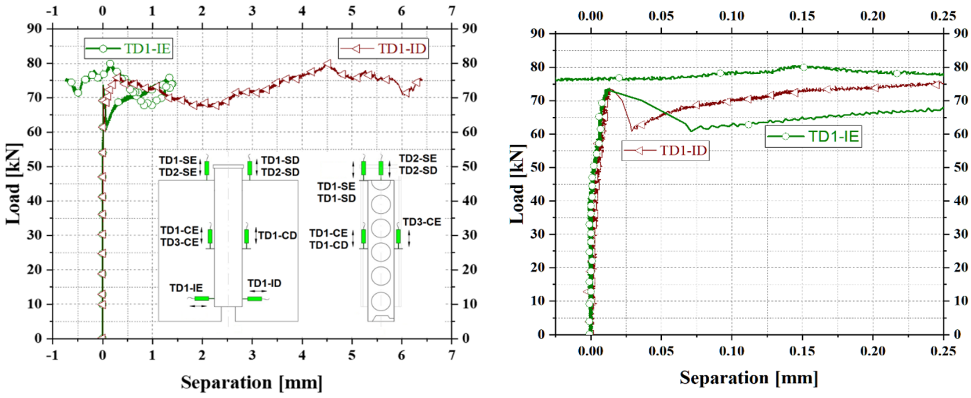


(a) General (b) First phase

Fig. 12: Horizontal separation between the steel profile and precast slab at the bottom of specimen

Regarding the failure mode, no cracks were observed in the precast concrete slabs. No visible failure was observed in the specimen and, apparently, the shearing of the virtual concrete dowel was the failure mode. This is compatible with the shear resistance value (Table 4) obtained considering one concrete dowel and the theoretical models described in item 2.1.

## 4.2 Ultimate load

The resistance of the concrete dowel ($R_c$) was predicted with the analytical models presented in Table 1. The theoretical values were compared to the ultimate load of the push-out test and the results are in Table 4.

**Table 4:** Comparison of experimental shear resistance and analytical results

| Shear resistance of one shear connection $R_c$ (kN) | | |
|---|---|---|
| Experimental | Theoretical values | |
| | Huo and D'Mello [9] | Chen et al. [10] |
| 80.44 | 114.42 (+42.2%) | 89.62 (+11.4%) |

The methods proposed by Huo and D'Mello [9] and Chen et al. [10] underestimated the shear resistance of the shear connection. Comparing the shear resistance capacity predicted using models of Huo and D'Mello [9] and Chen et al. [10] with the experimental result the differences were, respectively, 42.2% and 11.4% (Table 4). The difference between the shear resistance capacity predicted by analytical model of Chen et al. [10] was considered acceptable compared to experimental result.

In this exploratory study, it is not possible explain the reasons of the significant difference between experimental load and theoretical shear resistance capacity predicted by the calculation method of Huo and D'Mello [9].

## 5 CONCLUSIONS

The shear transfer mechanisms in composite slim floor system formed by precast hollow-core slabs and steel profile with web opening were investigated in the present study. The main objective was to evaluate the concrete dowel formed by the in-situ concrete that pass through and fill the opening of both, web of steel profile and voids of precast hollow-core slabs. The follow aspects are highlighted:

1) The Load vs. Slip curves showed that the chosen specimen type and the push-out test were adequate to investigate the shear transfer mechanism formed by the infill concrete in the web opening.
2) The shear connection formed by the concrete infill without any other elements demonstrated a ductile failure under the direct longitudinal shear force with a slip capacity of 19mm.
3) The analytical method of Chen et al. [10] showed good accuracy to predict the shear resistance of the shear connection between steel and concrete components of the composite slim floor system.
4) The proposed push-out test was efficient for evaluating the shear transferring mechanisms between the precast concrete hollow-core slab and the steel beam with web circular opening.

## 6 ACKNOWLEDGMENTS

This study was financed in part by the Coordenação de Aperfeiçoamento de Pessoal de Nível Superior – Brasil (CAPES) – Finance Code 001. The authors would also like to express their gratitude to CASSOL Pré-Fabricados Ltda for donating the precast hollow-core concrete slabs, Lafarge Holcim SA for the donation of cement, Soufer Industrial Ltda for the donation of steel plates and ConstruAço Construção Civil e Metálica São Carlos Ltda for welding the steel plates and compose the steel profile.

## 7 REFERENCES

[1] S. Chen and T. Limazie, "Composite slim floor beams with innovative shear connections," *Proc. Inst. Civ. Eng., Struct. Build.*, vol. 171, no. 1, pp. 29–37, 2018.

[2] R. M. Lawson, F. Hanus, and D. Sonck, "Large web openings in steel and composite beams," *Steel Constr.*, vol. 10, no. 2, pp. 168–175, 2017.

[3] S. De Nardin and A. L. H. C. El Debs, "Study of partially encased composite beams with innovative position of stud bolts," *J. Construct. Steel Res.*, vol. 65, no. 2, pp. 342–350, 2009.

[4] T. Limazie and S. Chen, "Effective shear connection for shallow cellular composite floor beams," *J. Construct. Steel Res.*, vol. 128, pp. 772–788, Jan 2017.

[5] Steel Construction. “Ultra Shallow Floor Beam.” Steelconstruction.info. https://www.steelconstruction.info/File:Westok-3.jpg (accessed Mar. 13, 2019).

[6] Steel Construction. “Ultra Shallow Floor Beam.” Steelconstruction.info. https://www.steelconstruction.info/File:Westok-2.jpg#filelinks (accessed Mar.13, 2019).

[7] European Committee of Standardization, *EN 1994-1-1: Eurocode 4 - Design of composite steel and concrete structures – Part 1-1: General rules and rules for buildings*, 2004.

[8] P. T. Souza, *Análise teórica e experimental de pisos mistos de pequena altura compostos por vigas metálicas e lajes alveolares de concreto*, São Carlos: Universidade de São Paulo, 2016.

[9] B. Y. Huo and C. A. D’Mello, "Push-out tests and analytical study of shear transfer mechanisms in composite shallow cellular floor beams," *J. Construct. Steel Res.*, vol. 88, pp. 191–205, 2013.

[10] S. Chen, T. Limazie, and J. Tan, "Flexural behavior of shallow cellular composite floor beams with innovative shear connections," *J. Construct. Steel Res.*, vol. 106, pp. 329–346, 2015.

[11] N. L. Tran and C. A. Graubner, "Uncertainties of concrete parameters in shear capacity calculation of RC members without shear reinforcement," in *16th International Probabilistic Workshop.*, A. Strauss, K. Bergmeister, and D. Proske, Eds. Sep. 2018.

[12] R. M. Lawson and S. J. Hicks, *Design of composite beams with large web openings*, P355 ed. London: The Steel Construction Institute, 2011.

[13] ArcelorMittal, *ACB Vigas alveolares*. Madrid: APTA - Asociación para la Promoción Técnica del Acero, 2014.

[14] American Society for Testing and Materials, *ASTM E8/E8M-09:2009. Standard test methode for tension testing of metallic materials., no T68*, 2009.

[15] ASSOCIAÇÃO BRASILEIRA DE NORMAS TÉCNICAS, *NBR 8800: Projeto de estruturas de aço e de estruturas mistas de aço e concreto de edifícios*, 2008.

[16] ASSOCIAÇÃO BRASILEIRA DE NORMAS TÉCNICAS, *ABNT NBR 6118: Projeto de estruturas de concreto — Procedimento*, 2014.

**Author contributions:** GC: conceptualization, data curation; SEPJ: conceptualization, methodology, writing; SDN: funding acquisition, supervision data curation, formal analysis, methodology.

**Editors:** José Marcio Calixto, Guilherme Aris Parsekian

IBRACON Structures and Materials Journal
Revista IBRACON de Estruturas e Materiais
ISSN 1983-4195 ismj.org

ORIGINAL ARTICLE

# Correlation between diffusion coefficient values of chloride ions obtained through column and ion migration tests in cementitious matrices with varying contents of silica fume and mortar

*Correlação entre valores de coeficiente de difusão de íons cloro obtidos por meio de ensaios de coluna e de migração iônica em matrizes cimentícias com variados teores de sílica ativa e de argamassa*

Silas de Andrade Pinto[a]
Sandro Lemos Machado[b]
Daniel Véras Ribeiro[b]

[a]Universidade Federal da Bahia – UFBA, Programa de Pós-graduação em Engenharia Civil – PPEC, Salvador, BA, Brasil
[b]Universidade Federal da Bahia – UFBA, Departamento de Ciência e Tecnologia dos Materiais, Salvador, BA, Brasil

Received 21 January2021
Accepted 06 October 2021

**Abstract:** Corrosion is one of the main phenomena that lead to pathological manifestations in reinforced concrete structures under aggressive environments. with the chloride ion being the most responsible for its occurrence. In this way, understanding the transport mechanisms of this ion through the microstructure of the concrete is of fundamental importance to prevent or delay the penetration of these aggressive agents to guarantee a durable structure. In the literature, there are extensive studies concerning the diffusion of chlorides in concrete and the influence of pozzolanic additions in this mechanism. However, only a few correlate the different methods of analysis. This work aims to determine the chloride ion diffusion coefficients in concrete containing various levels of silica fume (5%, 10%, and 15%) or varying the mortar content (54%, 80%, and 100%), and compares the results obtained through column tests and chloride migration tests. It was observed that, although the techniques used were quite distinct, the diffusion values obtained were similar, contributing to the validation of both techniques. Furthermore, the variation in the mortar ratio causes a reduction in the interfacial transition zone of coarse aggregate/mortars and an increase in the content of aluminates, which promotes a similar effect to the use of silica fume.

**Keywords:** Diffusion coefficient, concrete, mortar, chloride penetration, corrosion.

**Resumo:** A corrosão é um dos principais fenômenos que geram manifestações patológicas nas estruturas de concreto armado em ambientes agressivos, sendo o íon cloro o maior responsável por sua ocorrência. Desta forma, entender os mecanismos de transporte deste íon através da microestrutura do concreto é de fundamental importância para impedir ou retardar a penetração destes agentes agressivos, visando garantir uma estrutura durável. Na literatura são vastos os estudos referentes à difusão de cloretos em concreto e a influência das adições pozolânicas neste mecanismo, entretanto, poucos correlacionam os diferentes métodos de análise. Assim, este trabalho visa determinar os coeficientes de difusão do íon cloro em concretos contendo diversos teores de adição de sílica ativa (5%, 10% e 15%) ou com variação do teor de argamassa (54%, 80% e 100%), comparando os resultados obtidos por meio dos ensaios de migração iônica e de coluna. Observou-se que, apesar das técnicas utilizadas serem bastante distintas, os valores de coeficientes de difusão obtidos foram semelhantes, colaborando para a validação de ambas as técnicas. Além disso, a variação no teor de argamassa acarreta uma redução na zona de transição interfacial agregado graúdo/argamassas e um aumento no teor de aluminatos, o que promove efeito semelhante ao uso de sílica ativa.

**Palavras-chave:** Coeficiente de difusão, concreto, argamassa, penetração de cloreto, corrosão.

**Corresponding author:** Silas de Andrade Pinto. E-mail: silasandradepinto@gmail.com
**Financial support:** None.
**Conflict of interest:** Nothing to declare.
**Data Availability:** The data that support the findings of this study are available from the corresponding author, S. A. Pinto, upon reasonable request.

**How to cite:** S. A. Pinto, S. L. Machado and D. V. Ribeiro, "Correlation between diffusion coefficient values of chloride ions obtained through column and ion migration tests in cementitious matrices with varying contents of silica fume and mortar," *Rev. IBRACON Estrut. Mater.*, vol. 15, no. 3, e15307, 2022, https://doi.org/10.1590/S1983-41952022000300007

## 1 INTRODUCTION

Concrete is a durable material when well dosed and executed, however, concrete structures can deteriorate because of a series of deleterious mechanisms/reactions, bringing risks to the safety of users, besides the high costs of repairs.

The addition of supplementary materials with pozzolanic characteristics has been proving to be a good alternative for improve the concrete properties while also reducing cement consumption. The addition of silica fume (a byproduct with a high $SiO_2$ content) to concrete allows the formation of secondary calcium silicate hydrates (C-S-H), which promote the pore sealing and discontinuity, making the passage of chloride ions more difficult and increasing their adsorption on the surface of the formed C-S-H [1]–[3].

According to Helene [4], chlorides penetrate through the pores, reaching the rebar and starting the corrosion. Thus, understanding how these ions diffuse inside the concrete can indicate the most appropriate material to be used.

Among the techniques extensively studied in the literature for chloride diffusion in concrete, are those used by Ribeiro et al. [5], Shackelford [6] and Andrade [7], based on ASTM C 1202 [8], NT BUILD 492 [9], ASTM C 1556 [10], and ASTM C 1543 [11]. These aim to accelerate the natural process of penetration of these ions and allow the determination not only of diffusion but also of other transport parameters such as tortuosity and mechanical dispersion.

The most usual techniques for determining the diffusion coefficient in concrete with a short test time apply a potential difference to accelerate the passage of chlorides. Andrade [7] considers that with potential differences of around 10 to 15 VDC, the migration phenomenon becomes predominant and the agitation caused in the particles is reduced, avoiding the problem of overheating in the methodology employed by ASTM C 1202 [8], which significantly affects the results obtained.

Other studies evaluate the penetration of harmful substances in porous media, based on the phenomenon of diffusion, such as the bulk diffusion test standardized by ASTM C 1556 [10] that provides results closer to reality and takes longer. In the evaluation of soils, for example, there are tests in which no application of electrical potential difference but rather of pressure in a fluid containing contaminant. Thus, the results obtained portray the phenomenon studied more adequately while not altering the agitation of particles due to application of potential difference. This method has already been applied in cementitious matrices in the studies performed by Vilasboas et al. [12] and Visudmedanukul [13], an adaptation of the NBR 10786 [14].

Given the several methodologies with different physical principles used to measure chloride diffusion, this work aims to provide correlations between the chloride migration test standardized by UNE 83987 [15] and the column test, to verify the accuracy and reliability of these methods when applied to cement matrices. Furthermore, the influence of silica fume addition and the variation of mortar content on the diffusion results will be evaluated. This is because the covering layer in reinforced concrete structures has a higher mortar content than the concrete inside them due to the compaction and finishing of the structural elements.

## 2 MATERIALS AND EXPERIMENTAL PROGRAM

### 2.1 Materials

In this research Portland CP V-ARI RS cement, standardized by NBR 16697 [16], fine quartz aggregate from the metropolitan region of Salvador, coarse aggregate, silica fume and CEMIX 2000 plasticizer admixture were used.

The concrete formulation 1.00: 1.83: 2.37: x: 0.60 (cement: fine quartz aggregate: coarse aggregate: silica fume: water) was used. Its consistency, evaluated by slump test, was fixed at 180 ± 10 mm, and the content of silica fume added ranged from 5% (5-SA), 10% (10-SA) to 15% (15-SA) by mass of cement. The water/cement ratio was fixed at 0.60 and the reference concrete produced had C30 class for Brazilian compressive strength, according to NBR 8953 [17].

The samples were also prepared with varying amounts of mortar, from 54% (reference), 80% (80-AG), to 100% (100-AG). The materials used in the preparation of the concrete are presented in Table 1.

**Table 1.** Materials consumption per cubic meter of concrete.

| Mixture | Cement (kg/m³) | Fine quartz (kg/m³) | Coarse (kg/m³) | Silica fume (kg/m³) | Water (kg/m³) | Plasticizer admixture (l/m³) | Compressive strength at 28 days (MPa) |
|---|---|---|---|---|---|---|---|
| REF | 409.6 | 749.5 | 970.6 | - | 245.7 | - | 31.00 ± 0.85 |
| 5-SA | 407.6 | 745.9 | 965.9 | 20.5 | 244.5 | 0.48 | 31.35 ± 1.62 |
| 10-SA | 404.1 | 739.5 | 957.6 | 41.0 | 242.4 | 1.46 | 35.44 ± 0.67 |
| 15-SA | 400.7 | 733.2 | 949.5 | 61.4 | 240.4 | 1.88 | 37.67 ± 0.61 |
| 80-AG | 520.8 | 953.1 | 468.7 | - | 312.5 | - | 33.00 ± 1.00 |
| 100-AG | 622.5 | 1139.2 | - | - | 373.5 | - | 32.65 ± 1.32 |

The cement has a specific gravity (helium gas pycnometry - AccuPyc II 1340 Micromeritics) equal to 3.14 g/cm$^3$, specific surface area BET (Gemini 2370 V1.02 - Micrometrics) equal to 7480 cm$^2$/g and median equivalent diameter, $D_{50}$ (Mastersizer 2000 Malvern), equal to 0.038 mm.

The silica fume has a specific gravity equal to 2.35 g/cm$^3$, specific surface area equal to 14860 cm$^2$/g, and median equivalent diameter ($D_{50}$) equal to 0.0047 mm.

Table 2 presents the chemical compositions of the cement and silica fume obtained by X-ray fluorescence spectrometry (Shimadzu XRF-1800). It can be observed that the chemical composition of the Portland cement contains the following main components, such as calcium oxide (CaO), silica ($SiO_2$), alumina ($Al_2O_3$), iron oxide ($Fe_2O_3$), magnesium oxide (MgO), a small percentage of sulfur trioxide ($SO_3$) and other impurities. The presence of alumina (4.84%) is associated with $C_4AF$ (tetra-calcium aluminate iron) and $C_3A$ (tricalcium aluminate) phases. According to Shi et al. [18], Ribeiro et al. [5], and Yue et al. [19], the aluminate content delays the non-steady state diffusion of chlorides due to the formation of chloroaluminates in the concrete microstructure, in particular Friedel's salt ($C_3A{\cdot}CaCl_2{\cdot}10H_2O$).

**Table 2.** Chemical compositions of cement and silica fume used, in oxides.

| Content % | CaO | $SiO_2$ | $Al_2O_3$ | MgO | $Fe_2O_3$ | $SO_3$ | $K_2O$ | $Na_2O$ | ZnO | MnO | LOI.[a)] |
|---|---|---|---|---|---|---|---|---|---|---|---|
| Cement | 61.12 | 19.10 | 4.84 | 2.73 | 3.19 | 3.35 | 0.70 | 0.24 | - | - | 5.60 |
| Silica fume | - | 79.00 | - | - | - | - | - | - | 16.86 | 4.14 | 4.40 |

[a)] Loss on ignition.

In the chemical composition of the silica fume, mainly silica ($SiO_2$) is observed along with impurities such as zinc oxide (ZnO) and manganese oxide (MnO). However, the silica content in the silica fume used (79%) is lower than the minimum content established by the Brazilian standard NBR 13956 [20], which is 85%.

For the fine quartz aggregate, the specific gravity was determined according to NBR NM 52 [21]. The specific gravity of the coarse aggregate was determined according to NBR NM 53 [22]. Both aggregates were manually sieved, according to NBR NM 248 [23] to determine the granulometric composition. The results of this characterization can be seen in Table 3.

**Table 3.** Physical characterization of aggregates and methods used.

| Properties | Method | Fine quartz | Coarse |
|---|---|---|---|
| Specific gravity (g/cm³) | NM 52:2009 [a)] and NBR NM 53:2009 [b)] | 2.66 | 2.87 |
| Maximum diameter (mm) | NBR NM 248:2003 | 1.17 | 9.50 |
| Fineness Modulus | | 1.32 | 5.72 |

Obs.: [a)] Method used to fine aggregate characterization; [b)] Method used to coarse aggregate characterization.

## 2.2 Physical characterization of concretes

The water absorption by capillarity of each mix design was determined according to the procedure according to NBR 9779 [24]. Three cylindrical specimens (ϕ10 cm x 20 cm) were used, and after 28 days of curing, they were dried in an oven to a constant mass. Then, the specimens were positioned in a container with a water slide equal to 5 ± 1 mm above the lower face, and the masses were monitored until equilibrium.

To calculate the sorptivity (S), the slope of the line generated by the results of water absorption (A, kg/m$^2$) as a function of the square root of time (t) is used, according to Equation 1.

$$A = b + S \cdot \sqrt{t} \tag{1}$$

This test depends directly on the radius of the pores in the material, so the sorptivity is an indication of the diffusion results and consequently the durability of the concrete.

After 28 days, three specimens were tested using the Archimedes principle, according to NBR 9778 [25]. The specimens were dried in an oven and their dry masses ($M_d$) were determined, then the samples were immersed in water for 72h for complete saturation of the existing open porosity, and the immersed ($M_i$) and wet ($M_w$) masses were determined. The apparent porosity ($P_A$) and density ($D_A$) were calculated based on Equations 2 and 3, respectively, with $\rho_L$ being the density of the liquid (in this case, water, equal to 1 g/cm$^3$).

$$P_A = 100 \cdot \frac{M_w - M_d}{M_w - M_i} \tag{2}$$

$$D_A = \rho_L \cdot \frac{M_d}{M_w - M_i} \tag{3}$$

## 2.3 Chloride Migration Assessment in Concrete

### 2.3.1 Sample selection and calibration of conductivity curve

The selection of representative specimens of each composition is complicated because of the great diversity of elements (and their relative ratios). Therefore, an adaptation of ASTM E 562 [26] proposed by Ribeiro [5] was used. According to this standard, the relative amount (%) of a certain target phase (coarse aggregate, in this work) can be estimated by overlaying a grid on the specimen and then counting the intersecting nodes in the middle and edges of the target phase. In this example, which is illustrated in Figure 1, the grid contains 38 nodes, and intersections with gravel correspond to 15 points (12 in the middle + 6·0.5 at the edges). Thus, 15/38 would yield an estimated 39.5 vol.% of gravel in the sample.

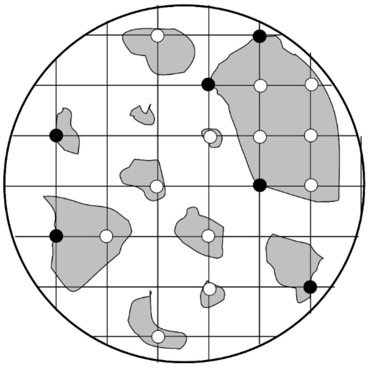


**Figure 1.** Process of sample selection and phase quantification for chloride migration tests, adapted from ASTM E 562–02 [5].

Prior to conducting the chloride migration tests, the specimens were submerged in distilled water for 24h, as in Ribeiro et al. [5], Castellote et al. [27], and Amorim Júnior et al. [28] studies, to saturate the specimens so that only the ionic migration occurred during the test. During the tests, the electrical conductivity of the anodic cell solution was monitored daily using a portable pen-type digital conductivity meter (Homis Model 42). The concentration of chlorides in the anodic cell was estimated using the equation y = 132.88·x ($R^2$ = 0.9969), where x is the conductivity in mS/cm and y is the concentration of $Cl^-$ in mol/l. This mathematical expression was obtained experimentally (Figure 2) with NaCl solutions, at 20 ºC.

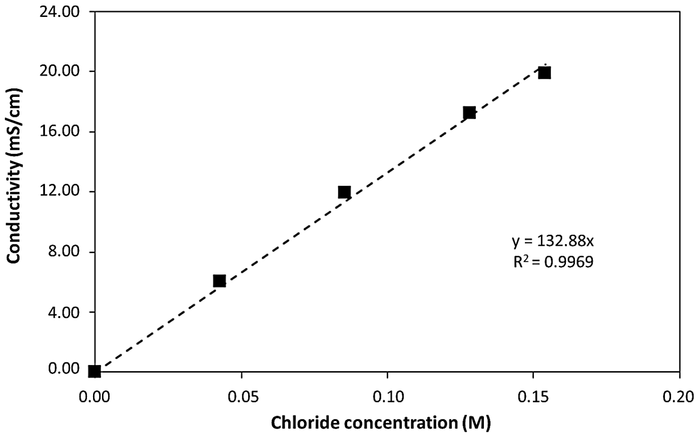


**Figure 2.** Experimental relationship between electrical conductivity and chloride concentration in the anodic compartment, which initially contains distilled water.

### 2.3.2. Accelerated migration test

This test uses the principle of applying a potential difference between two cells, one filled with a solution containing a contaminant (NaCl) and the other cell with distilled water. After 28 days in water, the specimen was prepared and positioned between the two cells as shown in Figure 3. In this method, the migration occurs due to the application of an electrical potential difference of 12 VDC through the electrodes contained in the cells.

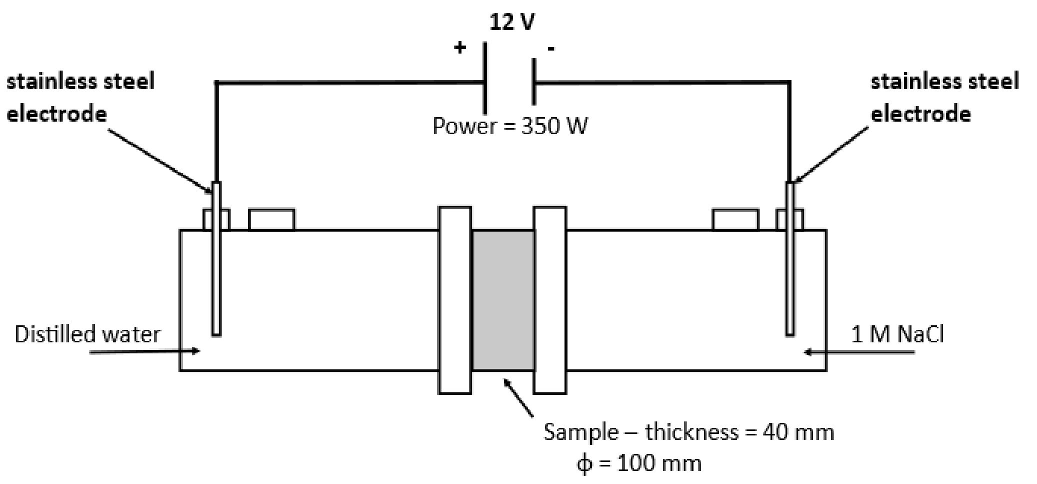


**Figure 3.** Schematic drawing of the chloride migration test apparatus.

For this test, a chloride migration apparatus was used, as suggested by Andrade [7] and developed by Ribeiro et al. [5], following the procedures presented in UNE 83987 [15]. The tests were carried out on three specimens of each series, each with a thickness of 40 mm, extracted from the central region of the cylindrical specimens ($\phi$ = 100 mm, h = 200 mm), using a diamond disc cutting machine.

At the start of the test, the concentration of chlorides passing through the anodic cell is not a constant flow, due to adsorption on the capillary walls, and the reactions of these ions with the aluminates present in the cement and in the mineral additions. These form a Friedel's salt at a non-steady state. When the pores are saturated and the reserves of aluminates depleted, the flow becomes constant, entering a steady-state condition.

Thus, the time required to start the stationary phase is called time lag ($\tau$) and is obtained through the intersection between the extension of the straight line that characterizes the steady-state condition and the abscissa axis (time), according to Figure 4.

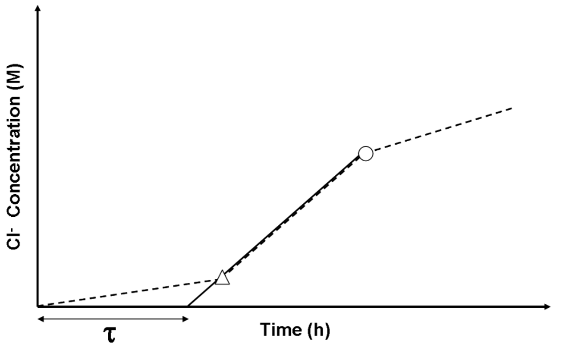


**Figure 4.** Experimental determination of the time lag (τ); onset (Δ) and end (○) of the steady-state diffusion stage (adapted from Castellote et al. [24]).

The diffusion coefficient in the transient or non-steady state ($D_{ns}$), in $cm^2/s$, can be measured, based on migration testing, using Equations 4 and 5, proposed by Castellote et al. [27]. The steady-state diffusion coefficient ($D_s$), in $cm^2/s$, was calculated applying the modified Nernst-Plank equation (Equation 6).

$$D_{ns} = \frac{2 \cdot l^2}{\tau \cdot \upsilon^2} \cdot \left[\upsilon \cdot \coth\frac{\upsilon}{2} - 2\right] \tag{4}$$

$$\upsilon = \frac{z \cdot e \cdot \Delta\Phi}{\mathrm{k} \cdot \mathrm{T}} \tag{5}$$

$$D_s = \frac{j_{Cl} \cdot R \cdot T \cdot l}{\mathrm{z} \cdot \gamma \cdot \mathrm{F} \cdot C_{Cl} \cdot \Delta\Phi} \tag{6}$$

Where $l$ is the thickness of the sample (cm), τ is the time lag (s), $z$ is the valence of the ions (equal to 1), $e$ is the electric charge of an electron ($1.6 \cdot 10^{-19}$ C), ΔΦ is the voltage (V), $k$ is the Boltzmann constant ($1.38 \cdot 10^{-23}$ J/K), and $T$ is the absolute temperature. Furthermore, $j_{Cl}$ is the ion flux [mol/(s.cm$^2$)], $R$ is a constant [1.9872 cal/(mol·K)], $F$ corresponds to the Faraday constant [23063 cal/(volt. eq)]. Finally, $C_{Cl}$ is the chloride concentration in the cathode cell (mol/cm$^3$), and $\gamma$ is a constant of activity coefficient (0.657 for $Cl^-$).

### 2.3.3. Column test

The column test aims to determine the transport parameters that interfere with the diffusion of contaminants by porous media in controlled laboratory conditions [6], [29] which reflect the real situation. This technique is extensively used to understand soil/contaminant interaction, but recently it has been applied in Portland cement matrices, such as soil-cement [13] and in mortars and concrete [12].

According to Vilasboas [12], Nascentes [30], and Bear [31] in the modeling of the transport of solutes by the column test, in which liquid flow occurs, it is not common to separate the diffusion process (D) from the dispersion process ($D_m$). They are treated in a combined way to define the parameter called hydrodynamic dispersion ($D_h$), as presented in Equation 7.

$$D_h = D + D_m \tag{7}$$

Dispersion-diffusion (D) is due to the flow of a chemical species in solution, however, when diffusion occurs inside the pores of the materials, it is reduced due to the tortuosity of the pores (w) and is expressed by Equation 8 [32]. The maximum value for tortuosity is equal to 1 because the maximum diffusion will happen when there are no blockages.

$$D = w \cdot D_{Cl} \tag{8}$$

Mechanical dispersion ($D_m$) is the process of mixing the contaminant resulting from the variation in the percolation speed of the fluid, which occurs in the interconnected pores. The contaminants percolate at different speeds depending on the tortuosity, friction, and size of the pores [33]. The mechanical dispersion is expressed by means of Equation 9.

$$D_m = \alpha \cdot vs \tag{9}$$

Where α is the mechanical dispersion coefficient (cm), vs is the solvent flow velocity (cm/s).

It can be noted that only the diffusion coefficient (D) can be correlated with the stationary diffusion ($D_s$) obtained from the migration test. This is because diffusion considers ionic movement without water flow, there being only the tortuosity of the matrix pores as blockages [31]. Moreover, the diffusion coefficient in the non-steady state ($D_{ns}$), obtained from the ion migration test, does not present a theoretically similar parameter in the column test.

To carry out this test, a column testing apparatus like the model indicated for concrete permeability tests was used, standardized by NBR 10786 [14], and used by Vilasboas et al. [12]. Three samples with 100 mm diameter and 40 mm thickness were taken from the central region of the cylindrical specimens using a diamond disc cutting machine.

Before the diffusion tests, the samples remained immersed in distilled water for 24 hours, like the conditioning performed for the accelerated migration test.

The test consists of forcing the contaminant fluid through the samples by applying a pressure (8 kgf/cm$^2$). To ensure lateral sealing of the specimens, pressurized $N_2$ is supplied, filling the outer part of the specimen and compressing a latex membrane that surrounds it. The same pressure as the $N_2$ is supplied to the reservoirs of the solution, however, because they are located at a lower elevation than the nitrogen cylinder, the solution leaving the reservoirs has a lower pressure when reaching the samples, due to the loss of load. Thus, the external pressure is higher than the internal pressure, ensuring lateral sealing. The diagrams of the system, chambers, and apparatus can be seen in Figures 5 and 6, respectively.

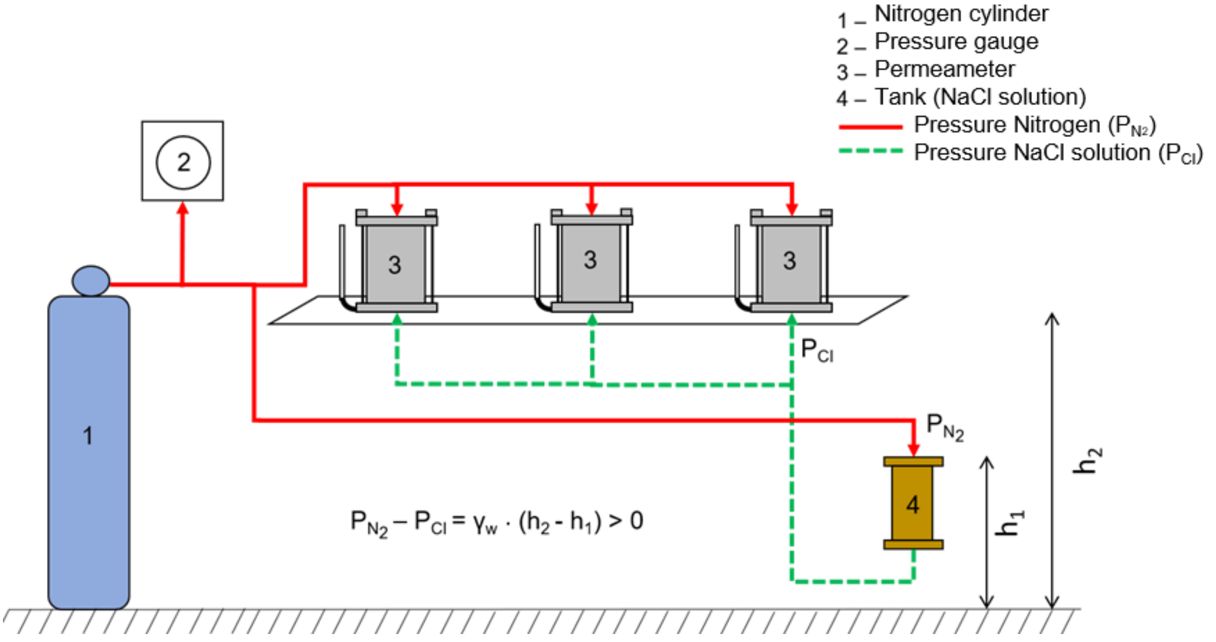


**Figure 5.** Schematic drawing of the column test apparatus.

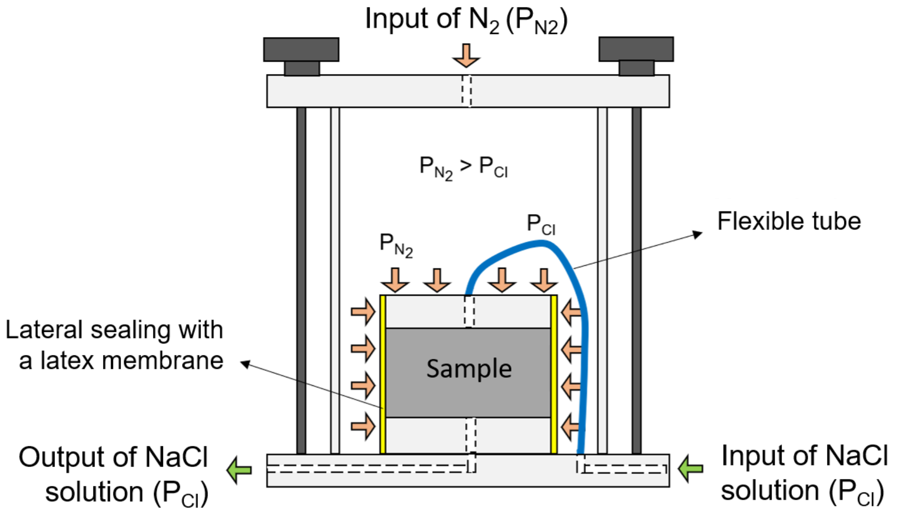


**Figure 6.** Schematic drawing of internal operation of the permeameter.

During the test, the solution that has percolated through the specimen is collected and its volume and chloride concentration over time is measured. Then an $N_{VP}$ x $C/C_0$ graph is drawn with $N_{VP}$ being the number of porous volumes that represents the time that the volume percolated through the sample filling its pores, determined by Equation 10.

$$\mathrm{N}_{VP} = \frac{V_{ol}}{\mathrm{n}} \tag{10}$$

Where $V_{ol}$ is the accumulated volume of the solution passing through the test ($cm^3$) and n is the porosity of the specimen ($cm^3$).

Based on experimental points, a theoretical curve is adjusted, based on Equation 11, modified by Freeze and Cherry [34], to obtain a maximum determination coefficient ($R^2$).

$$\frac{C(x,t)}{C_0} = \frac{1}{2}\left[erfc\left(\frac{R_d \cdot x - v_s \cdot t}{2\sqrt{R_d \cdot D_h \cdot t}}\right) + \exp\left(\frac{v_s \cdot x}{D_h}\right) erfc\left(\frac{R_d \cdot x + v_s \cdot t}{2\sqrt{R_d \cdot D_h \cdot t}}\right)\right] \tag{11}$$

Where C(x,t) is the concentration at a depth x and time t desired, $C_o$ is the initial concentration, $R_d$ is the retardation factor (≥ 1), $D_h$ is the hydrodynamic dispersion, $v_s$ is the velocity of fluid percolation.

The retardation factor ($R_d$) is directly influenced by the adsorption capacity of the porous media, which is related to its the specific surface and valence and size of the solute ions. Coarser soil fractions, for instance, tend to present $R_d$ close to unity (i.e., are unable to retain appreciable amounts of solute on their solid surfaces) [35]. This parameter has conceptual similarity with the time lag obtained with the migration test performed according to UNE 83987 [15], since both quantify the capacity of the matrix to retain a given substance.

## 3 RESULTS AND DISCUSSION

### 3.1 Physical characterization of concretes

It can be observed that the porosity of the matrix decreased as the silica fume content increased (Figure 7). This is due to the pozzolanic reaction, a consequence of the presence of amorphous silica in the silica fume used, which promotes the formation of hydrated calcium silicate (C-S-H). In addition, the silica fume has a filler effect caused by particles that do not react with $Ca(OH)_2$ and that contribute to the filling of voids, allowing better packaging of particles [36], [37]. By varying the mortar content, an increase in the porosity of the specimens was noted because mortar is more porous than coarse aggregate.

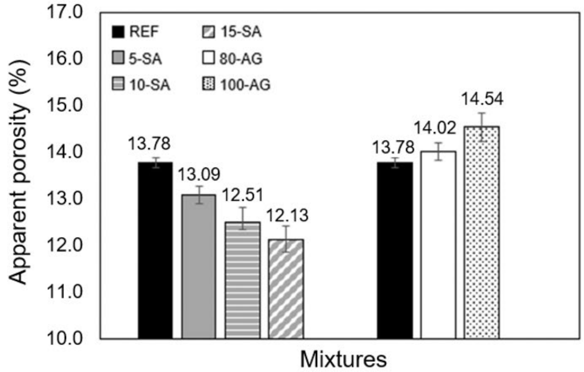


(A)

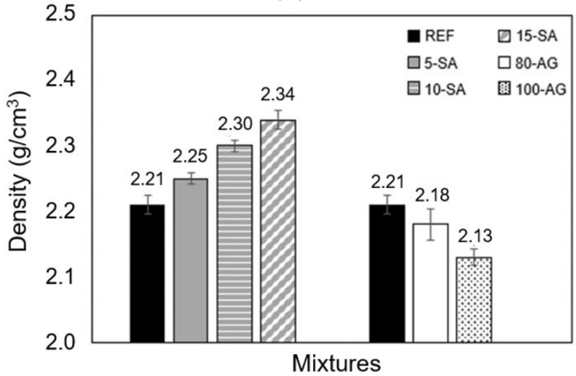


(B)

**Figure 7.** (A) Apparent porosity and (B) density of concretes with different silica fume and mortar contents.

The sorptivity of the concrete with varying contents of silica fume and mortar are presented in Figure 8. There is an increase in the rate of sorptivity of the concrete with the addition of higher contents of silica fume, up to the limit content of 10%. This is due to a reduction in the pore diameter, promoting an increase in the number of capillary pores and in turn increasing the water capillary absorption rate. With the addition of 15% of silica fume, there was a stabilization of the sorptivity due to a possible blocking and disconnection of the capillary pores [38].

There was also a reduction in the sorptivity in the specimens due to the increase in the mortar contents, however, this reduction was not statistically significant. This may have been due to the packaging factor of the system being more efficient when there are grains of different sizes, generating less porosity with the presence of the coarse aggregate. Furthermore, Scrivener et al. [39] reported that an increase in the content of fine quartz aggregate in the matrix makes the transition zone more tortuous. As a result, the capillary suction is made harder by the lack of a perfectly linear path, physically blocking the displacement of water.

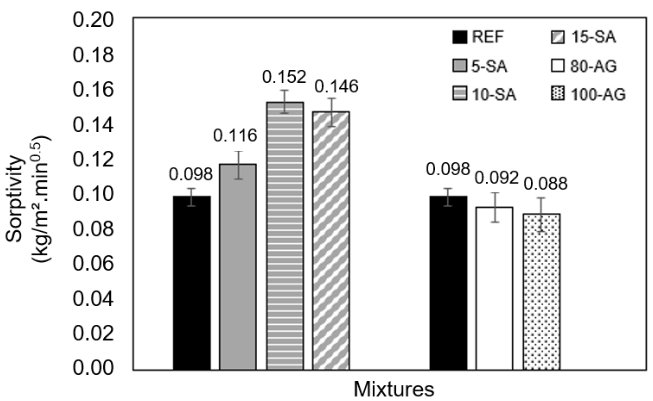


**Figure 8.** Sorptivity of the studied concretes.

## 3.2 Chloride Migration Assessment in Concrete

### 3.2.1 Accelerated migration test

Figure 9 shows the evolution of chloride concentration in the anodic chamber of reference concrete samples and those containing additions of 5%, 10%, and 15% silica fume. The concentration of chloride ions ($Cl^-$) increases with time, because of the application of the applied electric voltage, forcing these ions to migrate towards the positive pole of the system.

As more silica fume is added to the cement matrix, a deviation in the chloride concentration curve as a function of time can be seen to the right. This represents an increase in the time lag value up to 126% for a 15% addition of silica fume. Therefore, in concrete containing silica fume, the chlorides take longer to saturate and to cross the covering layer of the concrete, reaching the rebar and depassivating it. In the non-steady state condition, the solution containing chlorides adsorbs to the walls of the interconnected capillary pores and reactions between the chlorides and the aluminates present in the cement form Friedel's salt [40].

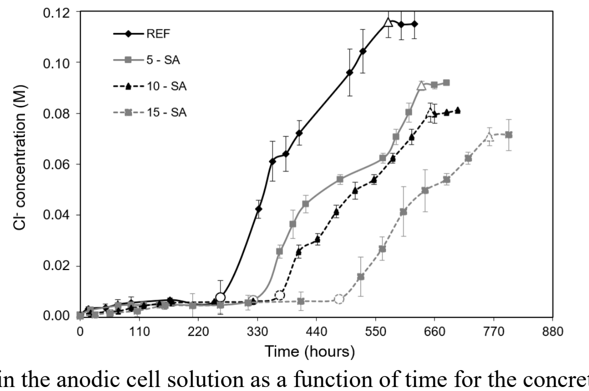


**Figure 9.** Chloride concentration in the anodic cell solution as a function of time for the concrete specimens with 0%, 5%, 10%, and 15% of silica fume (○ = beginning of steady state and Δ = end of steady state).

After the start of the steady-state condition, the flow of ions ($j_{Cl}$) becomes constant until the stability of the chloride concentration is reached [27]. For samples with varying silica fume contents, there is a reduction in the flow of ions. When present in the concrete (this can be visualized by the reduction in the inclination of the straight line in the steady-state condition), the addition of silica fume confers greater durability of the concrete as well as resistance to the action of chlorides. This finding is in line with the results obtained in studies by Aïtcin [41] and Ribeiro et al. [5], which showed that mineral additions reduce the movement of chlorides in the concrete microstructure due to the better distribution of pore diameters, resulting from the pozzolanic reactions, which difficult the ionic movement.

Figure 10 shows the evolution of chloride concentration in the anodic chamber when reference concrete samples are evaluated (with a mortar content equal to 54%) and with mortar contents equal to 80% and 100%.

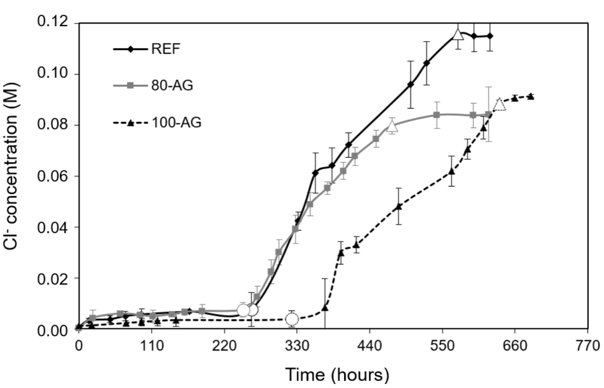


**Figure 10.** Chloride concentration in the anodic cell solution as a function of time for the concrete specimens with different mortar content (○ = beginning of steady state and Δ = end of steady state).

An approximate 49% increase in the time lag was observed by reducing the consumption of coarse aggregate, due to the higher consumption of cement and, consequently, higher content of aluminates. With an increase in the mortar content, the coarse aggregate/paste interface is reduced until non-existent (samples containing 100% mortar), which alters the connectivity of the pores and leads to an increase in tortuosity, making the passage of chloride ions difficult. These interfacial transition zones are of great importance in durability studies because it is through them that the preferential penetration of chloride ions occurs [5], [18].

In addition, due to the reduction in the aggregate/paste transition zone from a higher mortar content, the chloride flow is also reduced. This is because the solution containing chlorides will preferentially pass through this interface [42], [43] because of the change in the tortuosity of the pores, as previously discussed.

Furthermore, the diffusion coefficients in the steady and non-steady states obtained from concrete with different contents of silica fume and mortar, respectively, are shown in Tables 4 and 5. The results of the non-steady state diffusion coefficient ($D_{ns}$) were classified based on the limits established by Nilsson et al. [44] which refer to the $D_{ns}$ obtained by the NT Build 492 test [9]. According to Guignone et al. [45], the $D_{ns}$ values obtained by the method of UNE 83987 [15] and NT Build 492 [9] show similarities. However, according to Sell Júnior et al. [46], the difference between the diffusion coefficients determined by these methods is greater when evaluating the concretes that have greater permeability. However [28], [47], used this classification in articles that evaluated the chloride diffusion by the method of UNE 83987 [15].

**Table 4.** Classification of concretes with different silica fume contents as to resistance to chloride penetration, according to the limits established by Nilsson et al. [44].

| Mixture | Time lag (h) | Ion flow ($10^{-10}$ mol/s·cm$^2$) | $D_s$ ($10^{-8}$ cm$^2$/s) | $D_{ns}$ ($10^{-8}$ cm$^2$/s) | Resistance to chloride penetration |
|---|---|---|---|---|---|
| REF | 204.22 | 5.91 | 1.48 | 9.33 | High ($5 \cdot 10^{-8}$ cm$^2$/s < $D_{ns}$ < $10 \cdot 10^{-8}$ cm$^2$/s) |
| 5-SA | 298.00 | 3.41 | 0.85 | 6.30 | |
| 10-SA | 372.05 | 3.68 | 0.92 | 5.05 | |
| 15-SA | 461.12 | 3.92 | 0.98 | 4.08 | Very high ($2.5 \cdot 10^{-8}$ cm$^2$/s < $D_{ns}$ < $5 \cdot 10^{-8}$ cm$^2$/s) |

**Table 5.** Classification of concretes with different mortar contents as to resistance to chloride penetration, according to the limits established by Nilsson et al. [44].

| Mixture | Time lag (h) | Ion flow ($10^{-10}$ mol/s·cm$^2$) | $D_s$ ($10^{-8}$ cm$^2$/s) | $D_{ns}$ ($10^{-8}$ cm$^2$/s) | Resistance to chloride penetration |
|---|---|---|---|---|---|
| REF | 204.22 | 5.91 | 1.48 | 9.33 | High ($5 \cdot 10^{-8}$ cm$^2$/s < $D_{ns}$ < $10 \cdot 10^{-8}$ cm$^2$/s) |
| 80-AG | 218.03 | 2.88 | 0.72 | 8.61 | |
| 100-AG | 304.04 | 4.14 | 1.03 | 6.17 | |

Some researchers [47]–[49] have also observed that the addition of 10% silica fume in relation to the mass of cement promoted better refinement of the microstructure. However, according to the results presented in Table 5, it was found that this improvement also occurred with an increase in the mortar content.

### 3.2.2 Column test

The retention curves from the column test were plotted, presenting the mean curves as well as the standard deviation existing at all points on the curve (Figure 11). The retardation factor ($R_d$) was determined based on the curve that correlates the relative concentration of chloride ions ($C/C_0$) and the number of porous volumes ($N_{VP}$), which is a method used by Vilasboas et al. [12]. The retardation factor ($R_d$) corresponds to the number of pore volumes equivalent to a relative concentration of 50%. The other parameters were identified through the interaction of these coefficients to adjust a curve to present a higher correlation coefficient ($R^2$), from the experimental points obtained.

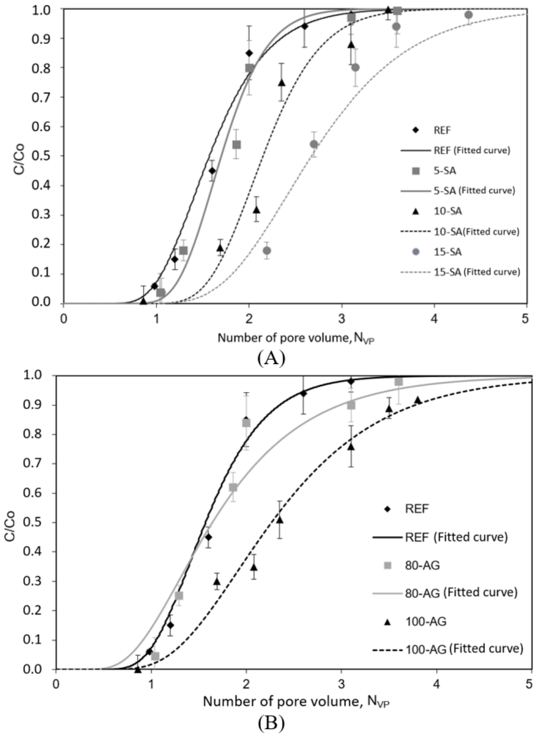


**Figure 11.** Relative chloride concentration curve in the concrete column test with different content of (A) silica fume and (B) mortar.

Table 6 shows the average transport parameters obtained by adjusting the column test data for the different types of concrete tested.

**Table 6.** Summary of transport parameters determined by the column test in concretes with different silica fume and mortar contents.

| Mixture | $R_d$ (-) | $v_s$ ($10^{-6}$ cm/s) | α (cm) | $D_m$ ($10^{-7}$ cm²/s) | w (-) | D 1) ($10^{-8}$ cm²/s) | $R^2$ |
|---|---|---|---|---|---|---|---|
| REF | 1.65 | 4.29 | 0.20 | 8.58 | 0.00100 | 1.60 | 0.98 |
| 5-SA | 1.70 | 3.04 | 0.10 | 3.04 | 0.00040 | 0.64 | 0.94 |
| 10-SA | 2.15 | 1.56 | 0.09 | 1.40 | 0.00054 | 0.86 | 0.96 |
| 15-SA | 2.80 | 2.32 | 0.07 | 9.24 | 0.00062 | 0.99 | 0.97 |
| 80-AG | 1.83 | 3.12 | 0.26 | 8.11 | 0.00045 | 0.72 | 0.93 |
| 100-AG | 2.45 | 1.56 | 0.18 | 2.81 | 0.00064 | 1.02 | 0.93 |

Obs.: 1) Using the diffusion of the chloride ion in water ($D_{cl} = 1.60 \cdot 10^{-5}$ cm²/s).

The values of $R_d$, which represents a parameter like the time lag (τ) of the ionic migration test, are in the range found by Vilasboas et al. [12] for concrete and mortar tests (1.40 to 3.50), and by Visudmedanukul [13] in soil-cement tests (1.03 to 2.77). As well as the time lag (τ) of the ionic migration test, the $R_d$ indicates the retention capacity of the substances.

This behavior is also reflected in the diffusion coefficients found for these materials because this is related to a constant (diffusion of chloride in water, equal to $1.60 \cdot 10^{-5}$ cm²/s [12], [51]) multiplied by the tortuosity factor of each analyzed sample ($w \cdot D_{Cl}$).

The results obtained corroborate those obtained by Shekarchi et al. [49], who verified small changes in the chloride diffusion coefficients in concrete with silica fume contents higher than 7.5%, when exposed in a maritime zone.

Although different methods were used in relation to ionic migration, the diffusion values obtained ($D_s$ and D) were similar because they have the same physical sense.

Unlike the method used by Vilasboas et al. [12], the tortuosity (W) was not fixed as this is a coefficient directly linked to the microstructure of the analyzed material, which undergoes alteration as the water/cement or water/binder ratio is altered. The mechanical dispersion coefficient (α) was like the results of porosity obtained, showing behavior like that observed by Vilasboas et al. [12].

When the input of chlorides in the cement matrix is evaluated, the mechanical dispersion ($D_m$) has a priority effect over the dispersion-diffusion (D) because it has a higher input velocity in the studied matrices. This shows that the contaminant penetration through the water flow is more significant than by diffusion, regardless of the microstructure of the tested samples.

### 3.2.3 Correlations between results obtained by different testing methods

The values of the steady-state diffusion coefficients, obtained through ionic migration tests ($D_s$) and column (D) were correlated, according to Figure 12. The adjustment was made to meet the existing physical parameters, where the linear equation generated cannot have a linear coefficient other than 0 (zero).

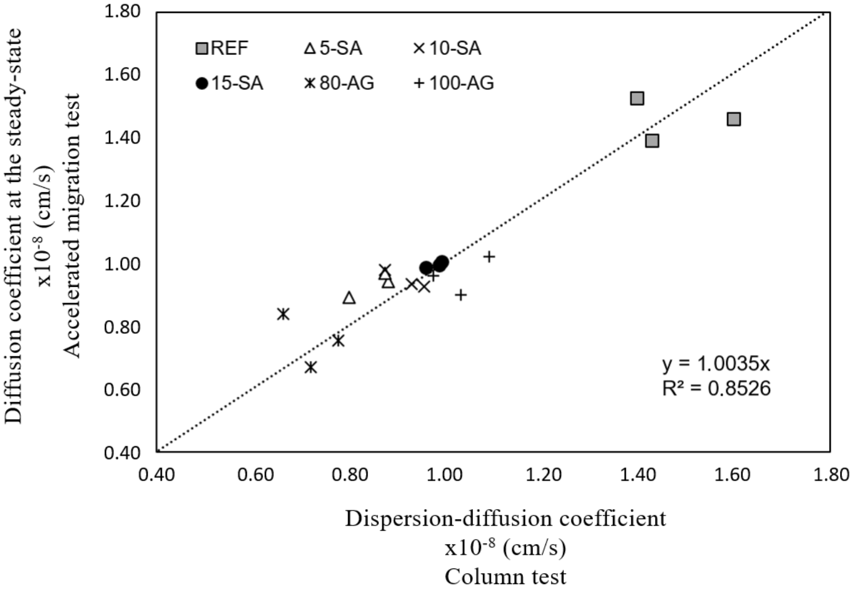


**Figure 12.** Correlation between ion migration tests and column test.

As observed in Figure 12, the data obtained in both tests have a linear correlation, with a significant determination coefficient ($R^2$) of 85.26%. It was also observed that the angular coefficient of the straight-line approaches 1, which would be the value of "perfect correlation", being equal to 1.0035. This means that besides having a good correlation, the values obtained are practically the same indicating that they represent equivalent parameters, despite being based on very distinct physical and methodological foundations.

This evaluation is also confirmed by Pearson's R test, in which the correlations can present values varying from 1 to -1, with the value equal to 1 being a perfect and directly proportional correlation, -1 an inverse proportional perfect correlation, and 0 when there is no correlation. For this test, an R approximately equal to 0.94 was found, indicating a strong direct correlation between the evaluated data ($R \geq 0.70$).

In addition, a good correlation ($R^2$ equal to 75.47%) between the values obtained from the time lag and the retardation factor was obtained (Figure 13) which, despite being numerically and conceptually distinct, measure the capacity to retain contaminants inside the material studied. Unlike the previous correlation, this adjustment may present a linear coefficient different from 0 (zero), because the minimum value of the retardation factor is equal to 1 (one) and, because they are numerically different parameters, the angular coefficient of the straight line is not close to 1.

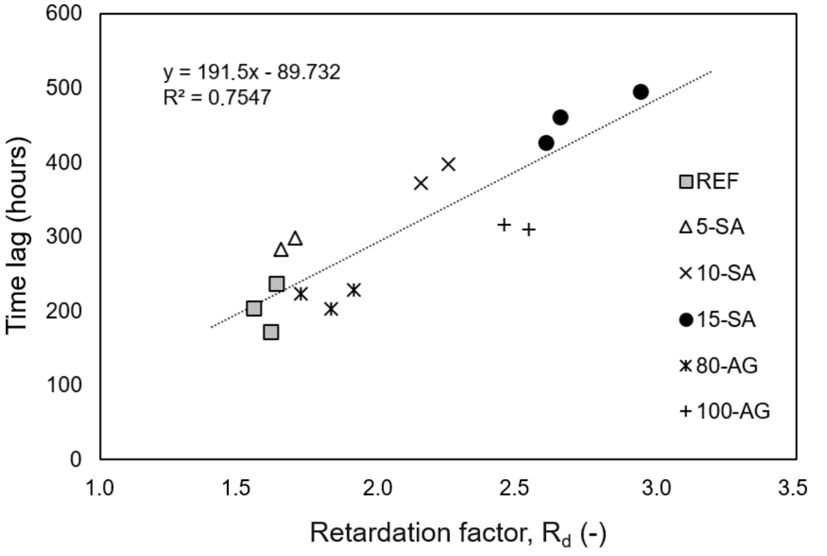


**Figure 13.** Correlation between time lag and retardation factor.

A linear correlation was only possible by removing data that did not obey a normal distribution. The result obtained with Pearson's R confirms the correlation obtained, it demonstrates a strong direct correlation ($R \geq 0.70$) with a value approximately equal to 0.87.

## 4 CONCLUSIONS

Based on the results obtained in this study, it can be concluded that:

- The addition of silica fume to the concrete promoted an increase of up to 126% in the time lag and reduced the chloride flow, compared to the reference concrete;
- The increase in mortar content resulted in a 49% increase in the time lag and reduced the flow of chloride ions when compared to the reference concrete;
- Chloride diffusion coefficients are lower because of the increase in mortar content. Similar behavior was observed when silica fume is added in contents up to 10%, indirectly demonstrating the importance of the transition zone for chloride passage in the matrix;
- The parameters $R_d$ and time lag have similar meaning that indicate the retention capacity of chloride ions in the matrix. The retardation factor ($R_d$) values obtained in column tests are directly proportional to the time lag values obtained in ionic migration tests, regardless of the mortar or silica fume content;
- In spite of the methodological differences between the column test and the ionic migration test, both are demonstrated to be effective in determining chloride diffusion coefficients in concrete and mortars, presenting a strong correlation between the diffusion values obtained;
- The steady-state diffusion coefficients, obtained through ionic migration tests ($D_s$) and column (D) presented practically equal values, indicating that they represent equivalent parameters, despite being based on very different physical and methodological foundations;
- The difference in the voltage used in the migration test (12 VDC) did not significantly affect the measured diffusion values. Therefore, this method can be used in durability design;
- As well as being a faster method, the ionic migration test provides important parameters for concrete quality evaluation, such as time lag and ion flow, making it more versatile than the column test.


## ACKNOWLEDGEMENTS

The authors want to thank FAPESB – Bahia Research Foundation and the PPEC/UFBA – Graduate Program in Civil Engineering at the Federal University of Bahia.

## REFERENCES


[1] U. Angst, B. Elsener, C. K. Larsen, and Ø. Vennesland, "Critical chloride content in reinforced concrete - a review," *Cement Concr. Res.*, vol. 39, pp. 1122–1338, 2009, http://dx.doi.org/10.1016/j.cemconres.2009.08.006.

[2] X. Huang et al., "The effect of supplementary cementitious materials on the permeability of chloride in steam cured high-ferrite Portland cement concrete," *Constr. Build. Mater.*, vol. 197, pp. 99–106, 2019, http://dx.doi.org/10.1016/j.conbuildmat.2018.11.107.

[3] S. M. M. Karein, A. A. Ramezanianpour, T. Ebadi, S. Isapour, and M. Karakouzian, "A new approach for application of silica fume in concrete: Wet granulation," *Constr. Build. Mater.*, vol. 157, pp. 573–581, 2017, http://dx.doi.org/10.1016/j.conbuildmat.2017.09.132.

[4] P. R. L. Helene *Corrosão em armaduras para concreto armado*, São Paulo, Brasil: Pini, 1986.

[5] D. V. Ribeiro, J. A. Labrincha, and M. R. Morelli, "Effect of the addition of red mud on the corrosion parameters of reinforced concrete," *Cement Concr. Res.*, vol. 42, pp. 124–133, 2012, http://dx.doi.org/10.1016/j.cemconres.2011.09.002.

[6] C. D. Shackelford, "Cumulative mass approach for column testing," *J. Geotech. Eng.*, vol. 121, no. 10, pp. 696–703, 1995, http://dx.doi.org/10.1016/0148-9062(96)85062-5.

[7] C. Andrade, "Calculation of chloride diffusion coeficients in concrete from ionic migration measurements," *Cement Concr. Res.*, vol. 23, pp. 724–742, 1993, http://dx.doi.org/10.1016/0008-8846(93)90023-3.

[8] American Society for Testing and Materials, *Standard Test Method for Electrical Indication of Concrete's Ability to Resist Chloride Ion Penetration*, ASTM C 1202, 2019.

[9] Nordtest Method. *Concrete, Mortar and Cement-Based Repair Materials: Chloride Migration Coefficient from Non-Steady-State Migration Experiments*, NT BUILD 492, 1999.

[10] American Society for Testing and Materials, *Standard Test Method for Determining the Apparent Chloride Diffusion Coefficient of Cementitious Mixtures by Bulk Diffusion*, ASTM C 1556, 2016.

[11] American Society for Testing and Materials, *Standard Test Method for Determining the Penetration of Chloride Ion into Concrete by Ponding*, ASTM C 1543, 2002.

[12] J. M. L. Vilasboas, S. L. Machado, S. A. Pinto, and J. S. Oliveira "Penetração de cloretos em argamassas e concretos armados: obtenção de parâmetros relativos ao transporte de substâncias solúveis na camada de cobrimento," In *56° Congr. Bras. Concr.*, 2014, 16 p.

[13] P. Visudmedanukul, M. Kamon, and T. Katsumi, "Chloride transport through cement-bentonite barriers," *J. Geotech. Geoenviron. Eng.*, vol. 133, no. 2, pp. 175–185, 2007, http://dx.doi.org/10.1061/(ASCE)1090-0241(2007)133:2(175).

[14] Associação Brasileira de Normas Técnicas, *Concreto endurecido - Determinação do Coeficiente de Permeabilidade à Água*, NBR 10786:2013, 2013.

[15] Normalización Española, *Durabilidad del Hormigón. Métodos de Ensayo. Determinación de los Coeficientes de Difusión de los iones cloruro en el hormigón endurecido, Método multirrégimen,* UNE 83987, 2014.

[16] Associação Brasileira de Normas Técnicas, *Cimento Portland – Requisitos*, NBR 16697:2018, 2018.

[17] Associação Brasileira de Normas Técnicas, *Concreto para Fins Estruturais - Classificação pela Massa Específica, por Grupos de Resistência e Consistência, NBR 8953:2015*, 2015.

[18] X. Shi, N. Xie, K. Fortune, and J. Gong, "Durability of steel reinforced concrete in chloride environments: An overview," *Constr. Build. Mater.*, vol. 30, pp. 125–138, 2012, http://dx.doi.org/10.1016/j.conbuildmat.2011.12.038.

[19] Y. Yue, J. J. Wang, P. A. M. Basheer, and Y. Bai, "Raman spectroscopic investigation of Friedel's salt," *Cement Concr. Compos.*, vol. 86, pp. 306–314, 2018, http://dx.doi.org/10.1016/j.cemconcomp.2017.11.023.

[20] Associação Brasileira de Normas Técnicas, *Concreto – Ensaio de Compressão de Corpos de Prova Cilíndricos*, NBR 13956-1:2012, 2012.

[21] Associação Brasileira de Normas Técnicas, *Agregado Miúdo - Determinação da Massa Específica e Massa Específica Aparente*, NBR NM 52:2009, 2009.

[22] Associação Brasileira de Normas Técnicas, *Agregado Graúdo - Determinação da Massa Específica, Massa Específica Aparente e Absorção de Água*, NBR NM 53:2009, 2009.

[23] Associação Brasileira de Normas Técnicas, *Agregados - Determinação da Composição Granulométrica*, NBR NM 248:2003, 2003.

[24] Associação Brasileira de Normas Técnicas, *Argamassa e Concreto Endurecidos — Determinação da Absorção de Água por Capilaridade*, NBR 9779:2012, 2012.

[25] Associação Brasileira de Normas Técnicas, *Argamassa e Concreto Endurecidos - Determinação da Absorção de Água, Índice de Vazios e Massa Específica*, NBR 9778:2009, 2009.

[26] American Society For Testing and Materials, *Standard Test Methods for Determining Volume Fraction by Sistematic Manual Point Count*, ASTM E 562, 2011.

[27] M. Castellote, C. Andrade, and C. Alonso, "Measurement of the steady and non-steady-state chloride diffusion coefficients in a migration test by means of monitoring the conductivity in the anolyte chamber - Comparison with natural diffusion tests," *Cement Concr. Res.*, vol. 31, pp. 1411–1420, 2001, http://dx.doi.org/10.1016/S0008-8846(01)00562-2.

[28] N. S. Amorim Jr., G. A. O. Silva, C. R. M. Dias, and D. V. Ribeiro, "Concrete containing recycled aggregates: Estimated lifetime using chloride migration test," *Constr. Build. Mater.*, vol. 222, no. 20, pp. 108–118, 2019, http://dx.doi.org/10.1016/j.conbuildmat.2019.06.136.

[29] C. D. Azevedo, C. R. Nascentes, A. T. Matos, and R. F. Azevedo, "Determination of transport parameters for heavy metal in residual compacted soil using two methodologies," *Can. J. Civ. Eng.*, vol. 33, pp. 912–917, 2006, http://dx.doi.org/10.1139/l06-038.

[30] C. R. Nascentes, "Estudo da mobilidade de metais pesados em um solo residual compactado," Ph.D. thesis, Univ. Fed. de Viçosa, Viçosa, MG, Brasil, 2006.

[31] J. Bear, *Dynamics of Fluids in Porous Media*, New York, United States, Dover Publications, 1988.

[32] J. P. V. Costa, N. F. Barros, A. W. Albuquerque, G. Moura Fo., and J. R. Santos, "Fluxo difusivo de fósforo em função de doses e da umidade do solo," *Rev. Bras. Eng. Agric. Ambient.*, vol. 10, no. 4, pp. 828–835, 2006., http://dx.doi.org/10.1590/S1415-43662006000400007.

[33] C. D. Shackelford, *Contaminant transport, Geotechnical Practice For Waste Disposal*. United Kingdom: Chapman & Hall, pp. 33-65, 1993.

[34] R. A. Freeze and J. A. Cherry, *Groundwater*, Englewood Cliffs, USA: Prentice Hall, vol. 12, pp. 145-165, 1979.

[35] L. Huo, T. Qian, J. Hao, and D. Zhao, "Sorption and retardation of strontium in saturated Chinese loess: experimental results and model analysis," *J. Environ. Radioact.*, vol. 116, pp. 19–27, 2013., http://dx.doi.org/10.1016/j.jenvrad.2012.09.002.

[36] R. Siddique, "Utilization of silica fume in concrete: review of hardened properties," *Resour. Conserv. Recycl.*, vol. 55, no. 11, pp. 923–932, 2011, http://dx.doi.org/10.1016/j.resconrec.2011.06.012.

[37] H. F. Campos, N. S. Klein, J. Marques Fo. and M. Bianchini, "Low-cement high-strength concrete with partial replacement of Portland cement with stone powder and silica fume designed by particle packing optimization", *J. Clean. Prod.*, vol. 261, pp. 121228, 2020, http://dx.doi.org/10.1016/j.jclepro.2020.121228.

[38] M. H. F. Medeiros and P. R. L. Helene, "Surface treatment of reinforced concrete in marine environment: Influence on chloride diffusion coefficient and capillary water absorption," *Constr. Build. Mater.*, vol. 23, no. 3, pp. 1476–1484, 2009., http://dx.doi.org/10.1016/j.conbuildmat.2008.06.013.

[39] K. L. Scrivener, A. K. Crumbie, and P. Laugesen, "The Interfacial Transition Zone (ITZ) between cement paste and aggregate in concrete," *Interface Sci.*, vol. 12, pp. 411–421, 2004., http://dx.doi.org/10.1023/B:INTS.0000042339.92990.4c.

[40] R. Talero et al., "Comparative and semi-quantitative XRD analysis of Friedel's salt originating from pozzolan and Portland cement," *Constr. Build. Mater.*, vol. 25, pp. 2370–2380, 2011., http://dx.doi.org/10.1016/j.conbuildmat.2010.11.037.

[41] P. C. Aïtcin, "The durability characteristics of high performance concrete: a review," *Cement Concr. Compos.*, vol. 25, no. 4-5, pp. 409–420, 2003, http://dx.doi.org/10.1016/S0958-9465(02)00081-1.

[42] P. Halamickova, R. Detwler, D. P. Bentz, and E. J. Garboczi, "Water permeability and chloride ion diffusion in Portland cement mortars: relationship to sand content and critical pore diameter," *Cement Concr. Res. N. Y.*, vol. 25, no. 4, pp. 709–802, 1995, http://dx.doi.org/10.1016/0008-8846(95)00069-O.

[43] K. Wu, J. Long, L. Xu, and G. De Schutter, "A study on the chloride diffusion behavior of blended cement concrete in relation to aggregate and ITZ," *Constr. Build. Mater.*, vol. 223, pp. 1063–1073, 2019, http://dx.doi.org/10.1016/j.conbuildmat.2019.07.068.

[44] L. Nilsson, M. H. Ngo, and O. E. Gjørv "High performance repair materials for concrete structures in the Port of Gothenburg," in *Proceedings, Second International Conference on Concrete under Severe Conditions – Environment and Loading*, London, 1998, pp. 1193–1198.

[45] G. C. Guignone, G. L. Vieira, R. Zulcão, G. Mion, and G. Baptista, "Analysis of the chloride diffusion coefficients by different test methods in concrete mixtures containing metakaolin and high-slag blast-furnace cement," *Rev. Materia*, vol. 24, no. 4, 2019, http://dx.doi.org/10.1590/s1517-707620190004.0837.

[46] F. K. Sell Jr., G. B. Wally, F. R. Teixeira, and F. C. Magalhães, "Experimental assessment of accelerated test methods for determining chloride diffusion coefficient in concrete," *Rev. IBRACON Estrut. Mater.*, vol. 14, no. 4, pp. e14407, 2021, http://dx.doi.org/10.1590/S1983-41952021000400007.

[47] D. V. Ribeiro, S. A. Pinto, N. S. Amorim Jr., J. S. Andrade No, I. H. L. Santos, S. L. Marques and M. J. S. França, "Effects of binders characteristics and concrete dosing parameters on the chloride diffusion coefficient," *Cement Concr. Compos.*, vol. 122, pp. 104114, 2021, http://dx.doi.org/10.1016/j.cemconcomp.2021.104114.

[48] A. Farahani, H. Taghaddos and M. Shekarchi, "Prediction of long-term chloride diffusion in silica fume concrete in a marine environment," *Cement Concr. Compos.*, vol. 59, pp. 10–17, 2015, http://dx.doi.org/10.1016/j.cemconcomp.2015.03.006.

[49] A. Neville, "Good reinforced concrete in the Arabian Gulf," *Mater. Struct.*, vol. 33, pp. 655–664, 2000., http://dx.doi.org/10.1007/BF02480605.

[50] M. Shekarchi, A. Rafiee, and H. Layssi, "Long-term chloride diffusion in silica fume concrete in harsh marine climates," *Cement Concr. Compos.*, vol. 31, pp. 769–775, 2009., http://dx.doi.org/10.1016/j.cemconcomp.2009.08.005.

[51] A. Tang and O. C. Sandall, "Diffusion coefficient of chlorine in water at 25-60 ºC," *Chem. Eng. J.*, vol. 30, pp. 189–191, 1995, http://dx.doi.org/10.1021/je00040a017.

---

**Author contributions:** SAP, SLM and DVR: conceptualization, formal analysis, methodology; SAP: data curation, writing; SLM and DVR: supervision, writing - review.

**Editors:** Lia Pimentel, Guilherme Aris Parsekian.

Rev. IBRACON Estrut. Mater., vol. 15, no. 3, e15308, 2022

IBRACON Structures and Materials Journal
Revista IBRACON de Estruturas e Materiais
ISSN 1983-4195 ismj.org

ORIGINAL ARTICLE

# Reliability analysis of slender columns using the general method with linear creep theory

*Análise da confiabilidade de pilares esbeltos usando o método geral com a teoria linear da fluência*

Kleyser Ribeiro[a]
Daniel Domingues Loriggio[a]
Mauro de Vasconcellos Real[b]

[a]Universidade Federal de Santa Catarina – UFSC, Florianópolis, SC, Brasil
[b]Universidade Federal do Rio Grande – FURG, Rio Grande, RS, Brasil

Received 21 April 2021
Accepted 11 October 2021

**Abstract:** To analyze the reliability of slender columns subjected to axial force and uniaxial bending moment, with a slenderness index between 100 and 140, 216 columns were modeled. The square cross-section was adopted, with three different configurations for longitudinal reinforcement. In the calculation, the general method with the linear creep theory was applied. Several factors were varied: slenderness index, reinforcement ratio, steel bars arrangement, compressive strength of concrete, and first-order relative eccentricity. For analysis purposes, the Monte Carlo method was adopted, followed by the First Order Reliability Method (FORM). Considering the results obtained, it was observed that the reliability index is usually higher for lower reinforcement ratios and varies according to the configuration of the cross-section.

**Keywords:** slender columns, reliability, general method, Monte Carlo, FORM.

**Resumo:** Buscando-se analisar a confiabilidade de pilares esbeltos submetidos a flexo-compressão normal, com índice de esbeltez entre 100 e 140, realizou-se a modelagem de 216 elementos. Adotou-se a seção transversal quadrada, com três configurações distintas para armadura longitudinal. No cálculo, aplicou-se o método geral com a teoria linear da fluência. Efetuou-se a variação de diversos fatores, incluindo-se: índice de esbeltez, taxa de armadura, disposição das barras de aço, resistência do concreto e excentricidade relativa de primeira ordem. Para fins de análise, adotou-se o método de Monte Carlo seguido pelo FORM. Considerando-se os resultados obtidos, observou-se que o índice de confiabilidade comumente é maior para taxas de armadura inferiores e sofre variação de acordo com a configuração da seção transversal.

**Palavras-chave:** pilares esbeltos, confiabilidade, método geral, Monte Carlo, FORM.

**How to cite:** K. Ribeiro, D. D. Loriggio, and M. V. Real, "Reliability analysis of slender columns using the general method with linear creep theory," *Rev. IBRACON Estrut. Mater.*, vol. 15, no. 3, e15308, 2022, https://doi.org/10.1590/S1983-41952022000300008

## 1 INTRODUCTION

To evaluate the reliability of slender reinforced concrete columns, designed according to the Brazilian Standard NBR 6118 [1], a numerical analysis was conducted with 216 columns, and these columns were modeled to failure exclusively for this research. For the parametric analysis, the following variations were considered: slenderness index, compressive strength of concrete, first-order relative eccentricity, reinforcement ratio, and arrangement of steel bars in the cross-section.

The study was limited to columns of square cross-section, constant along with the height, with slenderness index between 100 and 140. Cantilever columns with compressive load and moment due to the force eccentricity were

**Corresponding author:** Kleyser Ribeiro. E-mail: kleyser.ribeiro@gmail.com
**Financial support:** None.
**Conflict of interest:** Nothing to declare.
**Data Availability:** The data that support the findings of this study are available from the corresponding author, KR, upon reasonable request.

considered. The general method was used in all cases, determining the moment-curvature relationship and, subsequently, calculating the second-order local effects by finite difference method.

The numeric analysis was proposed to answer the question "what is the influence of the longitudinal reinforcement on the reliability of slender columns?" The main objective was to analyze the structural reliability of columns with a slenderness index between 100 and 140 to verify whether the safety level is adequate for building design.

This study is justified by the current usual slenderness of elements designed in buildings in Brazil, mainly with high strength concrete. Besides, there is few research emphasizing columns with a slenderness index greater than 90, designed including creep behavior and accurately considering physical and geometric nonlinearities.

Among the methodological procedures, computational development and numerical simulations were adopted, followed by statistical methods to analyze the results, based on Magalhães [2], Damas [3] and Barbosa [4].

## 2 GENERAL METHOD

The general method is defined as the one in which both physical and geometric nonlinearities are considered precisely. Therefore, the curvature in each section is determined using the moment-curvature relationship. Regarding the second-order local effects, it was decided to implement the finite difference method.

### 2.1 Moment-curvature relationship

The moment-curvature relationship was implemented based on Ribeiro [5], according to the flowchart in Figure 1.

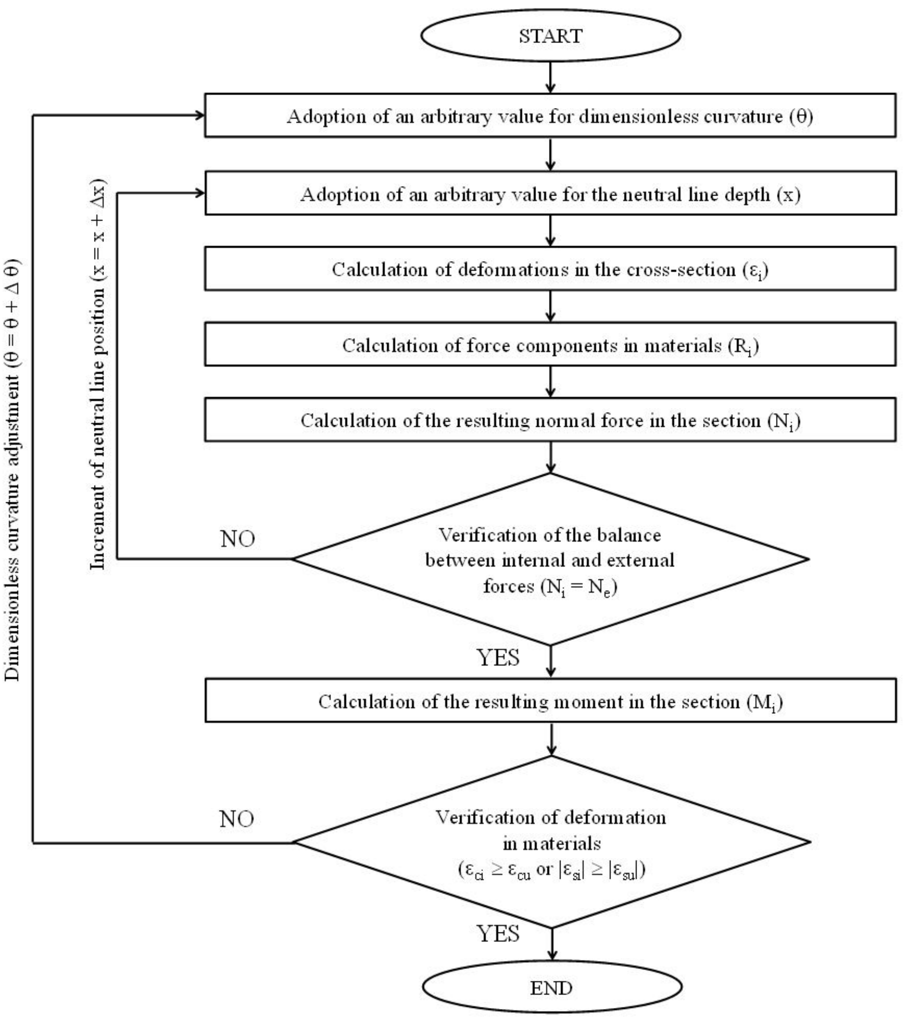


**Figure 1.** Flowchart of the moment-curvature relationship.

The dimensionless curvature θ was defined from Equation 1, depending on the overall depth of the cross-section h and the curvature 1/r. The curvature, as usually defined in the fundamentals of Solid Mechanics, is given by Equation 2.

$$\theta = 1000\, h \frac{1}{r} \tag{1}$$

$$\frac{1}{r} = \frac{M}{EI} \tag{2}$$

where M is the section bending moment and EI represents the flexural stiffness.

Two curves were considered for design, considering either the limit of $0.85f_{cd}$ or $1.10f_{cd}$, according to the Brazilian Standard NBR 6118 [1]. The design value of the concrete compressive strength ($f_{cd}$) is the quotient between the concrete characteristic compressive strength ($f_{ck}$) and the concrete partial material safety factor, given by $\gamma_c = 1.4$. In this case, the second curve is limited to the ultimate design moment ($M_{Rd}$) determined from the first. The moment-curvature relationship for design situations is shown in Figure 2.

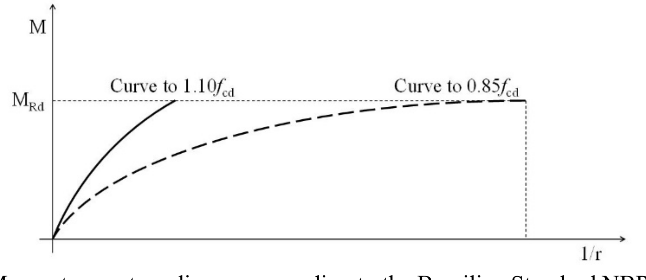


**Figure 2.** Moment-curvature diagram according to the Brazilian Standard NBR 6118 [1].

For mechanical modeling purposes, the safety factors are not used, and some adjustments must be made in the diagram, aiming to simulate the actual physical behavior of the columns. To determine the ultimate load, corresponding to the maximum load in experimental tests, the curve coefficients are not used in the numerical model either. In this case, a single curve is drawn using the average concrete compressive strength $f_{cm}$ instead of $f_{cd}$ and the ultimate moment is determined.

## 2.2 Finite Difference Method

Second-order effects were determined using the finite difference method. Given a cantilever column of length L, the member is divided into n equidistant sections of Δx, positioning the origin of the Cartesian system according to Figure 3.

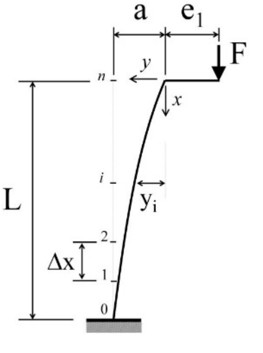


**Figure 3.** Cantilever column for application of the finite difference method.

The values of the normal force (F) and the first-order eccentricity ($e_1$) were admitted constant, with the variation of the maximum displacement (a) at the column top from zero until convergence. It was assumed that $y_0 = a$. Equation 3 is used to calculate the displacement ($y_i$) in section i = 1 and Equation 4 for the other points. The calculation algorithm is represented in the flowchart in Figure 4.

$$y_1 = y_0 - \frac{\Delta x^2}{2}\left(\frac{1}{r}\right)_0 \quad \text{if } i = 1 \tag{3}$$

$$y_{i+1} = 2y_i - y_{i-1} - \Delta x^2\left(\frac{1}{r}\right)_i \quad \text{if } i > 1 \tag{4}$$

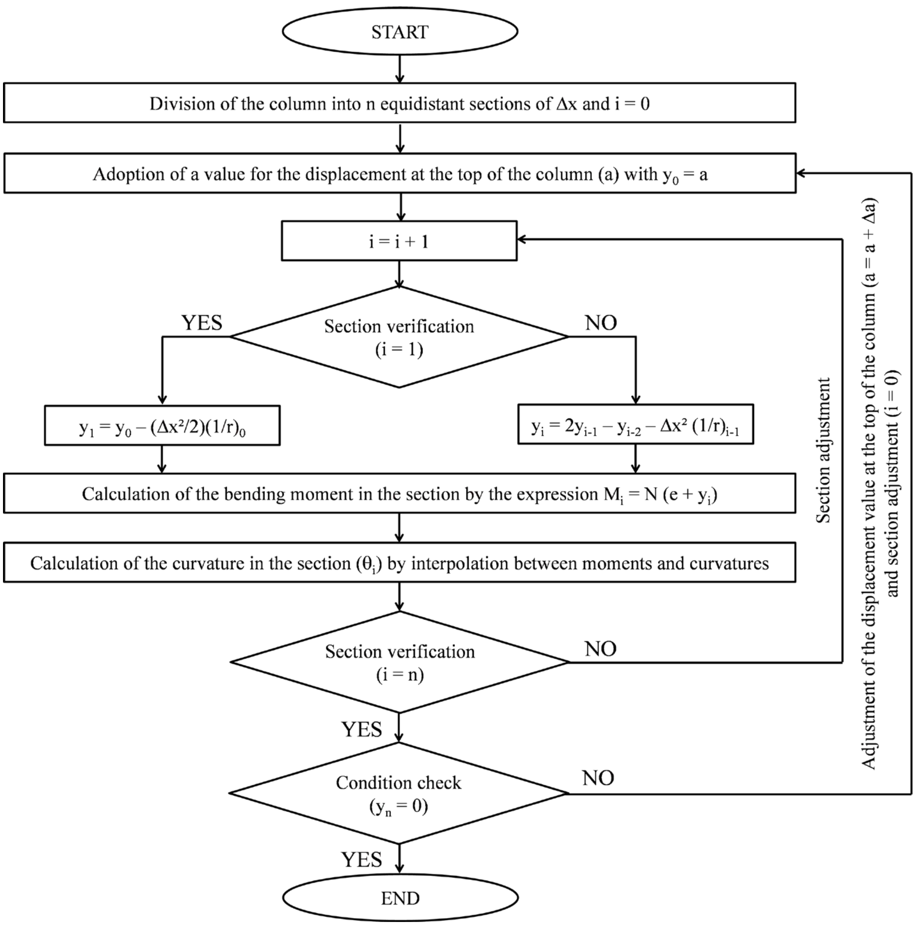


**Figure 4.** Flowchart of the finite difference method.

## 3 CONSTITUTIVE MODELS

### 3.1 Constitutive design models

#### 3.1.1 Constitutive model of concrete

To verify the design strength, the parabola-rectangle diagram proposed by the Brazilian Standard NBR 6118 [1] was considered to represent the behavior of the concrete subjected to compression, as shown in Figure 5, where $\sigma_c$ represents the stresses and $\varepsilon_c$ represents the strains. The creep displacement was considered according to the linear creep theory adopting a creep coefficient. In practice, the effective creep coefficient $\phi_{ef} = 1.18$ was used, referring to the creep coefficient $\phi = 2$ and the condition in which 75% of the loads are of long-term, based on Fusco [6] and Casagrande [7].

The creep coefficient value was kept constant in all columns modeled allowing to analyze the influence of the other parameters. The concrete design strength, $f_{cd}$, must be calculated from Equation 5 as a function of the characteristic compressive strength of concrete ($f_{ck}$), where $\gamma_c$ = 1.4 was admitted. This constitutive relationship is valid for $20 \leq f_{ck} \leq 90$ MPa and can be represented by Equations 6 to 9.

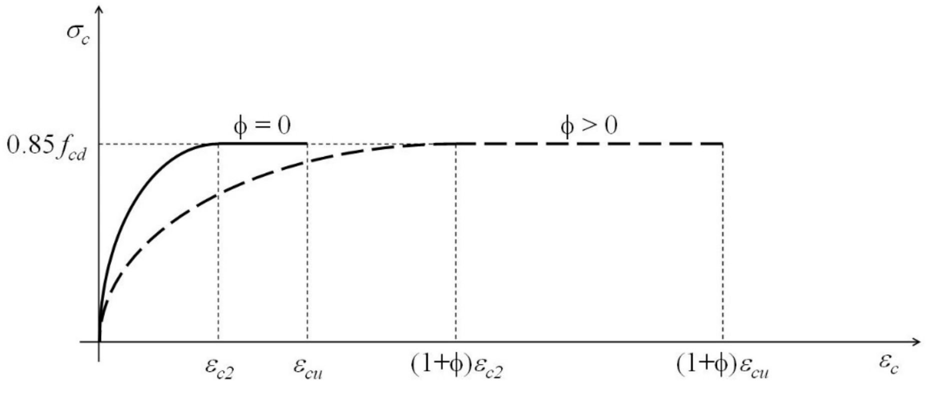


**Figure 5.** Simplified stress-strain diagram of concrete with creep.

$$f_{cd} = \frac{f_{ck}}{\gamma_c} \tag{5}$$

$$\sigma_c = 0.85\, f_{cd}\left[1 - \left(1 - \frac{\varepsilon_c}{\varepsilon_{c2}}\right)^n\right] \text{ for } 0 \leq \varepsilon_c \leq \varepsilon_{c2} \tag{6}$$

$$\sigma_c = f_{cd} \text{ for } \varepsilon_{c2} < \varepsilon_c \leq \varepsilon_{cu} \tag{7}$$

where

$$n = 2 \text{ if } f_{ck} \leq 50MPa \tag{8}$$

$$n = 1.4 + 23.4\left[(90 - f_{ck})/100\right]^4 \text{ if } f_{ck} > 50MPa \tag{9}$$

Concerning the deformation limits, the values were calculated from Equations 10 to 13.

$$\varepsilon_{c2} = 2.0\text{ ‰} \text{ if } f_{ck} \leq 50MPa \tag{10}$$

$$\varepsilon_{c2} = \left\{2.0 + 0.085(f_{ck} - 50)^{0.53}\right\}\text{ ‰} \text{ if } f_{ck} > 50MPa \tag{11}$$

$$\varepsilon_{cu} = 3.5\text{ ‰} \text{ if } f_{ck} \leq 50MPa \tag{12}$$

$$\varepsilon_{cu} = \left\{2.6 + 35\left[(90 - f_{ck})/100\right]^4\right\}\text{ ‰} \text{ if } f_{ck} > 50MPa \tag{13}$$

However, these values are changed by creep using the effective coefficient $\phi_{ef}$, according to Equations 14 and 15.

$$\varepsilon_{c2,ef} = (1 + \phi_{ef})\varepsilon_{c2} \tag{14}$$

$$\varepsilon_{cu,ef} = (1 + \phi_{ef})\varepsilon_{cu} \tag{15}$$

### 3.1.2 Constitutive model of steel

The simplified stress-strain diagram of Brazilian Standard NBR 6118 [1] for longitudinal reinforcement was adopted, considering the perfect elasto-plastic behavior of steel for reinforced concrete, as shown in Figure 6. It should be noted that this reinforcement diagram is valid for both compression and tension. The models consider $f_{yk}$ = 500 MPa for the characteristic yield strength of reinforcement, $E_s$ = 210 GPa for the design value of modulus of elasticity of reinforcing steel, and $\varepsilon_{su}$ = 10‰ for the ultimate strain.

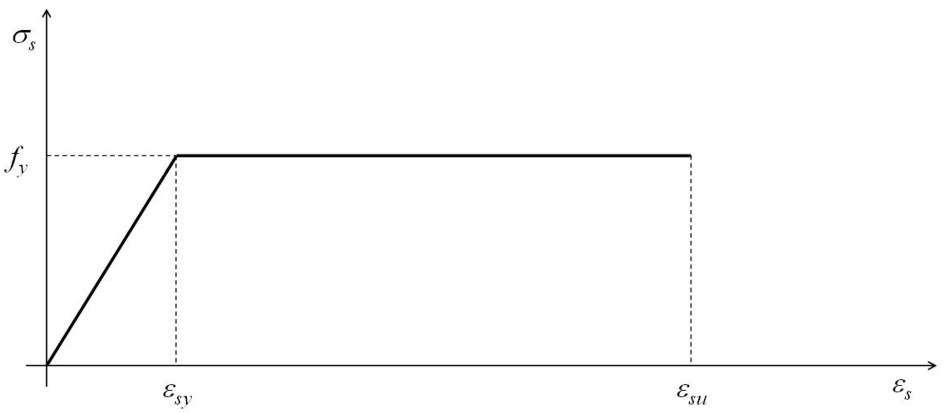


**Figure 6.** Simplified stress-strain diagram for longitudinal reinforcement.

For design situations, the design yield strength of reinforcement $f_{yd}$ was calculated from Equation 16, where $\gamma_s$ = 1.15 is admitted as the partial factor for reinforcing steel.

$$f_{yd} = \frac{f_{yk}}{\gamma_s} \tag{16}$$

### 3.2 Mechanical model

For determining the ultimate loads, the constitutive model presented in item 3.1.2 was used for longitudinal reinforcement without the safety coefficients. For concrete, the models shown below were used.

### 3.2.1 Compression in concrete

The non-linear model of Eurocode 2 [8] for the concrete subjected to compression was used to represent the column behavior in rupture, as shown in Figure 7. This constitutive model can be represented by Equations 17 to 19, using the average value of concrete compressive strength $f_{cm}$ and the secant modulus of elasticity of concrete $E_{cm}$.

$$\frac{\sigma_c}{f_{cm}} = \frac{k\,\eta - \eta^2}{1 + (k - 2)\,\eta} \tag{17}$$

where

$$\eta = \frac{\varepsilon_c}{\varepsilon_{c1}} \tag{18}$$

$$k = 1.05 \frac{E_{cm}}{f_{cm}} \left|\varepsilon_{c1}\right| \tag{19}$$

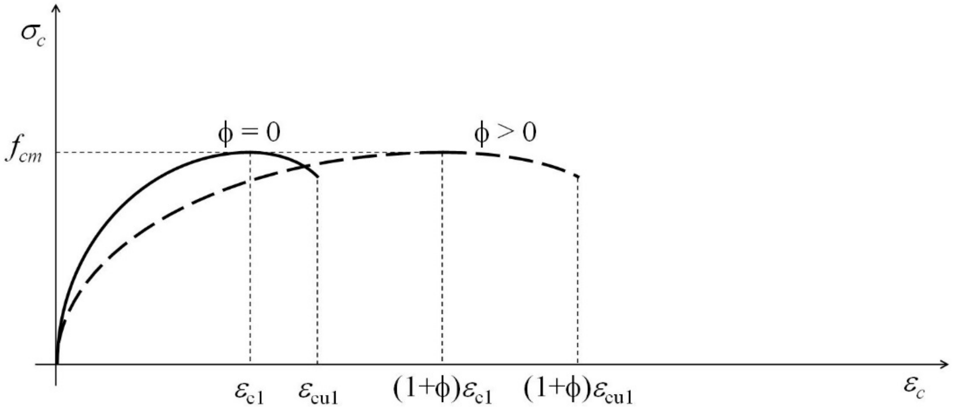


**Figure 7.** Constitutive model for non-linear analysis with creep.

In Figure 7, $\varepsilon_c$ is the compressive strain, $\varepsilon_{c1}$ represents the compressive strain at the peak stress, and $\varepsilon_{cu}$ represents the ultimate compressive strain in the concrete.

The values of $E_{cm}$, $\varepsilon_{c1}$ and $\varepsilon_{cu1}$ were obtained from Equations 20 to 23, considering the value of $f_{cm}$ in MPa.

$$E_{cm} = 22\left(f_{cm} / 10\right)^{0.3} GPa \tag{20}$$

$$\varepsilon_{c1} = 0.7\, f_{cm}{}^{0.31}\ ‰ \leq\ 2.8\ ‰ \tag{21}$$

$$\varepsilon_{cu1} = 3.5\ ‰\ \text{ if } f_{ck} \leq 50MPa \tag{22}$$

$$\varepsilon_{cu1} = \left\{2.8 + 27\left[\left(98 - f_{cm}\right)/100\right]^4\right\}‰\ \text{ if } f_{ck} > 50MPa \tag{23}$$

Also, creep effects must be considered, according to Equations 24 and 25.

$$\varepsilon_{c1,ef} = \left(1 + \phi_{ef}\right)\varepsilon_{c1} \tag{24}$$

$$\varepsilon_{cu1,ef} = \left(1 + \phi_{ef}\right)\varepsilon_{cu1} \tag{25}$$

### 3.2.2 Tension in concrete

The tensile strength and the tension-stiffening effect of the concrete were admitted, based on the simplified model adapted by Baptista [9] from Collins and Mitchell [10]. This model is shown in Figure 8, where $f_{cr}$ represents the cracking stress, $\varepsilon_{cr}$ represents the strain corresponding to the cracking, and $\varepsilon_{sy}$ represents the yield strain of reinforcement.

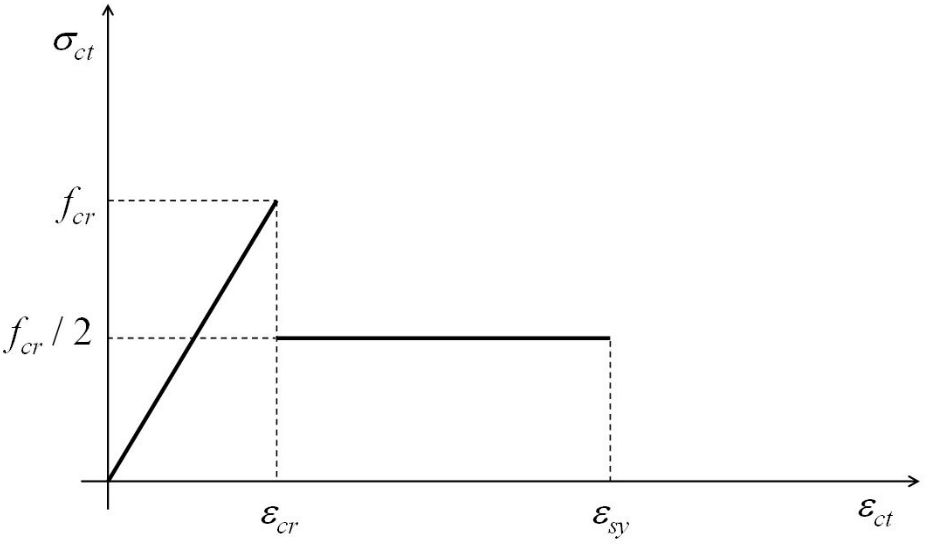


**Figure 8.** Constitutive model for tension in concrete with tension-stiffening effect.

For the cracking stress $f_{cr}$, the flexural tensile strength $f_{ctm,fl}$ of Eurocode 2 [8] was considered, with the application of Equation 26.

$$f_{ctm,fl} = \max\left\{(1.6 - h/1000) f_{ctm};\, f_{ctm}\right\} \tag{26}$$

where h is the overall depth of the section in mm and $f_{ctm}$ is the mean axial tensile strength given by Equations 27 and 28.

$$f_{ctm} = 0.30 f_{ck}^{2/3} \text{ if } f_{ck} \leq 50MPa \tag{27}$$

$$f_{ctm} = 2.12 \ln\left(1 + (f_{cm}/10)\right) \text{ if } f_{ck} > 50MPa \tag{28}$$

In Equation 27, $f_{ck}$ is used, while in Equation 28, $f_{cm}$ is used. The considered relationship between the two variables is given in Equation 29.

$$f_{cm} = f_{ck} + 8(MPa) \tag{29}$$

It is considered that the tension stresses act in a rectangular block, corresponding to the effective tension area of the cross-section, based on Eurocode 2 [8], as shown in Figure 9. The block is defined by the width of the cross-section b and the effective tension depth $h_{c,ef}$, given by Equation 30.

$$h_{c,ef} = \min\left\{2.5(h - d);\, \frac{h - y_{LN}}{3}\right\} \tag{30}$$

where h is the overall depth of the cross-section, d is the effective depth of the cross-section, and $y_{LN}$ is the depth of the neutral line in relation to the most compressed fiber.

Then, it is possible to obtain the effective tension area $A_{c,ef}$ by Equation 31.

$$A_{c,ef} = b h_{c,ef} \tag{31}$$

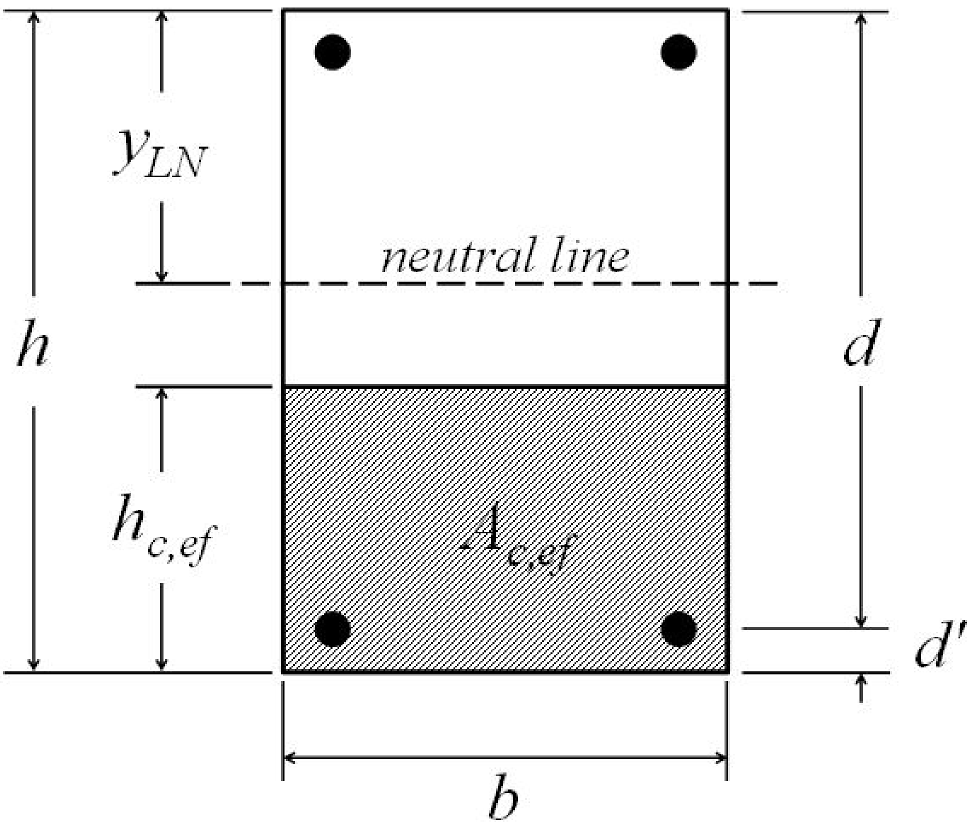


**Figure 9.** Rectangular block corresponding to the effective tension area.

## 4 ANALYSIS PROCESS

### 4.1 Random variables

Throughout the numerical tests, the following random variables were admitted, width of the cross-section (b), overall depth of the cross-section (h), effective depth of the cross-section (d), compressive strength of concrete ($f_c$), yield strength of reinforcement ($f_y$), permanent loading ($F_g$) and variable loading ($F_q$).

In this case, they are not mean, characteristic, or design values. Random variables are those for which values are generated from a draw that follows a probability density function (PDF). In turn, this function is defined based on an analysis of the behavior of the considered physical quantity. Therefore, a nomenclature is used to differentiate such values, generated by drawing lots, from their respective representative values. The randomly generated values correspond to the values that would actually occur in the structure, without any coefficient.

The probability density function adopted for each variable, as well as the mean ($\mu$) and standard deviation ($\sigma$) of the respective distribution, were chosen according to Table 1, based on Magalhães et al. [11], Damas [3] and Barbosa [4]. All distributions of random variables were automatically generated by the computational algorithm developed.

**Table 1.** Random variables.

| Random variable | Distribution | Mean (μ) | Standard deviation (σ) |
|---|---|---|---|
| Compressive strength of concrete ($f_c$) | Normal | $\mu_{f_c} = \frac{f_{ck}}{1 - 1.645 V_{f_c}}$ where $V_{f_c} = 0.10$ | $\sigma_{f_c} = \mu_{f_c} V_{f_c}$ where $V_{f_c} = 0.10$ |
| Yield strength of reinforcement ($f_y$) | Normal | $\mu_{f_y} = 1.09 f_{yk}$ | $\sigma_{f_y} = 0.05 \mu_{f_y}$ |
| Width of the cross-section (b) | Normal | $\mu_b = b$ (nominal design value) | $\sigma_b = 0.5$ cm |
| Overall depth of the cross-section (h) | Normal | $\mu_h = h$ (nominal design value) | $\sigma_h = 0.5$ cm |
| Effective depth of the cross-section (d), taking d < h | Normal | $\mu_d = d$ (nominal design value) | $\sigma_d = 0.5$ cm |
| Permanent load ($F_g$) | Normal | $\mu_{F_g} = 1.05 F_{gk}$ | $\sigma_{F_g} = 0.10 \mu_{F_g}$ |
| Variable load ($F_q$) | Gumbel max. | $\mu_{F_q} = F_{qk}$ (characteristic value) | $\sigma_{F_q} = 0.25 \mu_{F_q}$ |

### 4.2 Analysis procedure

The Monte Carlo method was used to determine the mean, standard deviation, and probability distribution for the ultimate loads of the mechanical model ($F_{u,mod}$). Through the analysis of the moving average, it was observed that statistical convergence occurs from two hundred tests, in most cases. For standardization purposes, five hundred simulations were adopted for all columns, as in Magalhães [2], Damas [3], and Barbosa [4]. Subsequently, the FORM was adopted based on data obtained by the Monte Carlo method.

The design load combination was considered, according to Equation 32, based on the Brazilian Standard NBR 8681 [12].

$$F_{Sd} = \gamma_g F_{gk} + \gamma_q F_{qk} \tag{32}$$

where $F_{Sd}$ is the maximum design load that can be applied to the column, $\gamma_g = 1.4$ represents the partial factor for permanent loads, and $\gamma_q = 1.4$ represents the partial factor for variable loads. This consideration is only valid for grouped loads referring to buildings whose accidental loads do not exceed 5 kN/m$^2$, in accordance with the Brazilian Standard NBR 8681 [12].

The process used for reliability analysis by Monte Carlo and FORM is shown in the Figure 10. To calculate the average values of the permanent and variable loads from the load combinations, the inverse process is conducted, so that the safety factors are removed to allow comparison with the failure values. For all cases, the FORM is applied using the mean value, the standard deviation value, and the corresponding probability distribution of the failure loads, determined by the Monte Carlo method.

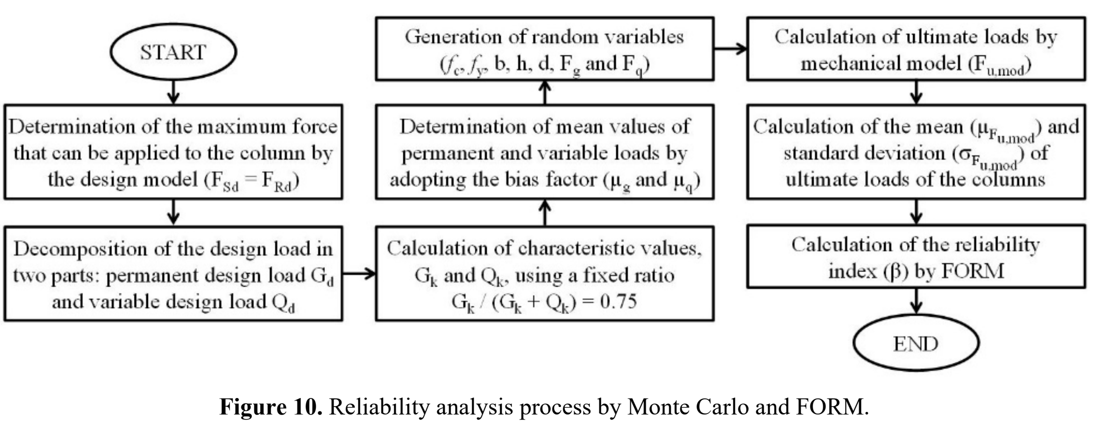


**Figure 10.** Reliability analysis process by Monte Carlo and FORM.

### 4.3 Model error

According to Magalhães [2], the model error ($e_{model}$) considers the imprecision of the numerical model used in the analysis. Its value can be estimated using Equation 33, based on Mirza and Skrabek [13], and Magalhães [2]. For this purpose, the coefficient of variation of column strength due to inaccuracies in the theoretical model $V_{model}$ is calculated using Equation 34.

$$e_{model} = \mu_{model}\left(1 + z\,V_{model}\right) \tag{33}$$

where $\mu_{model}$ = 1.0 and z is a Gaussian random variable with zero mean and standard deviation equal to one.

$$V_{model} = \sqrt{V_{t/c}^{\,2} - V_{in\text{-}batch}^{\,2} - V_{test}^{\,2}} \tag{34}$$

where $V_{t/c}$ is the coefficient of variation of the ratio of test to computed strengths, $V_{in\text{-}batch}$ is the coefficient of variation of column strength due to in-batch variabilities of all variables affecting its strength, and $V_{test}$ is the coefficient of variation of column strength due to testing procedures. Based on data from the columns considered in this article, it was assumed that $V_{test}$ = 0.04 and $V_{in\text{-}batch}$ = 0.044.

Then, the corrected value of the ultimate loads ($F_u$) is obtained by Equation 35.

$$F_u = e_{model}\,F_{u,mod} \tag{35}$$

### 4.4 FORM

When the probability distribution of the variables is known, the First Order Reliability Method (FORM) can be used. Based on Szerszen and Nowak [14], the general format of the limit state function presented in Equation 36 was adopted.

$$g = R - S = e_{model}\,F_{u,mod} - \left(F_g + F_q\right) \tag{36}$$

where g is the safety margin, R is the resistance (ultimate load), and S represents the effects of the load given by a combination of load components.

From Equation 36, a limit state surface is defined when g = 0, separating the failure domain (g < 0) from the safety domain (g > 0). The FORM algorithm of Magalhães [2] was used to determine the reliability index β, according to the flowchart in Figure 11.

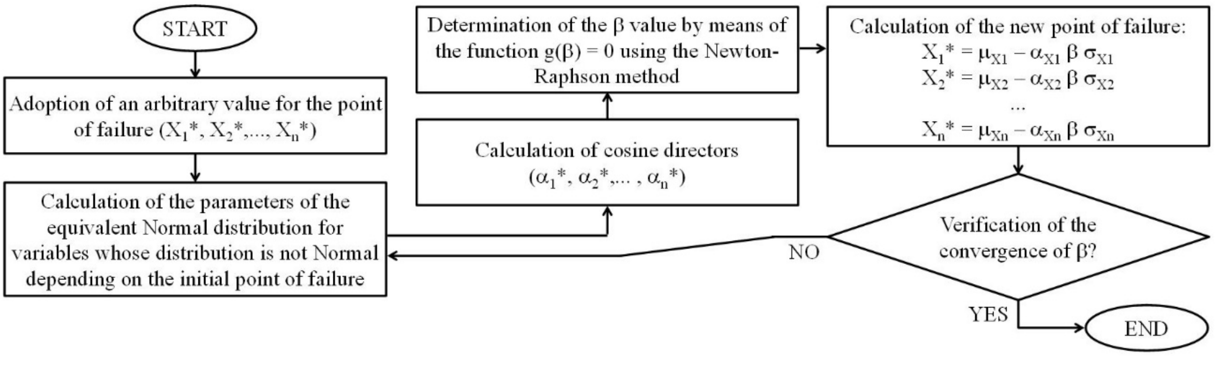


**Figure 11.** Flowchart of the FORM algorithm.

## 5 MODEL VALIDATION

It is necessary to validate the mechanical model for its use in determining the ultimate loads. For this, a summary of characteristics of the columns considered in the model validation is shown in Table 2, where n indicates the number of columns for each reference, including the value of concrete compressive strength $f_c$ measured in the tests and provided by the authors, reinforcement ratio ρ, slenderness index λ, and first-order relative eccentricity $e_1/h$.

**Table 2.** Main characteristics of the columns considered in the model validation.

| Reference | n | Cross-section (cm x cm) | $f_c$ (MPa) | ρ (%) | λ | $e_1/h$ |
|---|---|---|---|---|---|---|
| Short-term loading | | | | | | |
| Claeson and Gylltoft [15] | 12 | 12×12 or 20×20 | 33.0 to 93.0 | 1.99 to 3.11 | 52 to 69 | 0.10 to 0.17 |
| Dantas [16] | 5 | 25×12 | 33.9 to 37.6 | 1.57 | 87 | 0.12 to 0.50 |
| Enciso [17] | 4 | 25×15 | 46.9 to 53.6 | 1.26 to 4.29 | 69 | 0.13 |
| Goyal and Jackson [18] | 26 | 7.62×7.62 | 19.9 to 23.6 | 1.72 to 2.45 | 55 to 125 | 0.17 to 0.50 |
| Kim and Lee [19] | 4 | 10×10 or 20×10 | 27.0 | 2.13 to 2.84 | 42 | 0.40 |
| Kim and Yang [20] | 18 | 8×8 | 25.5 to 86.2 | 1.98 to 3.95 | 62 to 104 | 0.30 |
| Melo [21] | 17 | 25×12 | 37.2 to 45.8 | 1.57 | 58 to 87 | 0.05 to 0.50 |
| Sustained loading | | | | | | |
| Goyal and Jackson [18] | 20 | 7.62×7.62 | 19.9 to 23.6 | 1.72 to 2.45 | 55 to 125 | 0.17 to 0.50 |
| Kordina [22] | 10 | $26.4 \leq b \leq 27.2$<br>$17.2 \leq h \leq 17.6$ | 20.9 to 27.1 | 0.98 to 3.19 | 101 to 104 | 0.20 to 0.50 |
| Ramu et al. [23] | 8 | 25×15 | 21.5 to 37.2 | 1.66 to 4.21 | 100 | 0.03 to 0.25 |

The model results $F_{mod}$ were compared with the experimental values $F_{exp}$ of 124 columns, obtaining the ratio $F_{exp}/F_{mod}$. Square and rectangular section columns were considered, with different reinforcement arrangements. As it can be seen in Table 2, elements subjected to short-term and sustained loadings were considered.

For all columns with a rectangular cross-section, the element was subjected to an eccentric compression load applied in the direction of the lowest moment of inertia. The effective creep coefficient $\phi_{ef}$ was calculated for the columns subjected to sustained loading, whose value varied between 0.75 and 1.60. This value was obtained from data from columns subjected to long-term load considered for validation purposes, being a variable value dependent on several parameters.

Based on Klein et al. [24], the set of values was divided into groups to verify the distribution of the experimental database for the main characteristics to be considered in the parametric analysis, as shown in Figure 12. Despite noting that the distribution of data is not uniform, results were obtained within the various groups considered. It is also noteworthy that thirty-eight columns were subjected to sustained loading, allowing the analysis of the effects of concrete creep.

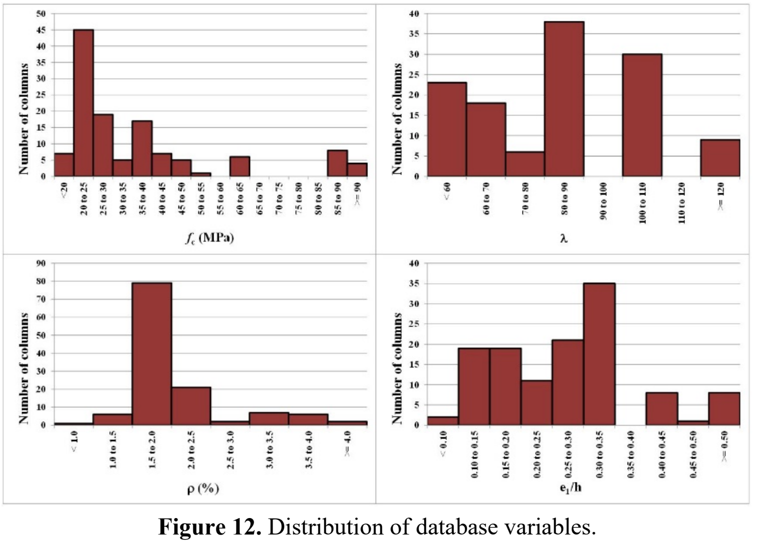


**Figure 12.** Distribution of database variables.

Thus, it can be supposed that the parameters considered to determine the model error can adjust the behavior of the mechanical model to the experimental data. Finally, it is observed that the results obtained are consistent with the results of the experimental tests, as shown in Table 3.

**Table 3.** Statistical synthesis of results of the validation process.

| Ratio | Minimum | Maximum | Range | Mean | Standard deviation | $V_{model}$ |
|---|---|---|---|---|---|---|
| $F_{exp}$ / $F_{mod}$ | 0.75 | 1.31 | 0.56 | 0.99 | 0.10 | 0.08 |

## 6 NUMERICAL RESULTS

### 6.1 Numerical test program

To conduct the numerical test program, the characteristics of the elements to be assessed are defined. The square cross-section was chosen, with the reinforcement arrangements shown in Figure 13.

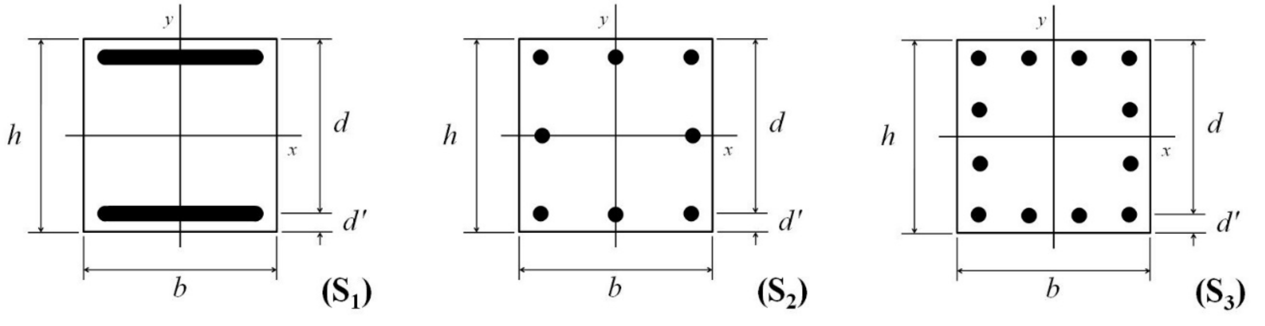


**Figure 13.** Cross-sections of the columns considered in the research.

For testing purposes, a square cross-section with a width of 40 cm was adopted. The experiment was divided into two groups according to the compressive strength of concrete. In each group, 108 models were defined from the variation of the parameters, totaling 216 elements.

In all columns, b = 40 cm, h = 40 cm, and d' = 6.0 cm (d'/h = 0.15) were considered. The reinforcement ratio (ρ) was varied from 0.75 to 3.00%. Three levels of slenderness were considered, varying the length of the element, adopting the slenderness index (λ) between 100 and 140. For the first-order relative eccentricity ($e_1/h$), ratios between 0.12 and 0.24 were adopted. Finally, 30 and 60 MPa were adopted for the characteristic compressive strength of concrete ($f_{ck}$).

Concerning the general method, the cross-section was divided into twenty horizontal strips for integration purposes. The variation $\Delta\theta = 1$ was adopted, with a precision of 0.1 for the curvature related to the rupture, with the depth of the neutral line varying by 0.1 cm. The column was divided into ten sections to determine the second-order local effects by the finite difference method, with an initial displacement value at the top equal to zero and an increase of 0.001 cm in the iterative process.

### 6.2 Numerical test results

The results obtained for the reliability index β of the columns analyzed in the numerical tests are shown in Table 4. The cross-section is indicated by the letter S followed by a number corresponding to the respective drawing shown in Figure 13.

**Table 4.** Reliability index of the tested columns.

| Cross-section | $e_1/h$ | ρ (%) | $f_{ck}$ = 30 MPa | | | $f_{ck}$ = 60 MPa | | |
|---|---|---|---|---|---|---|---|---|
| | | | Slenderness ratio (λ) | | | Slenderness ratio (λ) | | |
| | | | 100 | 120 | 140 | 100 | 120 | 140 |
| S1 | 0.12 | 0.75 | 4.15 | 4.15 | 4.26 | 3.87 | 3.93 | 3.99 |
| | | 1.50 | 3.77 | 3.84 | 3.82 | 3.65 | 3.67 | 3.71 |
| | | 2.25 | 3.53 | 3.53 | 3.56 | 3.48 | 3.47 | 3.50 |
| | | 3.00 | 3.47 | 3.32 | 3.36 | 3.37 | 3.33 | 3.35 |
| | 0.18 | 0.75 | 4.02 | 4.14 | 4.27 | 3.99 | 4.16 | 4.31 |
| | | 1.50 | 3.58 | 3.57 | 3.63 | 3.52 | 3.59 | 3.70 |
| | | 2.25 | 3.47 | 3.38 | 3.29 | 3.36 | 3.31 | 3.32 |
| | | 3.00 | 3.51 | 3.30 | 3.21 | 3.35 | 3.23 | 3.17 |
| | 0.24 | 0.75 | 3.88 | 3.98 | 4.02 | 4.01 | 4.11 | 4.36 |
| | | 1.50 | 3.60 | 3.49 | 3.41 | 3.50 | 3.51 | 3.53 |
| | | 2.25 | 3.49 | 3.38 | 3.31 | 3.45 | 3.35 | 3.29 |
| | | 3.00 | 3.54 | 3.29 | 3.26 | 3.29 | 3.30 | 3.19 |
| S2 | 0.12 | 0.75 | 4.27 | 4.33 | 4.41 | 3.97 | 4.04 | 4.17 |
| | | 1.50 | 3.96 | 4.04 | 4.04 | 3.81 | 3.86 | 3.88 |
| | | 2.25 | 3.71 | 3.73 | 3.77 | 3.65 | 3.64 | 3.70 |
| | | 3.00 | 3.53 | 3.52 | 3.56 | 3.47 | 3.47 | 3.51 |
| | 0.18 | 0.75 | 4.26 | 4.38 | 4.50 | 4.16 | 4.35 | 4.59 |
| | | 1.50 | 3.75 | 3.77 | 3.81 | 3.73 | 3.80 | 3.93 |
| | | 2.25 | 3.56 | 3.52 | 3.50 | 3.48 | 3.48 | 3.52 |
| | | 3.00 | 3.52 | 3.38 | 3.39 | 3.39 | 3.33 | 3.33 |
| | 0.24 | 0.75 | 4.08 | 4.16 | 4.34 | 4.21 | 4.38 | 4.65 |
| | | 1.50 | 3.75 | 3.61 | 3.67 | 3.62 | 3.74 | 3.71 |
| | | 2.25 | 3.57 | 3.54 | 3.47 | 3.55 | 3.45 | 3.48 |
| | | 3.00 | 3.53 | 3.43 | 3.39 | 3.47 | 3.42 | 3.32 |
| S3 | 0.12 | 0.75 | 4.30 | 4.40 | 4.45 | 3.99 | 4.01 | 4.20 |
| | | 1.50 | 4.00 | 4.07 | 4.09 | 3.80 | 3.88 | 3.91 |
| | | 2.25 | 3.74 | 3.79 | 3.83 | 3.67 | 3.68 | 3.73 |
| | | 3.00 | 3.55 | 3.56 | 3.58 | 3.49 | 3.51 | 3.56 |
| | 0.18 | 0.75 | 4.29 | 4.43 | 4.54 | 4.18 | 4.38 | 4.60 |
| | | 1.50 | 3.77 | 3.81 | 3.90 | 3.72 | 3.82 | 3.97 |
| | | 2.25 | 3.57 | 3.55 | 3.55 | 3.54 | 3.52 | 3.58 |
| | | 3.00 | 3.53 | 3.44 | 3.39 | 3.44 | 3.37 | 3.36 |
| | 0.24 | 0.75 | 4.15 | 4.25 | 4.37 | 4.22 | 4.48 | 4.70 |
| | | 1.50 | 3.74 | 3.66 | 3.74 | 3.66 | 3.77 | 3.74 |
| | | 2.25 | 3.60 | 3.58 | 3.50 | 3.61 | 3.48 | 3.54 |
| | | 3.00 | 3.52 | 3.49 | 3.41 | 3.52 | 3.42 | 3.35 |

## 7 RESULTS ANALYSIS

For the analysis of the obtained results, curves were drawn that relate the reliability index and the reinforcement ratio, as shown in Figure 14. It is also possible to evaluate the variation in the slenderness index and the compressive strength of concrete, among other parameters.

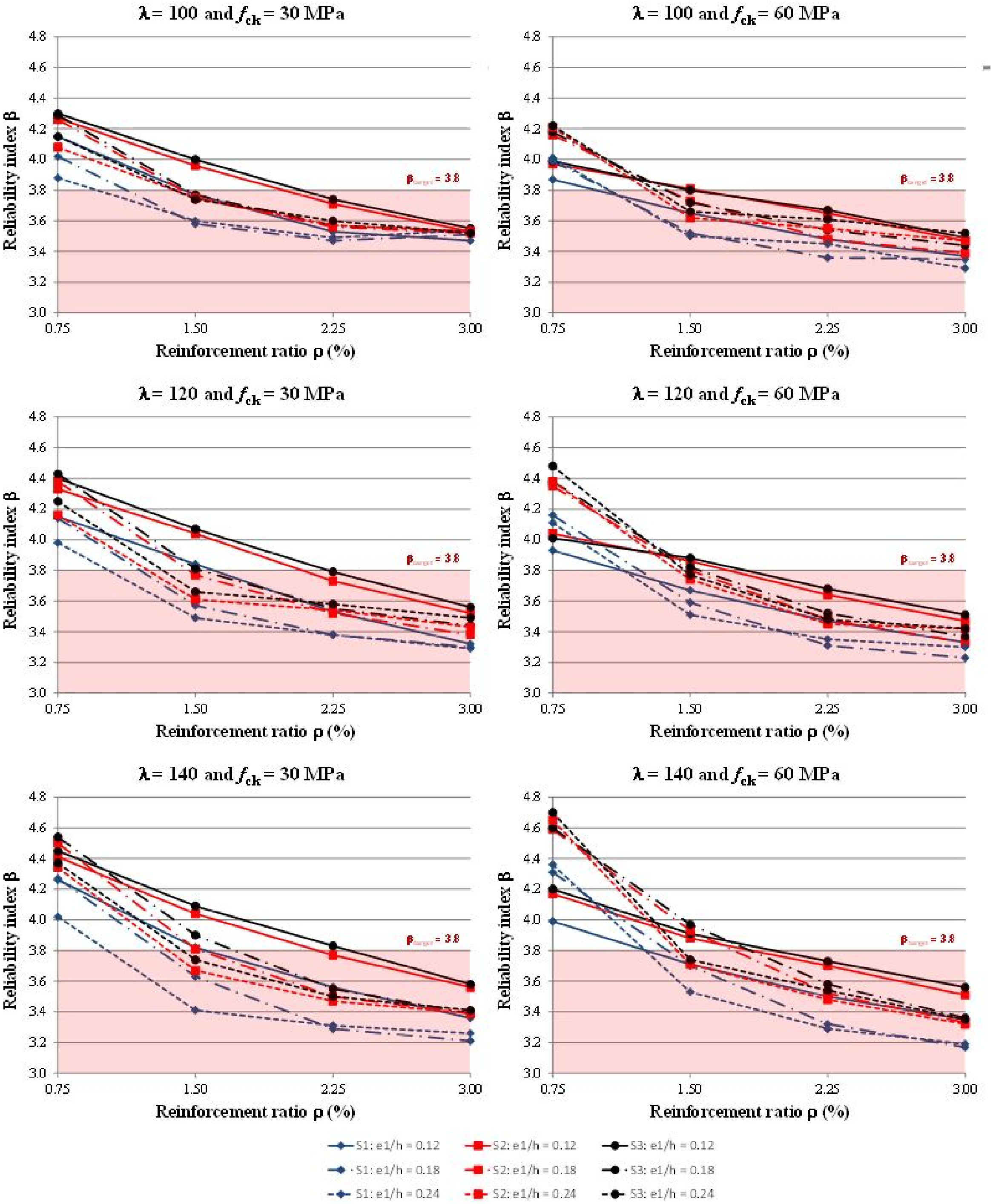


**Figure 14.** Comparative analysis of results.

In general, there is a reduction in reliability as the reinforcement ratio increases. Concerning the first-order relative eccentricity, the reliability index tends to be higher for smaller eccentricities ($e_1/h = 0.12$), but this can change for reduced reinforcement ratios.

Considering the target reliability index $\beta_{target}$ recommended by Model Code 2010 [25], for the 50 years reference period and the ultimate limit state with a high consequence of failure, $\beta_{target} = 4.3$ should be adopted. For the medium consequence of failure, $\beta_{target} = 3.8$ is recommended. In turn, if the relative cost of safety measure is moderate, $\beta_{target} = 3.8$ can be adopted for a great consequence of failure. It is not recommended to use smaller values due to the high probability of failure. The Brazilian Standard NBR 6118 [1] does not mention the target reliability index. For this reason, the value recommended by the Model Code 2010 [25] is used as a reference.

When analyzing Table 4, together with Figure 14, it is observed that the average reliability index is equal to 3.76 and the median is equal to 3.62 for $f_{ck}$ = 30 MPa. That is, the values obtained are close to 3.8. For $f_{ck}$ = 60 MPa, the situation is similar, with a mean of 3.71 and a median of 3.63.

It is observed that all columns with a reinforcement ratio ρ equal to 0.75% have a reliability index higher than 3.8 for $f_{ck}$ = 30 MPa and $f_{ck}$ = 60 MPa. On the other hand, all columns with a reinforcement ratio equal to 3.00% have a lower reliability index. It is considered that it would be important to improve the design criteria of the Brazilian Standard NBR 6118 [1] to obtain higher values for the reliability index of columns, to meet the design recommendations.

According to Nowak and Collins [26], the safety margin is determined from the difference between the resistance R and the load effect S, allowing the determination of the probability of failure. To analysis, the probability density function curves were plotted for columns with $f_{ck}$ = 30 MPa, λ = 120 and $e_1/h = 0.18$. The reinforcement ratio ρ and the reinforcement arrangement in the cross-section were varied, as shown in Figure 15, where S indicates the load effect; R indicates resistance; $\mu_S$ and $\sigma_S$ indicate the mean and standard deviation of the load effect; $\mu_R$ and $\sigma_R$ indicate the mean and standard deviation of the resistance; S1, S2, and S3 indicate the cross-section; 0.75% and 3.00% indicate the respective reinforcement ratio.

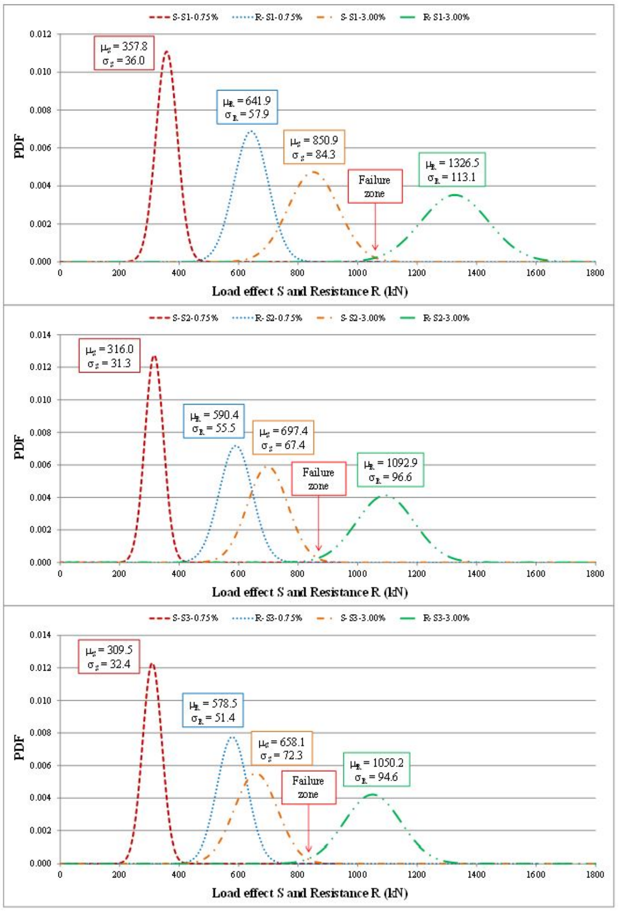


**Figure 15.** Analysis of load effect and resistance by probability density function (PDF).

It is observed graphically that the probability of failure $P_F$ increases with the increase in the reinforcement ratio ρ, as a greater region of overlap (failure zone) between the load effect and the resistance curves is visualized. An analysis of the load effect S, resistance R, and the respective safety margin g (R, S) can be performed by determining the respective mean μ, standard deviation σ and coefficient of variation COV values, as shown in Table 5.

**Table 5.** Analysis of load effect, resistance, and safety margin.

| Parameter | Measure | Cross-section S1 $f_{ck}$ = 30 MPa λ = 120 $e_1/h$ = 0.18 | | | Cross-section S2 $f_{ck}$ = 30 MPa λ = 120 $e_1/h$ = 0.18 | | | Cross-section S3 $f_{ck}$ = 30 MPa λ = 120 $e_1/h$ = 0.18 | | |
|---|---|---|---|---|---|---|---|---|---|---|
| | | (1) ρ = 0.75% | (2) ρ = 3.00% | Ratio (2)/(1) | (3) ρ = 0.75% | (4) ρ = 3.00% | Ratio (4)/(3) | (5) ρ = 0.75% | (6) ρ = 3.00% | Ratio (6)/(5) |
| **Load effect S** | **μ** (kN) | 357.8 | 850.9 | 2.38 | 316.0 | 697.4 | 2.21 | 309.5 | 658.1 | 2.13 |
| | **σ** (kN) | 36.0 | 84.3 | 2.34 | 31.3 | 67.4 | 2.15 | 32.4 | 72.3 | 2.23 |
| | **COV** | 0.10 | 0.10 | 0.98 | 0.10 | 0.10 | 0.98 | 0.10 | 0.11 | 1.05 |
| **Resistance R** | **μ** (kN) | 641.9 | 1326.5 | 2.07 | 590.4 | 1092.9 | 1.85 | 578.5 | 1050.2 | 1.82 |
| | **σ** (kN) | 57.9 | 113.1 | 1.95 | 55.5 | 96.6 | 1.74 | 51.4 | 94.6 | 1.84 |
| | **COV** | 0.09 | 0.09 | 0.95 | 0.09 | 0.09 | 0.94 | 0.09 | 0.09 | 1.01 |
| **Safety margin g (R, S)** | **μ** (kN) | 284.1 | 475.6 | 1.67 | 274.4 | 395.5 | 1.44 | 269.0 | 392.1 | 1.46 |
| | **σ** (kN) | 68.2 | 141.1 | 2.07 | 63.7 | 117.8 | 1.85 | 60.8 | 119.1 | 1.96 |
| | **COV** | 0.24 | 0.30 | 1.24 | 0.23 | 0.30 | 1.28 | 0.23 | 0.30 | 1.34 |

In Table 5, columns with $f_{ck}$ = 30 MPa, λ = 120 and $e_1/h$ = 0.18 are considered, for cross-sections S1, S2 and S3. It is observed that the coefficient of variation regarding the load effect is practically the same for all cases. The same occurs with the coefficient of variation of the resistance. However, the mean and standard deviation value increases more sharply for the load effect than the resistance as the reinforcement ratio increases. In this way, the safety margin is reduced, and the reliability index is also reduced.

Therefore, the reliability index reduction is justified by the increase of the load with the reinforcement ratio. This increases the variable load effect, which has the highest coefficient of variation among all random variables. Besides, it is noteworthy that the increase in load leads to a significant rise in second-order effects on slender columns.

It should be noted that, for a previously established reinforcement ratio, the design load is determined according to the NBR 6118 [1] recommendations. It can be seen from Table 5 that the design load obtained with the Brazilian Standard prescriptions increases more sharply than the ultimate load determined by the mechanical model for this slenderness interval.

With the increase in the reinforcement ratio, there is a more significant increase in the load effect in relation to the resistance, as can be seen in Table 5. Therefore, it is observed that the greater variability of the load effect generates a region of higher risk of failure, something that can be seen in Figure 14.

About the cross-section, it is observed that the sections S2 and S3, with reinforcement distributed along the faces, offer a higher reliability index than the section S1, with only two lines of reinforcement. Although S1 presents greater resistance, the distribution of steel bars of the longitudinal reinforcement on the cross-section faces, as in cross-sections S2 and S3, reduced the mean and standard deviation in both the load effect and resistance. Consequently, there is a reduction in the standard deviation of the safety margin. Also, the load increasing due to the reinforcement ratio increasing is not as significant in S2 and S3 as in S1.

## 8 CONCLUSIONS

The general method was presented using the moment-curvature relationship and the finite difference method to consider physical and geometric nonlinearity, respectively. According to the linear creep theory, creep was evaluated with the displacement obtained in the concrete stress-strain diagram in this model. In general, it is emphasized that these are iterative processes that require computational implementation.

A mechanical model was developed to determine the ultimate loads, considering the non-linear model of Eurocode 2 [8] for concrete subjected to compression and the simplified model adapted by Baptista [9] from Collins and Mitchell [10] for tension in concrete, with tension-stiffening effect. For longitudinal reinforcement steel, the perfect elasto-plastic model was considered.

Regarding numerical tests, it was observed that the reliability index varies according to the reinforcement arrangement and the reinforcement ratio in the cross-section. Higher levels of safety were verified for sections with reinforcement distributed on the faces instead of just two reinforcement lines. The cross-sections with lower reinforcement ratios showed a higher reliability index, with a reduction of the same as the reinforcement ratio increases.

It is observed that the increase in resistance does not necessarily increase the reliability index. This is because structural reliability depends on a statistical analysis that considers the resistance to rupture in the mechanical model and the value of the design load.

In the analysis of the target reliability index, it was observed that it would be necessary to evaluate the implementation of an additional safety coefficient in the Brazilian Standard NBR 6118 [1] for columns with slenderness index between $\lambda = 90$ and $\lambda = 140$. Such normative inclusion would increase the reliability index of very slender columns to ensure that its design leads to safety levels according to technical recommendations.

Finally, it is intended to evaluate a more considerable number of columns in the future, covering a broader range regarding the compressive strength of concrete and the slenderness index.

## ACKNOWLEDGEMENTS

The author K. Ribeiro thanks the Universidade Federal de Santa Catarina (UFSC), the Coordenação de Aperfeiçoamento de Pessoal de Nível Superior (Capes), and the Universidade do Estado de Santa Catarina (UDESC). The author M. de V. Real thanks the Conselho Nacional de Desenvolvimento Científico e Tecnológico (CNPq) for the research grant (Process 304211/2018-4).

## REFERENCES

[1] Associação Brasileira de Normas Técnicas, *Projeto de Estruturas de Concreto – Procedimento*, NBR 6118:2014, 2014.

[2] F. C. Magalhães, “A problemática dos concretos não conformes e sua influência na confiabilidade de pilares de concreto armado,” Ph.D. dissertation, PPGEC, UFRGS, Porto Alegre, 2014.

[3] A. P. Damas, “Estudo de confiabilidade no projeto de pilares esbeltos de concreto de alta resistência,” M.S. thesis, PPGEC, UFRGS, Porto Alegre, 2015.

[4] P. R. O. Barbosa, “Análise probabilística de pilares de concreto armado através do método dos elementos finitos,” M.S. thesis, PPGEC, UFRGS, Porto Alegre, 2017.

[5] K. Ribeiro, “Diagramas para verificação de pilares retangulares em concreto armado submetidos à flexão composta normal,” M.S. thesis, PPGEC, UFSC, Florianópolis, 2011.

[6] P. B. Fusco, *Estruturas de Concreto: Solicitações Normais*. Rio de Janeiro: Guanabara Dois, 1981.

[7] A. F. Casagrande, “Consideração da fluência no cálculo dos efeitos de segunda ordem em pilares de concreto armado,” M.S. thesis, PPGEC, UFSC, Florianópolis, 2016.

[8] European Committee for Standardization, *Eurocode 2: Design of Concrete Structures - Part 1-1: General Rules and Rules for Buildings*, EN 1992-1-1:2004, 2004.

[9] F. M. S. Baptista, “Análise de flechas imediatas e diferidas de vigas em concreto armado,” M.S. thesis, PPGEC, UFSC, Florianópolis, 2018.

[10] M. P. Collins and D. Mitchell, *Prestressed Concrete Basics*. Ontario: Can. Prestressed Concr. Inst., 1987.

[11] F. C. Magalhães, M. V. Real, and L. C. P. Silva Fo., "The problem of non-compliant concrete and its influence on the reliability of reinforced concrete columns," *Mater. Struct.*, vol. 49, pp. 1485–1497, 2015., http://dx.doi.org/10.1617/s11527-015-0590-x.

[12] Associação Brasileira de Normas Técnicas, *Ações e Segurança nas Estruturas – Procedimento*, NBR 8681:2003, 2003.

[13] S. A. Mirza and B. W. Skrabek, "Reliability of short composite beam-column strength interaction," *J. Struct. Eng.*, vol. 117, no. 8, pp. 2320–2339, Aug 1991, http://dx.doi.org/10.1061/(ASCE)0733-9445(1991)117:8(2320).

[14] M. M. Szerszen and A. S. Nowak, "Calibration of design code for buildings (ACI 318): part 2 – reliability analysis and resistance factors," *ACI Struct. J.*, vol. 100, no. 3, pp. 383–391, May-Jun 2003, http://dx.doi.org/10.14359/12614.

[15] C. Claeson and K. Gylltoft, "Slender high-strength concrete columns subjected to eccentric loading," *J. Struct. Eng.*, vol. 124, pp. 233–240, Mar 1998, http://dx.doi.org/10.1061/(ASCE)0733-9445(1998)124:3(233).

[16] A. B. Dantas, “Estudo de pilares de concreto armado submetidos à flexão composta reta,” M.S. thesis, PECC, UnB, Brasília, 2006.

[17] R. O. Enciso, “Comportamento de pilares esbeltos de concreto de alta resistência sujeitos à flexão composta reta,” M.S. thesis, PPGEC, PUC-Rio, Rio de Janeiro, 2010.

[18] B. B. Goyal and N. Jackson, "Slender concrete columns under sustained load," *J. Struct. Div.*, vol. 97, no. 11, pp. 2729–2750, Nov 1971, http://dx.doi.org/10.1061/JSDEAG.0003050.

[19] J.-K. Kim and S.-S. Lee, "The behavior of reinforced concrete columns subjected to axial force and biaxial bending," *Eng. Struct.*, vol. 22, no. 11, pp. 1518–1528, Nov 2000, http://dx.doi.org/10.1016/S0141-0296(99)00090-5.

[20] J.-K. Kim and J.-K. Yang, "Buckling behaviour of slender high-strength concrete columns," *Eng. Struct.*, vol. 17, no. 1, pp. 39–51, 1995, http://dx.doi.org/10.1016/0141-0296(95)91039-4.

[21] C. E. L. Melo, "Análise experimental e numérica de pilares birrotulados de concreto armado submetidos a flexo-compressão normal," Ph.D. dissertation, PECC, UnB, Brasília, 2009.

[22] K. Kordina, *Langzeitversuche an Stahlbetonstützen*. Braunschweig: Inst. Baustoffkunde und Stahlbetonbau, Tech. Univ. Braunschweig, June 1972.

[23] P. Ramu, M. Grenacher, M. Baumann, and B. Thürlimann, *Versuche an Gelenkig Gelagerten Stahlbetonstützen unter Dauerlast*. Zürich: Institut für Baustatik, Eidgenössische Technische Hochschule Zürich, 1969, https://doi.org/10.3929/ethz-a-004170564.

[24] O. Klein Jr., F. R. Stucchi, and R. L. Barbosa, "Evaluation of Brazilian standard ABNT NBR 6118 procedures for calculating the second-order effects of reinforced concrete slender columns subjected to uniaxial bending," *Struct. Concr.*, vol. 21, no. 1, pp. 81–93, Feb 2020, http://dx.doi.org/10.1002/suco.201800251.

[25] Fédération Internationale du Béton, *Model Code 2010: Final Draft, vol. 1* (Bulletin 65). Lausanne, March 2012.

[26] A. S. Nowak and K. R. Collins, *Reliability of Structures*. Boston: McGraw-Hill, 2000.

**Author contributions:** KR: conceptualization, methodology, computational programming, numerical tests, results analysis, writing; DDL: conceptualization, methodology, results analysis, supervision; MVR: conceptualization, methodology, results analysis, supervision.

**Editors:** Yuri Villagrán Zaccardi, Guilherme Aris Parsekian.

**IBRACON Structures and Materials Journal**
Revista IBRACON de Estruturas e Materiais
ISSN 1983-4195 ismj.org

ORIGINAL ARTICLE

# Short columns composed of concrete-filled steel tubes in a fire situation – Numerical model and the "air-gap" effect

*Pilares curtos compostos por tubos de aço preenchido com concreto em situação de incêndio – Modelo numérico e efeito do "air-gap"*

Fábio Masini Rodrigues[a]
Armando Lopes Moreno Júnior[a]
Jorge Munaiar Neto[b]

[a]Universidade de Campinas – UNICAMP, Department of Structures, Campinas, SP, Brasil.
[b]Escola de Engenharia de São Carlos – ESC, Universidade de São Paulo – USP, Department of Structural Engineering, São Carlos, SP, Brasil.

Received 10 January 2021
Accepted 18 October 2021

**Abstract:** The increase in temperature reduces the strength of steel and concrete, in such a way that it is essential to verify concrete-filled steel tube columns in fire situations. Numerical simulations, with lower costs than laboratory tests, have great importance in checking resistance and defining simplified methods for design practice. However, peculiarities of the thermal and mechanical behavior of heated confined concrete and the air-gap effect (a phenomenon inherent to concrete-filled steel columns) must still be better understood. Therefore, this study presents the development of a numerical model performed in the ABAQUS software (Dassault Systemes SIMULIA Corp., 2014) for the thermomechanical analysis of short columns composed of circular and square concrete-filled steel tubes considering the air-gap effect. The air-gap phenomenon is presented and analyzed according to possibilities of implementation to the numerical model and, finally, the proposed numerical model is validated with experimental results presented in the literature. According to the study results, the numerical model can be used to define and adjust simplified methods for verification of composite columns in fire situation. The importance of considering the air-gap effect in numerical modeling was confirmed, taking into account that disregarding its effect may result in overestimated responses of the steel tube resistance in fire situations. Moreover, it was suggested thermomechanical joint analysis and the use of the explicit solver as a strategy to minimize processing time.

**Keywords:** composite column, fire, numerical model.

Resumo: A verificação da resistência ao fogo de pilares tubulares preenchidos com concreto é necessária, uma vez que há uma drástica redução na resistência do aço e do concreto com a elevação da temperatura. A simulação numérica, com inquestionáveis vantagens econômicas em relação aos ensaios em laboratório, tem grande importância na verificação da resistência e na definição e ajustes de modelos analíticos para uso na prática de projeto. Entretanto, parâmetros intervenientes como o comportamento térmico e mecânico do concreto confinado quando aquecido ou mesmo do chamado "air-gap", fenômeno inerente a pilares de aço preenchidos com concreto quando aquecidos, ainda carecem de melhor aprofundamento quanto à modelagem numérica. Para tanto, neste trabalho, apresenta-se o desenvolvimento de um modelo numérico no software ABAQUS (Dassault Systemes SIMULIA Corp., 2014), para análise térmico-mecânica de pilares curtos compostos por tubos de aço de seção circular e quadrada, preenchidos com concreto, considerando o efeito do"air-gap". O fenômeno do "air-gap" é apresentado e discutido em função das possibilidades de implementação no modelo numérico e, por fim, o modelo desenvolvido é validado por meio de resultados experimentais retirados da literatura. Com base nos resultados obtidos, se conclui que o modelo numérico pode ser utilizado para avaliação, ajustes e desenvolvimento de processos simplificados para verificação de pilares mistos em situação de incêndio; sendo recomendada a análise conjunta térmico-mecânica e a utilização do solver explicit como estratégia para minimizar o tempo de processamento. Aimportância da consideração

**Corresponding author:** Fábio Masini Rodrigues. E-mail: fabiosecfmr@gmail.com
**Financial support:** None.
**Conflict of interest:** Nothing to declare.
**Data Availability:** the data that support the findings of this study are available from the corresponding author, FMR, upon reasonable request.

do efeito do "air-gap" foi confirmada e desprezar o seu efeito pode resultar em avaliação superestimada da capacidade resistente do tubo de aço em situação de incêndio.

**Palavras-chave:** pilare misto, fogo, modelo numérico.

**How to cite:** F. M. Rodrigues, A. L. Moreno Júnior and J. Munaiar Neto, "Short columns composed of concrete-filled steel tubes in a fire situation – Numerical model and the "air-gap" effect," *Rev. IBRACON Estrut. Mater.*, vol. 15, no. 3, e15309, 2022, https://doi.org/10.1590/S1983-41952022000300009

# 1. INTRODUCTION

The columns composed of tube filled with concrete have proved to be an interesting structural solution in combining the benefits of both materials, including with regard to fire resistance [1], [2] and their use can be observed in buildings and bridge structures [3]–[5].

However, with the drastic reduction in the strength of steel and concrete with elevated temperature, further studies are needed to mitigate the possibility of accidents of catastrophic proportions.

Numerical tests are of great importance to chevk the resistance of structural members in a fire situation and in defining and adjusting simplified methods to design practice, reducing the need for many experimental tests, examples that can be found in the literature [6]–[9]. Furthermore, normative references refer to numerical models without deepening and detailing the parameters for the development of the numerical model, as verified in eurocode standards and Brazilian standards [10], [11].

The effect called air-gap occurs in columns composed of steel tubes filled with concrete when heated and consist in the formation of a gap between the steel tube and the concrete. The air-gap is basically formed by the expansion of the cross section, which occurs differently for steel and concrete, due to the properties of each material. The intensity of the axial force and the concrete shrinkage can contribute to the gap formation even before heating. Some numerical and experimental studies have been developed to simulate the effect of air-gap [8], [12], [13]. However, difficulties presented in the literature, such as the precision in determining material properties and modeling parameters, the complexity of representing the behavior of concrete at high temperatures, the movement of the water flow contained in the concrete, among others, make the phenomenon still uncertain.

The radiation heat transfer mechanism must be considered in the steel-concrete interface, since disregarding it leads to less accurate models. However, the adoption of wrong values of emissivity can deviate the results of the numerical models from those experimentally investigated [14].

Ghojel [15] carried out studies on the air-gap effect and presented tests with circular concrete-filled steel tubes specimens, heated in an electric oven to the temperature of 900 °C. The author describes that at the steel-concrete interface, joint thermal conductance ($h_j$) can be considered as the sum of contact thermal conductance ($h_c$) and the gap thermal conductance ($h_g$). Moreover, he describes that as the temperature of the steel increases, the conductance in the interface decreases.

To obtain more realistic temperature fields, the researcher highlights the importance of determining the conductance in the steel-concrete interface, considering the thermal conductivity of the air and the width of the gap that is formed between the steel tube and the concrete. When the steel temperature exceeds 200 °C, the water contained in the concrete, which migrated to the steel-concrete interface, has already evaporated, thus little interfering in the thermal conductivity in this interface. As the gap increases, the thermal conductivity at the steel-concrete interface decreases; however, the heating of water vapor generates an increase in its thermal conductivity, which causes an increase in thermal conductivity in the steel-concrete interface.

This paper presents a three-dimensional numerical model developed in the ABAQUS software (Dassault Systemes SIMULIA Corp., 2014) [16], to perform the thermomechanical analysis of short columns composed of concrete-filled steel tubes of circular and square sections. As an alternative for specific heat transfer analyses, a two-dimensional model was developed aiming at reducing computational effort, maintaining parity with the results obtained from the three-dimensional model.

To propose the numerical model, the types of modeling employed, and the effect of air gap were evaluated. Despite interfering in the thermal response, according to Hong & Varna [17], this effect is traditionally neglected in numerical models of columns filled with concrete and, until then, such simplification is considered conservative in columns without fire protection. Finally, the proposed numerical model was validated based on experimental results from the literature.

## 2. NUMERICAL MODELING

2.1 Development and parameterization of the numerical model

The numerical model presented in this paper was developed using the ABAQUS code, with transient thermal analysis and mechanical analysis (stress-strain) performed simultaneously in the same model. The specimens considered in this study consist of 500-mm high short columns composed of steel tubes filled with concrete of circular and square sections. The initial parameters were chosen based on the bibliographic references presented in the present study, as follows:

i. For three-dimensional models, meshes with the C3D8 element were used (Figure 1). The mesh refinement adopted consists of two or three elements along the thickness of the tube, depending on the thickness of the tube. For the concrete core, the finite element adopted has an area between 7% and 9% of the cross-sectional area. Along the height of the column the length of the elements was set to 10% of the column length.

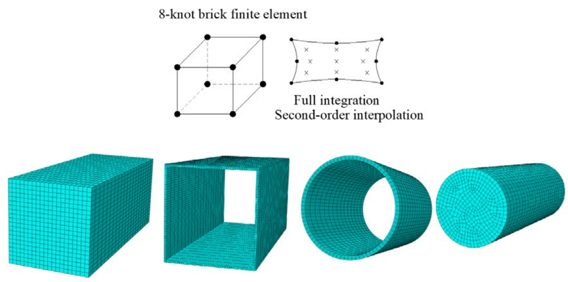


**Figure 1.** Refinement and type of element and mesh in the steel tube and concrete core.

A sensitivity study was performed with the three-dimensional models to define the mesh refinement required . The study was carried out considering four columns, two with circular sections and two with square sections. Two external dimensions were modeled, 14-5 mm (tube external dimension - tube thickness) equal to, and 200-8 mm. The analysis was developed with the implicit solver. Table 1 and Figure 2 show the results of the square section column with dimensions of 200-8 mm. The refinement adopted was one whose answers practically do not change in relation to an immediately superior refinement.

**Table 1.** Mesh sensitivity study (specimen - PQ200-8)

| fire exposure time | Mesh 1 | | Mesh 2 | | Mesh 3 - adopted | |
|---|---|---|---|---|---|---|
| | Temperature (ºC) | | | | | |
| | Tube | Core | Tube | Core | Tube | Core |
| 30 min. | 698.5 | 95 | 702.4 | 76.6 | 702.4 | 76.7 |
| | Axial displacement (mm) | | | | | |
| | 1.49 | | 1.31 | | 1.31 | |
| | processing time (minutes) | | | | | |
| | 102 | | 206 | | 127 | |
| 50 min. | Temperature (ºC) | | | | | |
| | 854.6 | 299.7 | 854.9 | 276.9 | 854.8 | 277.1 |
| | Axial displacement (mm) | | | | | |
| | 22.72 | | 21.79 | | 21.80 | |
| | Processing time (minutes) | | | | | |
| | 162 | | 307 | | 189 | |

PQ - square section, 200 mm of external diameter of the tube and 8 mm of thickness of the steel tube.

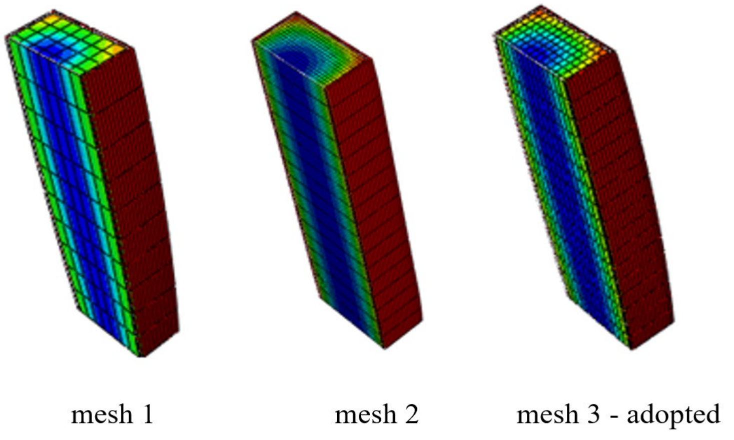


**Figure 2.** Finite element mesh density levels.

ii. The emissivity resulting from the exposed face of steel and fire was adopted equal to 0.7 [18], [19]; and in the steel-concrete interface, the emissivity of steel and concrete was set at 0.32 and 0.97, respectively [12].
iii. The Stefan-Boltzmann constant is expressed by the constant value equal to $5.67\times10^{-8}$ $Wm^{-2}K^{-4}$.
iv. The convection coefficient is equal to 25 $W/m^{2\circ}C$ for the standard fire curve, expressed by the equation: $\theta = 345 \log(8t+1) + 20$ °C, where θ is the temperature of hot gases in the burning environment in degree Celsius and t, the time of exposure to fire in minutes [20].
v. Fire action was uniformly considered around the entire exposed surface of the column, and the initial temperature of the element/specimen was set at 20 °C.
vi. The axial force applied to thermomechanical models was set at 50% of the plastic capacity of the section at room temperature, equal to $N_{pl,Rd} = A_{afy} + A_{cfc}$, where: $A_a$ is the cross-sectional area of steel; $f_y$ is the yield strength of steel; $A_c$ is the cross-sectional area of concrete; and $f_c$ is the compressive strength of concrete.
vii. The mechanical behavior in the steel-concrete interface connection was defined by a hard contact that allows the separation between the different surfaces and does not allow overlap between them, and by a penalty contact, considering the Coulomb law with a constant coefficient of friction equal to 0.3 (in the literature this value is reported between 0.2 and 0.3) [21].

Figure 3 shows the geometry of the composite column, consisting of a steel tube filled with concrete, which is positioned inside the steel tube and connected to it by hard and penalty surface contacts method.

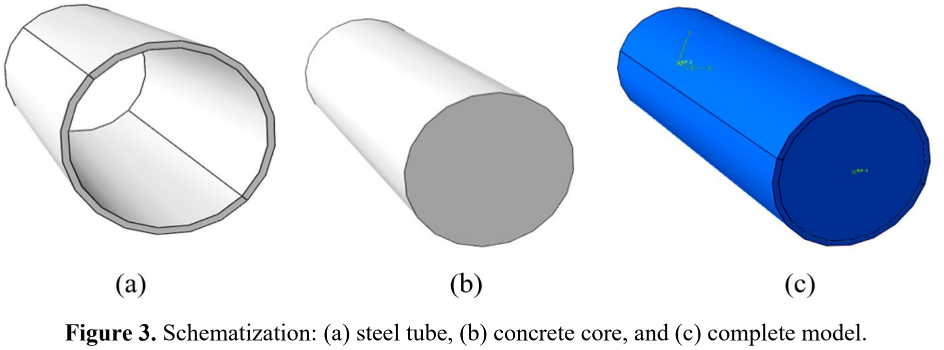


**Figure 3.** Schematization: (a) steel tube, (b) concrete core, and (c) complete model.

viii. The model used to simulate the concrete behavior was the CDP (Concrete Damage Plasticity), which considers the Drucker-Prager model [22], including the von Mises yield criterion, for verifying the hydrostatic pressure effect on the shear strength of the material [23]. The values of the parameters used to characterize the model were: dilatancy angle $\psi$=35º; ratio of initial equibiaxial compressive yield stress to initial uniaxial compressive yield stress $\sigma_{bo}/\sigma_{co}$ =1.16;

eccentricity ρ=0.1; ratio between the distance from the hydrostatic axis in the deviatoric plane $K_c$=2/3; viscosity parameter μ=0 [8], [16], [21].

ix. The two-dimensional model run with the *static-implicit* solver and the three-dimensional model runs with the *dynamic-explicit* solver. Although the response obtained from the explicit solver is considered as an approximation, the *dynamic-explicit* method leads to a significant reduction in computational effort and to the stability of the analysis [24], [25].

## 2.2. Properties of steel and concrete at elevated temperatures

### 2.2.1. Physical and thermal properties of steel and concrete

The thermal conductivity, density, thermal expansion and specific heat of steel and concrete at high temperatures were determined from the equations described in EN 1994-1-2 (2005) [10]. The moisture contained in the concrete is usually represented by the peak value of the specific heat that ranges between 100 °C and 115 °C, linearly decreasing between 115 °C and 200 °C. After 200 °C, the values obtained for dry concrete is assumed. The peak value is indicated for 2020 and 5600 J/kgK, respectively, with 3% and 10% of moisture content. The equivalent area model was also tested to represent the specific heat proposed by Rush [13], however, there were few differences in the thermal response of the model.

### 2.2.2. Mechanical properties of steel and concrete

The modulus of elasticity of steel at elevated temperature ($E_{a,\theta}$), in MPa, is defined according to the Equation 1, where $K_{Ea,\theta}$, reduction factor of the modulus of elasticity of steel at elevated temperature indicated by EN1994-1-2 (2005) [10] and $E_a$ is the steel elastic modulus at room temperature, equal to 210,000 MPa.

$$E_{a,\theta} = k_{Ea,\theta} \cdot E_a \tag{1}$$

The steel stress-strain constitutive law was defined according to the equations presented in Eurocode EN1994-1-2 (2005) [10]. The Poisson's ratio of steel is adopted equal to 0.3, regardless of temperature.

Compressive strength of concrete at high temperatures is defined by a reduction factor ($K_{C\theta} = \frac{f_{C\theta}}{f_C}$), according to the indicated normative reference and showed in Figure 4. The tensile strength of concrete at high temperatures is defined similarly, considering a reduction factor ($f_{Ck,t\theta} = K_{C,t\theta} \cdot f_{Ck,t}$).

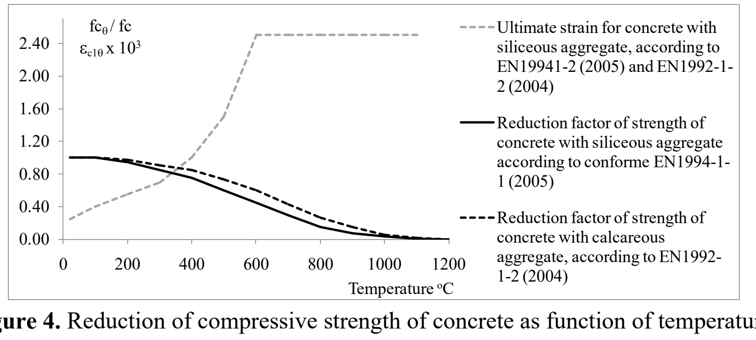


**Figure 4.** Reduction of compressive strength of concrete as function of temperature.

The compressive strength of concrete at elevated temperature is represented in Figure 5 and is expressed according to Equation 2 and to EN 1994-1-1 (2005) [10].

$$\boldsymbol{\sigma_{c,\theta}} = \frac{3\varepsilon_{c,\theta} f_{c,\theta}}{\varepsilon_{c1,\theta}\left[2+\left(\frac{\varepsilon_{c,\theta}}{\varepsilon_{c1,\theta}}\right)^3\right]} \tag{2}$$

Where: $f_{c,\theta} = K_{C,\theta} \cdot f_c$;$K_{c,\theta}$, reduction factor for the compressive strength of concrete; $f_c$ = compressive strength of concrete at room temperature; $f_{c,\theta}$ = compressive strength of concrete at temperature (θ) expressed in MPa; $\boldsymbol{\varepsilon_{c1,\theta}}$ = strain corresponding to the ultimate strength of concrete at temperature (θ). The notation $\varepsilon_{c1,\theta}$ is presented in EN1992-1-2 (2004) [26], however, in EN1994-1-2 (2005) [10] it is denominated as $\varepsilon_{cu,\theta}$.

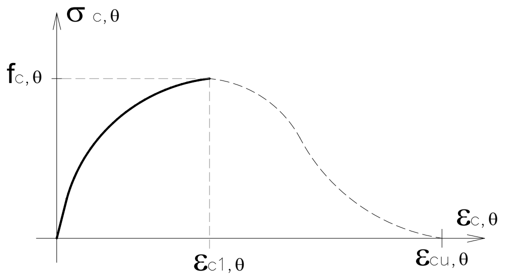


**Figure 5.** Stress-strain relationship of concrete at elevated temperature.

The reduction factor of the elasticity modulus of concrete at elevated temperature is determined based on the ratio presented in Equation 3, according to EN1992-1-2 (2004) [26], where $\varepsilon_{c1}$ is the strain corresponding to concrete at room temperature. The Poisson's ratio of concrete is indicated with a value equal to 0.2, regardless of temperature.

$$\mathrm{K}_{\mathrm{Ec,è}} = \mathrm{K}_{\mathrm{C,è}} \cdot \frac{\mathrm{å}_{\mathrm{c1}}}{\mathrm{å}_{\mathrm{c1,è}}} \tag{3}$$

## 3. "AIR-GAP" EFFECT AND ITS IMPLEMENTATION IN THE NUMERICAL MODEL

The main objective of the study on the air gap is to conceptually present the phenomenon, to implement it in the numerical model, and to verify its influence in the evolution of the temperature field in the specimens considered in the present research.

### 3.1. Phenomenon description

In columns composed of steel tube filled with concrete in fire situation, the steel tube heats and expands faster than concrete, because the steel has a thermal conductivity greater than the concrete. This differential expansion forms a gap between the two elements, which is usually filled with water and air up to 200 °C, temperature at which the water vaporizes, so only the air remains (Figure 6).

The air-gap layer at the steel-concrete interface provides thermal insulation, which reduces heat transfer at the interface, that mainly occurs by conduction. Air, which has lower thermal conductivity than steel and concrete, provides resistance to the transfer of thermal energy, thus increasing the temperature in the steel tube and decreasing it in the concrete. The air gap formation depends on the tube dimensions, temperatures of steel and concrete, thermal properties of the materials, and on the stress level of the column due to the axial force load. Therefore, it is difficult to precisely determine the temperatures and the gap that is formed in the steel-concrete interface [27]. The air gap is characterized by the distance (*d*), between surface of the tube and surface of the concrete core, represented by nodes 1 and 2, with temperatures $\theta_1$ and $\theta_2$ (Figure 5).

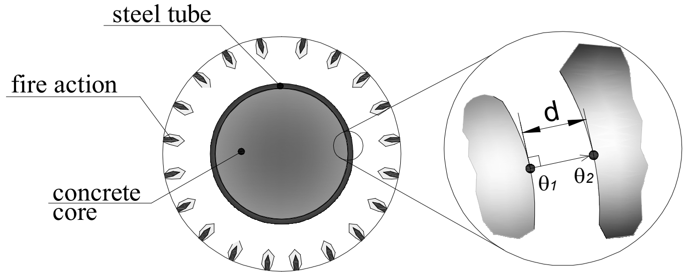


**Figure 6.** Gap between the two surfaces.

The gap between the concrete and the steel tube can also be formed prior to the heating of the element by the phenomenon of concrete shrinkage. In this situation, the thermal conductance at the steel-concrete interface is affected, changing temperatures and the gap formation as temperature increases. Heat transfer through the air gap can be defined by the sum of the air conductivity and the radiation between the two surfaces [28], with thermal equilibrium described as: $q = q_{ar} = q_c + q_r$.

### 3.2. Implementation in numerical models

To consider the air-gap effect on the numerical models developed in the ABAQUS software, a variable thermal conductivity value can be defined in the steel-concrete interface depending on the distances between the contact points. For example, the heat transfer between surfaces in contact is defined by Equation 4, where: $q$ = heat transfer between nodes 1 and 2; $h$ = conductivity coefficient (W/m$^2$K,); $\theta_1$ and $\theta_2$ are the temperatures corresponding to nodes 1 and 2.

$$q = h(\theta_1 - \theta_2) \tag{4}$$

Considering thermal equilibrium at the steel-concrete interface, Equation 4 can be described according to Equation 5. In a fully coupled thermomechanical analysis it is possible to approximate Equation 5 by considering finite differences in a subroutine, which is solved in each increment time defined in the analysis [28].

$$h(\theta_1 - \theta_2) = \frac{\lambda_{ar}}{d} + \left(\frac{1}{\varepsilon_1} + \frac{1}{\varepsilon_2} - 1\right)^{-1} \sigma\left(\frac{\theta_1^4 - \theta_2^4}{\theta_1 - \theta_2}\right) \tag{5}$$

In equation 5 the symbol $\lambda_{ar}$ represents the thermal conductivity of the air.

In the model, the distance between the steel tube and the concrete (*d)* is determined by the thermomechanical analysis; deformations of each point on each surface in contact are obtained from each iteration step, and so are temperatures $\theta_1$and $\theta_2$. Emissivity of surfaces ($\varepsilon_1$and $\varepsilon_2$) and air conductivity ($\lambda_{ar}$) are parameters difficult to determine, and the adoption of inconsistent values can produce very inaccurate responses. In addition to difficulties in determining the resulting emissivity and air properties, another aspect worthy of consideration is the computational complexity and time to solve the model, with several interactions in a highly nonlinear and interdependent system, with great possibility of convergence problems in the analysis [13].

An alternative approach to consider the air-gap effect is to define a thermal resistance in the steel-concrete interface by defining a calibrated thermal conduction value at this interface. The mentioned thermal conductance can be defined by an average and constant value or as a function of temperature, in such a way that the effect is like the air-gap effect, which suggests the need for experimental evaluation. The adoption of a thermal resistance in the tube-concrete interface can be easily implemented in exclusively thermal models and can also be used in thermomechanical models.

In the analyses with two or three-dimensional numerical models, the air-gap effect can be considered with the inclusion of a coefficient of thermal conductance, according to Equation 6 proposed by Ghojel, 2004 [15], where: *hj* is the joint thermal conductance at the steel-concrete interface (W/m$^2$K); $\theta_a$ is the temperature of steel in Celsius degree.

$$h_j = 160{,}5 - 63{,}8exp\,(-339{,}9{\theta_a}^{-1{,}4}) \tag{6}$$

Ghojel [15] also defined a specific equation for situations in which the column is not subjected to an axial force. However, Equation 3 can be used for both situations, with and without the presence of axial force, considering that the existence of axial force, in actual design situations, causes small changes in the temperature field [29]. Considering the joint thermal conductance at the steel-concrete interface (*hj*), according to Ghojel, 2004 [15], the heat flux (*q*) is defined by Equation 7.

$$q = hj \cdot \Delta\theta \tag{7}$$

### 3.3. Models with the air layer explicitly modeled

A reference model was developed considering the effective modeling of an air layer placed between the steel tube and the concrete core, to evaluate the accuracy of the thermal behavior response with the assumptions usually adopted to consider the air gap in the numerical models. The study initially describes the properties of air, as reported in the literature, and then presents the model with the air layer and other models with assumptions usually adopted in numerical modeling.

### 3.3.1. Air properties

Air´s properties found in the literature are usually obtained from experimental tests and indicated with values: density = 1225 kg/m$^3$; specific heat = 1000 J/kg·K; elasticity modulus = 1.42 x 105 Pa; Poisson's ratio = 0; thermal conductivity = 0.023 W/m$^2$K and convection = 8 W/m$^2$K [14].

The specific heat of the air is presented in the literature as a function of temperature, with values varying from 1007 to 1234 J/kgK [30]; the density of the air ranges from 1204 to 199 kg/m$^3$; and the air conductivity, from 0.025 to 0.1 W/mK, which are limit values described for temperatures of 20 and 1500 °C [30], respectively. In Figure 7 the graphs represent the air density, specific heat and thermal conductivity.

The thermal conductivity of the air is also reported in the literature with different values and considering two literature references [14], [30], the conductivity of the air is expressed according to Figure 7. Conversely, the continuous line expresses the values determined by the least squares between the functions compiled from the literature, and its equation was used to define the values of the thermal conductivity of the air adopted in the numerical models.

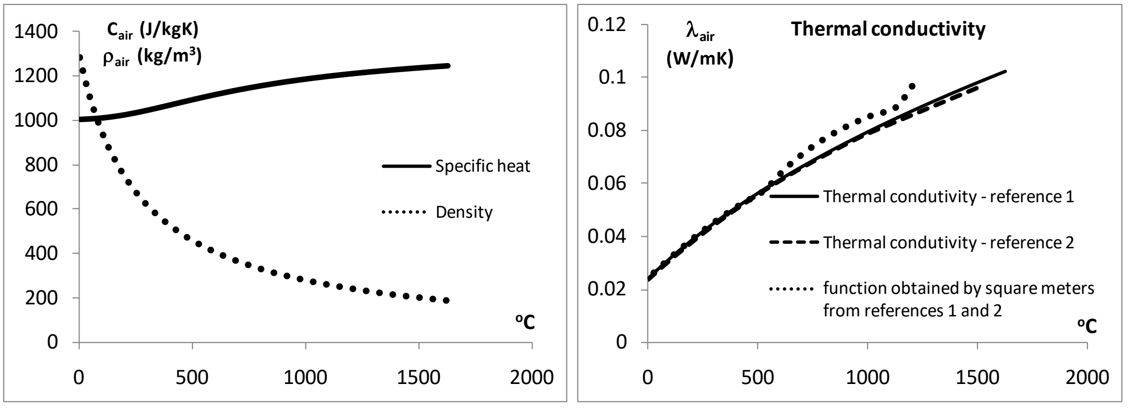


**Figure 7.** Density, specific heat and thermal conductivity of the air.

By adjusting the graphs to a maximum error of 5%, Equations 8 and 9 were defined to describe the thermal conductivity of the air (W/mK) and the specific heat of the air (J/kgK).

$$\lambda_{ar} = -12{,}78 \times 10^{-9}\theta^2 + 6{,}75 \times 10^{-5}\theta + 2{,}52 \times 10^{-2} \quad (8)$$

$$C_{ar} = -5{,}1 \times 10^{-5}\theta^2 + 0{,}244\theta + 987 \quad (9)$$

In the model with the effective air gap layer, equation 10 was used. The equation describes the air density (kg/m$^3$) and was obtained in the present work by correlation, where: φ is the temperature in °C.

$$\rho_{ar} = 55.5 \times 10^{-5}\theta^2 - 1{,}15\theta + 1000 \ (10)$$

### 3.3.2. Effective modeling of the air gap

To identify and evaluate the air-gap effect, a three-dimensional model was developed with heat transfer analysis considering the air layer between the steel tube and the concrete, modeled using solid elements. The evaluation was carried out in the three-dimensional specimens shown in Table 2, with a 4% moisture content in the concrete.

**Table 2.** Specimens for the model with heat transfer analysis.

| Reference | Cross Section | D (mm) | t (mm) | l (mm) |
|---|---|---|---|---|
| 1. PC-168-6 | Circular | 168.3 | 6.4 | 500 |
| 2. PC-168-10 | Circular | 168.3 | 10 | 500 |
| 3. PC-300-10 | Circular | 300 | 10 | 500 |
| 4. PC100-6 | Circular | 100 | 6 | 500 |
| 5. PC-168-16 | Circular | 168.2 | 16 | 500 |
| 6. PC-200-6 | Circular | 200 | 6 | 500 |
| 7. PC-200-16 | Circular | 200 | 16 | 500 |
| 8. PC-500-6 | Circular | 500 | 6 | 500 |
| 9. PC-500-16 | Circular | 500 | 16 | 500 |
| 10. PC-100-6 | Circular | 100 | 6 | 500 |

D - Outer diameter of circular section; t - tube thickness; l - tube length

The evaluation of the behavior of specimens indicated in Table 2 with the air layer effectively incorporated into the model was assessed considering the air layer thicknesses of 0.5 mm, 1.0 mm and 2.0 mm. Figure 8 shows the temperature field, obtained from specimen 1. Model (a) and (c) consider the perfect thermal contact; and model (b) and (d) considers the gap effectively filled with air, both for the same fire exposure times from the ISO-834-1999 curve [20].

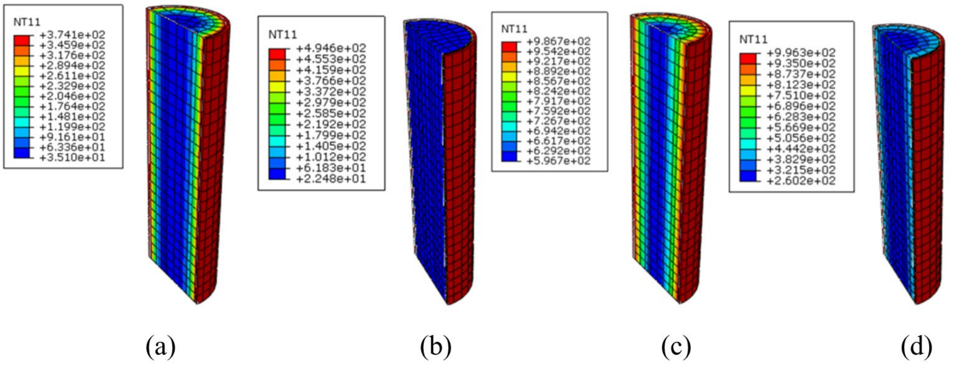


**Figure 8.** Models for assessing the air-gap effect: (a) perfect thermal contact (15 min.), (b) with air-gap layer of 2-mm thickness (15 min.), (c) perfect thermal contact (90 min.) and (d) with air-gap layer of 2-mm thickness (90 min.)

In Figure 9, the responses of models are presented considering specimen 4, with a thickness of 1.0 and 2.0 mm for the modeled air layer, response of model with perfect thermal contact and response model with thermal resistance proposed by Ghojel, 2004 [15].

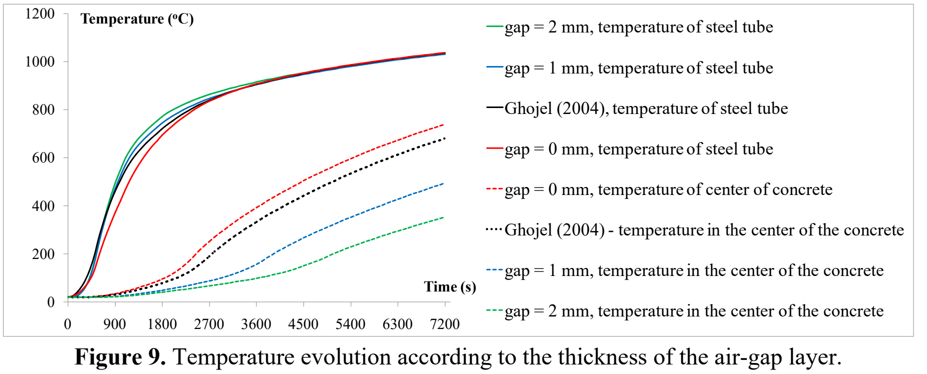


**Figure 9.** Temperature evolution according to the thickness of the air-gap layer.

From the models indicated in Table 2, the sensitivity of the model was verified considering differences in air properties, as reported in the literature [14], [30] and considering the inclusion of the combined properties of air and water, remembering that the gap may contain water and air. The air gap was considered with thicknesses of 0.2, 0.5, 1.5, and 3.0 mm. The models were also developed without the air layer and with the thermal resistance in the steel-concrete interface, imposed by the thermal conductance values conveniently adopted. To define the thermal conductance and, in turn, the thermal resistance at the steel-concrete interface, some alternatives were modelled, namely, model 1 according to the equation presented by Ghojel [15]; model 2 with thermal resistance constant value ranging between 100 and 200 $m^2K/W$; model 3 with air layer effectively modeled with the thermal conductivity equal to 0.024 W/mK; model 4 with the air layer effectively modeled with the thermal conductivity as function of temperature (Equation 8); model 5 with the air layer effectively modeled considering Equation 8, except for temperatures ranging from 0 to 200 °C when the mean value between air conductivity and water conductivity was set at 0.6 W/mK. Figures 10 and 11 show the results concerning the specimen 4.

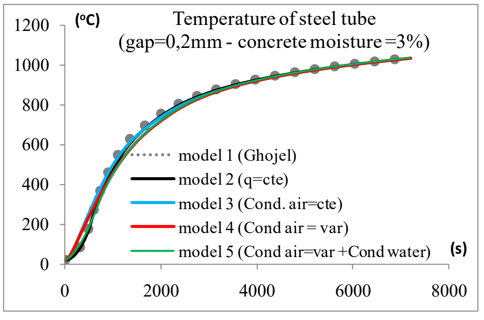

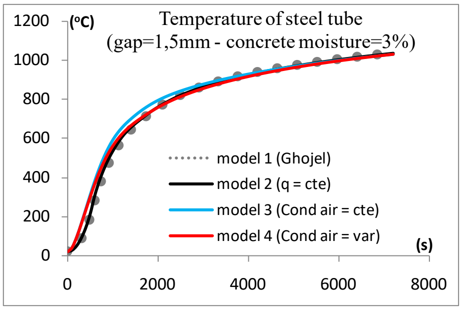


**Figure 10.** Temperature of steel tube according to the gap (3% concrete moisture).

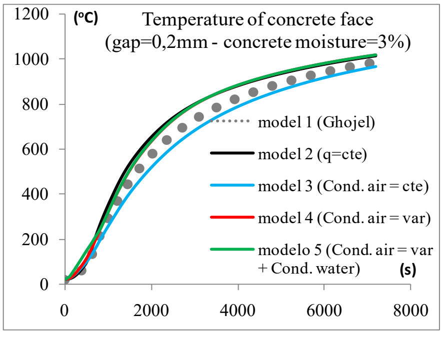

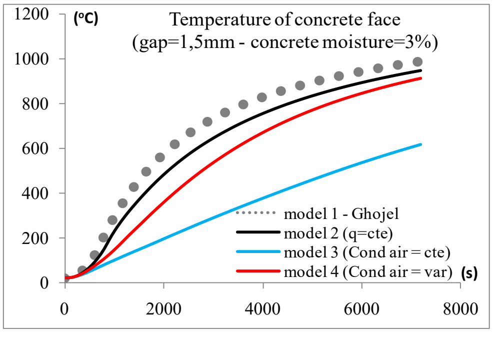


**Figure 11.** Temperature of concrete face according to the gap (3% concrete moisture).

Shrinking concrete can result in an initial gap before heating the element, between the steel tube and the concrete filling. Considering this effect, it is observed that the evolution of the gap with increased temperature is significantly amplified (Figure 12).

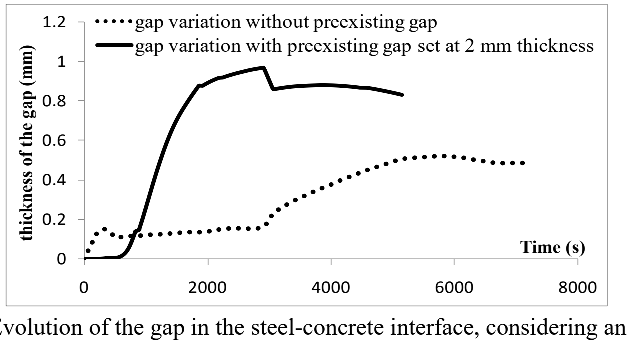


**Figure 12.** Evolution of the gap in the steel-concrete interface, considering an initial gap.

Assessing the result it can be observed that, (a) considering the constant value of the thermal conductivity of the air, temperatures were higher in the steel tube and lower in the concrete face, compared with the models with the air conductivity as a function of temperature; (b) from a practical point of view, the adoption of the thermal conductivity of the air with the presence of water has little influence on the evolution of temperature over the usual required fire resistance time; (c) considering a preexisting gap, prior to heating, it is verified that the development speed of the gap between the tube and the concrete significantly increases and, likewise, the temperature in the steel considerably increases, though reducing the temperatures in the concrete.

### 3.4. Air-gap effect modelled as equivalent to the thermal energy transfer resistance

The evaluation of the effect of thermal resistance between the steel tube and the concrete core was performed by comparing the temperature fields obtained from the numerical models of the specimens indicated in Table 2, considered in the steel-concrete interface, (a) perfect thermal contact; (b) thermal resistance according to conductance as defined by Equation 6; (c) thermal resistance considered with constant conductance values of 100 and 200 $m^2K/W$. Figure 13 shows the model responses for specimen 7.

According to Figure 13 it was observed that responses with the formulation proposed by Ghojel [15] have a similar behavior compared with models that adopted a constant value for thermal resistance, ranging between 100 and 200 $W/m^2K$. In this analysis, the axial force was fixed at 50% of the plastic capacity at room temperature.

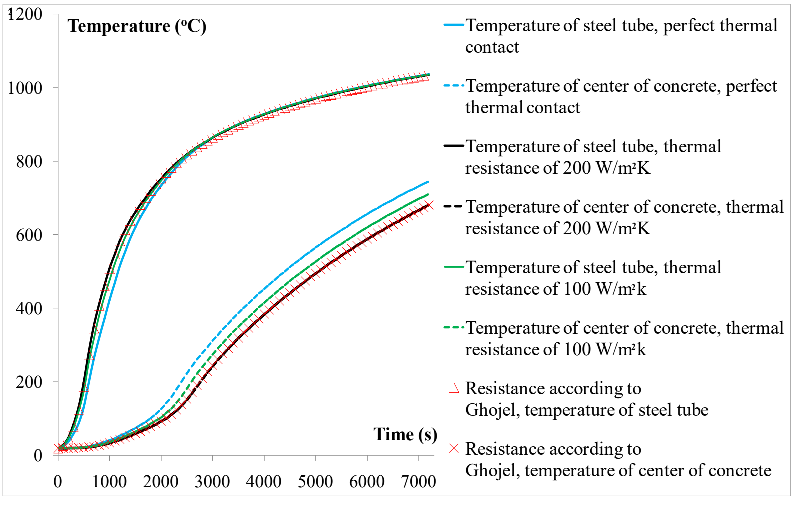


**Figure 13.** Temperature vs. time, according to thermal resistance tube-concrete interface.

Figure 14 graphs show the evolution of the gap and temperature in the steel tube and in the center of the concrete core for the model of specimen 7.

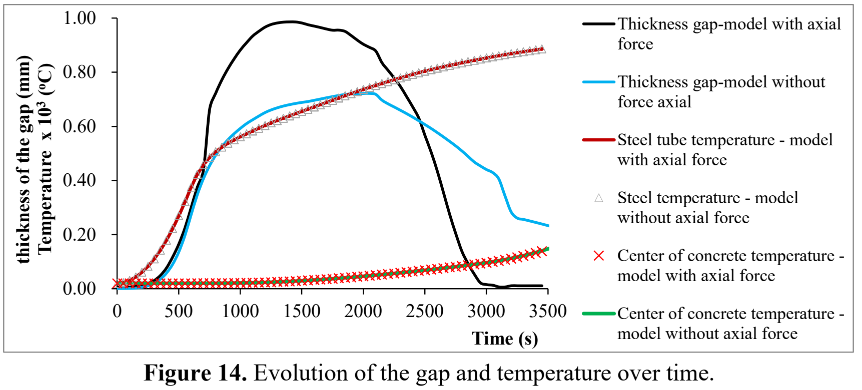


**Figure 14.** Evolution of the gap and temperature over time.

Based on the studies performed, the consideration of the axial force in the column altered the thickness of the gap in the tube-concrete interface; however, the resulting temperatures in the steel tube and in the concrete remained virtually the same. Experimental tests developed by Kado [29] also demonstrated a small influence on the temperature field with the application of axial force to concrete-filled steel columns.

## 4. VALIDATION OF THE PROPOSED MODEL

To verify the accuracy of the numerical model including the air-gap effect, its results were compared with the experimental results presented in the literature. Related to exclusively thermal analyses, a two-dimensional model was used. The specimens were modeled with the same properties as the experimental specimens.

### 4.1. Three-dimensional model

For the thermomechanical analysis proposed in the present study, a pinned support at the base of the column was imposed in the model, while a rigid adiabatic surface was defined at the top of the column (Figure 15), without its own weight, to improve the axial force transfer to the steel and concrete core, avoiding problems of stress concentration and convergence in the analysis.

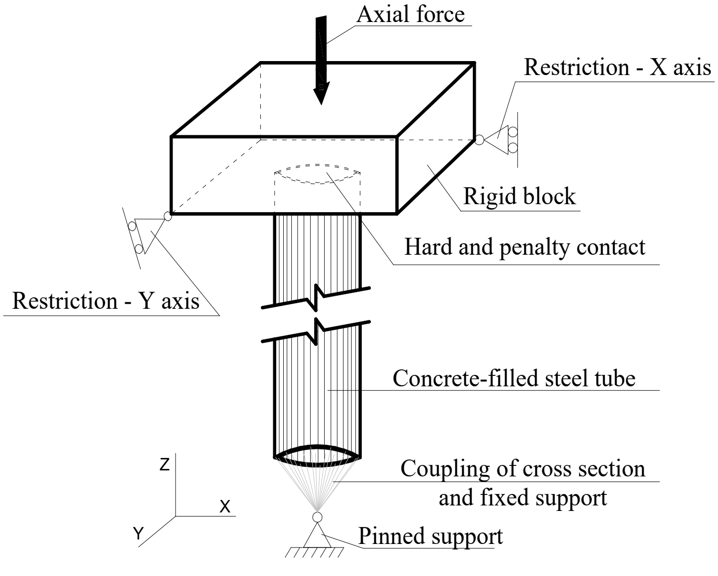


**Figure 15.** Boundary conditions and interactions imposed in the model.

Figure 16 presents the models in ABAQUS, with deformations that occur in response to the axial force applied to the top of the rigid surface and in response to heating, whose isotherms in the longitudinal section can be observed in the figure (c).

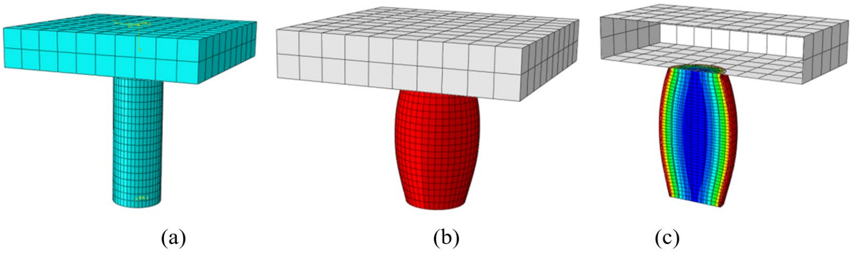


**Figure 16.** Schematization: (a) numerical model, (b) corresponding axial deformation, and (c) temperature field.

The validation models considered three specimens experimentally tested and reported in the literature, whose characteristics are indicated in Table 3.

**Table 3.** Characteristics of specimens and experimental results.

| Reference/ specimens | Cross Section | L or D (mm) | t (mm) | fc (MPa) | $f_{ys}$ (MPa) | l (m) | Axial force kN | FRT (min.) |
|---|---|---|---|---|---|---|---|---|
| 1- PC 159-3.6 | Circular | 159 | 3.6 | 34 | 289 | 0.80 | 335 | 28 |
| 2- PQ 200-4.5 | Square | 200 | 4.5 | 28 | 293 | 1.32 | 293 | 76 |
| 3- PQ 120-2.9 | Square | 120 | 2.9 | 53.2 | 340 | 0.38 | 388 | 90 |

D- Outer diameter or L-outer edge dimension of the square section tube; FRT-fire resistance time. Reference: 1- Hass et al. [31]; 2-Suzuki et al. [32] and 3-Han et al. [33].

The parameters used in the modeling and the properties of steel and concrete were determined according to items 2 and 3 of this paper, while the steel and concrete strength were adopted equal to those described in the actual experimental tests [31]–[33].

The level of mesh refinement followed the definitions of the sensitivity study presented in this research, and the thermal resistance between the concrete and the steel tube was considered using Equation 6 proposed by Ghojel [15]. The axial force applied to each specimen numerically tested followed the force identified in the respective experimental test, as shown in Table 3. Likewise, the experimental specimens were heated with the standard fire curve. The content of water contained in the concrete was not explained in the references but was set at 5% in the numerical modelling.

To determine the capacity of the specimen numerically tested at elevated temperatures, the criterion indicated in EN 1363-1 (1999) [34] was adopted, which defines the failure limit equal to as 1% for the axial contraction and equal to 0.3%/min for the axial contraction rate.

Figure 17 show the curves of the axial displacement and the axial displacement rate for the three specimens numerically tested, verifying the fire exposure time at which the resistance capacity of each specimen reaches its limit.

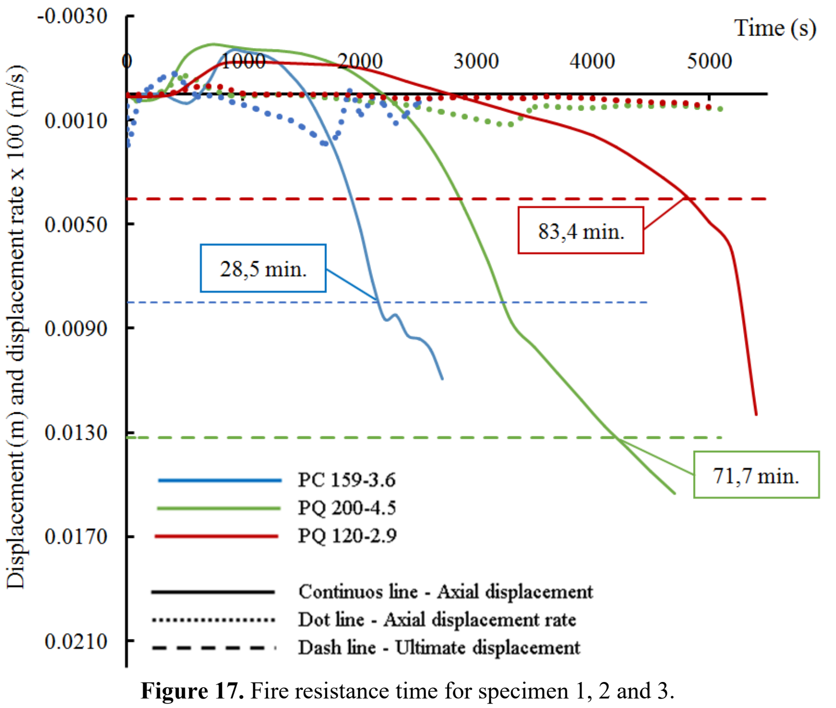


**Figure 17.** Fire resistance time for specimen 1, 2 and 3.

According to the response presented in the graphs, it is observed that the capacity of specimens 1, 2, and 3 (Table 3) occurs, at the times of 28.5, 71.67, and 83.4 minutes, respectively, with differences of 1.78%, -5.7%, and -7.3% from the times determined in the experimentally tested specimens.

### 4.2. Two-dimensional thermal analysis model

For the exclusively thermal analysis, the use of two-dimensional models is common, which results in a much less computational effort than three-dimensional models. In the present study, a two-dimensional model was presented for the analysis of heat transfer, derived from the three-dimensional model, disregarding parameters and properties of materials inherent in the mechanical analysis, considering that the thermal properties of the materials were maintained. The steel tube and the concrete core were separately modeled as two-dimensional elements and then coupled, considering the thermal resistance at the interface between tube and concrete to contemplate the air-gap effect.

The heat transfer analysis was performed with the quadrilateral D2D3 finite element for the square sections; and the three-node DC2D3 element for the circular sections. The thermal load (fire) heats the exposed face according to standard fire curve considering the convection with heat transfer coefficient equal to 25 $W/m^2K$ and the radiation with emissivity coefficients of fire and exposed face (steel) equal to 0.7 and 1.0, respectively. The emissivity coefficient at the steel-concrete interface adopted was 0.32 and 0.97, respectively for steel and concrete. The thermal load (fire) was uniformly considered around the entire section, and the initial temperature was set at 20 ºC. The contact between the steel pipe and the concrete core was established by a "surface contact", in which the thermal resistance is inserted to represent the air-gap effect.

Figure 18 illustrates the two-dimensional model with the temperature field established for a given time of exposure to fire.

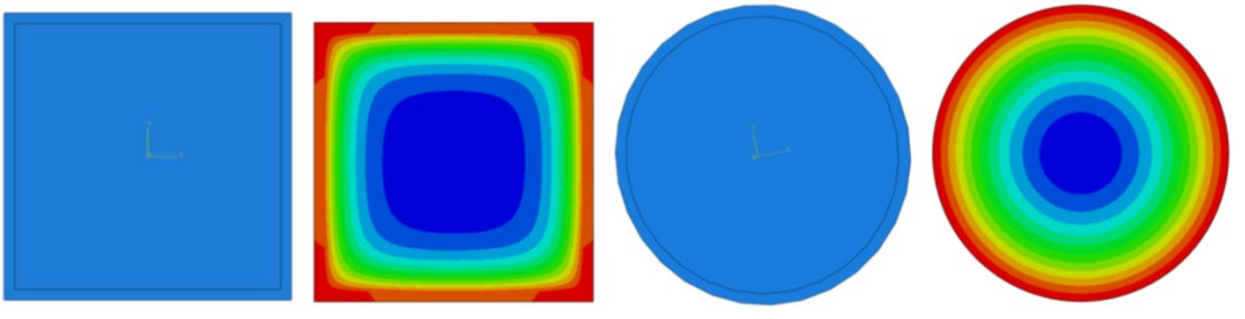

**Figure 18.** Illustration of the two-dimensional model with temperature fields.

The models presented next were developed to better define the numerical model demonstrated. Differences found in the response of the numerical model were effectively investigated, according to the type of analysis and adopted solver.

The validation of the two-dimensional model considered the experimental results presented by Rush [13] as reference. The specimen experimentally tested and reproduced by the two-dimensional numerical model has the following characteristics, circular section steel tube with 219.1 and 10 mm in diameter and thickness, respectively; water content in the concrete set at 6% of the concrete mass, and emissivity resulting from fire and exposed face set at 0.38, as indicated in the description of the experimental test. The properties of steel and concrete are indicated in item 3.

Table 4 describes the temperatures at the points indicated in Figure 19, as well as the percentage differences in relation to the experimental model. The results presented in Table 4 refer to specimen 1 (Table 3) and the notations "Exp.", "1-Num." and "2-Num." correspond to the experimental response, response obtained by the numerical model considering the effect of air gap and response of the numerical model with perfect thermal contact between the steel tube and the concrete core, respectively.

**Table 4 –** Temperatures found in experimental and numerical models.

| | Temperature (ºC) | | | | | | | | |
|---|---|---|---|---|---|---|---|---|---|
| | Steel tube | | | External face of concrete | | | Center of concrete | | |
| | 30 min | 90 min | 120 min | 30 min | 90 min | 120 min | 30 min | 90 min | 120 min |
| Exp. | 503 | 887 | 971 | 285 | 770 | 885 | 47 | 180 | 330 |
| 1-Num. | 553 | 902 | 984 | 377 | 792 | 920 | 46 | 178 | 376 |
| 2-Num. | 502 | 873 | 968 | 432 | 799 | 924 | 55 | 221 | 398 |
| % Exp vs 1-Num | 9.0 | 1.7 | 1.3 | 24.4 | 2.8 | 3.8 | -2.2 | -1.1 | 12.2 |
| % Exp vs 2-Num | -0.2 | -1.6 | -0.3 | 34.0 | 3.6 | 4.2 | 14.5 | 18.6 | 17.1 |

Figure 19 shows the points chosen for the identification of temperatures in the cross section.

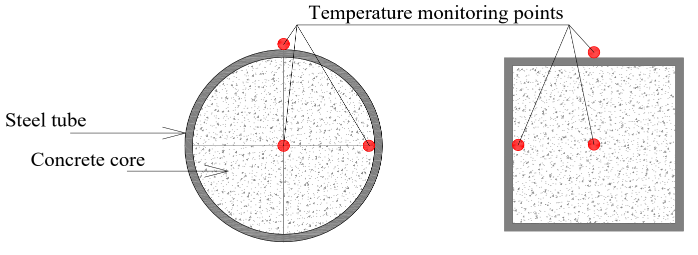


**Figure 19.** Monitoring points in the cross section.

Figures 20 and 21 show the temperature fields of the validation specimens indicated in Table 4 for fire exposure times of 60 and 120 minutes.

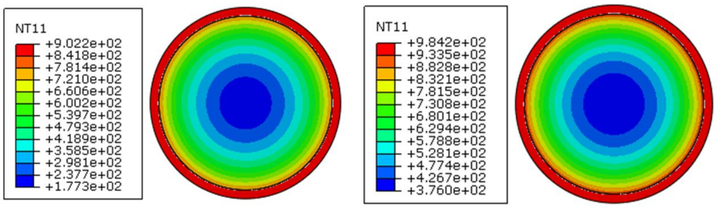


(a) fire exposure time – 60 min. (b) fire exposure time – 120 min.

**Figure 20.** Temperature field obtained from the numerical model with air gap

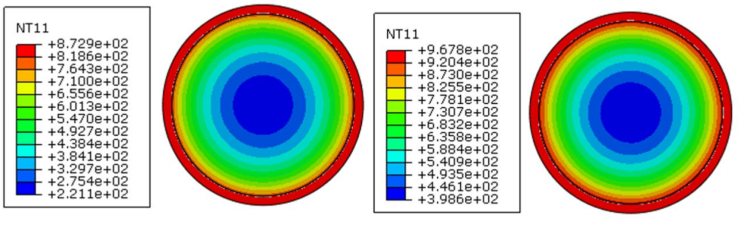


(a) fire exposure time – 60 min. (b) fire exposure time – 120 min.

**Figure 21.** Temperature obtained from the numerical model with perfect thermal contact

## 5. CONCLUSIONS

The presented three-dimensional models and the two-dimensional model, the last being exclusive to heat transfer analysis, provided results close to experimental tests reported in the literature. The two-dimensional model used for specimens of symmetrical geometry and uniform fire action proved to be an effective alternative to determine temperature fields in tubular concrete-filled columns.

The three-dimensional model with thermomechanical analysis aims on the behavior of tubular columns filled with concrete in a fire situation, yielding fire resistance time 8% smaller than the experimental result.

The inclusion of the air-gap effect, influence the temperature field and, in turn, the determination of the ultimate axial force at a given fire exposure time.

Related to heated tubes filled with concrete, the air opening formed in the steel-concrete interface behaves as a thermal insulation, influencing the heat transfer from the steel tube to the concrete core. Its inclusion in the models results in higher temperatures in the steel tube and lower temperatures in concrete, and by disregarding this effect, the temperature in steel is underestimated and the concrete temperature is overestimated. In the cases analyzed the result differences reach 25% in the temperature of the steel tube and 20% in the concrete core.

The air-gap effect can be considered as a thermal resistance in the steel-concrete interface, with thermal conductance and values established based on the equation proposed by Ghojel (Equation 6). The adoption of this equation produced equivalent results to those obtained with the inclusion of 0.1 to 0.5 mm openings filled with air in the steel-concrete interface, in the numerical models tested.

Although considering the effect of the air gap on the model, with the responses of the numerically resolved specimens close to the responses obtained experimentally, there are still uncertainties on how to define it, since the flow of water contained in the concrete can affect their behavior. Another issue is due to the possible existence of a gap between the steel tube and the concrete before heating the element and that is caused, for example, by the effect of the concrete shrinkage. This previous gap amplifies the evolution of the gap and, consequently, its effect.

Therefore, it is noteworthy the importance of considering the air-gap effect in the model and performing further research on the subject, seeking to improve the numerical and analytical procedures.

A conservative, but recommended in the present stage of knowledge, approach for the definition of practical procedures for the design of columns composed of tubes filled with concrete is to consider the thermal resistance according to the equation proposed by Ghojel (2004), to determine the temperatures in the steel tube only, neglecting the effect of the air gap to determine the temperatures in the concrete core.

The thermomechanical analysis performed in the model (coupled analysis), in which the structural limb is heated with an imposed axial force, better represents the structural behavior, considering that strains, stresses are obtained together with the formation of the temperature field

It is important to point that the use of dynamic-explicit solver in the thermal-mechanical analyses results in shorter computational processing time, avoiding convergence problems resulted with the use of the implicit solver.

A good approximation among the experimental and numerical models was obtained considering the steel and concrete properties indicated in EN1994-1-2 (2005). The model with the specific heat considering the water contained in the concrete should be improved and the model proposed by Rush [13] did not result in significant changes in the temperature field, however, this model was verified with only one specimen simulation, not enough to evaluate the proposal result.

## ACKNOWLEDGEMENTS

We would like to thank University of Campinas and Universidade Católica de Santos.

## REFERENCES

[1] V. R. Kodur. Guidelines for fire resistant design of concrete-filled steel HSS columns - state-of-the-art and research needs. *Int. J. Steel Struct.*, vol. 7, no. 3, pp. 173-182, 2007.

[2] D. Hernández, “Estudio experimental del pandeo de perfiles tubulares retangulares de aço, rellenos de hormigón de alta resistência, bajo carga axial y diagrama de momentos variable”, Tesis Doctoral. Univ. Politècnica de València, España, 2011.

[3] M. T. Stephens, D. Lehman, and C. W. Roeder, "Seismic performance modeling of concrete-filled steel tube bridges: tools and case study," *Eng. Struct.*, vol. 165, pp. 88–105, 2018.

[4] N. K. Brown, M. J. Kowalsky, and J. M. Nau, "Impact of D/t on seismic behaviour of reinforced concrete-filled steel tubes," *J. Construct. Steel Res.*, vol. 107, pp. 111–123, 2015.

[5] S. Morino and K. Tsuda, "Design and construction of concrete-filled steel tube column system in Japan," *Earthq. Eng. Eng. Seismology*, vol. 4, no. 1, pp. 51–73, 2003.

[6] F. Sciarretta, "Modeling of mechanical damage in traditional brickwork walls after fire exposure," *Adv. Mat. Res.*, vol. 919-921, pp. 495–499, 2014.

[7] T. Nguyen, F. Meftah, R. Channas, and A. Mebarki, "The behaviour of masonry walls subjected to fire: Modelling and parametrical studies in the case of hollow burnt-clay bricks," *Fire Saf. J.*, vol. 44, no. 4, 2008.

[8] A. Espinós Capilla, “Numerical analysis of the fire resistance of circular and elliptical slender concrete filled tubular columns”, Doctoral thesis, Univ. Politècnica de València, España, 2012.

[9] C. Renaud, CTICM. Report reference INSI – 04/75b – CR/PB, France, 2004.

[10] European Committee for Standardization, *Eurocode 4: Design of Composite Steel and Concrete Structures – Part 1.2: Structural Fire Design*, EN 1994-1-2:2005, 2005.

[11] Associação Brasileira de Normas Técnicas, *Fire Design of Steel Structures and Composite Steel and Concrete Structures*, NBR 14323:2013, 2013.

[12] E. O’Loughlin, D. Rush, and L. Bisby ”Concrete-filled structural hollow sections in fire: accounting for heat transfer across a gap”, in *Proc. 15th Int. Conf. on Exp. Mech.* (pp. 1–17). Porto, Portugal, 2012.

[13] D. Rush, “*Fire performance of unprotected and protected concrete filled steel hollow structural sections*,” Doctoral thesis, University os Edinburgh, 2013.

[14] Z. G. Han and M. Gillie, “Temperature Modeling for Concrete-filled Steel Tube’s Cross Section in Fire”. in *Proc. Int. Conf. Mech. Civ. Eng.*, 2014.

[15] J. Ghojel, "Experimental and analytical technique for estimating interface thermal conductance in composite structural elements under simulated fire conditions," *Exp. Therm. Fluid Sci.*, vol. 28, pp. 347–354, 2004.

[16] Dassault Systemes Simulia Corp. *ABAQUS/CAE User’s Guide*, 2012.

[17] S. Hong, and H. Varma, "Analytical modeling of the standard fire behavior of loaded CFT columns," *J. Construct. Steel Res.*, vol. 65, pp. 54–69, 2009.

[18] European Committee for Standardization, *Eurocode 1: Actions on Structures – Part 1.2: General Actions - Actions on Structures Exposed to Fire*, EN 1991-1-2, 2002.

[19] European Committee for Standardization, *Eurocode 3: Design of Steel Structures – Part 1.2: General Rules - Structural Fire Design*, EN 1993-1-2, 2005.

[20] International Organization for Standardization, *Fire-resistance Tests – Elements of Building Construct: General Requirements*, ISO 834-1, 1999.

[21] Rodrigues, J. P., *European Project FRISCC - Finite Element Modeling of Innovative Concrete-Filled Tubular Columns Under Room and Elevanted Temperatures*, España: Univ. Politècnica de València, 2012.

[22] D. C. Drucker and W. Pragger, "Soil mechanics and plastic analysis or limit design," *Q. Appl. Math.*, vol. 10, pp. 157–165, 1952.

[23] W. F. Chen, *Plasticity in reinforced concrete*, McGraw-Hill, 1982.

[24] D. Y. Yang et al., “Comparative investigation in to implicit, explicit, and iterative implicit/explicit schemes for the simulation of sheet-metal forming processes," *J. Mater. Process. Technol.*, vol. 50, pp. 39–53, 1995.

[25] M. F. Rodrigues and A. L. Moreno Júnior, “Análise numérica de pilares mistos curtos, através dos métodos implicit e explicit”, in *Proc. 4th CILASCI*, pp. 85-98, Recife - Pernambuco, 11 out. 2017.

[26] European Committee for Standardization, *Eurocode 2: “Design of Concrete Structures – Part 1.2: General Rules - Structural Fire Design,* EN 1992-1-2, 2004.

[27] J. Ding and Y. C. Wang, "Realistic modelling of thermal and structure behaviour of protected concrete filled tubular columns in fire," *J. Construct. Steel Res.*, vol. 64, pp. 1086–1102, 2008.

[28] S. Afazov, “Modelling of thermal gap condutance in casting using finite element analysis,” *Manuf. Technol. Center.*, pp. 1-11, 2013. Accessed: Jan. 10, 2021. [Online]. https://www.researchgate.net/publication/262450677

[29] B. Kado, S. Mohammad, Y. I. I. Lee, P. N. Shek, and M. A. A. Kadir “Experimental investigation on temperature distribution of foamed concrete filled steel tube column under standard fire,” in *Proc. IOP Conf. Ser.: Earth Environ. Sci.*, vol. 140, pp. 012136, 2018, https://doi.org/10.1088/1755-1315/140/1/012136.

[30] Shpilrain, E. E., “Air (Properties of),” *Thermopedia*, 2011, https://doi.org/10.1615/AtoZ.a.air_properties_of.

[31] R. Hass, J. Ameler, H. Zies, and H. Lorenz, *Fire Resistance of Hollow Section Composite Columns with High Strength Concrete Filling*, Brunswick: CIDECT, 2001. Final Report.

[32] T. Suzuki, M. Kimura, A. Kodaira, and M. Fushimi, “Experimental study on fire resistance of concrete filled square steel columns: structural behaviour under constant axial force in fire,” *J. Struct. Constr. Eng.*, vol. 350, pp. 77–85, 1985.

[33] L. N. Han et al., "Compressive and flexural behaviour of concrete filled steel tube safe exposure to standard fire," *J. Construct. Steel Res.*, vol. 61, pp. 882–901, 2005.

[34] European Committee for Standardization, *Fire Resistance Tests - Part 1: General Requirements, EN 1363-1:1999*, 1999.

**Author contributions:** FMR: conceptualization, development, methodology, modeling, writing; ALMJ: conceptualization, methodological analysis, supervision and JMN: conceptualization, methodological analysis, supervision.

**Editors:** Bruno Briseghella, Guilherme Aris Parsekian.

IBRACON Structures and Materials Journal
Revista IBRACON de Estruturas e Materiais
ISSN 1983-4195 ismj.org

ORIGINAL ARTICLE

# Crestbond shear connector for load transfer on concrete filled composite columns in fire

*Conector Crestbond para transferência de carga em pilares mistos preenchidos com concreto em situação de incêndio*

Luiz Fernando Pereira do Prado[a]
Larice Gomes Justino Miranda[a]
Rodrigo Barreto Caldas[a]

[a]Universidade Federal de Minas Gerais – UFMG, Departamento de Engenharia de Estruturas, Belo Horizonte, MG, Brasil

Received 18 September2020
Accepted 02 Mach 2021

**Abstract:** This paper presents a numerical study of the Crestbond shear connector, characterized by a steel plate with regular cuttings, when used as a load transfer element in concrete filled composite columns in fire. The developed numerical model was calibrated with experimental results of composite columns in fire and later the load transfer devices were inserted. Numerical analyzes were performed with the software Abaqus and comprised the variation of the composite column diameter and of the loading levels, as well as the comparison with the results obtained when is used a through steel plate without cuttings (Shear Flat) as a load transfer device. With the analyzes performed, it was observed that the Crestbond shear connector and the Shear Flat present very similar thermomechanical performance in relation to the load transfer capacity. Thus, the Crestbond shear connector has the potential to be applied alternatively to the Shear Flat as a load transfer device in concrete filled composite columns, with the advantage of the possibility of associate use of longitudinal and manly transverse reinforcement.

**Keywords:** concrete filled composite column, load transfer, shear connector, shear flat, fire.

**Resumo:** Esse trabalho apresenta um estudo numérico do conector Crestbond, caracterizado por uma chapa de aço com recortes regulares trapezoidais, quando utilizado como elemento para transferência de cargas em pilares mistos preenchidos com concreto em situação de incêndio. O modelo numérico desenvolvido foi calibrado com resultados experimentais de pilares mistos em situação de incêndio e posteriormente foram inseridos os elementos de transmissão de carga. As análises numéricas foram realizadas com o auxílio do software Abaqus e compreenderam a variação do diâmetro do pilar misto e dos níveis de carregamento, bem como a comparação com os resultados obtidos quando é utilizada uma chapa de aço passante sem recortes como dispositivo de transferência de carga. Com as análises realizadas, observou-se que o conector Crestbond e a chapa passante apresentam desempenho termomecânico muito semelhantes em relação à capacidade de transferência de carga. Sendo assim, o conector Crestbond tem potencial para ser aplicado em alternativa à chapa passante como dispositivo de transferência de carga em pilares mistos preenchidos, tendo como vantagem a possibilidade do uso associado de barras de armadura longitudinais e, principalmente, transversais.

**Palavras-chave:** pilar misto preenchido com concreto, transferência de carga, conector de cisalhamento, chapa passante, incêndio.

**How to cite:** L. F. P. Prado, L. G. J. Miranda and R. B. Caldas, "Crestbond shear connector for load transfer on concrete filled composite columns in fire," *Rev. IBRACON Estrut. Mater.*, vol. 15, no. 3, e15310, 2022, https://doi.org/10.1590/S1983-41952022000300010

**Corresponding author:** Larice Gomes Justino Miranda. E-mail: laricejustino@yahoo.com.br
**Financial support:** None.
**Conflict of interest:** Nothing to declare.
**Data Availability:** The data that support the findings of this study are available from the corresponding author, L. G. J. M., upon reasonable request.

## 1 INTRODUCTION

The concrete filled composite column (CFCC) are basically composed of an external steel tube and a concrete core, the interaction of which provides greater resistance and ductility when compared to the individual application of each of these components [1]. To ensure the interaction between the components of the composite columns and thus an adequate load transfer, shear connectors can be used, especially in the region where loads are introduced [1], [2]. In view of this premise and the need for the load transfer devices used to be compatible with the use of reinforcement and easy to install, a constructive solution was developed at the Federal University of Minas Gerais, which consists of using Crestbond shear connectors as load transfer device at the steel-concrete interface, while integrating the beam-column connection [3]–[8] (Figure 1).

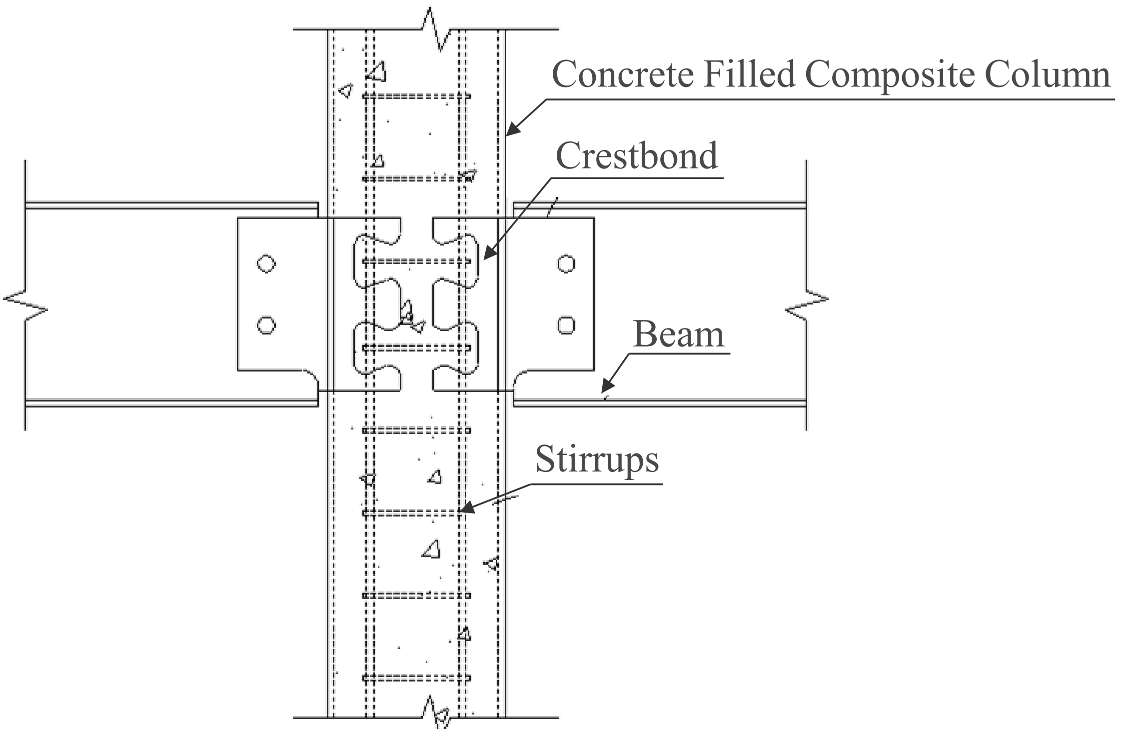


**Figure 1.** Crestbond shear connector as load transfer device [3].

Given the possibility of the widespread use of this constructive solution and the growing concern with the safety and integrity of the structures, it is essential to study it also in fire, since, as the temperature rises, the resistance and stiffness of steel and concrete degrade, which can lead to structural failure or states of excessive deformation. For the specific case of the load transfer device studied, it is also noteworthy that the thermal expansion can cause excessive cracking of concrete, especially in the connection region, resulting in a reduction in the resistance of the CFCC.

Thus, in this work, a numerical study was carried out, using Abaqus software, on the thermomechanical behavior of the Crestbond shear connector used as a load transfer device in CFCC of circular cross section, considering the dimensional variation of the steel tube, different load levels, the effect of thermal expansion and the comparison with the use of plates without cuttings (Shear Flats).

## 2 LITERATURE REVIEW

The Crestbond shear connector (Figure 2) consists of a steel plate with regular cuttings, which favor the arrangement of the reinforcements and promote the confinement of concrete [9]. Although this type of composite dowel connection was conceived for application in composite beams [10]–[13], its application as a device for transferring loads in composite columns (Figure 1) has shown to be promising.

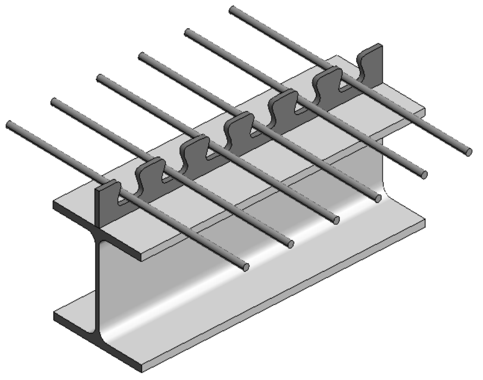

**Figure 2.** Composite beam with Crestbond shear connector [9].

Oliveira et al. [3] and Cardoso [7] carried out an experimental study composed of CFCCs of circular and rectangular cross section in which the Crestbond shear connector was applied as a load transfer device. The tests were conducted based on the guidelines in annex B of EN 1994-1-1:2004 [14] for standard push test (Figure 3a), and the results obtained were used for the development of a representative numerical model [4]–[6] (Figure 3b). This finite element (FE) model was created in Abaqus using 8-node brick elements (C3D8), with seed size of 8 mm in the Crestbond and surroundings. A classic elastoplastic model was used to simulate the steel and the Concrete Damaged Plasticity model was used to simulate the concrete. The load was gradually increased by Riks method.

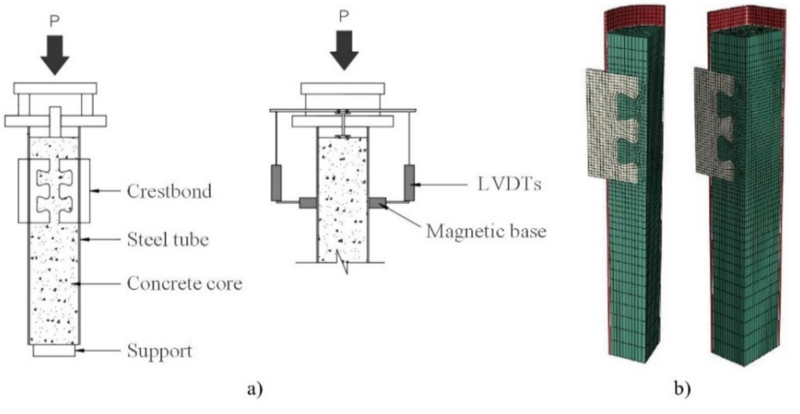


**Figure 3.** a) Test setup [7] and b) numerical model [4] in ambient temperature.

Although this structural solution is promising, there is no research on its structural behavior in fire, being an alternative, for the constitution of numerical models, to add the load transfer devices in the validated numerical models of CFCC in fire.

The numerical models of CFCC in fire developed by Hong and Varma [15] and Wang and Young [16] in Abaqus software basically comprise an uncoupled thermomechanical analysis, in which, in the first step (thermal analysis), the model is discretized with 8-node linear brick elements (DC3D8) and, in the later step (mechanical analysis), which starts from the results achieved in the first step, C3D8 elements are used. Espinós et al. [17] and Pires et al. [18] used the same methodology above, however, Espinós et al. [17] used elements with reduced integration in the mechanical analysis step and Pires et al. [18] used the elements C3D20R and DC3D20 of 20 nodes, in the first and second steps, respectively. Laím et al. [19] performed a coupled thermomechanical analysis, so that initially axial loading is applied and then the temperature rise is considered. The model was discretized with 8-node displacement and temperature solid elements with reduced integration (C3D8RT).

In these works, it is observed the need for adjustments in the models present in the technical standards that represent the characteristics of the materials with the increase in temperature, especially of concrete, which is confined by the steel tube, and the definition of an initial imperfection level aiming the calibration of the FE model.

## 3 NUMERICAL MODELING

Given the absence of experimental CFCC models with Crestbond shear connectors as a load transfer device in fire, a numerical CFCC model was initially developed, which was validated with experimental results and, subsequently, the shear connectors were added to the validated model.

### 3.1 CFCC at elevated temperatures

The CFCC FE model in fire was developed in Abaqus software, based on the methodology employed by Espinós et al. [17] and considering the symmetry of the models. The analysis was performed in an uncoupled manner and in two sequential steps, the first being a thermal analysis and the second a mechanical analysis with prescribed temperatures, according to the previous analysis.

In the thermal analysis step, the properties of steel and concrete were defined according to EN 1992-1-2:2004 [20], EN 1993-1-2:2005 [21] and EN 1994-1-2:2005 [22], the model was subjected to standard fire [23]-[24] and, at the materials interface, a thermal conductivity coefficient equal to 200 $W/m^2K$ [17] was adopted. The models were discretized with DC3D8 elements, with seed size of 10 mm, defined through a mesh refinement study.

In the mechanical analysis step, the data from the previous analysis were imported and, for the concrete, in addition to the properties provided in the European Standard, those provided in Lie [25] were considered. In this step, the FE models were discretized with C3D8R elements, and a thermal expansion coefficient equal to $6.10^{-6}$ °$C^{-1}$ was considered for concrete, according to Hong and Varma [15].

An isotropic elastoplastic model with the Von Mises yield criterion was used to representing the mechanical behavior of steel and the Concrete Damaged Plasticity (CDP) model was selected for characterizing the mechanical behavior of concrete. The input parameters used in CDP model are presented in Table 1.

**Table 1.** Parameters adopted in CDP model.

| Parameter | Value |
|---|---|
| Dilation angle ($\psi$) | 36 ° |
| Biaxial/uniaxial compressive strength ratio ($\sigma_{b0}/\sigma_{c0}$) | 1.16 |
| Parameter for defining the yield surface ($K$) | 0.8 |
| Viscosity parameter ($\mu$) | 0.1 |

#### 3.1.1 Validation of thermal analysis

The validation of the FE model in the thermal analysis step consisted of comparing the evolution of temperature over time of exposure to fire observed in the numerical simulation and observed in the test. In the Figure 4, the temperatures obtained from the FE model were compared with those measured at the external surface and at various depths of the column 3 from Wang and Young [16]. It was observed that there is a good agreement between the FE and the test results, with the exception of the initial stages of fire exposure, for deeper locations in the concrete core. This difference might be due the water evaporation and the mass transfer that were simulated approximately by modifying the specific heat.

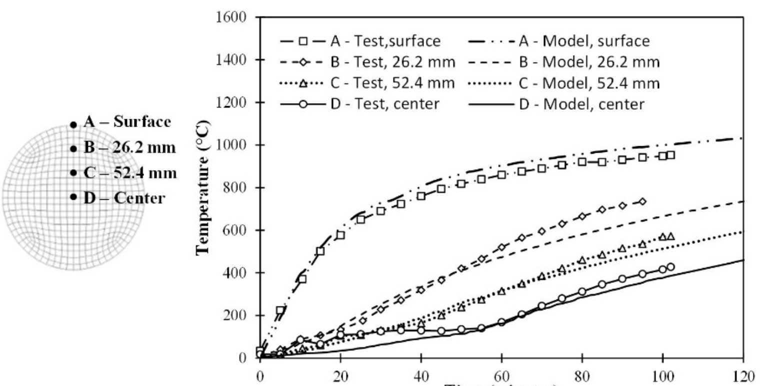


**Figure 4.** Time-temperature relationships obtained experimentally by Wang and Young [16] and numerically in this paper for column 3.

### 3.1.2 Validation of decoupled thermal and mechanical analyzes

To validate the decoupled thermal and mechanical analyses, the models C-05, C-13 and C-17 from Espinós et al. [17] were simulated. These models consist of three parts: the concrete core, the steel tube and the loading plate (Figure 5). The CFCC top, which was in contact with the rigid loading plate, had free translation and the CFCC bottom had fixed translation. An initial imperfection of 0.1% of the CFCC depth and a friction coefficient equal to 0.55 in the steel-concrete interface were considered. The comparison between the axial displacements measured in the test and predicted by the FE model (Figure 6a), as well as the final deformed configuration (Figure 6b) showed that it is possible to prescribe a model with reasonable precision in relation to the experimental data, despite the high complexity of the numerical simulations and the definition of thermal and mechanical properties of the materials, mainly of the concrete in fire. It should also be noted that the constitutive model of concrete provided by EN 1992-1-2:2004 [20] proved to be more conservative than the Lie's model [25]. Although only the results of model C-17 were presented, similar results and conclusions were observed for models C-05 and C-13.

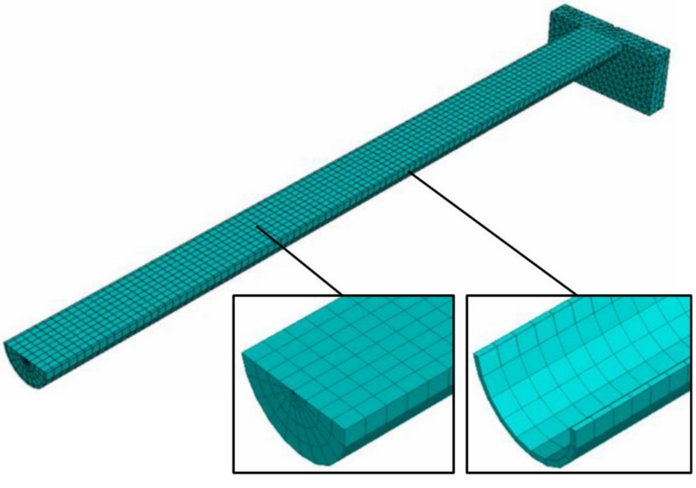

**Figure 5.** FE model of CFCC with loading plate, concrete core and steel tube in detail (Adapted from [17]).

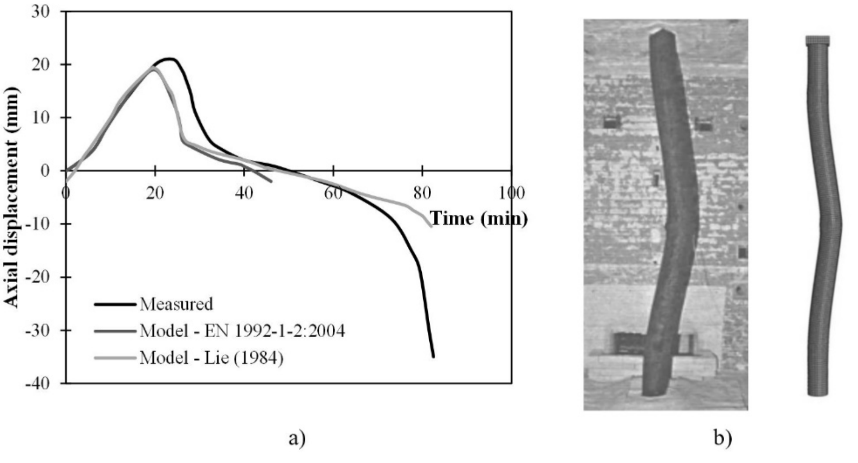


**Figure 6.** Comparison of measured and predicted a) axial displacement and b) deformed configuration for column C-17.

## 3.2 CFCC with load transfer devices at elevated temperatures

The load transfer devices were added to the validated FE models of CFCC in fire and the analysis occurred in the same way as the previous ones, except for the loading, which was applied directly in the shear connectors. They were modeled 3 m CFCCs (Figure 7), considering the symmetry of the models, with external diameters ($D$) of 200, 400 and

600 mm, steel tube with a thickness of 8 mm and load transfer devices (Crestbond and Shear Flat) with height of 292.2 mm and thickness of 12.5 mm, positioned 150 mm from the top of the column (Figure 7a). Using multi-point constraint the load was applied in a reference point (RP) located on the outer face of the connector (Figure 7b) with fixed rotations to simulate a beam-column connection. The CFCC top and botton had the longitudinal translation fixed to simulate its continuity like in an intermediate storey. Figures 7c and 7d show the discretization of the mesh with elements of maximum dimensions equal to 8 mm in the connectors and adjacent concrete with a gradual increase in the longitudinal direction with a length of up to 25 mm at the top end and up to 50 mm at the bottom end.

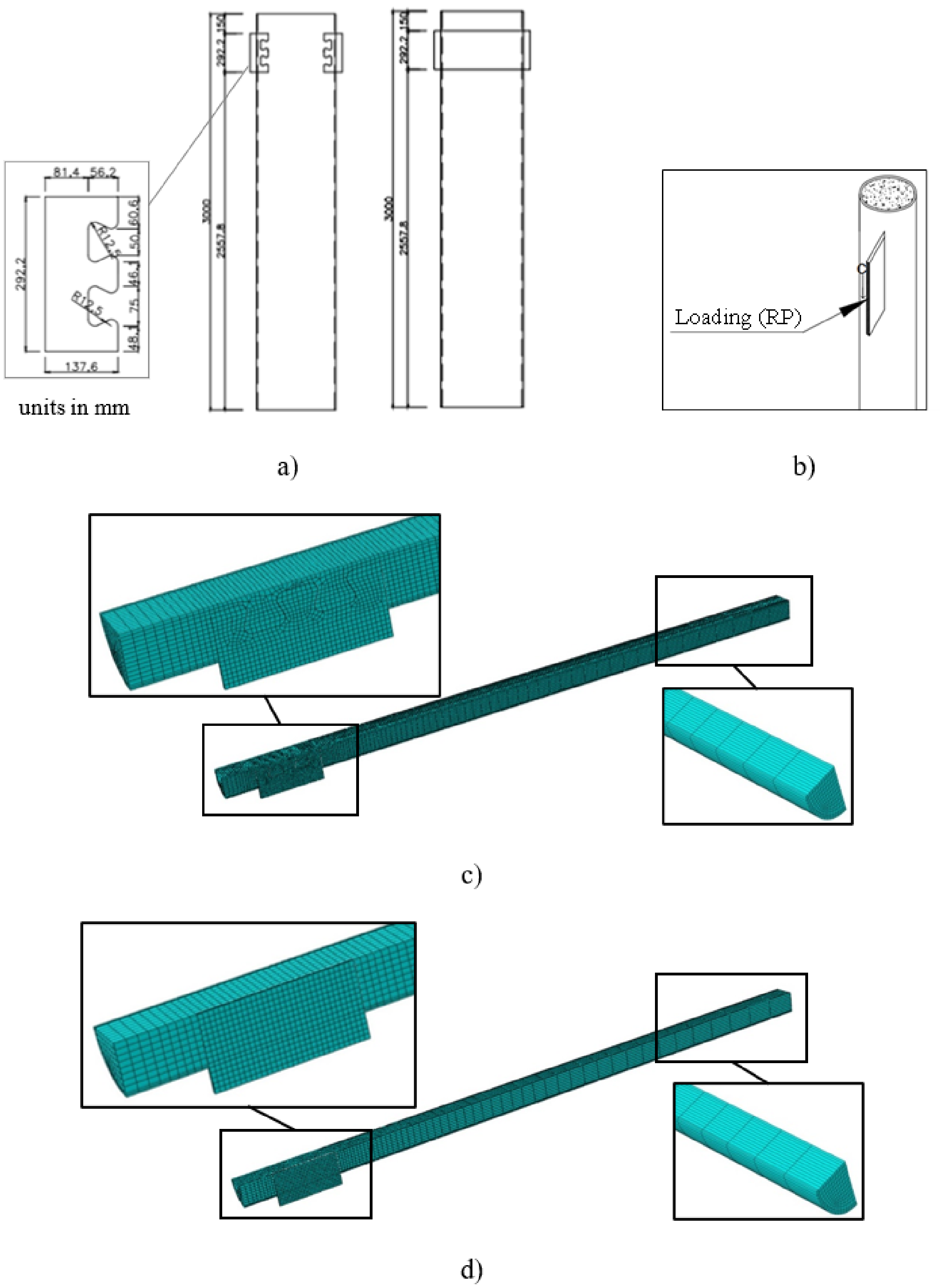


**Figure 7.** Details of a) CFCC with Crestbond and Shear Flat, b) loading point, c) Crestbond FE model and d) Shear Flat FE model.

Loads corresponding to fractions of the design resistance at ambient temperature (676.4 kN) were applied and the constitutive model of Lie [25] was used for the characterization of concrete, since this model favored the convergence of the analysis and the obtaining of the resistance at ambient temperature. A yield strength ($f_y$) of 345 MPa was adopted for the steel of the tube and of the shear connector and a compressive strength ($f_c$) of 40 MPa was adopted for the concrete.

Figure 8 presents the results obtained in the numerical simulations for the different diameters and loading levels studied, for the Crestbond shear connector and for the Shear Flat. For the failure time was considered the processing time in the FE models until convergence. Then, the models were analyzed to verify the failure mode, considering the displacement of the connector external edge, strain and stress in steel and concrete. It is possible to observe that, for the diameter of 200 mm, there is no difference between the results obtained for Crestbond and for Shear Flat for load levels above 50% and that the Crestbond is slightly more resistant than Shear Flat for load levels below 50%. It can also be noted that, for the diameters of 400 and 600 mm, the Shear Flat is more resistant than Crestbond for all load levels. These results are due to the greater mass of the Shear Flat, which results in a slower increase in temperature in this device compared to the Crestbond and, consequently, the lowest reduction in the yield strength of the connector steel ($f_{y,connector}$); and due to the distribution of stresses in a larger area in the concrete core for the Crestbond in 200 mm diameter CFCC and for the Shear Flat in the other cases.

The contact length of the Crestbond with the concrete core is around 383 mm regardless of the CFCC diameter, and the contact length of the Shear Flat with the concrete core is 184 mm for the 200 mm diameter CFCC, 384 mm for the 400 mm diameter CFCC e 584 mm for the 600 mm diameter CFCC, i.e., the greater the CFCC diameter the greater the contact length of the Shear Flat. And, the greater the contact length, the greater the area where the stress is distributed and the greater the resistance of the connection, which occurs for Crestbond for the 200 mm diameter CFCC and in the Shear Flat in the other cases.

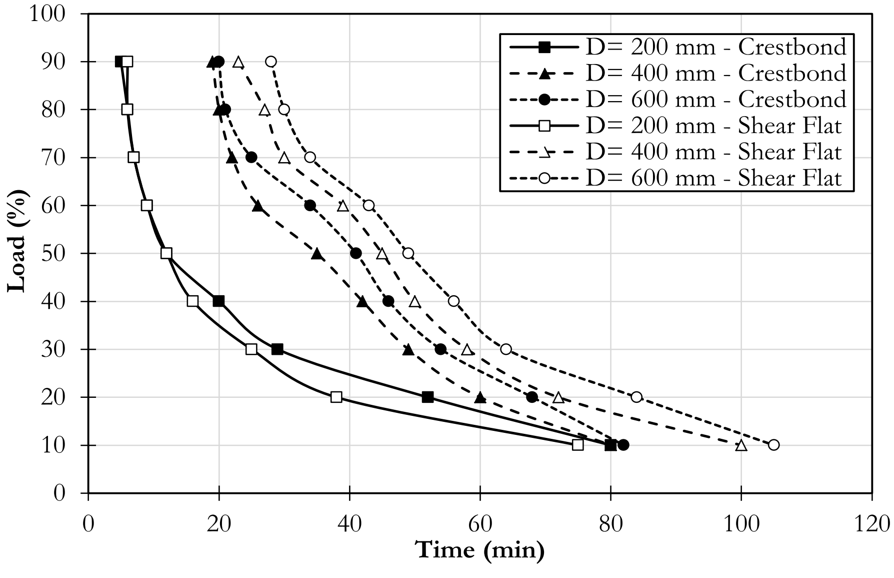


**Figure 8.** Time-load relationships obtained numerically for CFCC with load transfer devices.

Figures 9 to 12 show the temperature distribution, von Mises stresses, concrete tensile stresses and the deformed configuration of 400 mm diameter CFCCs with Crestbond shear connector and with Shear Flat for the loading levels of 30 and 50%, as well as the displacement of the central point of the external surface of the connector over time of fire exposure. It was observed that, with the increase in temperature, the consequent reduction in strength and stiffness of the steel tube and the thermal expansion of the CFCC components there was a separation between the concrete core and the steel tube during the fire exposure (Figures 9c, 10d, 11c and 12c) and the reduction of the concrete confinement, wherein the Crestbond and the Shear Flat were responsible for maintaining the steel tube and the concrete connected.

It was observed the shear failure of the external part of the load transfer devices (Figure 10d) in the cases where the reduction factor for yield strength ($k_y$), due to the increase in temperature, reaches a value equal to or less than the load level; this failure mode is the same one that occurs at ambient temperature. For the other cases, it was observed a concrete related failure (Figures 9c, 11c and 12c), which is due the loss of the concrete confinement, the tensile stresses resulting from the thermal effects and the deformations resulting from the load transfer from the connector to the concrete core. It is noteworthy that the shear failure of the external part of the connector is more common at low load levels (≤ 30%), in which higher temperatures are observed at the interface between the connector and the steel tube and hence greater reduction in the yield strength of the connector steel ($f_{y,connector}$).

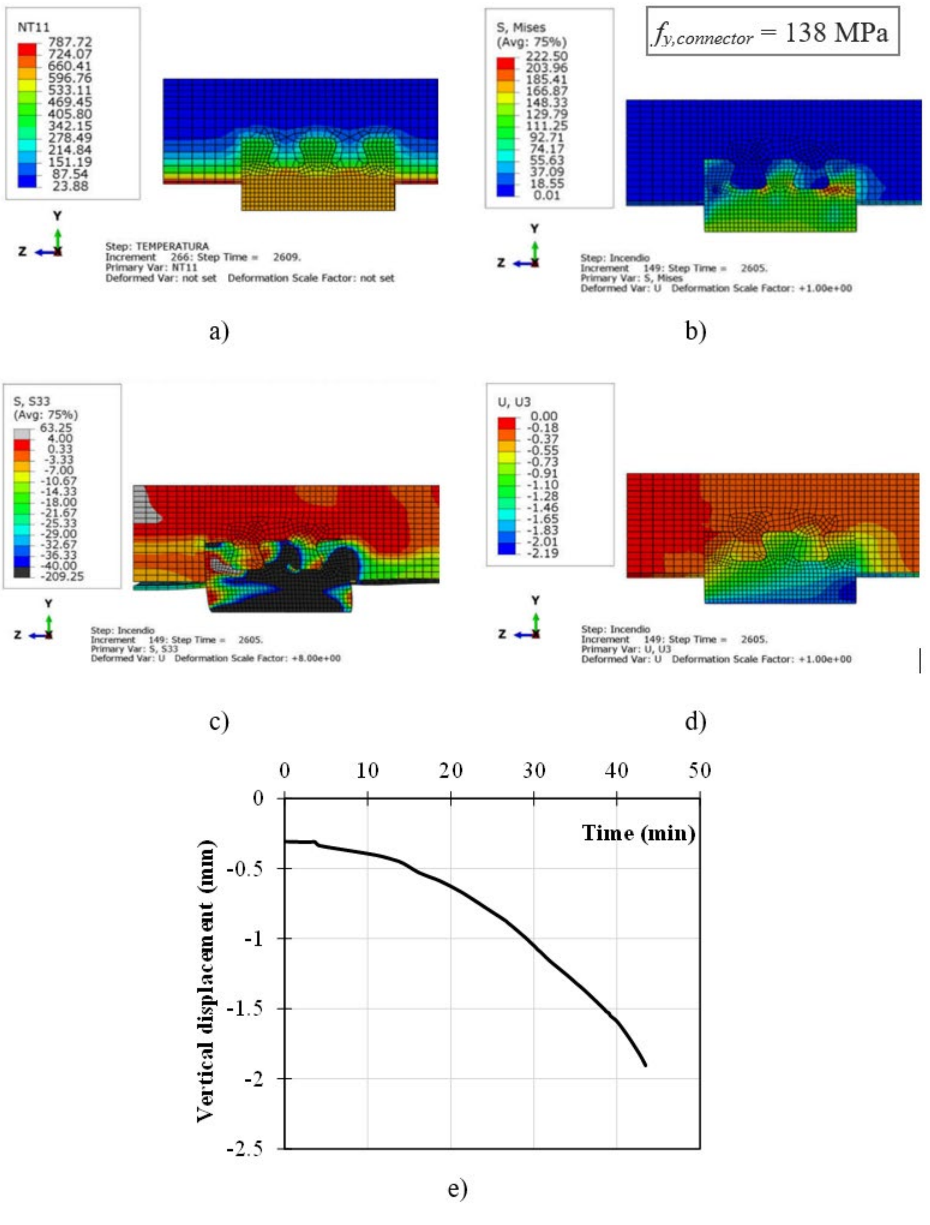


**Figure 9.** a) Temperature distribution, b) von Mises stresses, c) concrete tensile stresses, d) deformed configuration and e) displacement of the central point of the external surface of the connector of 400 mm diameter CFCCs with Crestbond shear connector for the loading level of 30%.

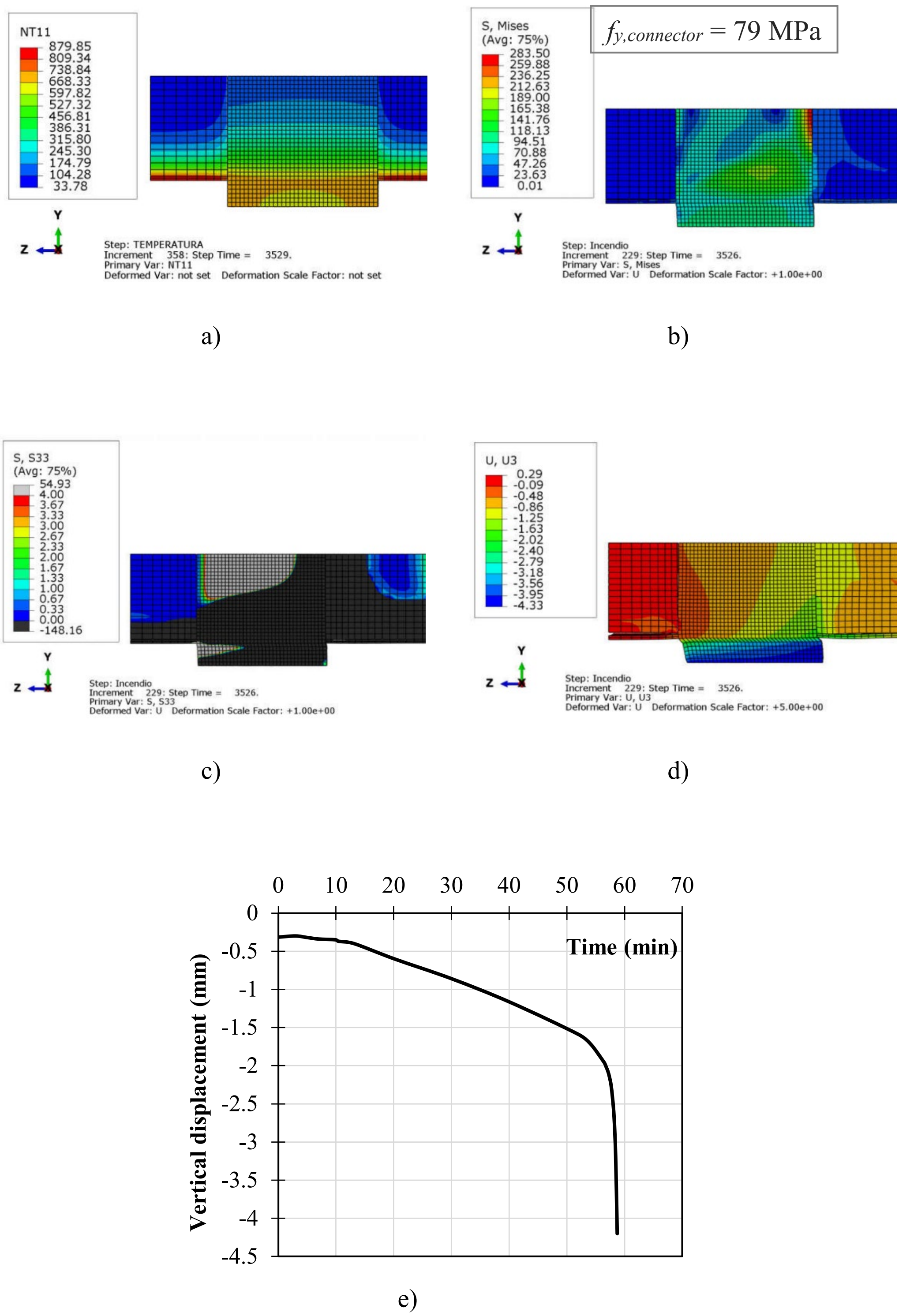


**Figure 10.** a) Temperature distribution, b) von Mises stresses, c) concrete tensile stresses, d) deformed configuration and e) displacement of the central point of the external surface of the connector of 400 mm diameter CFCCs with Shear Flat for the loading level of 30%.

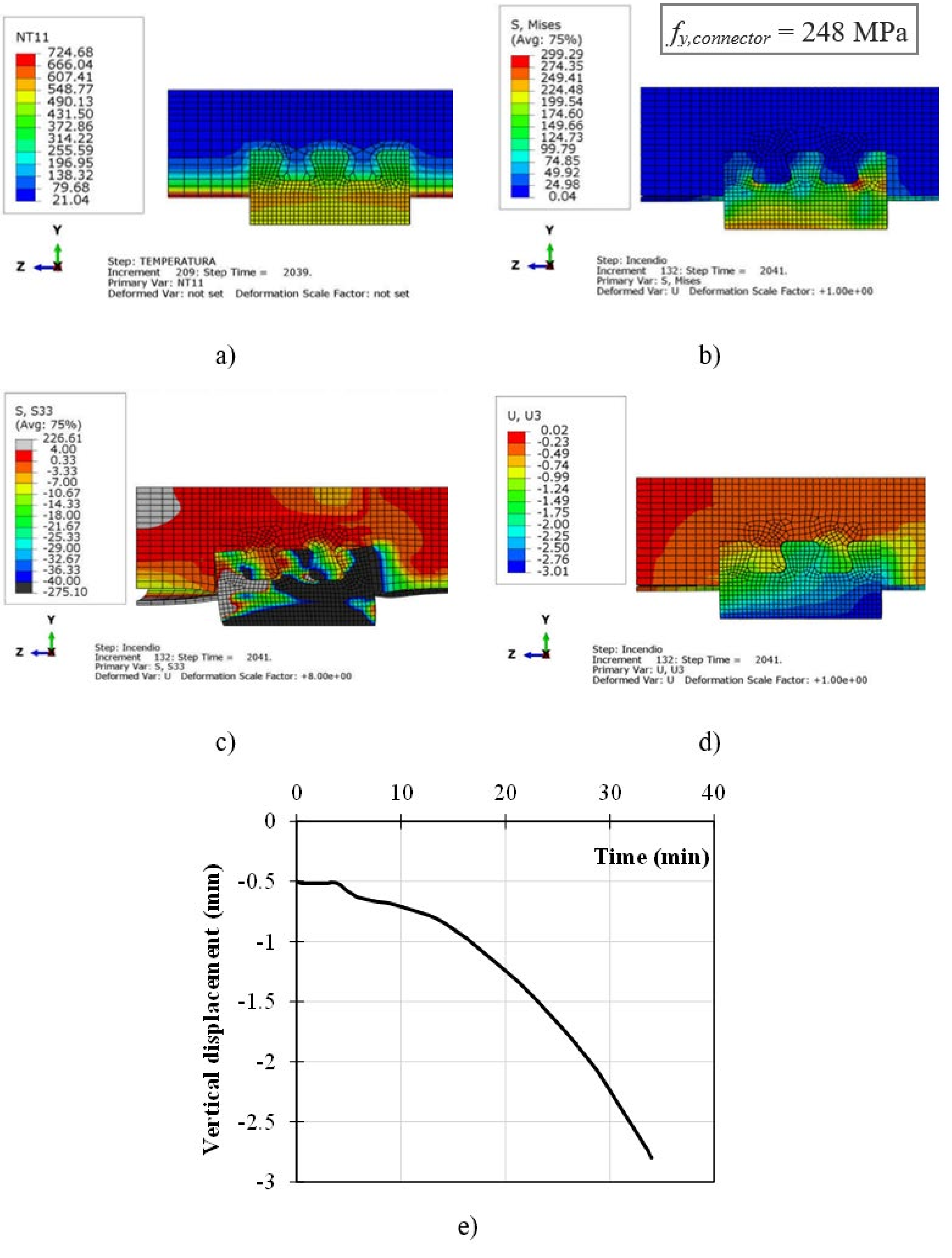


**Figure 11.** a) Temperature distribution, b) von Mises stresses, c) concrete tensile stresses, d) deformed configuration and e) displacement of the central point of the external surface of the connector of 400 mm diameter CFCCs with Crestbond shear connector for the loading level of 50%.

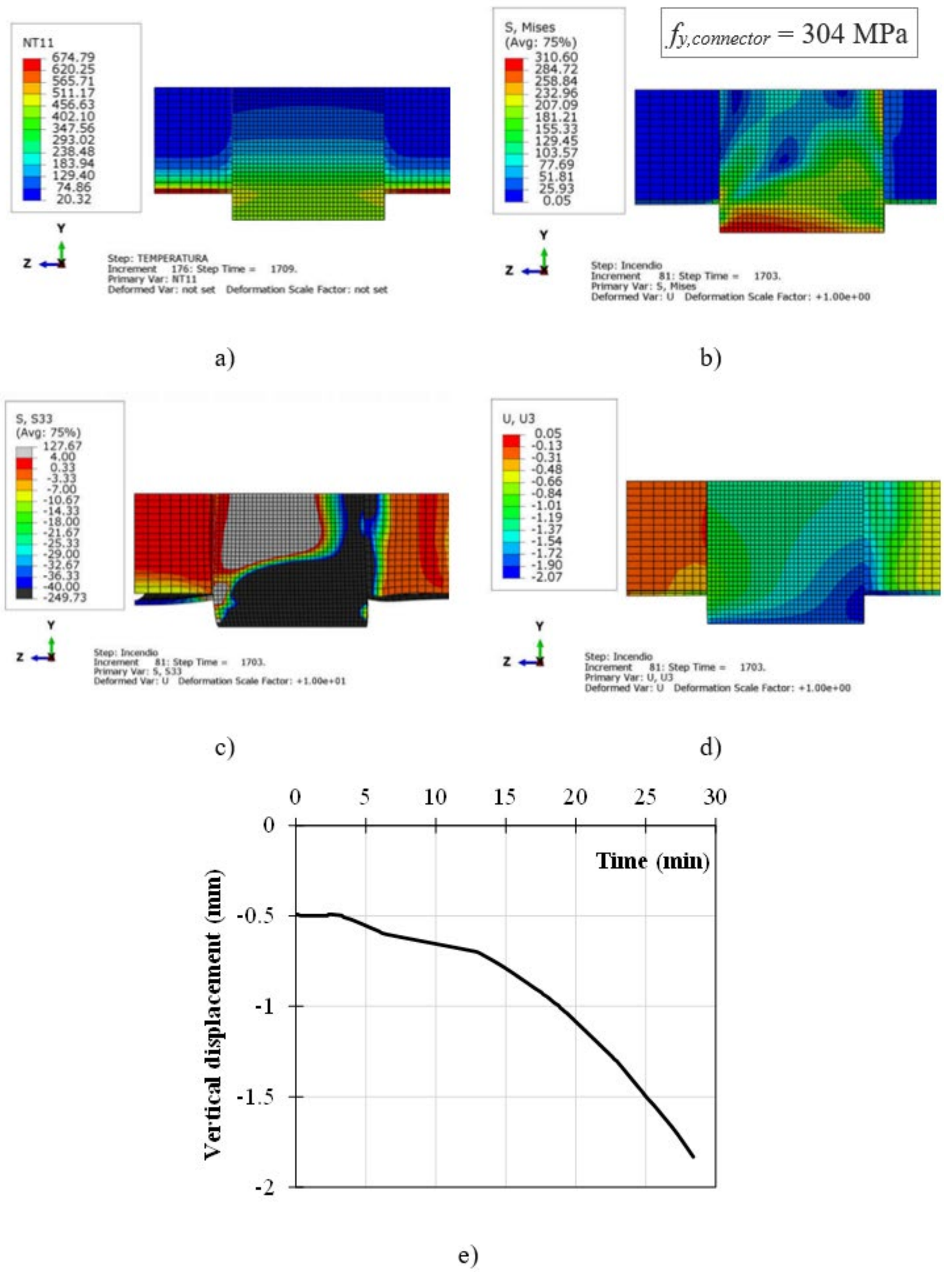


**Figure 12.** a) Temperature distribution, b) von Mises stresses, c) concrete tensile stresses, d) deformed configuration and e) displacement of the central point of the external surface of the connector of 400 mm diameter CFCCs with Shear Flat for the loading level of 50%.

## 4 CONCLUSIONS

This paper presents the numerical modeling of CFCCs with load transfer devices (Crestbond and Shear Flat) in fire. With the numerical simulations it was possible to evaluate the resistance and the structural behavior of the studied solutions in face of the temperature rise.

From the curves that relate the failure time and the load level, it was observed that, for smaller diameters, the behavior of Crestbond and Shear Flat is very similar and that, for larger diameters, the Shear Flat proved to be slightly more resistant, given its greater mass and greater contact area with the concrete core. It was also observed that, for low load levels (≤ 30%), the failure mode is mostly related to the connector, given the reduction of its resistance with the increase in temperature, and that, for load levels above 30%, the failure mode is related to the loss of confinement of the concrete.

No studies were found in which the cost of the two studied solutions (Shear Flat and Crestbond) is compared. However, for larger diameters and, considering a symmetric cut to obtain Crestbond connectors, the cost can be lower than for Shear Flat. For several connections in different radial directions, the Crestbond is a simpler application than the Shear Flat and favors the use of transverse reinforcement. Although Shear Flat has a slightly higher resistance than Crestbond and only with the thermomechanical analyzes performed, it is not possible to conclude which is the best solution in fire and additionally experimental analyzes should be performed. However, the similar performance observed for the load transfer devices analyzed leads to the conclusion that the composite dowel shear connector Crestbond is a potential alternative to the Shear Flat, already standardized by Eurocode.

## ACKNOWLEDGEMENTS

The authors thank FAPEMIG (Fundação de Amparo à Pesquisa do Estado de Minas Gerais), CAPES (Coordenação de Aperfeiçoamento de Pessoal de Nível Superior), CNPq (Conselho Nacional de Desenvolvimento Científico e Tecnológico) and UFMG (Universidade Federal de Minas Gerais) for their financial support in this research.

## REFERENCES

[1] L. H. Han, W. Li, and R. Bjorhovde, "Developments and advanced applications of concrete-filled steel tubular (CFST) structures: Members," *J. Construct. Steel Res.*, vol. 100, pp. 211–228, Sep 2014, http://dx.doi.org/10.1016/j.jcsr.2014.04.016.

[2] W. L. A. Oliveira, “Análise teórico-experimental de pilares mistos preenchidos de seção circular,” Ph.D. dissertation, Escola Eng. de São Carlos, Univ. de São Paulo, São Carlos, SP, Brasil, 2008.

[3] H. M. S. Oliveira et al. “Uso do conector Crestbond em pilares mistos formados por perfis tubulares de aço preenchidos com concreto,” in *XXXVI Jornadas Sudamericanas de Ingenieria Estructural*, Montevidéu, 2014.

[4] O. P. Aguiar, “Estudo do comportamento de conectores Crestbond em pilares mistos tubulares preenchidos com concreto,” M.S. thesis, Dept. Eng. Estrut., Univ. Federal de Minas Gerais, Belo Horizonte, MG, Brasil, 2015.

[5] O. P. Aguiar, R. B. Caldas, H. M. S. Oliveira, and R. H. Fakury, "Estudo de conectores Crestbond em pilares mistos preenchidos com concreto," *Rev. Estrutura Aco*, vol. 4, no. 3, pp. 181–199, Dec 2015.

[6] O. P. Aguiar, R. B. Caldas, F. C. Rodrigues, R. H. Fakury, and G. S. Veríssimo, "Crestbond Shear connectors for load transfer in concrete filled tube columns," *Rev. IBRACON Estrut. Mater.*, vol. 11, no. 5, pp. 960–965, Sep/Oct 2018, http://dx.doi.org/10.1590/s1983-41952018000500004.

[7] H. S. Cardoso “Avaliação do comportamento de conectores constituídos por chapas de aço com recortes regulares – ênfase em conectores de geometria Crestbond aplicados em pilares mistos,” Ph.D. dissertation, Dept. Eng. Estrut., Univ. Federal de Minas Gerais, Belo Horizonte, MG, Brasil, 2018.

[8] H. S. Cardoso, O. P. Aguiar, R. B. Caldas, and R. H. Fakury, "Composite dowels as load introduction devices in concrete-filled steel tubular columns," *Eng. Struct.*, vol. 219, pp. 1–15, Sep 2020., http://dx.doi.org/10.1016/j.engstruct.2020.110805.

[9] G. S. Veríssimo, “Desenvolvimento de um conector de cisalhamento em chapa dentada para estruturas mistas de aço e concreto e estudo do seu comportamento,” Ph.D. dissertation, Dept. Eng. Estrut., Univ. Federal de Minas Gerais, Belo Horizonte, MG, Brasil, 2007.

[10] C. M. Dutra, “Estudo do comportamento estrutural do conector Crestbond considerando variações geométricas e mecânicas,” M.S. thesis, Dept. Eng. Civil, Univ. Federal de Viçosa, Viçosa, MG, Brasil, 2014.

[11] A. R. Alves, I. B. Valente, W. B. Vieira, and G. S. Veríssimo, “Avaliação do comportamento de vigas mistas com conector Crestbond,” in *5th Jornadas Portuguesas de Engenharia de Estruturas*, Lisboa, 2014.

[12] A. R. Alves, I. B. Valente, W. B. Vieira, and G. S. Veríssimo, "Prospective study on the behavior of composite beams with an indented shear connector," *J. Construct. Steel Res.*, vol. 148, pp. 508–524, Sep 2018, http://dx.doi.org/10.1016/j.jcsr.2018.06.015.

[13] M. C. Petrauski, “Simulação numérica do comportamento de vigas mistas de aço e concreto com conectores Crestbond,” M.S. thesis, Dept. Eng. Civil, Univ. Federal de Viçosa, Viçosa, MG, Brasil, 2016.

[14] European Committee for Standardization. *Eurocode 4: Design of Composite Steel and Concrete Structures – Part 1-1: General Rules and Rules for Buildings*, EN 1994-1-1, 2004.

[15] S. Hong and A. H. Varma, "Analytical modeling of the standard fire behavior of loaded CFT columns," *J. Construct. Steel Res.*, vol. 65, pp. 54–69, Jan 2009, http://dx.doi.org/10.1016/j.jcsr.2008.04.008.

[16] K. Wang and B. Young, "Fire resistance of concrete-filled high strength steel tubular columns," *Thin-walled Struct.*, vol. 71, pp. 46–56, Oct 2013, http://dx.doi.org/10.1016/j.tws.2013.05.005.

[17] A. Espinós, M. L. Romero, and A. Hospitaler "Finite element analysis of the fire behavior of concrete filled circular hollow section columns," in *Finite element modelling of innovative concrete-filled tubular columns under room and elevated temperature - European Project FRISCC: Fire Resistance of Innovative and Slender Concrete Filled Tubular Composite Columns*, A. Espinós and M. L. Romero, Editorial Universitat Politècnica de València, 2013, pp. 3–12.

[18] T. A. C. Pires, J. P. C. Rodrigues, J. J. R. Silva, and I. Garcia "Estudo paramétrico do comportamento ao fogo de colunas tubulares de aço preenchidas com betão," in *IX Cong. Construção Metálica e Mista & I Cong. Luso-brasileiro de Construção Metálica Sustentável*, Porto, 2013.

[19] L. M. S. Laím, J. P. Rodrigues, A. M. Correia, and T. A. Pires "Numerical analysis of composite steel-concrete columns under fire conditions," in *Finite element modelling of innovative concrete-filled tubular columns under room and elevated temperature - European Project FRISCC: Fire Resistance of Innovative and Slender Concrete Filled Tubular Composite Columns*, A. Espinós and M. L. Romero, Editorial Universitat Politècnica de València, 2013, pp. 33–44.

[20] European Committee for Standardization. *Eurocode 2: Design of concrete structures – Part 1-2: General rules – Structural fire design*, EN 1992-1-2, 2004.

[21] European Committee for Standardization. *Eurocode 3: Design of Steel Structures – Part 1-2: General Rules – Structural Fire Design*, EN 1993-1-2, 2005.

[22] European Committee for Standardization. *Eurocode 4: Design of composite steel and concrete structures – Part 1-2: General rules – Structural fire design*, EN 1994-1-2, 2005.

[23] Associação Brasileira de Normas Técnicas. *Fire-resistance requirements for building construction elements – Procedure*, NBR 14432, 2005.

[24] International Organization for Standardization. *Fire-resistance tests: elements of building construction - part 1.1: general requirements for fire resistance testing*, ISO 834, 1999.

[25] T. T. Lie, "A procedure to calculate fire resistance of structural members," *Fire Mater.*, vol. 8, pp. 40–48, Mar 1984, http://dx.doi.org/10.1002/fam.810080108.

**Author contributions:** Luiz Fernando Pereira do Prado developed this study under the guidance of Rodrigo Barreto Caldas; Larice Gomes Justino Miranda contributed in the analysis of the results and in the conclusion.

**Editors:** Bernardo Horowitz, Guilherme Aris Parsekian